Engineering Carbon-Based Porous Materials from Selected Precursors for High-Capacity CO_2 Capture

Bing Jun Zhu

Thesis submitted in part fulfilment of the requirement for the degree of Doctor of Philosophy

University College London

January 2015

I, Bing Jun Zhu, confirm that all the content presented in this thesis is based on my own work. Where information is from the literature or work by collaborators, I confirm that these have been referenced and acknowledged in the thesis.

Signed .....

Date .....

Abstract

The mitigation of climate change is one of the major global challenges in the 21st Century. Carbon capture and storage (CCS) is a promising technology to effectively reduce anthropogenic CO_2 emissions into the Earth's atmosphere. There are various candidate materials for CO_2 capture but each has its own advatanges and disadvantages. Carbon-based materials are of low-cost and have relatively high cyclicity for CO_2 and its porous structure and surface functional groups can be tailored to improve CO_2 capture performance. Effective but low-cost carbon precursors need to be explored for potential mass production in the furture. This research aims to explore various polymeric, biomass and graphitic materials as the precursors for the development of effecive carbon sobents for CO_2 capture. In addition, the influence of porous structures and chemical dopants on CO_2 sorption are also experimentally studied in relation to the porosities and surface chemistry of the sorbents.

Five distinct synthesis approaches are explored comparatively to determine the potential of polymeric, biomass and graphitic materials as precursors for effective carbon sorbents. These approaches include a novel method of producing millimetre-sized carbon spheres from poly(acrylonitrile-co-acrylamide)/DMSO solution, chemical activation of London Plane leaves, spruce pine cones and graphite oxide, and ball-milling of graphite. The work on the polymer-derived carbon spheres produced desirable carbon macro-spheres with radially channelled and hierarchically porous structures, via a "one-pot" solvent exchange process. The structure shows excellent CO_2 capacity of 16.7 wt% at 25 ℃ and under 1 bar CO_2, enhanced by rich nitrogen doping and microporosities. The biomass-derived carbon sorbents further clarify the influence of metal-dopants, inherited from the biomass precursors, on CO_2 adsorption. It was noted that besides nitrogen dopant and ultramicropores (<0.7 nm), residual calcium and magnesium in biomass-derived carbon also enhanced CO_2 adsorption on carbon sorbents. The CO_2 uptake of a pine cone-derived carbon sorbent (20.9 wt%) has matched the highest CO_2 uptake (21.2 wt%) reported in the literature at 25 ℃ and under 1 bar CO_2, though the latter has a relatively large ultramicropore volume. To further clarify the influence of microporous structure and chemical dopants on CO_2 uptake,

graphite oxide (GO) and ball-milled graphite (BG) were studied as graphitic precursors as these have known chemical structures and their resulting sorbents contain no other chemical dopants. The characterisation results show chemical activation with potassium hydroxide can develop a similar porous structure in GO- and BG-derived carbon, compared with those of polymer- and biomass- derived carbon. However, the former show comparatively lower CO_2 capture capacities under the same test conditions (25 ℃ and 1 bar CO_2), which is believed to be due to less well-developed ultramicroporous structure and the absence of chemical dopants.

Based on the present experimental data, further analysis reveals that there is a difference between specific surface area calculated by the Brunauer-Emmett-Teller (BET) equation and the Density Functional Theory (DFT) model. The cause of this is the intrinsic difference in the method of calculation, where the BET equation assumes a flat and homogeneous surface, while the DFT model takes the pore shape into consideration. Furthermore, both CO_2 uptake and specific CO_2 uptake (CO_2 uptake/porosity) are plotted against three porosity parameters, namely BET surface area, total pore volume and ultramicropore volume. The plots show those samples with higher nitrogen and metal contents exihibit higher specific CO_2 uptakes. To extend the interpretation of results, an Artificial Neural Network (ANN) is adopted as a simulation tool to study the influence of ultramicropore, nitrogen and metal dopants on CO_2 uptake. Characteristic results from both the present work and the literature are used as the input data for the simulation. The simulated results show CO_2 uptake increases considerably with increasing ultramicropore volume and metal content. However, the nitrogen content has relatively limited influence, compared with the former two, contrary to common belief.

Finally, several future lines of work are proposed to further improve the performance of the materials. For the synthesis of carbon spheres, DMSO can be added into the water bath to slow the solvent exchange process. As a result, the macroporous strucure of the sphere can be modified to enhance its mechanical strength. For the study on the biomass-derived carbon, several other leaves can also be used as carbon precursors. The porosities, chemical compositions and CO_2 uptakes of the cabon sorbents derived from these leaves can be compared with those of the London Plane leaf-derived carbon, to further clarify the influence of the biological structures and chemical properties of

biomass precursors on the resulting carbon. For the work on ANN, the simulation is limited by the available experimental data for metal-doped carbon. The accuracy of prediction by ANN can be further improved when more experimental data are reported in the literature and used for training the network.

Acknowledgements

I would like to express my sincere gratitude to my primary supervisor Prof. Zhengxiao Guo for his guidance and support throughout my research in this project. He has been very helpful and patient in many discussions on my experimental work. More importantly, I appreciate his persistence in the fundamental understanding of scientific problems and his attitude of digging into the root of the problem. I am also grateful for the helps and advices from my secondary supervisor Prof. Julian Evans. I will miss all the interesting "lunchtime discussion/argument" in the last four years.

I would like to thank my colleagues in Xiao's group for their help in the past four years. I really enjoy all the group activities with everyone. I will keep all the cheerful time in heart that we spend on organising conferences and attending seminars. I will also cherish all the joyful moments in our dinner and pub events together. Moreover, I would like to thank all the technical and supporting members of staff in UCL Chemistry for their instructions on operating departmental facilities, such as SEM, TEM, XRD, XPS and FTIR.

I would like to further thank all my friends outside the university for their moral support and encouragement since my arrival in the UK. A special thank to my landlord and landlady for offering me a warm and comfortable place to stay for my four-year study (particularly with an extremely favourable rent!).

Last but not least, I would like to thank my parents for their selfless dedication to my education in past years. Without their endless care and support, it would not be possible for me to finish the last twenty-one-year's study since my primary school.

Table of contents

Abbreviations

Full	Abbreviation
Acrylamide	AM
Acrylonitrile	AN
Azoisobutyronitrile	AIBN
Ball-milled Graphite	BG
Brunauer-Emmett-Teller	BET
Carbon Capture and Storage	CCS
Diethanolamine	DEA
Dimethyl Sulfoxide	DMSO
Fourier Transform Infrared Spectroscopy	FTIR
Gigatones	Gt
Goddard Institute of Space Studies	GISS
Graphite Oxide	GO
Heat of Adsorption	HoA
Integrated Gasification Combined Cycle	IGCC
Intelligent Gravimetric Analyser	IGA
Intergovernmental Panel on Climate Change	IPCC
International Energy Agency	IEA
Metal-organic frameworks	MOFs
Methyldiethanolamine	MDEA
Monoethanolamine	MEA
National Aeronautics and Space Administration	NASA
N-methyl-2-pyrrolidone	NMP
Non-Local Density Functional Theory	NLDFT
Polyacrylamide	PAM
Polyacrylonitrile	PAN
Pressure Swing Adsorption/Desorption	PSA
Scanning Electron Microscope	SEM
Standard Temperature and Pressure	STP
Temperature Swing Adsorption/Desorption	TSA

The International Union of Pure and Applied Chemistry	IUPAC
Thermogravimetric analyser	TGA
Transmission Electron Microscope	TEM
X-ray Diffractometer	XRD
X-Ray Photoelectron Spectrometer	XPS

List of figure captions

List of tables

Chapter 1:
Introduction

1.1 Aims and objectives

Carbon dioxide capture and storage (CCS) is an environmental technology that aims to reduce global anthropogenic CO_2 emission into the Earth's atmosphere. CCS has found many ways to be adapted into different types of power plant. Many candidate materials have been under intensive study to demonstrate their applications in CCS. The general aim of this Ph.D. project focuses on the study of carbon-based materials and their applications in CO_2 capture. Five distinct studies on polymeric, biomass and graphitic precursors are presented in the following chapters of this thesis. The underlying mechanism that influences CO_2 capture performance is also analysed and presented in the thesis.

The objectives of this Ph.D. project are as follows:

1. To understand the concept of carbon capture and storage, its development, prospects, and impact on human society;

2. To be familiar with state-of-the-art CO_2 capture systems adapted with power plants, potential candidate materials for those systems, and advantages and disadvantages associated with those CO_2 capture materials;

3. To explore various economically feasible carbon precursors (including polymers, biomass, and graphitic materials) to produce effective porous carbon sorbents and test their CO_2 capture capabilities; and

4. To clarify the influence of porous structures and chemical dopants on CO_2 capture performance.

1.2 Overview of carbon capture and storage

1.2.1 The challenge of anthropogenic CO_2 emission

The reduction of CO_2 emissions into the Earth's atmosphere is recognised as one of the major global challenges in the 21st Century. The combustion of fossil fuels for energy applications is considered to be the major cause of anthropogenic CO_2 emissions. Fossil fuels still provide over 85% of the world's energy consumption today and are likely to dominate energy supply for many decades to come.[1]

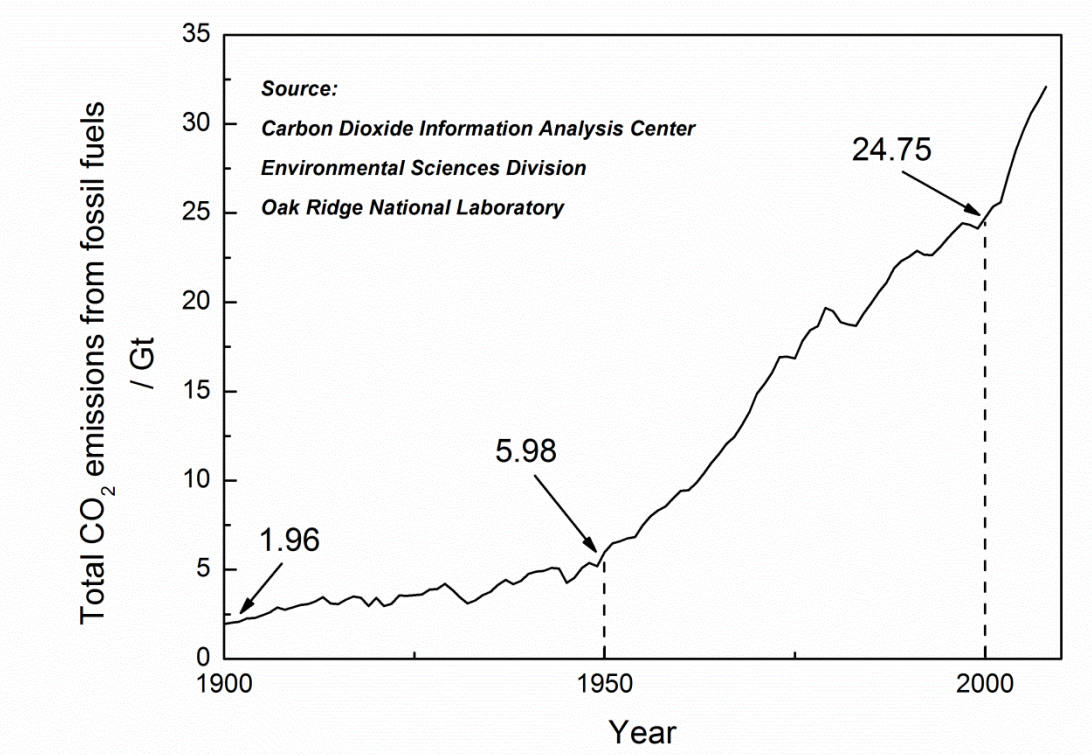

Figure 1: Global CO_2 emissions from fossil fuels in the 20th Century and early 21st Century. The diagram is reproduced according to the original source data.[2]

Figure 1 shows the trend of increasing global CO_2 emissions in the 20th Century and the first decade of the 21st century. It is plotted based on the data from the statistical report prepared by the Oak Ridge National Laboratory, U.S. Department of Energy.[2] The plot clearly shows an accelerated increase of total CO_2 emissions from 1990 to 2000, in particular an increase since 1950. Compared with the amount of CO_2 emission in 1900, the value had tripled by 1950 and increased 12 times by 2000. Since then, the

International Energy Agency (IEA) reported the total CO_2 emission had reached 30.3 Gt in 2010, with 41% of the CO_2 generated from electricity generation and heat, 20% from industry, 22% from transport, 6% from residential and 10% from other sources (including commercial/public services, agriculture, etc.).[3] This suggests that power plants for electricity generation are the major CO_2 emitters among all energy sectors. Moreover, the IEA also reported that 43% of the CO_2 was generated from the burning of coal fuels, while 36% was from oil and 20% from gas.[3] This indicates coal fuels play a dominant role in the current energy market, although efforts have been made to promote coal-to-gas energy transition.[4] Furthermore, in 2013, the IEA warned that the total CO_2 emission had hit a new record high of 31.6 Gt in 2012, and for the first time in several hundred millennia the CO_2 level in the Earth's atmosphere had exceeded 400 ppm.[4]

To sum up, the amount of CO_2 emissions from anthropogenic sources is increasing fast and has been accelerating in recent decades. As a consequence, the level of CO_2 concentration in the Earth's atmosphere is rising. One of the major concerns caused by the ever increasing CO_2 level is its impact on global climate. Although there are still debates on this topic,[5, 6] many studies led by world-leading research institutes and organisations have demonstrated the links between anthropogenic CO_2 emissions and global climate change. In the 2013 climate report prepared by the Intergovernmental Panel on Climate Change (IPCC), it claims "Scientists are 95% certain that humans are the "dominant cause" of global warming since the 1950s".[7, 8]

1.2.2 CO_2 and climate change

CO_2 is referred to as one of the "greenhouse gases" in the Earth's atmosphere along with water vapour, methane and nitrous oxides. Solar radiation is the major source of thermal energy for living-beings on earth. Sunlight passes through the Earth's atmosphere and transmits solar energy to the surface of the earth in the form of solar radiation. The Earth's surface re-emits radiation into the Earth's atmosphere in order to balance the thermal energy accumulated on the Earth's surface. Part of this terrestrial radiation is then absorbed by the greenhouse gas molecules in the Earth's atmosphere. The trapped energy is later radiated back and warms the Earth's surface. This series of energy transfer processes and the consequent warming effect caused by the greenhouse

gas molecules is well known as the "greenhouse effect", which is illustrated in Figure 2. [9]

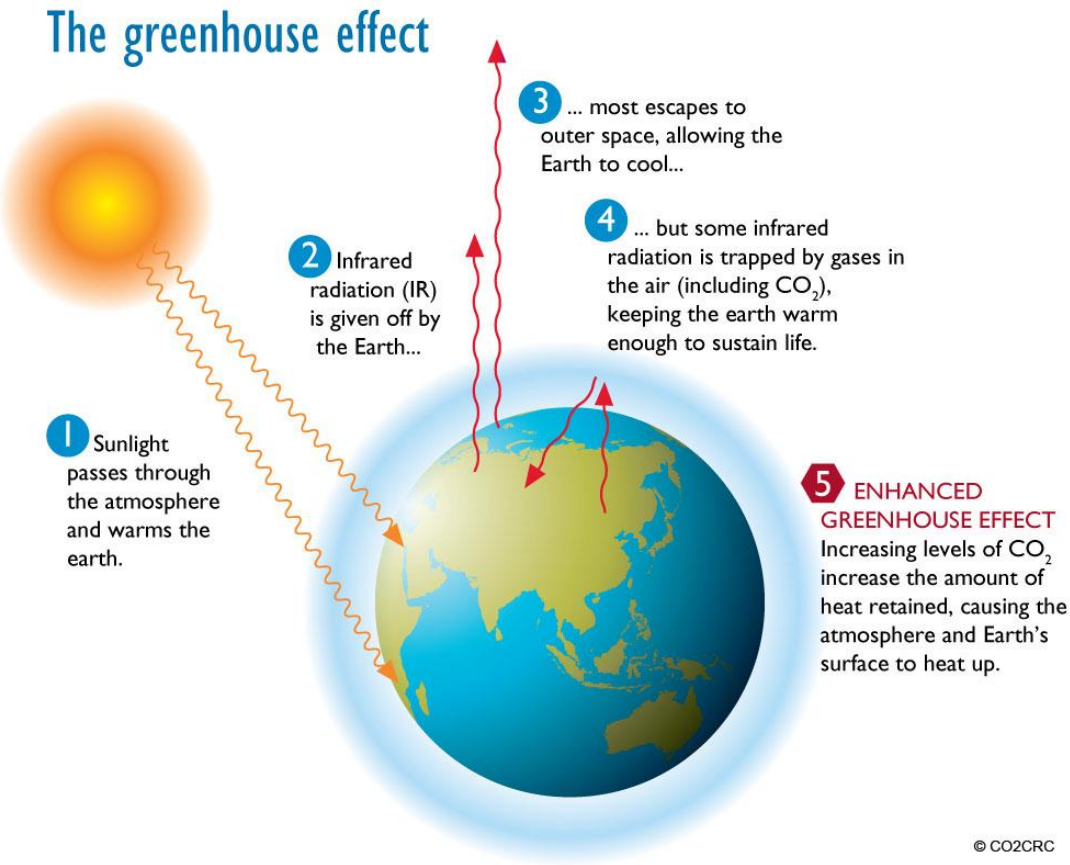

Figure 2: An illustration of greenhouse effect.[10]

The greenhouse effect is a direct result of the internal energy level change in greenhouse gas molecules caused by the terrestrial radiation. A gas molecule only absorbs radiation with a given wavelength, which excites the molecule to a higher energy level. In the case of greenhouse gas molecules, they absorb radiation of wavelengths from 5 to 50 μm, which covers most of the terrestrial radiation (5-20 μm) but excludes most of the solar radiation (< 1 μm). The excited molecule tends to return to the stable state so that simultaneously it emits radiation within the infrared spectrum back to the Earth's surface, which leads to the warming effect on the Earth's surface.[11]

The greenhouse effect is an important mechanism to maintain the Earth's surface temperature at an appropriate level for living beings. However, too high a concentration of greenhouse gases in the Earth's atmosphere causes an excessive reserve of thermal

energy and thus further raises the temperature on the Earth's surface. Water vapour is a major greenhouse gas and makes the greatest natural contribution to the greenhouse effect, thanks to its abundant reserve in the Earth's atmosphere and its strong absorption in the infrared spectrum.[11, 12] However, water vapour has a short lifespan in the atmosphere (about 9 days),[13] because once it reaches saturation, it precipitates back to the Earth's surface. This process constitutes the water circulation of the Earth's environmental system. Compared with water vapour, atmospheric CO_2 has a much longer lifespan (about 100 years) and thus it has much longer impact on the Earth's climate system.[11] As mentioned previously, anthropogenic activities release a large amount of "unnatural" CO_2 into the Earth's atmosphere. The increased concentration of CO_2 traps more terrestrial radiation and thus enhances the greenhouse effect, resulting in increased global average temperatures. Besides this, the rise of the Earth's surface temperature may lead to other negative effects. For example, the increased temperature caused by anthropogenic CO_2 emissions can encourage the evaporation and precipitation of water, resulting in changes to the natural atmospheric and ocean circulation system.[11] It may also cause reduced ice cover, resulting in weakened reflection of solar radiation.[14] This positive feedback on the climate system may further raise the Earth's surface temperature. All the above changes in the earth environmental system can result in global climate changes, as more evidence reveals its link to anthropogenic CO_2 emissions. For example, Figure 3 is plotted from data provided by the Goddard Institute of Space Studies, National Aeronautics and Space Administration, USA (GISS, NASA).[15, 16] Although temperatures have risen and fallen repeatedly throughout the years, Figure 3 reveals a clear trend of temperature rise since 1900. The difference between the minimum and maximum temperatures on the graph is 1.13 ℃. To minimise the impact of global climate change, a long-term target of limiting the global mean temperature rise to 2 ℃ above pre-industrial levels (1861-1890) was adopted in 1996 and confirmed by the European Council in 2005.[17]

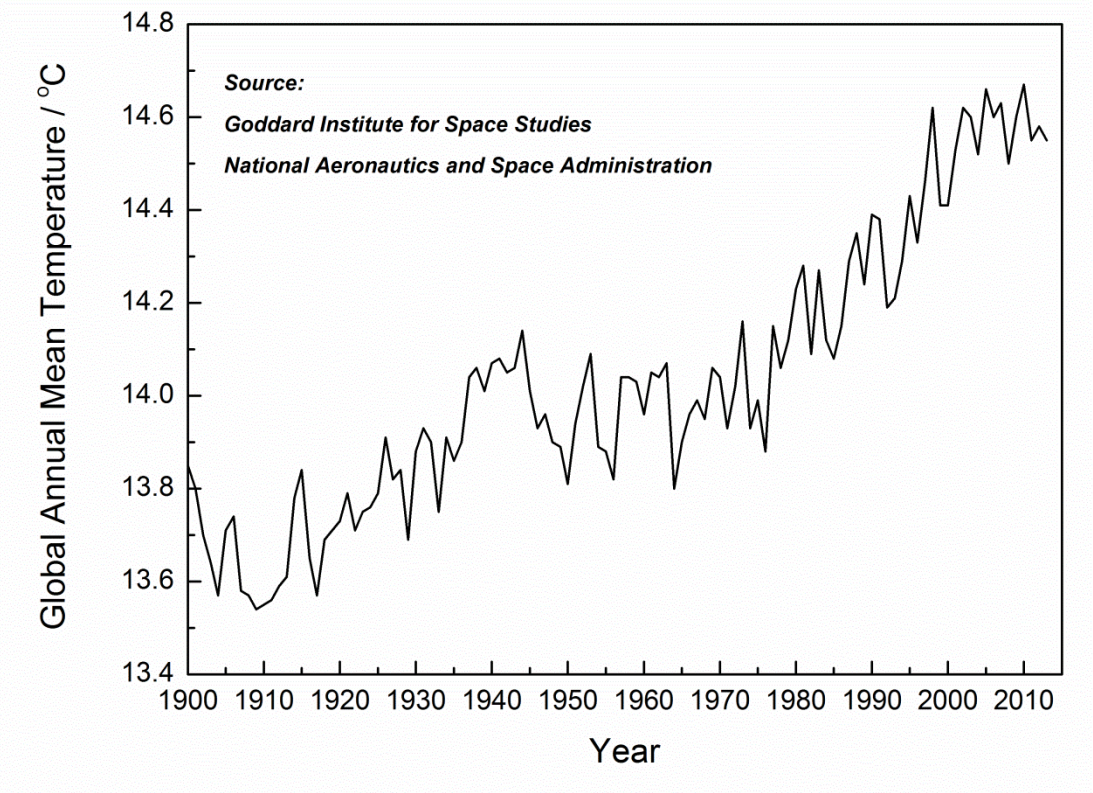

Figure 3: The variation of global annual mean temperature since 1900. The diagram is reproduced according to the original source data.[15, 16]

1.2.3 Introduction to CO_2 capture and storage

1.2.3.1 Background

To meet the 2 ℃ target and minimise the impact of global climate change, the reduction of anthropogenic CO_2 emissions is an unavoidable and urgent issue to be faced by both scientific researchers and policy makers. The IPCC recommends a goal of reducing global CO_2 emissions by at least 50% - 85% of the CO_2 level in 2000, in order to confine the temperature rise in the range of 2 – 2.4 ℃ by 2050.[18, 19]

One approach to the objective of carbon emission reduction is to develop low-carbon technologies. Various modern energy technologies can be applied to either improve energy harvest efficiency or replace fossil fuels with clean and/or renewable energy resources, such as solar, hydro, biomass and nuclear power. However, all of these alternatives face their own challenges in their paths from research and development to practical applications and commercialisation. The utilisation of solar power is limited

by inefficiencies of light harvesting and electricity conversion.[20] It is also restricted by local weather conditions where solar cells are installed, i.e. the available hours of sunlight throughout the year. Hydropower is limited by available installation locations. Its impact on local environments also triggers wide debate among the public and the scientific community.[21] The conversion of biomass materials into biofuels has been gaining attention in modern industries. However, a large quantity of biomass is required for fuel conversion and this is in direct conflict with another global challenge - food shortage.[22] The development of nuclear power suffers from the issues of public acceptance and the disposal of nuclear waste. In particular, the Fukushima Daiichi nuclear disaster in 2011 has had significant repercussions for nuclear power developments around the world. Public and governmental concerns over nuclear power safety issues were raised again and several countries announced their plans to either pause or phase out corresponding nuclear power plants in construction or operation.[23] To sum up, both technical and societal issues with the above clean and renewable energy technologies slow their adaption to modern industries and replacement of traditional fossil fuel energy technologies. Even if their drawbacks might be overcome in the near future, it is still necessary to face the reality that the reserve of fossil fuels is still abundant and our society and industries are still heavily reliant on fossil fuel energy resources.[1] At this point, CO_2 capture and storage (CCS) emerges as a transitional environmental technology to fill the gap in the long period of transition from fossil fuels to clean and renewable energy society. CCS provides a practical solution to the currently urgent problem of CO_2 emissions and allows human society to continue enjoying the benefits from burning fossil fuels. The International Energy Agency (IEA) proposed the "BLUE Map Scenario", which aims to halve global energy-related CO_2 emissions by 2050, compared with the level of CO_2 emissions in 2005.[18] This target is to be achieved by adopting various new and existing low-carbon technologies. Figure 4 illustrates the IEA's estimated weighing of key technologies to reduce CO_2 emissions under this scenario by 2050. It shows that carbon capture and storage as a carbon negative technology is expected to play a significant role in cutting CO_2 emissions into the Earth's atmosphere and meeting the target of this scenario.

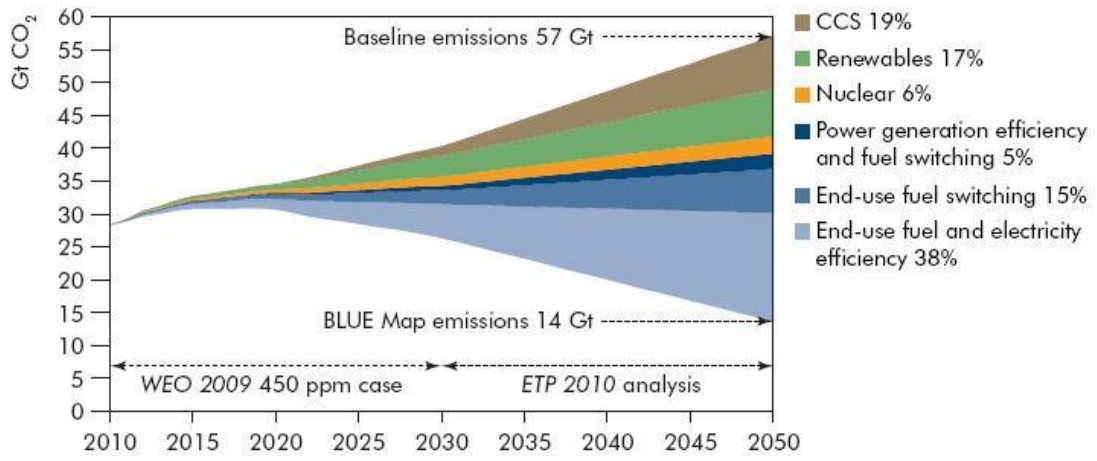

Figure 4: Key technologies for reducing CO_2 emissions under the BLUE Map scenario.[18]

1.2.3.2 The concept of CCS

CCS is a promising carbon negative technology, which aims to capture CO_2 from anthropogenic emission sources and thus cut down the overall CO_2 level in the Earth's atmosphere. In 2005, the Intergovernmental Panel on Climate Change (IPCC) produced a special report - "Carbon Dioxide Capture and Storage". This report describes CCS as "a process consisting of the separation of CO_2 from industrial and energy-related sources, transport to a storage location and long-term isolation from the atmosphere".[24]

Figure 5 illustrates a CCS project launched by the Total Company in the Lacq basin in France.[25] It shows the complete path of anthropogenic carbon within a CCS project, including carbon sources (coal, oil, natural gas, biomass, etc.), applications (electricity generation, cement/steel production, etc.), transportation (pipeline, shipping, vehicles, etc.), and end management (reuse, storage, etc.). These can be interpreted as a four-stage CO_2 capture and storage process: gas production, CO_2 capture, CO_2 transportation and CO_2 storage. It reveals that CCS is not an independent technology but a comprehensive system that needs to be integrated with the entire life cycle of modern industry.

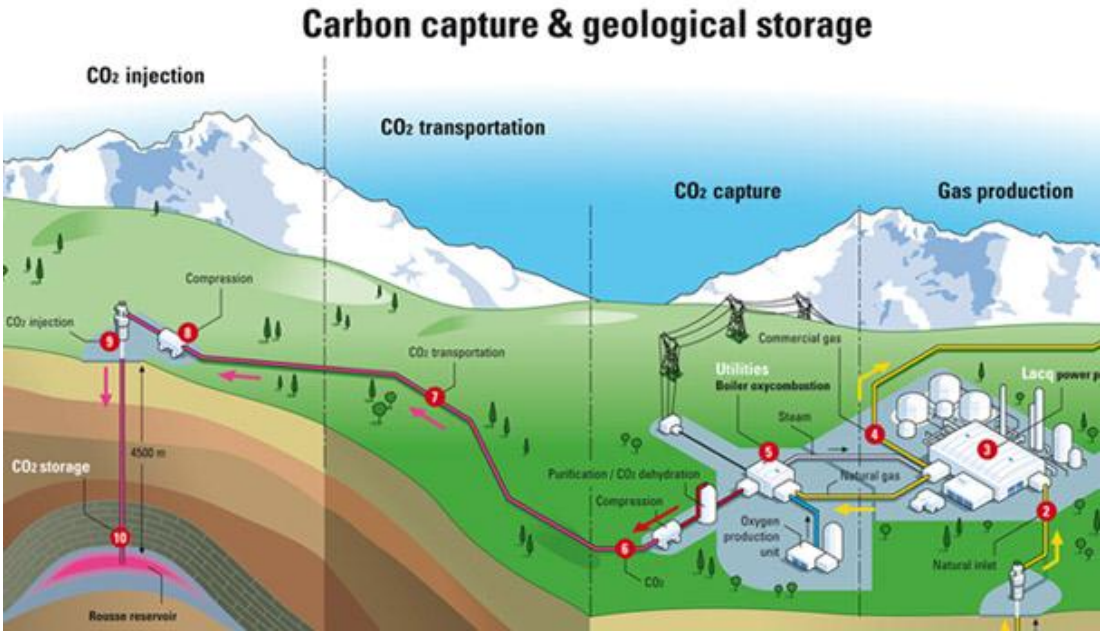

Figure 5: An illustration of Total's CCS pilot project, showing CO_2 capture from a power station, transportation via pipelines, and injection to storage in an underground reservoir.[25]

1.3 CO_2 capture systems for power plants

As previously mentioned, the largest anthropogenic CO_2 emission source is fossil fuel power plants for electric power generation. Electric power generation is carried out through the combustion of fossil fuels by means of turbine rotations.[26] Fossil fuel power plants can be classified in terms of fuels, turbines and layouts used for power generation.[27] Accordingly, different power plants generate CO_2 at different stages of their power generation processes. They also produce flue gases with different components and temperatures. Therefore, these differences need to be taken into consideration in the design of a CO_2 capture system. Currently, there are three main CO_2 capture systems: pre-combustion, oxyfuel-combustion and post-combustion. Note that all the above CO_2 capture systems are still at the demonstration stage and the author finds no reference to capture systems currently operating at large-scale fossil fuel power plants.

1.3.1 Pre-combustion

Pre-combustion CO_2 capture is the process that captures CO_2 before fuel combustion. Figure 6 illustrates the flow chart of the pre-combustion process.

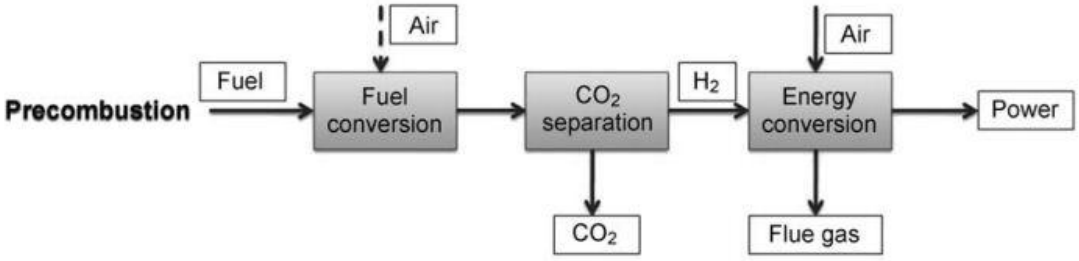

Figure 6: A flow chart of the pre-combustion CO_2 capture process.[28, 29]

Pre-combustion CO_2 capture mainly consists of three stages:

Fuel conversion: this stage involves the conversion of primary fossil fuels (such as coal and methane) into gaseous products at high temperatures and pressures.[29] The primary fuels react with steam to produce syngas, which is primarily a mixture of carbon monoxide and hydrogen. This solid-to-gas conversion is called "gasification":[30]

$H_2O + C \rightarrow H_2 + CO$ (Coal gasification)

$H_2O + CH_4 \rightarrow 3H_2 + CO$ (Natural gas sweetening)

Water-gas-shift: carbon monoxide from the fuel conversion process further reacts with steam. It is converted into CO_2 and more hydrogen is generated. The stage is known as the "water-gas-shift reaction":[31]

$H_2O + CO \rightarrow H_2 + CO_2$

After this stage, the gas stream generally consists of 61.5% H_2, 35.5% CO_2 and 3% other components like N_2, H_2S, H_2O and CO.[28]

CO_2 separation: CO_2 capture takes place at this stage, where CO_2 is separated from H_2 for transportation and storage. H_2 is either delivered to the combustion chamber for power generation or stored as a chemical feedstock for other applications.

First of all, high CO_2 concentration (partial pressure) in the gas mixture is a significant advantage of a power plant with a pre-combustion CO_2 capture system. It is estimated that a pre-combustion system cuts the energy consumption to half of the energy penalty by comparison with that of a post-combustion system.[32] Moreover, H_2 is the major product after it is separated from CO_2. Hence the pre-combustion process converts an unclean energy source (fossil fuels) into a clean energy source (H_2). H_2 may be used for power generation. However, more importantly, it can be stored in the form of a chemical feedstock, which is a convenient method of energy storage.[28] Furthermore, the pre-combustion CO_2 capture system is expected to be integrated with the new generation of fossil fuel power plants, such as Integrated Gasification Combined Cycle (IGCC) plants. IGCC plants have features similar to those of pre-combustion capture system. They convert fossil fuels into syngas and thus CO_2 can be captured before combustion. Impurities (SO_x, NO_x, H_2S) are removed from the syngas before combustion, which also helps to prevent the failure of sorbents that is caused by such contaminants.[33]

However, there are some challenges on the path of promoting the pre-combustion CO_2 capture system. The very first issue is the high capital cost to build up the infrastructure of the system. Both gasification and water-gas-shift reactions are carried out at high temperatures and pressures.[30] Therefore, a large amount of capital investment is required to build system units, such as combustion chambers and turbines, which can sustain such temperatures and pressures. More importantly, due to different layouts, it is difficult for pre-combustion capture systems to be integrated with existing power plants. As a result, the development and commercialisation of pre-combustion capture systems are tightly attached to those of gasification power plants. To date, there are only a few IGCC plants operating at small demonstration scales. Currently, the largest IGCC plant is the 618 MW Edwardsport power plant constructed in Indiana, USA by Duke Energy Corporation. The project has been delayed for one year and has overspent by $1.5 billion. More than 36 IGCC projects have been abandoned in the last ten years (before 2013).[34]

1.3.2 Oxyfuel-combustion

An oxyfuel-combustion CO_2 capture system retrieves a high concentration of CO_2 in the flue gas after fossil fuels are combusted in an oxygen-enriched environment rather than air.

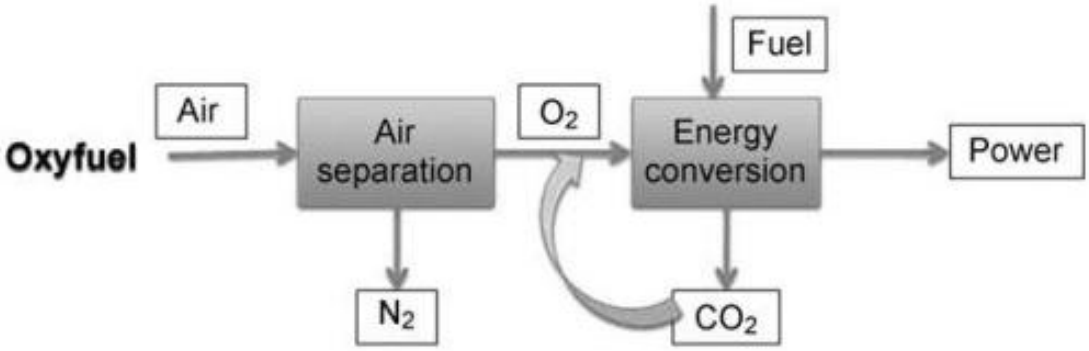

Figure 7: A flow chart of an oxyfuel-combustion capture process.[28, 29]

Figure 7 shows a flow chart of a two-stage oxyfuel-combustion capture process. The first stage involves the extraction of oxygen and removal of other gas components (mainly nitrogen) in the air. The required oxygen concentration for oxyfuel-combustion is normally over 95%. Then, the highly purified oxygen gas stream is introduced to the combustion chamber, mixed with fossil fuels, and combusted to generate power and flue gas with a CO_2 concentration which can be as high as 80% ~ 98%.[28] In this case, the flue gas is suitable for direct CO_2 transportation and sequestration without the need for capturing.

The oxyfuel-combustion system possesses several advantages. Firstly, the pressurised and oxygen-enriched environment ensures a sufficient fuel combustion process, which improves energy conversion efficiency. Secondly, conventional power plants carry out combustion in the air. However, dry air contains multiple gas components, including 78% N_2, 21% O_2 and 1% other minor gas components.[35] Most of the N_2 does not take part in the fuel combustion reaction. Therefore, thermal energy can be lost by means of the emission of unreacted N_2 in the flue gas. Finally, oxyfuel-combustion power plants produce highly concentrated CO_2 in the flue gas. Among the three CO_2 capture systems, this is the one that actually eliminates the need for "CO_2 capture" but provides an almost pure CO_2 stream for direct transportation and storage. Theoretically,

this enables the design and construction of "Zero Carbon Dioxide Emission Cycle" plants based on the oxyfuel-combustion system.[28]

Although the oxyfuel-combustion capture system has the aforementioned superiorities, it suffers from similar weaknesses of the pre-combustion capture system. In the first place, the early stage of oxyfuel-combustion is also an energy intensive and costly process, because the current process of oxygen separation is still based on cryogenic distillation.[24] Therefore, alternative efficient O_2 separation techniques, such as membrane-based methods, are in pressing demand. Furthermore, fuel combustion in a pressurised and oxygen-enriched environment also generates a large amount of thermal energy. Therefore, the corresponding facilities are required to sustain such high pressure and temperature combustion conditions, which entails a high capital cost. In addition, equipment such as turbines need to be redesigned to survive operation under these conditions.[28] A solution here is to recirculate CO_2 flue gas to the combustion chamber to reduce the combustion temperature. However, this brings in a series of other issues, such as the change of flame pattern.[36] Last but not least, it is also inconvenient for the oxyfuel-combustion capture system to be retrofitted into existing power plants because of the issues mentioned above. Therefore, there is no report of commercial operation of oxyfuel-combustion power plants on a large scale. There are demonstration plants currently running across the world. Notable oxyfuel combustion demonstration plants currently include the Callide Project (Biloela, Queensland, Australia),[37] Lacq-Rousse Project (Lacq, France)[38] and CIUDEN Project (CIUDEN, Spain)[39].

1.3.3 Post-combustion

The post-combustion CO_2 capture system captures CO_2 directly from the flue gas after the combustion process. This system is designed to fit the configuration of most existing power plants and thus is considered to be more practical in modern industries.

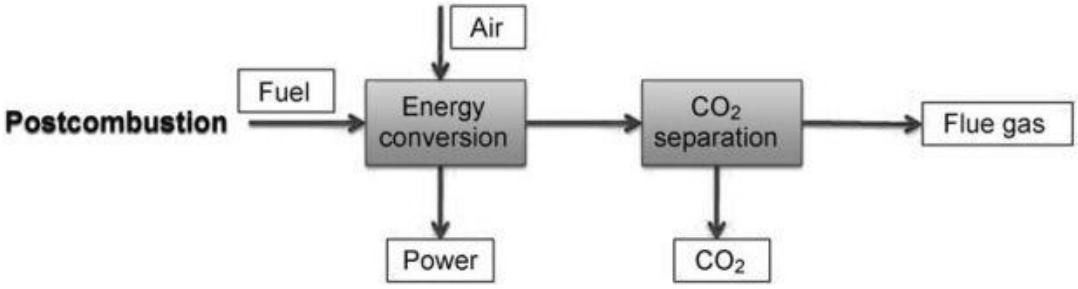

Figure 8: A flow chart of the post-combustion capture process.[28, 29]

Figure 8 illustrates the post-combustion capture process, which shows CO_2 is captured from the flue gas after the combustion of fossil fuels in air. Unlike the previous two systems, post-combustion capture systems capture CO_2 from flue gas with a low concentration of CO_2 and a much more complex gas environment, that is, 15% CO_2, 5% H_2O, 70% N_2, and 10% other gas components (O_2, H_2S, SO_x, NO_x).[28] Although it does not have the technical advantages of the previous two systems, the post-combustion capture system benefits from technologically and commercially proven experience over the last several decades. Because the majority of existing power plants possess a similar configuration to the post-combustion capture system, the system is well received in both the research and industrial communities. As a result, quite a few post-combustion demonstrations have already been integrated with power plants and are operating at small commercial scales.[40] There is even an interesting report of carbonated drinks being produced with the captured CO_2 from one of the post-combustion plants operated by Huaneng Group using chilled ammonia (Gaobeidian, China).[41]

However, a key issue is the low concentration of CO_2 (ca. about 15%) and the total pressure of the flue gas (ca. less than 1 bar). These factors dramatically limit the performance of CO_2 capture. Although a higher pressure can be applied externally, this implies additional costs of pressurisation equipment and corresponding energy consumption. Moreover, because chemical sorbents are preferred for the post-combustion capture, the system also suffers from penalties introduced by this technique, including energy consumption for the regeneration of sorbents, separation of CO_2 from other gas components and degradation of sorbents. It is estimated that the

energy penalty of a coal-fire power plant using amine solvents for post-combustion capture can be up to 40%.[28, 42]

Table 1: Summary of operation conditions, merits and drawbacks of pre-, oxyfuel- and post-combustion CO_2 capture systems.

System	Gases	P/bar	CO_2%	Merits	Drawbacks
Pre-combustion	CO_2/H_2	30	35.5	High CO_2 concentration Clean fuel conversion Chemical energy feedstock	Additional fuel conversion High capital investment Difficult to retrofit
Oxyfuel-combustion	CO_2	N/A	80~98	Near pure CO_2 flue gas Direct CO_2 storage High combustion efficiency	High capital investment Costly O_2 separation Difficult to retrofit
Post-combustion	CO_2/N_2	1	15~16	Easy retrofitting Mature technology	Complex flue gas environment Low CO_2 concentration Energy penalty

In summary, all three capture systems have their own strengths and weaknesses. The application of a specific capture system depends on the working conditions of the power plant in question, including pressures, CO_2 concentrations, temperatures and gas compositions before or after combustion processes. Table 1 summarises key operating conditions, advantages and disadvantages of the three CO_2 capture systems. These CO_2 capture systems aim to recover 80-90% of the total generated CO_2 before considering energy efficiencies. 10-40% of the energy produced by power plants is required to operate capture systems.[24]

Further studies of capture systems focus on increasing energy efficiencies, reducing costs and better integration with existing power plants. An improved performance can be also achieved by careful choice of suitable capture techniques and materials.

1.4 CO_2 capture techniques

Currently, there are various proposed CO_2 capture techniques, including gas sorption, gas separation and cryogenic distillation. Among these, gas sorption and gas separation are two classes of promising techniques for CO_2 capture. Sometimes, the differences between the two are not distinctive, as in the situation where gas separation is carried out by competitive gas sorption. They are versatile and applicable to power plants. The foremost advantage is that they require less energy to operate, compared with techniques such as cryogenic distillation.

This section is a comprehensive review of the definitions, principles, merits and drawbacks of primary gas sorption and separation techniques. The specifications of sorption properties of materials are reviewed in the section "CO_2 capture materials".

Gas sorption is the process where CO_2 molecules are either absorbed by a chemical compound and become a new compound or just a mixture, or adsorbed at the surface of a material. The sorbents can be either liquid or solid. The interaction between sorbates and sorbents can consist of either covalent bonding (chemical sorption) or weak van der Waals interaction (physical sorption).[28]

1.4.1 Chemical absorption

Chemical absorption has contributed to waste gas disposal in power plants and heavy industry over the last 50 years.[28] Chemical absorption is the absorption process involving the formation of chemical bonds. In the case of CO_2 capture, CO_2 is absorbed by chemical absorbents and transformed into other carbon compounds. Chemical absorption is highly suitable for the applications in the aforementioned post-combustion CO_2 capture system. The flue gas from a post-combustion power plant contains a low partial pressure of CO_2 and CO_2 is also mixed with other gas components (mainly N_2). Therefore, a strong and selective binding between CO_2 and sorbent is preferred in this case. Most chemical sorbents are alkaline materials. Hence they can form strong chemical bonds with acidic CO_2 molecules.

Figure 9 illustrates the work flow of chemical solvent absorption process. It consists of two main parts: an absorber tower and a desorber tower. CO_2 is injected at the bottom

of the absorber tower, while an absorbent solvent, such as amines, is fed from the top of the tower. This forms a counter flow with the flue gas from the bottom, in order to increase the efficiency of absorption. Then, the liquid solvent is transferred to the desorber tower, where the CO_2-containing solution is heated and CO_2 is released. Then, the regenerated absorbent is transferred back to the absorption tower again for reuse. Primary chemical solvent absorbents include chilled ammonia, alkali metal hydroxide solutions and alkanolamines. Alkanolamines are favoured by industry for their high CO_2 absorption capacities and commercial availability. Most importantly, alkanolamines have been used as amine-based absorbents for decades in the gas processing industry to remove acidic components from gas streams for multifarious purposes such as flue gas treatments. Rich handling experience is a unique advantage against other materials. However, taking monoethanolamine as an example, the stability, energy penalty, corrosive products, high heat of absorption and consequent increase in capital investment restrict its large-scale application. Therefore, there is an urgent requirement for alternative solutions to CO_2 capture. Further studies continue on advanced amine solvents to reduce the negative influences.[28, 43]

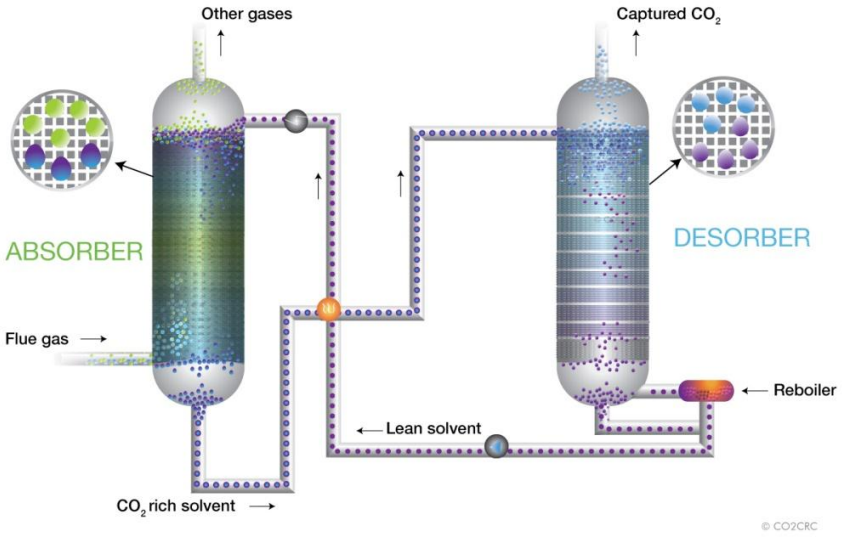

Figure 9: Schematic of absorber and desorber tower in a chemical absorption process.[44]

Alternatively, solid sorbents can be used for chemical absorption as well. In this case, CO_2 is absorbed on the surface of a solid sorbent, reacted with the sorbent material and transformed into a solid carbon compound (combination reaction). After absorption,

the solid sorbent can be calcined to release CO_2 (decomposition reaction). Usually, both combination and decomposition reactions need to be carried out at high temperatures. The decomposition temperature is normally higher than the combination temperature. A disadvantage of solid sorbents is that the absorption reaction is limited at the surface of the sorbent, which makes the interior region of the material unavailable for absorption. A direct solution is to grind solid sorbents into small particles to increase the contact area between CO_2 and the surface of the sorbent. Another method is to manufacture the sorbent into porous material to achieve the same goal. Typical solid sorbents based on chemical absorption include alkaline metal oxides, hydroxides and carbonates, such as calcium oxide, potassium hydroxide and calcium carbonate.[28]

1.4.2 Physical absorption

In contrast to chemical absorption, physical absorbents absorb CO_2 without chemical reaction. Rather than chemical bonds, the interactions between CO_2 and absorbents are mainly intermolecular forces, such as weak van de Waals or electrostatic forces.[45] The absorption process does not involve dramatic change in the electronic structures of the interacting species.[46] Physical absorbents are usually in liquid form. Typical physical absorbents include rectisol, selexol and ionic liquids.

Physical absorbents obey Henry's Law, which states that "at a given temperature the mass of dissolved gas in a given volume of solvent is proportional to the pressure of the gas with which it is in equilibrium".[47] This indicates that the absorption capacity of a physical absorbent may have a linear relationship with the partial pressure of the absorbate. This behaviour can help to distinguish between chemical and physical absorption. Figure 10 compares of CO_2 sorption isotherms of a range of solvents.[45, 48] There is a remarkable distinction between isotherms of physical absorbents and those of chemical absorbents, where the CO_2 loading capacities of physical absorbents increase with the increasing CO_2 partial pressures at constant rates. On the other hand, chemical absorbents have maximum CO_2 loading capacities at relatively low CO_2 pressures, and they do not further increase with the CO_2 partial pressure. Moreover, for the same physical absorbent, such as methanol c (-15 ℃) and d (-30 ℃) in Figure 10, the CO_2 loading capacity is higher at high pressures. This preference of physical absorption implies that physical absorption is a promising candidate for high CO_2

partial pressure applications, where high CO_2 partial pressure is a key feature of the pre-combustion CO_2 capture system. In addition, because of the weak interaction, the absorption and desorption cycle can be carried out by cycling through a relatively small range of temperatures and pressures. This lowers the energy demand for the heating of absorbents, leading to a more efficient regeneration, compared with that of chemical absorption.[28]

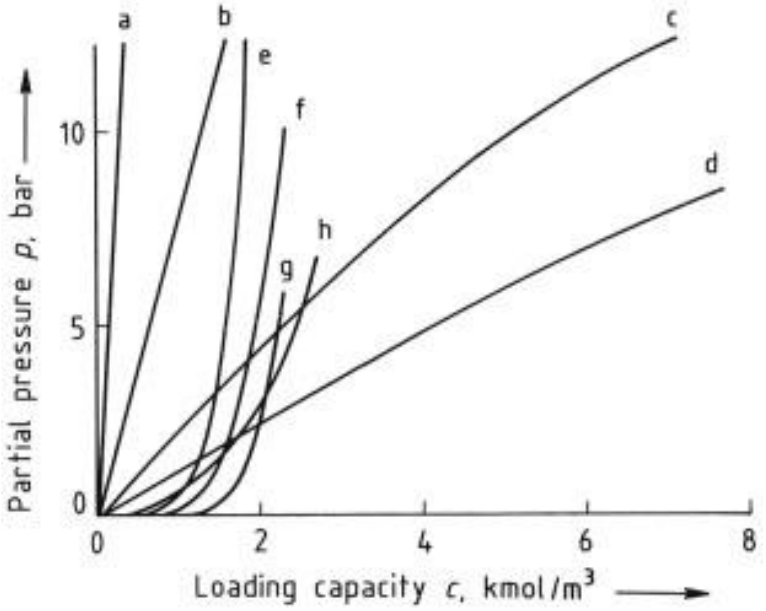

Figure 10: Comparison of CO_2 sorption isotherms of various solvents: a (water, 30 ℃), b (N-methyl-2-pyrrolidone, 110 ℃), c (methanol, -15 ℃) and d (methanol, -30 ℃) are physical sorbents; e (potassium carbonate solution, 110 ℃), f (sulfinol solution, 50 ℃), g (diethanolamine solution, 50 ℃) and h (amisol diethylenetriamine solution) are chemical sorbents.[45, 48]

Rectisol and selexol are two conventional commercial solvents for the acidic gas removal process. The major component of rectisol is methanol, and for selexol, they are dimethyl ether and polyethylene glycol. Therefore, both of them contain chemical compounds that are volatile at the ambient temperature, which can be a problem in practice. In addition, they need to be operated at relatively low temperatures (-30 ℃ for rectisol and 0-40 ℃ for selexol).[30] Ionic liquids are the new generation physical sorbents for CO_2 capture, which have much less volatilities and operating temperatures.[28, 49] A higher operating temperature means lower energy consumption for the refrigeration of the solvent for CO_2 absorption, compared with

those physical absorbets in Figure 10. However, the higher viscosity also results in a decreased CO_2 absorption rate due to a lower mass tranfer rate. Moreover, compared with chemical absorption, physical absorption is a non-selective process and thus it can be difficult to separate different flue gas components. In order to increase the selectivity of CO_2 over other gas molecules, a solution is to introduce amine functional groups.[28]

1.4.3 Physical adsorption and desorption

Physical adsorption share common operating mechanisms and conditions of physical absorption. However, physical adsorption is more about the interaction between CO_2 molecules and the surface of a physical adsorbent, rather than the dissolution of CO_2 within the bulk of a sorbent in the case of physical absorption.[28] CO_2 is adsorbed at the surface of physical adsorbents mainly through weak van der Waals force and thus gas adsorption and desorption can be swapped by varying temperatures or pressures in a small range as illustrated in Figure 11.[50] Furthermore, because gas sorption is based on the surface interaction, physical adsorbents are usually solids, such as zeolites, activated carbon and metal-organic frameworks. The adsorption capacity mainly depends on the porous structures of adsorbents. Structural characteristics, such as specific surface area and pore volume, are primary factors that determine the CO_2 uptakes of an adsorbent, because surface and pores can play the role of "host sites" for CO_2 molecules. Besides, the affinity of CO_2 gas molecules towards the surface of an adsorbent, i.e. the strength of CO_2 binding is another important factor that determines the CO_2 uptake of an adsorbent. An adsorbent with a well-developed porous structure, i.e. high specific surface area and large pore volume, provides a basic "framework" for CO_2 adsorption but unnecessary "attractive" to CO_2 molecules. This is particularly true when it comes to low total pressure or low CO_2 partial pressure conditions because the gas molecules tend to leave the surface of adsorbents under the external "evacuation force" or have to "compete" with other gas molecules for the "host sites". To enhance the CO_2 binding on adsorbents, nitrogen and metal doping can be introduced and these will be discussed in accordance with specific cases of materials for CO_2 capture.

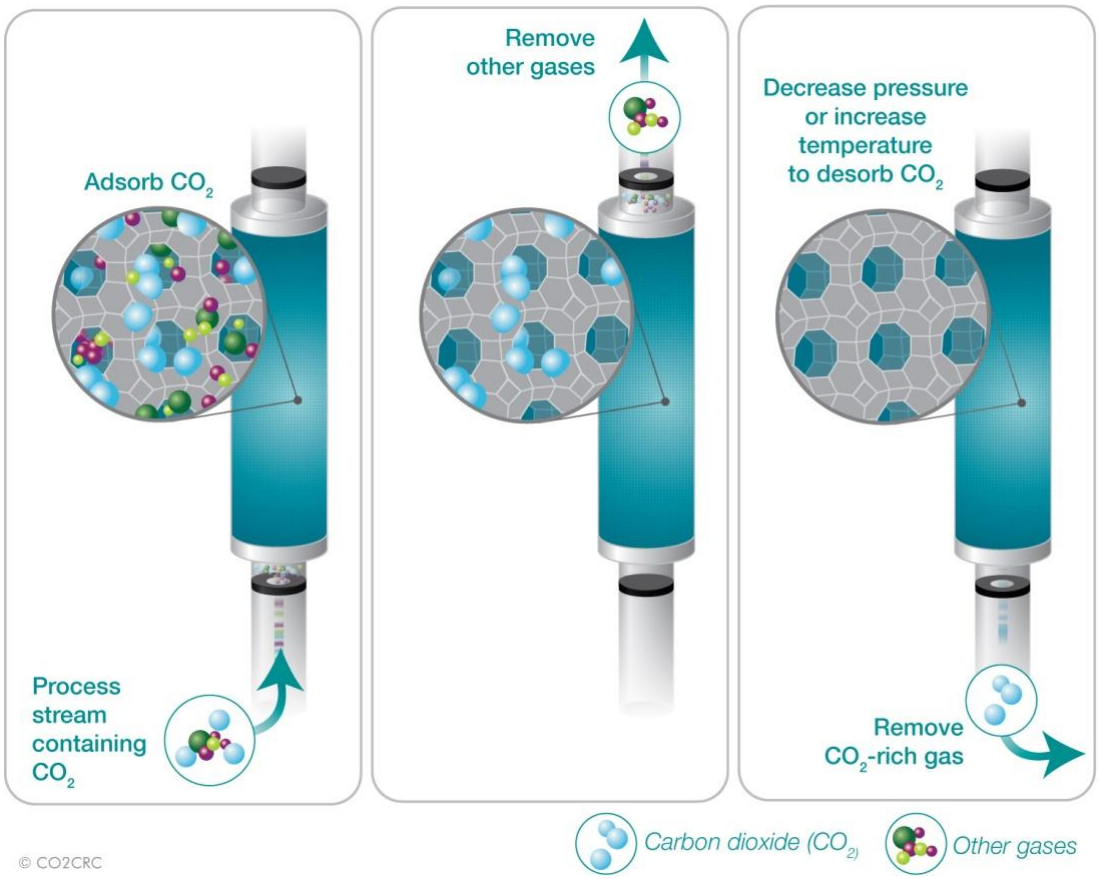

Figure 11: An illustration of a typical physical adsorption process.[51]

Physical adsorption shares similar advantages and disadvantages with physical absorption. On the positive side, due to the weak surface interaction, the adsorption and desorption can be switched rapidly. Both temperature and pressure swing adsorption/desorption can be applied to regenerate adsorbents and return them to their initial states before adsorption. It is a key characteristic of physical adsorbents because it indicates low energy consumption for material regeneration, i.e. reduced energy penalty for CO_2 capture. Moreover, it suggests physical adsorbents can preserve their CO_2 capture capabilities after multiple adsorption/desorption cycles.[28] However, on the negative side, physical adsorbents normally have low CO_2 uptakes at low CO_2 partial pressures (below 1 bar) and ambient (typically 25 ^oC) or higher temperatures. It is a significant drawback of physical adsorbents, because in practice, from the exhaust of an existing power plant, the flue gas stream contains a low concentration of CO_2 (typically 15 vol%). A common solution is to recirculate the flue gas and mix it with air for fuel combustion, because it helps to raise the concentration of CO_2 in the exhaust gas. Another method is to introduce dopants in physical sorbents to increase their

affinities to CO_2. The latter will be discussed in detail for specific adsorbents in later sections. In addition, there is a dilemma that adsorption requires a relatively strong interaction to bind CO_2 molecules onto the surface of the adsorbents, but desorption requires a relatively weak interaction, in order to release CO_2 from adsorbents with minimum energy consumption. These contrary requirements need to be carefully balanced to achieve optimal CO_2 capture performance.

As important as adsorption, desorption involves regeneration of sorbents and release of sorbates. The difference in energy consumption can be enormous at this stage, in accordance with the strengths of the interactions between sorbates and sorbents. As previously stated, adsorbents are usually regenerated by raising temperatures or reducing pressures, i.e. temperature swing (TSA) and pressure swing adsorption/desorption (PSA), respectively, because of the weak interaction between CO_2 and surface of the adsorbents.

TSA is a technique in which CO_2 is physically adsorbed on the surface of an adsorbent at a lower temperature, and released from its surface at a higher temperature. The mechanism of TSA is to overcome the weak interaction between the adsorbed CO_2 molecules and surface of the adsorbent by increasing the kinetic energy of the gas molecules. The TSA technique can be also applied to chemical absorbents. In this case, it involves chemical decomposition of the absorption products and the breaking of chemical bonds. Therefore, it requires much higher operating temperatures with a consequent energy penalty. For example, regeneration of calcium oxide needs to be carried out at 900 ℃ or even higher temperatures.[52]

TSA has the potential to completely remove CO_2 and fully regenerate absorbents. Taking zeolites as an example, Tezel et al. reported that the zeolite 13X can be fully regenerated after it is heated at 200 ℃ for 12 hours.[52, 53] It is important to note that the degree of regeneration of adsorbents is determined by the regeneration temperatures, types of adsorbents and other competitive adsorptive gases in the system. For example, Siriwardane et al. carried out a competitive gas adsorption study on zeolite 13X with 15% CO_2 in water vapour. The result showed that the zeolite was only fully regenerated at 350 ℃; for another commercial zeolite WE-G 592 that was tested

under the same conditions, the regeneration temperature needed to be raised to 400 ℃.[52, 54]

Although TSA is a common technique that is used to regenerate both chemical and physical sorbents, TSA involves intensive energy consumption to heat sorbents. It also requires time dwelling at regeneration temperatures to achieve the full recovery of CO_2 capture capacities, which further increases the demand for energy.[24]

PSA is a process that physically removes adsorbates from adsorbents' surface by lowering pressures. PSA is frequently applied to separate CO_2 from other gas components such as H_2 and CH_4. Taking the syngas from pre-combustion power plants as an example, CO_2 rather than H_2 is preferentially adsorbed on a set of physical adsorbents. At this stage, H_2 can be exported from the PSA chamber to the combustion chamber for power generation. In this way, the purity of H_2 can reach up to 99.999%.[24] Later, the pressure is reduced to release CO_2 for later transportation and storage, and the adsorbent is ready for the next cycle.

A significant advantage of PSA is its short cycle time. The adsorption and desorption can be quickly switched between each other by simply pumping more gases into the PSA chamber to increase the pressure and evacuating the chamber to reduce the pressure. The interval between adsorption and desorption can be short, indicating PSA is a fast material regeneration technique. Chue et al. reported a pressure swing experiment on zeolite 13X. They carried out a quick cycle of pressure swing in 7 minutes by switching the pressure from about 1.11 bar to 0.07 bar at 30 ^{o}C.[55] The experimental result showed the zeolite 13X helped to produce a high purity (99%) CO_2 stream with a reasonable degree of adsorbent regeneration. The short cylce time is essential to physical adsorption, as it allows more CO_2 to be captured per unit time. Despite the faster cycle, it is still an energy intensive technique that demands energy for compressing the gas at the adsorption stage.

To sum up, both fast adsorption-desorption cycles and low energy demand for regeneration of adsorbents are key advantages of physical adsorption. Although physical adsorbents generally have lower sorption capacities than those of chemical absorbents is in current stage of research, the former has the potential to further improve their CO_2 uptakes while maintaining it merits of low energy consumption.

1.4.4 Gas separation

Differing from gas sorption, gas separation mainly focuses on separating CO_2 from other gas components by various means. To date, CO_2 separation techniques have been widely applied to natural gas treatment and ammonia production.[24] Membrane is usually used for gas separation.

(a)

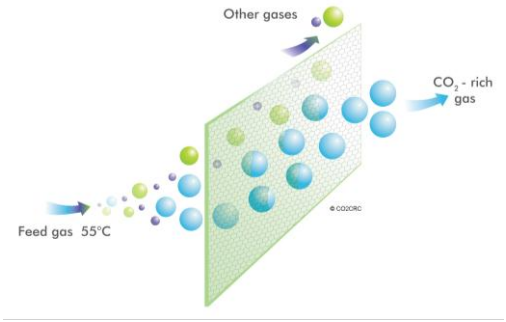

(b)

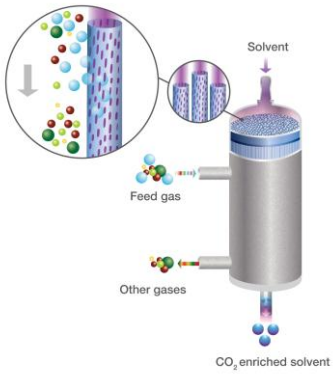

(c)

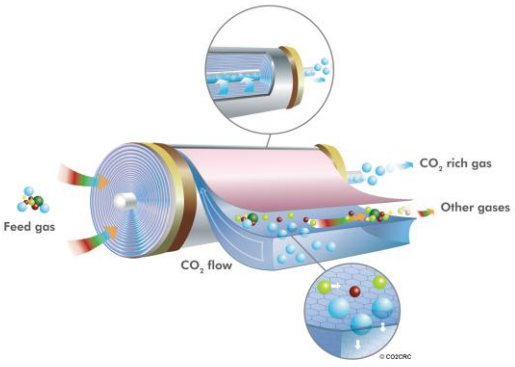

Figure 12: Three forms of membrane: a) Flat sheet membrane;[56] b) Hollow fibre membrane;[57] c) Spiral wound membrane.[58]

Table 2: Typical gas molecules from pre-combustion, oxyfuel-combustion and post-combustion power plants and their kinetic diameters.

Gas molecule	CO_2	N_2	H_2O	H_2	O_2
Kinetic diameter / Å	3.30	3.64	2.65	2.89	3.45

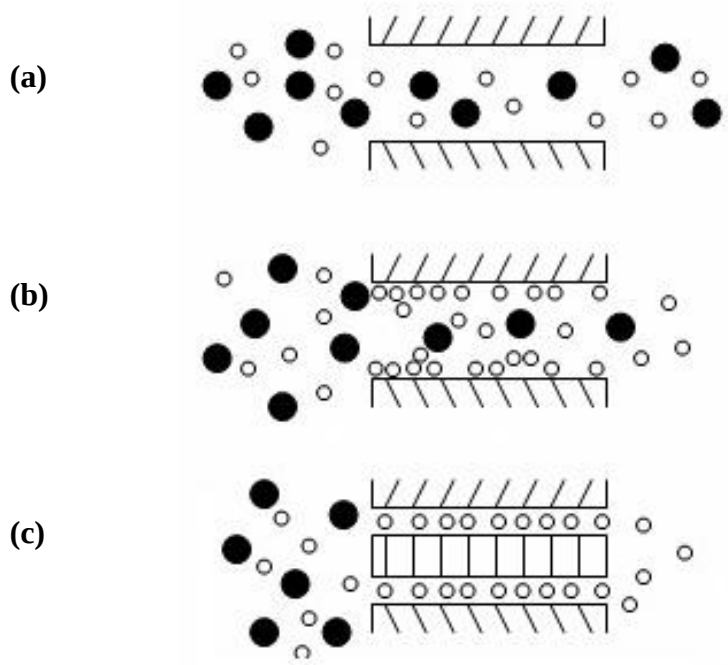

Figure 13: Three main separation mechanisms: a) Kinetic effect ; b) Thermodynamic effect; c) Molecular sieving.[59]

Membranes are sieves at a microscopic level, which can be manufactured in different forms. Figure 12 illustrates three common types of membrane and their corresponding operating mechanisms. They allow required gas molecules to pass through, while preventing the others from doing so. For post-combustion power plants, the primary target is CO_2/N_2 separation; for pre-combustion, CO_2/H_2; and for natural gas sweetening and recovery, CO_2/CH_4.[28] Therefore, with regard to membranes, selectivity is more important than sorption capacity, although sometimes sorption can be regarded as one of the approaches to separation. It sorbs unwanted gas components, but allows the required gas component to pass through, or vice versa. Besides selectivity, permeability, lifetime and consistency of performance over multiple cycles are other important parameters.

There are three primary gas separation mechanisms:[28, 60]

- The kinetic effect: gas molecules are separated by differences in diffusion rates;
- The thermodynamic equilibrium effect: gas molecules are selected by competitive interaction between adsorbates and the membrane; and
- The molecular sieving effect: the size of gas molecules and pore structures in membranes are the determining factors for the gas separation.

Figure 13 illustrates the diffusion behaviours of gas molecules in accordance with these three gas separation mechanisms. Although they are independent separation mechanisms, in most circumstances, these mechanisms work synergistically.

Membrane materials can be classified into three major categories: inorganic, organic and hybrid. Inorganic materials include ceramics, metals and metal oxides. Organic materials include celluloses and polymers. Hybrid materials mainly comprise metal-organic frameworks.[28] Membrane techniques face several significant challenges for future development: Firstly, membranes must possess a corresponding pore size to selectively separate a specific type of gas molecule.[28, 61] Table 2 lists the kinetic diameters of several typical gas molecules from pre-combustion, oxyfuel-combustion and post-combustion power plants. It is clear that these gas molecules have similar kinetic sizes. Therefore, it is crucial to produce membranes with controlled pore sizes and pore size distribution. Secondly, an additional compression is required to increase the pressure of the gas stream, in order to enhance the selection efficiency, which means additional energy consumption.[28, 62] Finally, membranes suffer from a gradual decrease in permeability due to the deposition of gas molecules on the surface.[28]

1.5 Materials for CO_2 capture

1.5.1 Amine solvents

Amine solvents are a group of nitrogen-containing functional chemicals. Of them, monoethanol amine (MEA) is still recognised to be the most likely candidate for scrubbing CO_2, mainly because of mature experience of handling amines in the last 30

years for waste gas disposal. Bergman et al. estimated that it costs about $40 for enough MEA to capture a tonne of CO_2, including removing impurities and compressing it to a supercritical pressure.[45, 52]

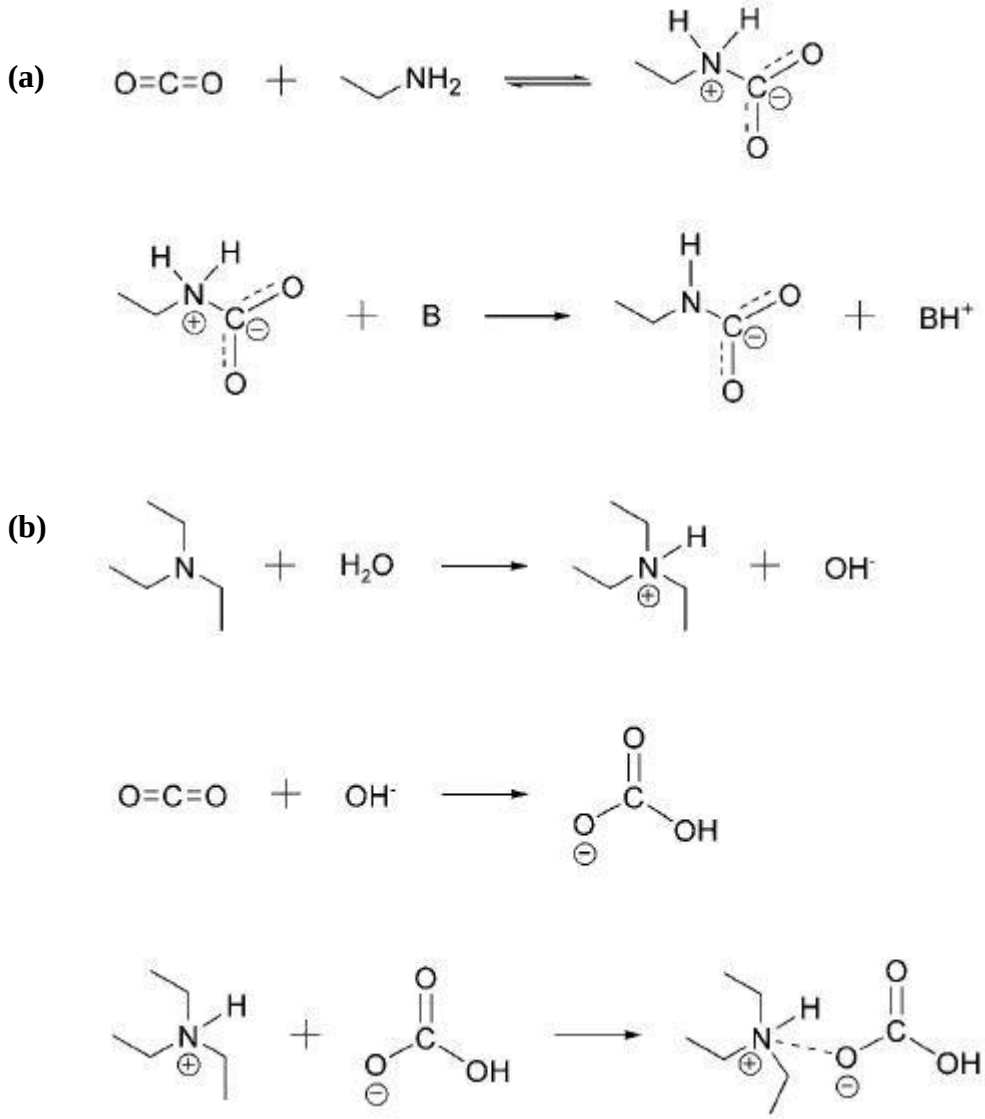

Figure 14: a) Primary and secondary amine reaction; b) Tertiary amine reaction.[28, 50]

The reaction of CO_2 and amine solvents follows two major mechanisms, that is, a zwitterion mechanism and a base-catalysed bicarbonate formation.[52] Figure 14 depicts the reaction process of these two mechanisms. Primary and secondary amines follow the zwitterion mechanism, where the lone pair electrons of the amine interacts with CO_2 to create the zwitterion. The zwitterion is deprotonated to form carbamate.

Tertiary amines follow the based-catalysed bicarbonate formation, where a tertiary amine molecule receives a proton from a water molecule to create a hydroxyl radical. Then, it initiates the base-catalysed hydration of CO_2 to form a bicarbonate anion, which finally associates with the protonated tertiary amine molecule.[52]

As a result, the absorption capacity is influenced by the type of amine used for CO_2 capture. Tertiary amines can reach CO_2 absorption capacities as high as 1 mol CO_2/mol amine. For primary or secondary amine solvents, the absorption capacity varies from 0.5-1 mol CO_2/mol amine, due to the side reaction of hydrolysis of some carbamates. Although the tertiary amine has a higher absorption capacity than those of primary and secondary amines, it exhibits a lower absorption rate. Therefore, in practice, it is necessary to add a small amount of primary and secondary amines to balance the performance.[28]

A major disadvantage of amine solvents is the energy penalty of the regeneration (up to 165 kJ mol^{-1} regenerated CO_2).[45] There are three main reasons for this: the first is that the regeneration process involves heating both amines and water. The second is the strong binding between CO_2 and amines. The last is the degradation of amine caused by impurities in the flue gas. It is estimated to result in about 20% reduction in electricity production in pulverised fuel power plants.[24] Besides, conventional amine solvents are highly corrosive, and they have high heat of absorption (72 kJ mol^{-1}),[45] which further raises the capital cost of equipment.

In order to resolve these issues, advanced amine solvents, such as diethanolamine (DEA) and methyldiethanolamine (MDEA) are used. They generate lower heat of absorption and less stable reaction products so that these amine solvents become more suitable for commercial applications.[28, 50] This is so because the lower heat of absorption reduces the capital cost of plant, and the absorbent can be regenerated from a less stable product at a lower temperature. Another method is using dilute MEA solution (about 18 wt%), where a lower concentration of MEA decreases the heat of absorption and reduces the degree of corrosion.[52] A third method is steric hindrance. The control is achieved by sterically hindering the amine groups with substituents, subsequently producing less stable carbamates.[45]

1.5.2 Ionic liquids

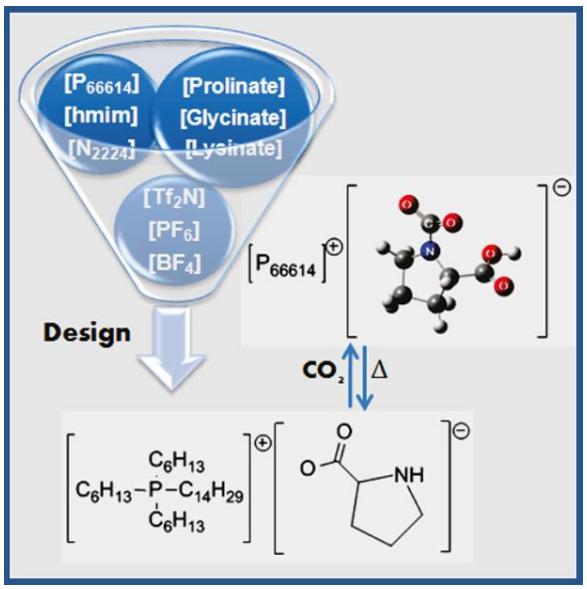

Figure 15: Various combinations of cations and anions for CO_2 capture.[63]

Ionic liquids are a type of low melting salt, which consists of numerous combinations of cations and anions.[28, 63] Ionic liquids are normally used as physical absorbents. Figure 15 introduces several combinations for CO_2 capture.

As physical absorbents, the mechanism of CO_2 capture by ionic liquids is based on physical absorption with the heat of absorption around -11 kJ mol^{-1}.[28, 64, 65] The weak interaction allows an ionic liquid to remove CO_2 after absorption by TSA or PSA. The absorption performance of ionic liquids is determined by various factors. First of all, as a physical absorbent, the CO_2 absorption capacity increases with the increasing CO_2 partial pressure. Therefore, ionic liquids are preferentially considered for natural gas sweetening and pre-combustion capture systems, where high CO_2 partial pressure conditions are applied. Moreover, distinct anions and cations influence the absorption capacities as well. Aki et al. reported that ionic liquids with the bis(trifluoromethylsulfonyl)imide anion had a higher CO_2 absorption capacity than those with a nitrate anion.[63, 66] Tang et al. also reported differences in CO_2 absorption capacities of poly(ionic liquids) with various combinations of anions and cations.[67] Figure 16 presents the CO_2 absorption capacities of ionic liquids with different cations and anions.

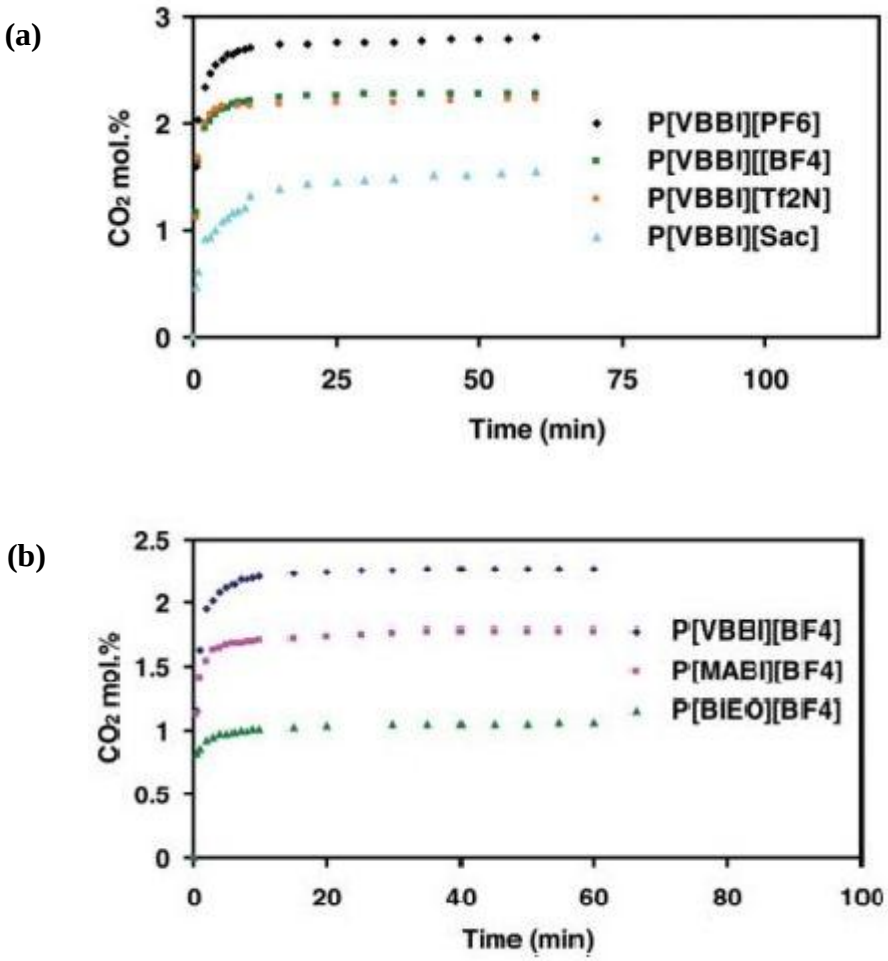

Figure 16: CO_2 absorption capacities of ionic liquids with: a) different anions; b) different cations.[67]

Low heat of absorption, low vapour pressure and high viscosity are significant advantages of ionic liquids. A lower heat of absorption indicates a lower energy requirement for desorption. A lower vapour pressure and higher viscosity help to prevent absorbent loss from volatilisation and leeching. With the addition of other advantages, for example, tunable functionality, non-flammability, low ecological impact and high thermal stability, ionic liquids show great potential to achieve exceptional CO_2 absorption or separation capabilities with balanced energy and operational demands. Besides, compared with amine solvents, ionic liquids possess less water content, which minimises energy loss due to water heating.[63]

Despite the many exceptional characteristics of ionic liquids, several limitations impede their application to large-scale operation. The very first practical issue is the high molecular weight of ionic liquids in general. Because of this, it is necessary to

employ a large mass of ionic liquid to operate the capture system. Taking 1-hexyl-3-methylpyridinium bis(trifluoromethylsulfonyl)imide as an example, it is learnt that 33 mol of this ionic liquid is required to absorb 1 mol of CO_2, that is, 15.1 kg of this ionic liquid is required to absorb 44 g CO_2. The weight absorption capacity is only 0.3% weight of the absorbent.[68] Furthermore, because of the low CO_2 partial pressure, ionic liquids are not suitable for post-combustion capture systems, which are the most adaptable capture systems for existing power plants. In addition, sulfur dioxide and hydrogen sulfide are the competitive gas components to CO_2 in the flue gas from the post-combustion power plants, because they also show considerable absorption capacities in ionic liquids, as has been discovered by Anderson et al.[69] and Rahmati-Rostami et al.[70], respectively.

1.5.3 Minerals

Minerals are a class of naturally occurring solid material. In CCS, minerals can be used for either chemical absorption or physical adsorption. The following section introduces the two most representative minerals that are based on different sorption mechanisms.

1.5.3.1 Lime

Calcium minerals possess the most abundant reserve among all alkaline earth metal oxides in nature.[50] Calcium oxide (lime) is used for CO_2 capture because its precursor $CaCO_3$ (limestone) is inexpensive and possesses abundant reserve.[71] As a solid chemical absorbent, the theoretical absorption capacity is 78.32 wt% (17.8 mmol g^{-1}). However, with the consideration of surface area and pore structures, capacities can vary from 35.2 wt% (8 mmol g^{-1}) to 74.8 wt% (17 mmol g^{-1}).[72]

The absorption is based on the carbonation reaction. At a temperature of about 600 ℃,[28] CaO absorbs a large amount of CO_2, and then forms calcium carbonate ($CaCO_3$):

$$CaO + CO_2 \xrightarrow{600\,℃} CaCO_3$$

The desorption mechanism is based on the calcination reaction, where calcium carbonate is calcined at about 800 ℃,[28] sequentially regenerating CaO and releasing CO_2:

$$CaCO_3 \xrightarrow{800\,℃} CaO + CO_2$$

Every two reactions form a cycle, called the "Carbonation-Calcination Cycle".

The major advantage of calcium oxide is that it can maintain high absorption capacities at high temperatures. This merit prompts its applications in pre-combustion power plants and hydrogen production plants, which produce high temperature gas streams before or after combustion.

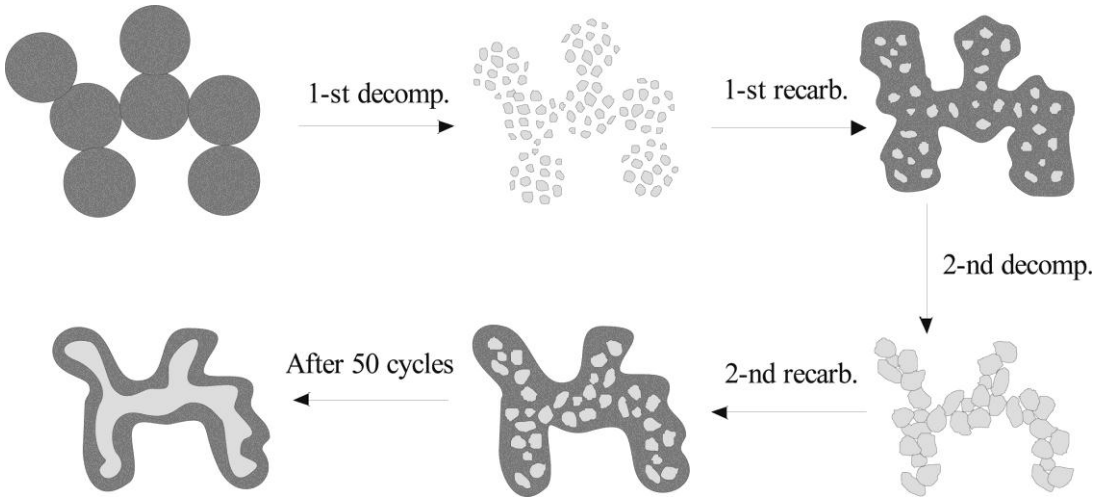

Figure 17: Schematic of the absorbent sintering process. The dark area represents $CaCO_3$, and the grey area represents CaO.[73]

However, calcium oxide also suffers from some severe problems. For example, both carbonation and calcination reactions take place at high temperatures, which implies high energy consumption at both stages. Furthermore, it takes a long time for the calcium oxide to reach its maximum absorption capacity. It takes about 6 hours for the calcium oxide to reach 70% of its maximum absorption capacity at 550 ℃.[74]

It is also observed that the absorption capacity decreases dramatically after several carbonation-calcination cycles. This is due to the pore blockage[75] and absorbent sintering,[73] which is caused by incomplete carbonation and calcination. This increases the cost of replacing disfunctional absorbents. In 1973, Barker raised the issue of pore blockage in the regeneration of calcium oxide.[72] However, the reason for pore blockage wasn't well understood. Further research shows that there is still residual calcium carbonate left in the absorbent after several carbonation-calcination cycles.

These residues form layers of calcium carbonate on the walls of the pores, and finally occupy the pores and impede the carbonation reaction in the next cycle. In addition, every calcination process is followed by an incomplete recarbonation process. It results in absorbent sintering that is illustrated in Figure 17. With the increasing amount of unreacted calcium oxides, a rigid layer of calcium carbonate is formed outside the unreacted calcium oxides, and it prevents further carbonation of calcium oxide inside this layer.[73]

1.5.3.2 Zeolites

Zeolites are a class of porous crystalline aluminosilicate materials (Figure 18a).[50] By virtue of the molecular sieving structure, zeolites provide negative framework charges that can be offset by exchangeable alkali cations such as Na^+. This structure enables zeolites to capture a wide range of acidic gas molecules that include CO_2.[76] Besides their extensive applicability, zeolites show good performance under mild conditions. Figure 18b shows a collection of zeolites' CO_2 adsorption isotherms at 22 ℃. It shows zeolites have varied performance but zeolite 13X can reach a capacity of 19.8 wt% (4.5 mmol g^{-1}) under 1 bar CO_2. Secondly, the regeneration of zeolites can be carried out by TSA or PSA, and the capacities of the zeolites can be recovered to almost virgin states after regeneration. Finally, zeolites have fast adsorption rates. For example, Hernandez-Huesca studied the adsorption kinetics of CO_2 on a natural zeolite.[77] At 20 ℃ amd 0.1 bar, it can reach 70% of the total capacity in 20 seconds, and the rest in a further 30 seconds. This is notably faster than the performance of calcium oxide.

(a)

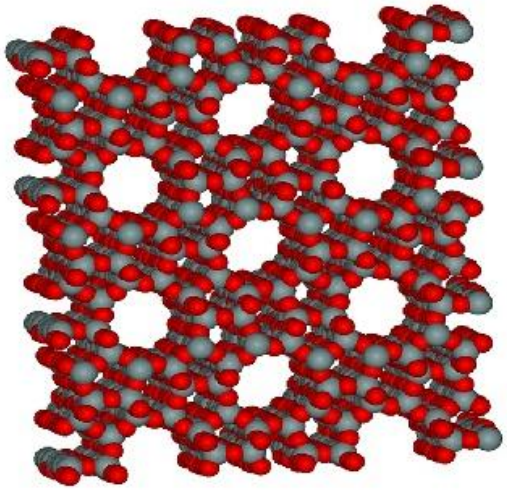

(b)

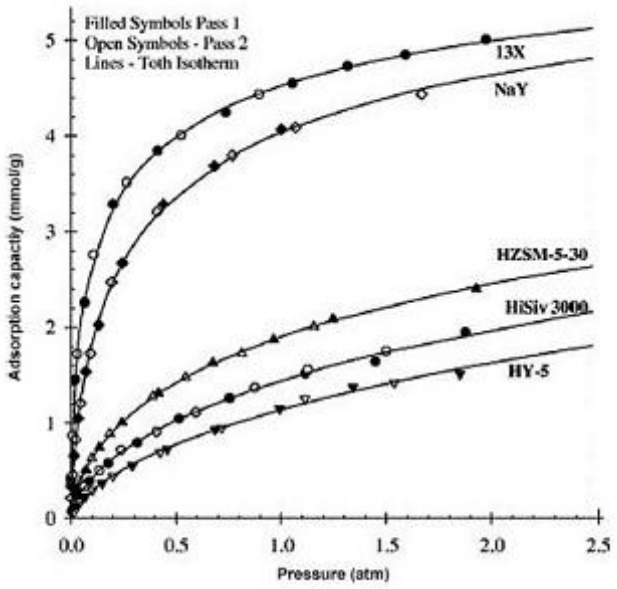

Figure 18: a) Porous frameworks of zeolites; b) CO_2 adsorption capacities of various commercial zeolites.[50, 53]

Regardless of the superiority of zeolites, the most pressing problem is their high susceptibility to moisture. The impact of moisture finds its expression in dramatically reducing the adsorption capacities of zeolites due to competitive adsorption. Therefore, in order to remove the influence of moisture, before and after CO_2 capture, zeolites need to be dried at high temperatures above 300 ℃. This results in additional cost at the preparation and regeneration stages.[50]

1.5.4 Metal-organic frameworks

Metal-organic frameworks (MOFs) are a class of three dimensional microporous crystalline materials that consist of metal nodes and organic bridging ligands.[28] MOFs have attracted great attention for their various tailorable structures and chemical properties in association with a great diversity of potential applications to CCS.

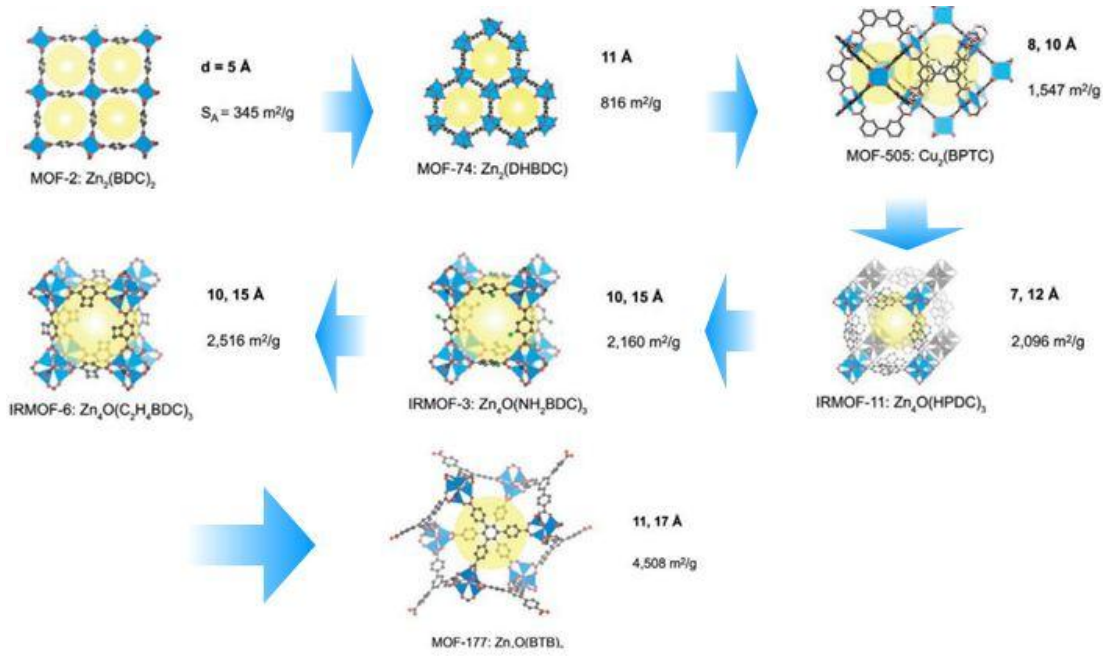

Figure 19: Various metal-organic frameworks and their specific surface area.[78]

MOFs possess a range of significant advantages over aforementioned solid adsorbents. The common advantages comprise unprecedented internal surface areas (1500 to 4500 $m^2\ g^{-1}$), high void volumes (55-90%), and low densities (from 0.21 to 1.00 g cm^{-3}).[28, 79] Figure 19 shows various MOFs of different specific surface area. What is more important, MOFs possess a regular monodisperse nature of crystalline array of micropores, which gives them the unique advantage over all other porous materials.[28] A specific example is MOF-177 ($Zn_4O(btb)_2$, btb=1,3,5-benzenetribenzoate). It has a surface area of 4500 $m^2\ g^{-1}$ and an adsorption capacity of 1474 wt% (33.5 mmol g^{-1}) at 32 bar, while benchmark material zeolite 13X has a surface area of 1500 $m^2\ g^{-1}$ and an adsorption capacity of 32.6 wt% (7.4 mmol g^{-1}) at the same pressure.[28, 78] Figure 20b shows the comparison between CO_2 adsorption capacities of MOF-177 and other adsorbents.

(a)

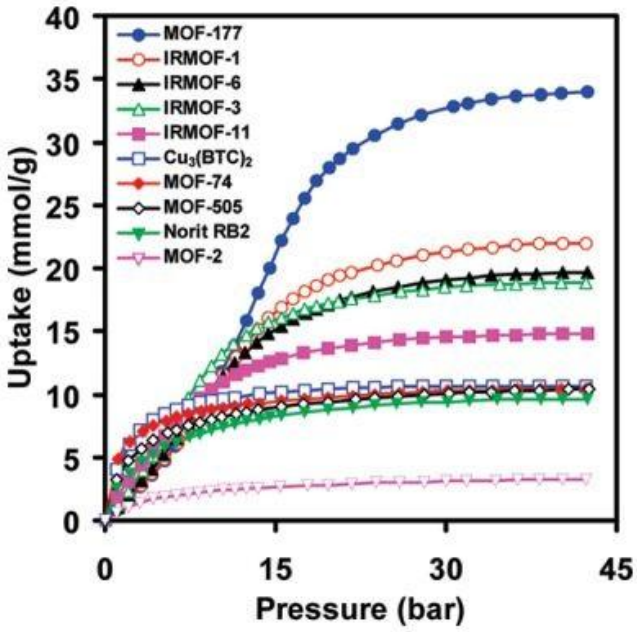

(b)

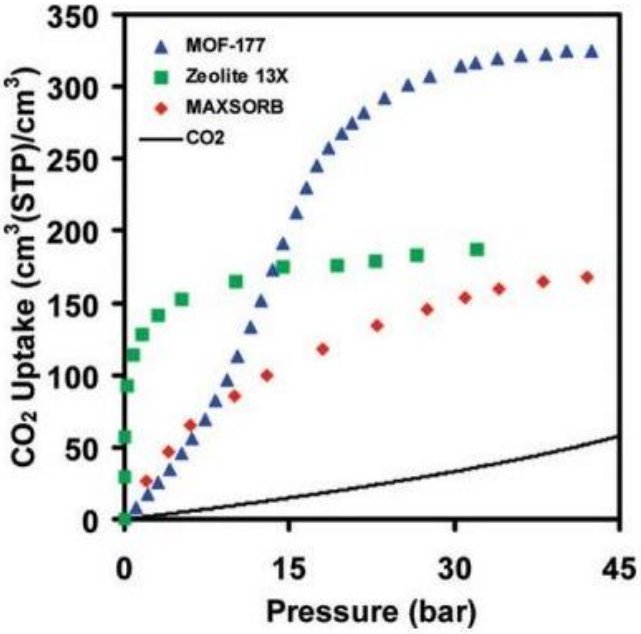

Figure 20: Comparison between CO_2 adsorption capacities of MOF-177 and a) other MOFs; b) zeolite 13X, MAXSORB commercial carbon.[78]

Despite all the remarkable advantages of MOFs, they are still at the preliminary stage of research, and this brings many practical issues. For example, the complex and costly synthesis, susceptibility to flue gas impurities (SO_x, NO_x, O_2, etc.) that cause degradation and decrease in capacities caused by competitive adsorption from other gas components.[28, 50] Therefore, future research on MOFs may focus on simplifying

the synthesis processes, reducing the expense and increasing the thermal and chemical stability.

1.5.5 Carbon

There are various issues with the aforementioned materials, so it is imperative to find an alternative class of solid materials, which has relatively good CO_2 capture performance and low cost. Carbon materials, such as activated carbon as a representative, possess advantages of inexpense and relatively high CO_2 uptake, compared with those of some previously-mentioned physical solid sorbents, as shown in Figure 21b.[50] Besides the relatively high surface area, it can host abundant functional groups, such as nitrogen-containing groups. These functional groups can be tailored to increase the adsorption capacity.[80] It also shows good chemical and thermal stability so that it can endure various critical environments, for example, high temperature, acidic and basic environments. When it comes to carbon materials, it is necessary to discuss the corresponding precursor materials, synthesis methods and characteristic properties.

(a)

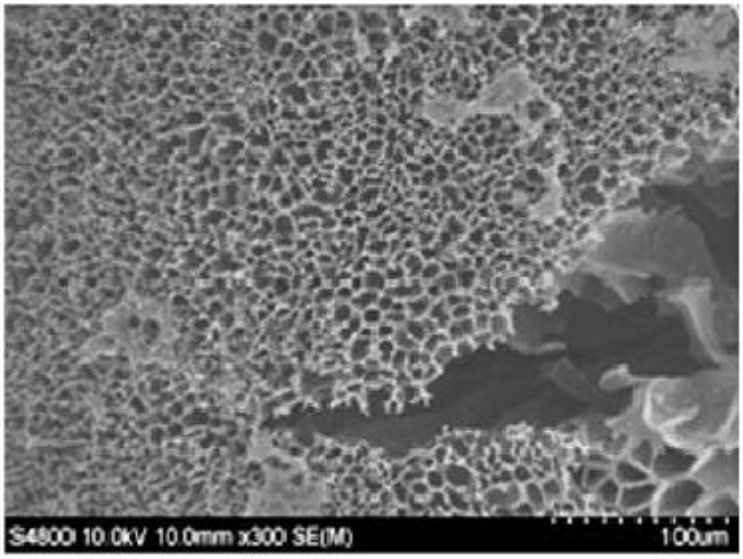

(b)

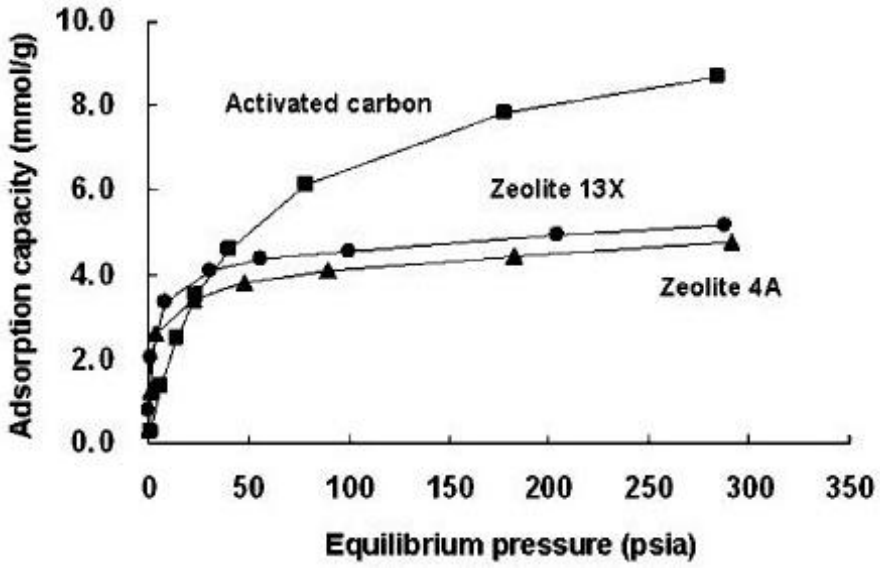

Figure 21: a) Porous structure of an activated carbon (macropores);[81] b) Comparison between CO_2 adsorption capacities of activated carbon and zeolite 13X.[50]

1.5.5.1 Precursors

Carbon materials can be obtained by pyrolysing (carbonising) either biomass (such as coconut shell) or synthetic precursors (polymer and MOFs). At high temperatures, precursors debond heteroatom elements, such as hydrogen and oxygen, mainly leaving carbon in resulting compounds. This is referred to as the "carbonisation" process. Besides the removal of heteroatoms, the remaining carbon atoms migrate for a short distance that is less than 1 nm to occupy more stable positions. Herein, the resulting structure contains segments of ordered and defective graphene sheets, which are randomly bonded with linear carbon atoms.[82] These defects within the structure exist in the form of voids. These voids, or in another word, pores, play an important role as hosting sites for CO_2 adsorption.

Each precursor has its own merits when compared with others. Generally speaking, polymer precursors can be tailored to meet specific applications, such as introducing nitrogen functional groups or metal dopants in polymer precursors. The use of nitrogen-containing polymer precursors is to introduce nitrogen dopants into the corresponding derived carbon. It has been widely discussed in the literature that nitrogen dopants can help to enhance CO_2 sorption on carbon due to their basicity.[83-87] About metal dopants, the use of rare earth metal dopants in a phenolic resin precursor is reported to

modify the resulting porous structure of its derived carbon.[88] It is also argued that some metal dopants, such as lithium[89] and potassium[90], have positive effects on CO_2 sorption on carbon materials. However, little experimental study has been carried out to demonstrate enhanced CO_2 sorption by metal doping. The following table presents carbon materials that are derived from various precursors by means of chemical activation:

Table 3: Summary of specific surface area and CO_2 uptakes (25 ℃ and 1 bar CO_2) of carbon materials derived from various precursors.

Sample	**Precursor**	**S_{BET} / m^2 g^{-1}**	**CO_2 / wt%**	**Ref.**
Biomass-derived carbon				[91]
AA-4-700	Starch	2190	15.2	
AC-4-700	Cellulose	2370	15.5	
AS-4-700	Sawdust	2250	12.8	
Nitrogen-Doped Porous Carbon RFL-700	Resorcinol, formaldehyde, L-lysine	519	13.7	[85]
Polypyrrole CP-2–700	Polypyrrole	2940	13.7	[86]
Nitrogen-rich porous carbon	Terephthalaldeyde melamine	993	14.1	[87]
Nitrogen doped Carbon CRHC221-DES	Resorcinol, 3-hydroxypyridine, choline chloride	666	14.5	[92]

*Note: "S_{BET}" stands for specific surface area calculated by the Brunauer-Emmett-Teller (BET) equation, "CO_2" for CO_2 uptake.

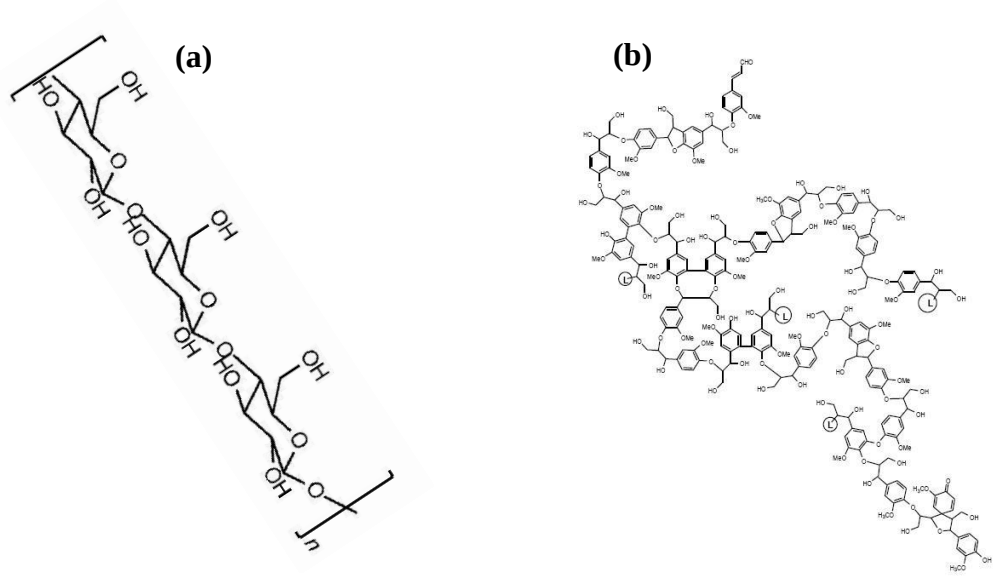

Figure 22: Typical chemical structures of (a) polysaccharides (starch and cellulose)[93] and (b) softwood lignin[94].

Table 3 summarises carbon sorbents derived from various carbon precursors. Under the same preparation conditions (KOH/precursor weight ratio 4:1 and activation temperature 700 ℃), Sevilla et al. found that cellulose (AC-4-700), starch (AA-4-700) and eucalyptus sawdust (AS-4-700) exhibit similar levels of porous structure development and thus CO_2 uptakes at 25 ℃ and 1 bar CO_2, due to similar chemical properties of carbon precursors and mechanisms of carbonisation. Polysaccharide is the major chemical in starch and celluloses. For sawdust, it is lignin. Their chemical structures are illustrated in Figure 22. This shows that aromatic carbon and heterocyclic carbon-oxygen rings are the main constituents in both chemical structures. Besides, hydroxyl is the major functional group grafted to the edges of those rings. The similarity in the chemistry of the precursors leads to a similar carbonisation process.

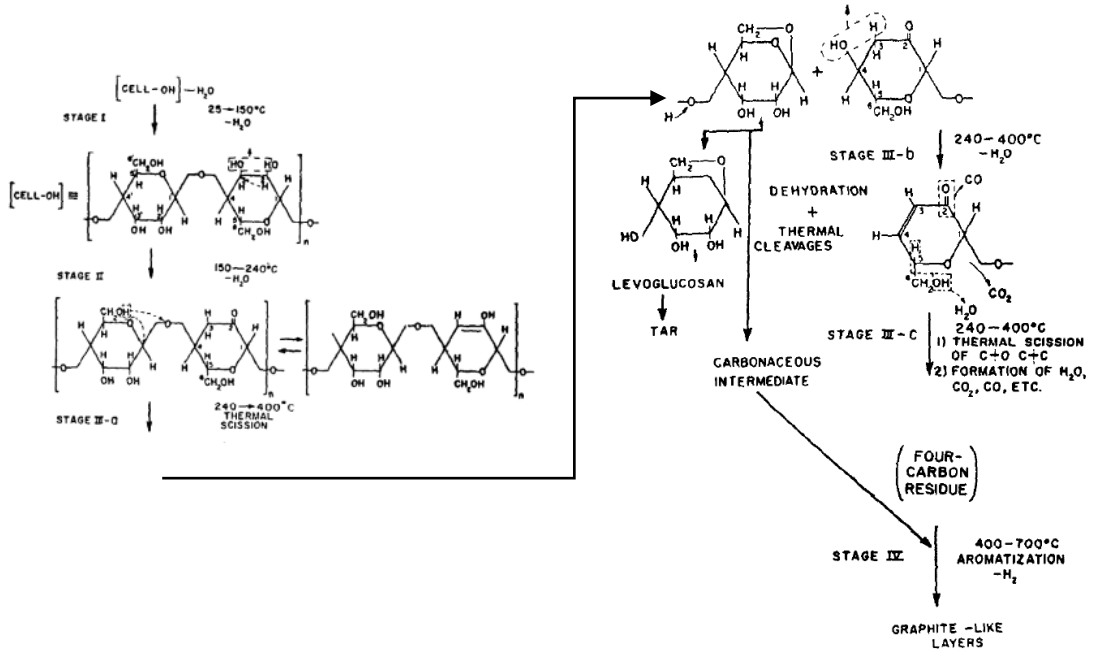

Figure 23: Carbonisation mechanism of cellulose.[95]

Taking the carbonisation of cellulose as an example, Figure 23 illustrates its underlying mechanism. Its carbonisation process involves four main stages:

Stage I: 25 → 150 °C, desorption of physically adsorbed gas molecules, such as H_2O.

Stage II: 150 → 240 °C, thermal dehydration reaction between adjacent hydroxyl groups, hydroxyl groups and adjacent hydrogen, alcohol groups and adjacent oxygen.

Stage III: 240 → 400 °C, thermal scission and cleavage to further remove non-carbon elements (mainly oxygen and hydrogen).

Stage IV: 400 ℃ and above, aromatisation to form the final carbon structure.

In consideration of specific surface area, for the cellulose and starch derived carbon, the slightly higher surface area of the former may be the reason for a higher CO_2 uptake. However, according to Table 3, this is not applicable to sawdust-derived carbon. Further analysis on pore size distribution reveals the cause of the difference, and this will be discussed in a later section. Although without the advantage of large surface area, other carbon adsorbents that are derived from nitrogenous carbon precursors show comparative results to porous carbon with large surface area. This is mainly thanks to the basic nature of nitrogen dopants in the resulting carbon.

1.5.5.2 Carbonisation and activation

Table 4: Summary of carbon materials derived from two different carbon precursors and prepared at various activation temperatures.

Sample	T / ℃	N / wt%	S_{BET} /m^2 g^{-1}	CO_2 /wt%	Ref.
Sawdust-derived carbon, KOH/carbon = 2:1					[91]
AS-2-600	600	N/A	1260	21.2	
AS-2-700	700	N/A	1390	19	
AS-2-800	800	N/A	1940	17	
Sawdust-derived carbon, KOH/carbon = 4:1					
AS-4-600	600	N/A	2370	12.8	
AS-4-700	700	N/A	2250	12.8	
AS-4-800	800	N/A	2850	13.0	
Polypyrrole-derived carbon, KOH/carbon = 2:1					[86]
CP-2–600	600	10.14	1700	16.9	
CP-2–700	700	2.14	2940	13.7	
CP-2–800	800	0.78	3410	11.7	
Polypyrrole-derived carbon, KOH/carbon = 4:1					
CP-4-600	600	2.52	2050	9.1	
CP-4-700	700	0.72	3480	9.5	
CP-4-800	800	0.47	3450	11.3	

Note: "T" stands for activation temperature, "N" for nitrogen content, "S_{BET}" for specific BET surface area, "CO_2" for CO_2 uptake.

As mentioned previously, carbon materials are normally produced by the carbonisation of carbon precursors. This involves pyrolysis of carbon precursors at high temperatures in an inert atmosphere, such as nitrogen flow, resulting in an increase in the carbon content and a decrease in the hereroatom content. In order to optimise the performance, it is necessary to further modify the porous structures of carbon materials. The modification involves selectively removing carbon atoms from the original structure. This is normally done by introducing activating agents to react with the carbon. Steam and potassium hydroxide are among the most commonly used and representative

activating agents for activated carbon production.[82] The major functions of activation are not just to create new pores and increase the specific surface area, but also to connect pores of different sizes to form a hierarchical open porous structure. Steam activation involves water molecules diffusing in carbon, subsequently removing some carbon atoms by means of gasification, creating new pores or enlarging pore sizes.[96] Potassium hydroxide activates the carbon structure in a similar way but the reaction takes place at a solid/solid rather than a gas/solid interface. Activation is a significant approach to the development of hierarchical porous carbon structure.

Activation temperature is a major factor influencing the adsorption capacity of the resulting carbon. Table 4 presents two types of carbon precursors activated at different temperatures and KOH/carbon weight ratios. The table shows that specific surface area increases with the elevating temperature, which is mainly due to more aggressive carbon removal reactions. The mechanisms of KOH activation reactions at different activation temperatures are as follows:

Below 700 ℃, the mechanism is mainly based on the dehydration reaction of KOH and the reduction reactions between dehydration products and carbon. Potassium carbonate is formed as a by-product:[97]

$$2KOH \rightarrow K_2O + H_2O \quad (1)$$

$$C + H_2O \rightarrow CO + H_2 \quad (2)$$

$$CO + H_2O \rightarrow CO_2 + H_2 \quad (3)$$

$$CO_2 + K_2O \rightarrow K_2CO_3 \quad (4)$$

Conversely, above 700 ℃, the decomposition of potassium carbonate generates potassium oxide and carbon dioxide, both of which take part in further reduction reactions with carbon:[98]

$$K_2CO_3 \rightarrow CO_2 + K_2O \quad (5)$$

$$CO_2 + C \rightarrow 2CO \quad (6)$$

$$K_2CO_3 + 2C \rightarrow 2K + 3CO \quad (7)$$

$$C + K_2O \rightarrow 2K + CO \quad (8)$$

These reactions above 700 ℃ play an important role to further enlarge the surface area and pore volume. However, they also widen the pore size range and alter the pore size distribution.

Besides the activation temperature, a higher ratio of potassium hydroxide to precursor also helps to develop a porous structure with a higher specific surface area. However, a high specific surface area does not guarantee an excellent CO_2 uptake as indicated in Table 4. For example, AS-4-600 uses more potassium hydroxide, compared with that used in AS-2-600. Its resulting specific surface area almost doubles that of AS-2-600. However, its CO_2 adsorption capacity is 40% lower than that of AS-2-600. The same phenomenon can be observed from AS-2-600 and AS-2-800 with different activation temperatures. This has much to do with the constitution of pore structures, or in other words, pore size distribution. Besides, the dosage of an activation agent also has an influence on the nitrogen-doped carbon sorbents. CP-4-600 doubles the usage of potassium hydroxide, compared with that used in CP-2-600. This results in a dramatic drop in its nitrogen content from 10.14 (CP-2-600) to 2.52 wt% (CP-4-600). The detrimental effect on their adsorption capacities is clearly shown in Table 4.

1.5.5.3 Specific surface area and pore size distribution

Studies on activated carbon used to focus on the competition for the highest specific surface area, because conventional viewpoints considered that all the surface area was available for adsorbing gas molecules. However, not all the surface area may act as the host site for steady gas adsorption. Gas sorption also depends on the strength of the interaction between adsorbents and adsorbates. The International Union of Pure and Applied Chemistry (IUPAC) defines macropores as having pore sizes larger than 50 nm; mesopores, 2 – 50 nm; micropores, less than 2 nm.[99] Some literature has discussed the influence of ultramicropore (less than 0.7 nm) on CO_2 uptakes.[86, 91] Figure 24a illustrates the configuration of a porous structure with hierarchical pore

sizes. These pores of different sizes play different roles in CO_2 capture. Macro- and mesopores provide an interconnected network for CO_2 diffusion, while micro- and ultramicropores are the major host sites for CO_2 molecules where adsorption occurs. Micro- and ultramicropores are usually considered in the form of "slits" in many experimental and computational studies on the CO_2 adsorption in porous carbon, as illustrated in Figure 24b. A "slit pore" is usually made of a few layers of graphene planes, where one or two layers are removed from the middle of the graphite structure. As a result, it leaves a void between two separated graphene planes. According to the Steele's 10-4-3 potential,[100] the interaction (adsorption potential) between adsorbents and adsorbates is much higher in the micropore range than the mesopore range, due to CO_2 interaction with the walls on both sides of the slit pore.[101]

(a)

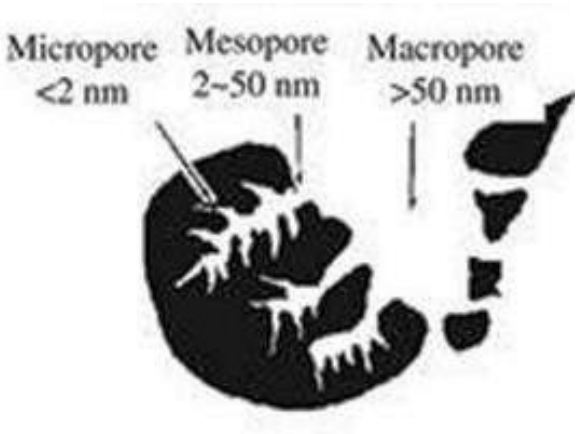

(b)

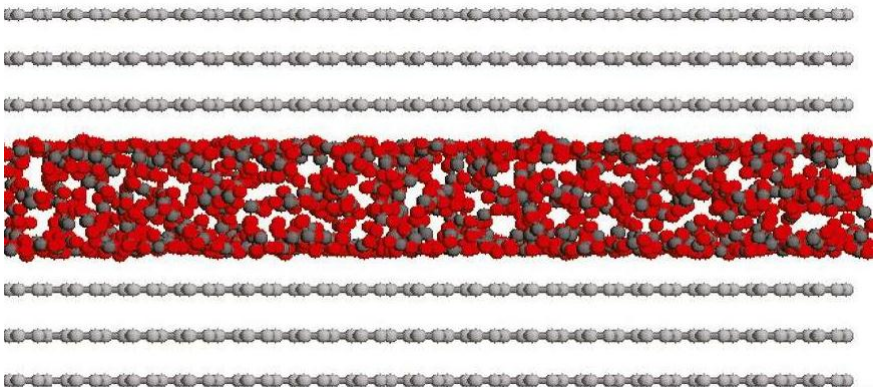

Figure 24: (a) An illustration of macro-, meso- and micropore in porous carbon;[102] (b) A simplified model of CO_2 adsorption in a 1.4 nm carbon slit pore (C: grey, CO_2: black and red).[103]

Based on the slit pore configuration, assuming two multi-layer graphene planes separated by a distance of H, the interaction potential between a gas molecule and both carbon walls can be described as:

$$\varphi_{sf} = \varphi_{sf}(z) + \varphi_{sf}(H - z) \quad \text{Equation 1}$$

where φ_{sf} is the solid-fluid interaction potential, z is normal distance between a gas molecule and one of the solid walls.

According to the Steele's 10-4-3 Solid-Fluid Potential[104]:

$$\varphi_{sf}(z) = 2\pi\rho_s\varepsilon_{sf}\sigma_{sf}^2\Delta\left(\frac{2}{5}\left(\frac{\sigma_{sf}}{z}\right)^{10} - \left(\frac{\sigma_{sf}}{z}\right)^{4} - \left(\frac{\sigma_{sf}^4}{3\Delta(0.61\Delta+z)^3}\right)\right) \quad \text{Equation 2}$$

where ρ_s is the number density of solid (for solid carbon, ρ_s=114 nm^{-3})[105], Δ is the distance between lattice planes (for graphite, Δ=0.335 nm), ε_{sf} and σ_{sf} are the cross interaction parameters.

According to Lorentz-Berthelot combining rules[106]:

$$\sigma_{ij} = \frac{\sigma_{ii}+\sigma_{jj}}{2} \quad \text{Equation 3}$$

$$\varepsilon_{ij} = \sqrt{\varepsilon_{ii}\varepsilon_{jj}} \quad \text{Equation 4}$$

In the case of CO_2 – C interaction, $\sigma_{CO_2} = 0.372\ nm$, $\frac{\varepsilon_{CO_2}}{k_B} = 236.1\ K$,[107] $\sigma_{carbon} = 0.335\ nm$, $\frac{\varepsilon_{carbon}}{k_B} = 28.0\ K$,[105] where k_B is the Boltzmann's constant.

Assuming there is only one CO_2 molecule in a slit pore and the CO_2 molecule stays at the centre of the slit pore, that is, z=H/2, then, the interaction potential can be re-written as:

$$\varphi_{sf} = \varphi_{sf}(z) + \varphi_{sf}(H - z) = 2\varphi_{sf}\left(\frac{H}{2}\right)$$

$$= 4\pi\rho_s\varepsilon_{sf}\sigma_{sf}^2\Delta\left(\frac{2^{11}}{5}\left(\frac{\sigma_{sf}}{H}\right)^{10} - 2^4\left(\frac{\sigma_{sf}}{H}\right)^{4} - \left(\frac{\sigma_{sf}^4}{3\Delta(0.61\Delta+\frac{H}{2})^3}\right)\right) \quad \text{Equation 5}$$

By plotting Equation 5 (as illustrated in Figure 25), it can be found that φ_{sf} reaches a minimum value. This indicates that the maximum interaction potential is attained at H=0.7 nm. The above calculation is an idealised representation of CO_2 adsorption on carbon, whereas in practice, the optimal pore size may vary with different pore geometries. However, the above mathematical derivation demonstrates why in theory micropores are important in the case of CO_2 capture..

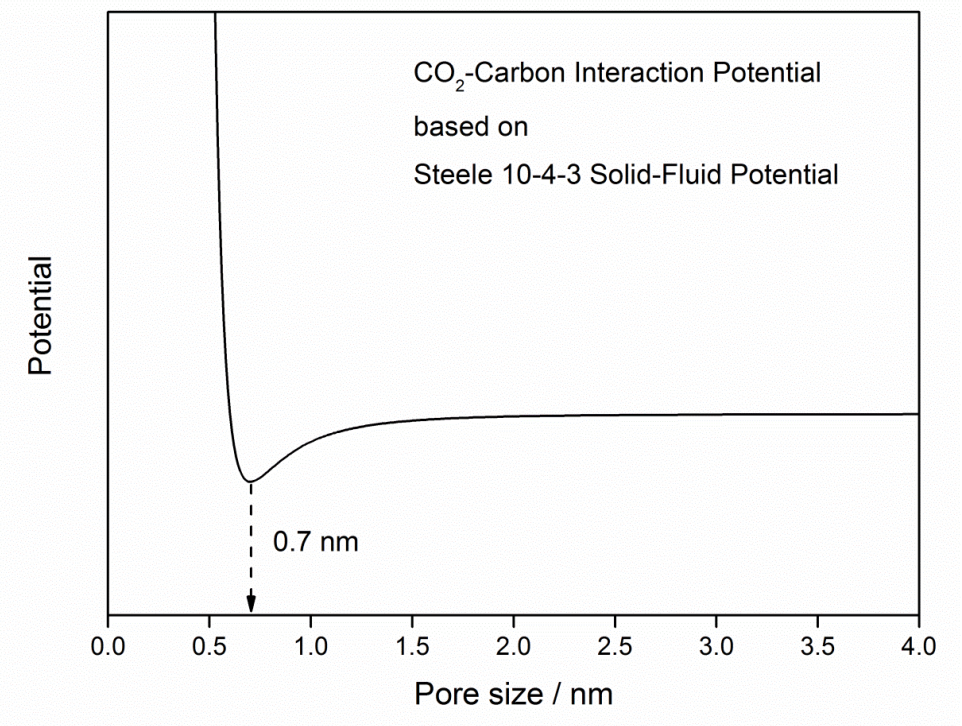

Figure 25: CO_2-Carbon interaction potential calculated based on the Steele's 10-4-3 Solid-Fluid Potential. For a CO_2 molecule in the middle of a slit pore, theoretically, the maximum potential is reached when the pore size is tailored to 0.7 nm.

Table 5 reveals that although a higher ratio of activating agents (potassium hydroxide in this case) to precursor can help to develop a porous structure with a larger specific surface area, it doesn't necessarily help to improve CO_2 capture capacity because the development of micropores plays a more important role here. For example, the sawdust-derived carbon sample AS-4-600 (KOH/Sawdust: 4:1) possesses a high specific surface area of 2370 $m^2 g^{-1}$. This is almost double that of the sample AS-2-600 (KOH/Sawdust: 2:1). However, further analysis shows that the drop in CO_2 uptakes is mainly due to the enlargement of ultra-micropore (<0.7 nm). For example, for the sawdust-derived carbon prepared with the KOH/carbon ratio of 2:1, its micropore is

made up of 95% ultramicropore, while for the material prepared with the ratio of 4:1, the proportion dramatically drops to 34%. It results in the corresponding CO_2 uptake drop from 21.2 to 12.8 wt%. In addition, for the sample activated at 800 ℃, its ultramicropore proportion and CO_2 uptake drops to 55% and 17 wt%, respectively.

Table 5: Summary of the specific surface area and pore size distribution of various carbon adsorbents.

Sample	S_{BET} /m^2 g^{-1}	S_{micro} /m^2 g^{-1}	V_{total} /cm^3 g^{-1}	V_{micro} /cm^3 g^{-1}	V_{ultra} /cm^3 g^{-1}	CO_2 /wt%	Ref.
Sawdust-derived carbon							[91]
AS-2-600	1260	1230	0.62	0.55	0.52	21.2	
AS-2-700	1390	1360	0.69	0.62	0.60	19.0	
AS-2-800	1940	1840	0.97	0.82	0.45	17.0	
AS-4-600	2370	2050	1.15	0.91	0.31	12.8	
Polypyrrole-derived carbon							[86]
CP-2–600	1700	N/A	0.88	0.74	0.39	16.9	
CP-2–700	2940	N/A	1.37	1.14	0.32	13.7	
CP-2–800	3410	N/A	1.94	1.21	0.24	11.7	
CP-4–600	2050	N/A	1.03	0.74	0.21	9.1	

Note: "S_{BET}" stands for specific BET surface area, "S_{micro}" for specific micropore surface area, "V" for total pore volume, "V_{micro}" for micropore volume, "V_{ultra}" for ultramicropore volume, "CO_2" for CO_2 uptake.

1.5.5.4 Adsorption temperature

As mentioned previously, physical adsorbents tend to lose their adsorption capacities with an increase in temperature. Carbon materials are no exception. The following table

shows the influence of elevated temperatures on the two carbon samples discussed previously.

Table 6: CO_2 uptakes of carbon materials at different adsorption temperatures.

Sample	Adsorption T/°C	CO_2/wt%	Ref.
Sawdust-derived carbon AS-4-700	0	24.3	[91]
	25	12.8	
	50	7.9	
Resorcinol Formaldehyde-derived carbon RFL-500	25	13.7	[85]
	60	7.2	
	80	5.4	

It is not beyond expectation that the CO_2 adsorption capacities decrease dramatically with the increasing adsorption temperature. For the sample AS-4-700, when its adsorption temperature increases from 0 to 25 ℃, it loses 47% of its CO_2 adsorption capacity. With a further increase from 25 to 50 ℃, it loses an additional 38% of its adsorption capacity at 25 ℃. For the sample RFL-500, there is a 47% loss of CO_2 adsorption capacity from 25 to 60 ℃, and a further 25% loss from 60 to 80 ℃.

This is a significant issue for the practical application of carbon materials for capturing CO_2 from power plants. As presented in the previous section of CO_2 capture system, the flue gas from either post-combustion or pre-combustion possesses a slightly elevated temperature (40 to 70 ℃) from room temperature (25 ℃).[28] However, Table 6 has shown the deviation in this range is enough to have a negative impact on the adsorption capacities of carbon materials. A direct solution is to allow the flue gas to cool to the ambient temperature before capture, but it may not be practical because it requires additional time and space to store the flue gas for the cooling process. From the material's perspective, dopants can be introduced to enhance CO_2 binding with carbon materials at elevated temperatures. This will be discussed in detail in the discussion of specific materials.

In summary, the merits and drawbacks of each material for CCS applications have been discussed with an emphasis on carbon materials. In conclusion, key challenges for large-scale CCS applications are capacity, regenerability, working life, energy penalty, and integration with power plants or other primary CO_2 emitters.

1.6 Challenges

1.6.1 Challenges in modern industries

Despite recent advances in CCS, it still faces many challenges. For example, a typical 500MW coal-fire power plant generates 7 tonnes (30000 m^3) of CO_2 per minute.[63] Such high CO_2 emission intensity places a great demand on capacities and efficiencies of CO_2 capture technologies. The focus of these challenges is to reduce the overall cost of capture technologies.

Energy consumption is the primary obstacle to the introduction of CO_2 capture technologies to modern industry. The IPCC reported that the capture of 90% CO_2 by present CO_2 capture technologies would cut the power generation efficiency by 24–40% for new supercritical pulverised coal plants (PC), 11–22% for natural gas combined cycle plants (NGCC), and 14–25% for coal-based integrated gasification combined cycle plants.[24] By this token, currently, integration of power plants with CO_2 capture technologies greatly decreases the overall efficiency of power generation. Subsequently, the reduced efficiency inevitably increases the prime cost of electricity.

Within the above challenge, the regeneration of sorbents is the major cause of high energy consumption because most sorbed CO_2 gas molecules are released by TSA and PSA methods. The operation of both TSA and PSA requires additional energy for heating and evacuation. For example, liquid chemical solvents, such as MEA, are required to be heated to 100 - 140 ^oC, in order to release CO_2. For solid chemical sorbents, such as calcium oxide, the regeneration of those sorbents needs to be carried out at an even higher temperature, typically 900 ^oC or so.[24] These indicate a high energy requirement at the regeneration stage and cause the high cost of regeneration of sorbents. Besides energy consumption, the regeneration of sorbents also faces the

challenges of corrosive products, degradation of sorbents and a large amount of heat that is generated by the exothermic reaction of absorption. These further increase capital and maintenance costs.

Another significant challenge is to retrofit existing CO_2 capture technologies to modern industry, especially to power plants. As mentioned previously, there are three main CO_2 capture systems. The integration of those CO_2 capture systems into a power plant is not a simple task. The task is not just to install the system behind the last gas exhaust outlet, but comprehensively to understand the features of a specific type of power plant. Different power plants use different fuels for the combustion process (coal, hydrogen or syngas), burn fuel in different environments (air or pure oxygen), generate CO_2 at different stages (before or after the combustion process), and produce exhaust gases with different components (hydrogen, nitrogen mixed with different concentrations of CO_2). Investment in retrofitting may further raise the prime cost of electricity. The IPCC predicts that it will increase the price of electricity at a NGCC plant by 0.01-0.02 US$/kWh, and the increase will be 35-70%. Similarly, the increase would be 0.02-0.03 US$/kWh (40-85%) for a supercritical PC plant, and 0.01 to 0.02 US$/kWh (20–55%) for an IGCC plant.[24]

1.6.2 Challenges in CO_2 capture research

All in all, the development of CO_2 capture is still at its early demonstration stage. Therefore, the challenges of CO_2 capture in modern industries are actually the challenges in CO_2 capture research. Overall, material is the core issue. Researchers are pursuing approaches to the enhancement of CO_2 capture capabilities of various materials, including monoethanolamine and calcium oxide as representative chemical sorbents, with zeolites, activated carbon and metal-organic frameworks as representative physical sorbents. Currently, chilled ammonia and amine solvents are favoured by modern industries due to their merits (especially rich in handling experience) discussed in the previous section of CO_2 capture materials. However, it is also mentioned that these CO_2 capture materials possess some intrinsic disadvantages due to their chemical nature. High energy consumption and corrosive (even toxic) products are the two major problems in practical large-scale CO_2 capture applications. Although intensive studies have been carried out to address these challenges, the

corresponding solutions are always a compromise between material performance, costs and energy consumption. As shown above, a good example is the dilution of monoethanolamine in exchange of less corrosiveness but higher energy penalty.

The limitations of conventional CO_2 capture materials are driving the search for alternatives with higher CO_2 capture efficiencies, where physical solid sorbents have emerged as a solution. Fast gas adsorption/desorption switch (less energy penalty) and environmental friendliness (less corrosiveness and toxicity) are the two significant advantages of these types of materials over the conventional ones. In addition, as a representative type of solid sorbents, other merits of carbon materials are that they are chemically stable, low cost, easily produced and are derived from abundant precursor materials. A key challenge for carbon materials is the improvement of their CO_2 adsorption capacities in a single cycle of adsorption/desorption. As discussed previously, the comparatively low adsorption capacities of carbon materials are due to the weak interaction between CO_2 molecules and carbon structure (the van der Waals force). Therefore, in order to improve the CO_2 uptake of a carbon material, it is essential to enhance the CO_2 binding with carbon materials. The enhanced interaction can be achieved through tailoring porous carbon structures and introducing dopants in carbon materials. More specifically, the former was once eagerly pursued by means of maximising the surface area of carbon materials. As a result, earlier literature is keen to report the achievement of porous carbon materials with larger specific surface area and pore volumes. For the latter, surface modification with nitrogen-containing functional groups (such as amines) and intrinsic nitrogen doping (from nitrogen-containing carbon precursors) are usually adopted to obtain nitrogen-containing carbon sorbents. Similar to the studies on surface area, carbon sorbents with richer nitrogen content spring up in the literature and it is proposed that CO_2 uptake increases with the increasing amount of nitrogen contained.

However, larger surface area and higher nitrogen content does not necessarily lead to a better CO_2 uptake, because they don't guarantee a stronger interaction between gas molecules and materials. In the case of porous structure modification, an enhanced interaction can be achieved by optimising the pore size distribution, where the interaction is enhanced due to the overlap of interaction potential of CO_2 molecules with the surrounding walls in the pores. For nitrogen doping, it is the types of nitrogen

that determine the strength of the interaction. Therefore, it is important to selectively control the types of nitrogen groups in carbon sorbents to effectively enhance CO_2 uptakes. In this case, amines and pyridinic nitrogen groups are favoured because they have a lone pair of electrons and thus higher basicity. CO_2 is acid gas and thus it has higher affinity towards more basic nitrogen groups.

In addition, despite some computational studies, there is little experimental work on metal doping in carbon sorbents and its influences on CO_2 uptakes. Besides the control of intrinsic properties of carbon materials, some practical CO_2 capture applications have specific requirements on bulk structures as well. For example, in the case of fluidised-bed applications, it is preferable to shape carbon sorbents into the spherical form due to a smooth rotational impact and less abrasion. To date, most carbon sorbents reported in the literature are prepared in the form of powders at micro- or nanometre-scale. Carbon powders can be used for fixed-bed applications, although extra care is required to prevent loss of materials and block of filters due to the size issue. In summary, the research on carbon materials for CO_2 capture faces challenges and opportunities at the same time. In order to compete with conventional materials and realise its applications in large-scale CO_2 capture, the above issues need to be addressed to further improve the performance of carbon sorbents.

Therefore, the general objective of this project is to explore various ways to improve the CO_2 capture performance of carbon materials with the preservation of its established merits, such as low-cost and easy production. Based on the literature review, it can be concluded that carbon precursors, porous structures and chemical dopants are three key factors that determine the performance of a carbon sorbent. Therefore, the corresponding experimental work focuses on optimising and balancing the influence of the above three factors.

This thesis reports the studies on two aspects of work - materials and methods. In respect of materials, firstly, biomass precursors are used as low cost natural sources of carbon, nitrogen and metals. The residual metal elements in the so-derived carbon sorbents are studied to unveil the role of atomic metal doping on CO_2 uptakes in laboratory experiments. Secondly, polymeric and graphitic precursors are studied because of well-defined chemical structures and compositions, in order to understand

their consequent influences on carbon sorbents. With regard to sample preparation, chemical activation, as a widely used method to develop porous structures, is adopted in all experimental work to produce porous carbon structures at different levels. This is to study the influence of the specific surface area and pore size distribution on CO_2 uptakes. In addition, a novel method is introduced to produce carbon spheres of millimetre sizes for fluidised-bed CO_2 capture applications. The corresponding experimental details, results and discussions are presented in the following chapters.

Chapter 2:

Experimental Section

2.1 General experimental details

2.1.1 General sample preparation

Unless specified otherwise all chemicals were used as purchased from manufacturers. For collected biomass wastes, they were cleaned by distilled water and dried in a vacuum oven at 80 ℃ overnight. The chemical activation method was applied in all experiments to generate different levels of microporous carbon structures and KOH was used as the activating agent to react with carbon. Each carbon precursor was mixed with KOH in distilled water to form a uniform suspension. This suspension was then dried in the vacuum oven to form a solid mixture of precursor and KOH for the subsequent chemical activation. The carbonisation and chemical activation reactions were carried out in a horizontal tube furnace (Model VTF 15/75/450, Lenton, UK) at elevated temperatures with a constant nitrogen (BOC, UK) flow through the furnace. The temperature ramping rate and dwell time are specified in each experiment in the following sections. After chemical activation of carbon precursors, the samples were repeatedly washed with distilled water and filtered to remove the residual potassium within the samples. During the washing procedure, the wet samples and filtered water were also repeatedly tested with pH strips to indicate the neutrality of the washed samples. Then, the wet samples were dried in the vacuum oven overnight at elevated temperatures.

2.1.2 General sample characterisation

Unless specified otherwise sample characterisations were carried out with the presented experimental equipment. Any additional characterisation equipment is specified in each experimental description in the following sections.

For sample imaging, a field-emission scanning electron microscope (SEM, JSM 6301F, JEOL, Japan) was used for imaging sample morphology, macro- and mesoporous structures. Before imaging, samples were fixed to conductive carbon tabs onto SEM sample holders and then gold coated to avoid electron charging. If necessary, samples were cut by a scalpel in order to image their cross-sectional morphology. High resolution images were obtained from a transmission electron microscope (TEM, JEOL

2100, Japan). Samples were ground, suspended in methanol and agitated by an ultrasonicator to achieve uniform suspension. A drop of the suspension was dropped onto a carbon-film coated copper grid (300 mesh) and then dried in air before being loaded into the TEM.

For elemental analysis, a Fourier transform infrared spectroscopy (FTIR, NICOLET iS10, Thermo Scientific, USA) and an X-ray photoelectron spectrometer (XPS, K-ALPHA, Thermo Scientific, USA) were used to analyse the chemical compositions and surface functional groups of the samples. For the XPS, the monochromatic aluminum-Kα X-ray was used. The identities of elements and chemical compounds were retrieved from either the literature or from the NIST XPS online database by searching their corresponding binding energies in the database.[108]

For porosity analysis, an automated gas sorption analyser (Autosorb-iQ C, Quantachrome, USA) was used to analyse the sample porosity. The specific surface area, specific micropore surface area, micropore volume and pore size distribution were derived from the corresponding nitrogen sorption isotherm at 77 K (liquid nitrogen) and calculated by both the Brunauer-Emmett-Teller equation (BET) and the Non-Local Density Functional Theory (slit/cylindrical pores) equilibrium model (NLDFT). The total pore volume was derived from the amount of gas adsorbed at the partial pressure P/P_0 of 0.99. The ultramicropore volume (pore size < 0.7 nm) was derived from the 0 ℃ CO_2 sorption isotherm and calculated by the 273 K CO_2 on Carbon NLDFT model. In addition, the macropore volume was measured by means of a mercury porosimeter (AutoPore IV, Micromeritics, USA) between 0.03 and 248 bar. In addition, a Raman spectroscopy (inVia, Renishaw, UK) was used to compare the disorder in chemical structures of carbon materials. The source of the Raman laser was Argon and the corresponding wavelength was 514.4 nm.

For CO_2 sorption analysis, the same gas sorption analyser was also used to obtain CO_2 (Carbon dioxide research grade, BOC, UK) adsorption isotherms at 0, 25 and 50 ℃. The sample was firstly degassed at the degassing station at 150 ℃ in vacuum for at least 2 hours. Then, the sample was moved to the analysis station for measuring CO_2 uptake at different pressures below 1 bar. The corresponding heat of adsorption was

calculated by the Clausus-Clapeyron equation based on the CO_2 adsorption isotherms at 0, 25 and 50 ℃.

2.2 Infrared spectroscopy

In an infrared spectrometer, a radiation beam of all interested infrared frequencies is irradiated on a sample KBr disk. As a result, a proportion of waves with particular frequencies can be absorbed by the sample. For an infrared radiation to be absorbed by a molecule, the frequency of the oscillating radiation needs to match the natural frequency of a particular vibrational mode of a molecule (or a chemical bond in the molecule). Therefore, the absorption of infrared radiation can be used to identify a molecule or a chemical bond within. When a photon of infrared radiation is absorbed by a molecule, the molecule changes from the ground to the excited vibrational state. The difference between these two energy states is a characteristic of the molecule and can be presented as wavenumber. Then, an infrared spectrum can be obtained by plotting absorption (or transmittance) intensity vs. wavenumber. Characteristic peaks related to infrared absorption can be observed in the spectrum and thus be used to identify molecules and chemical functional groups in a material.[109]

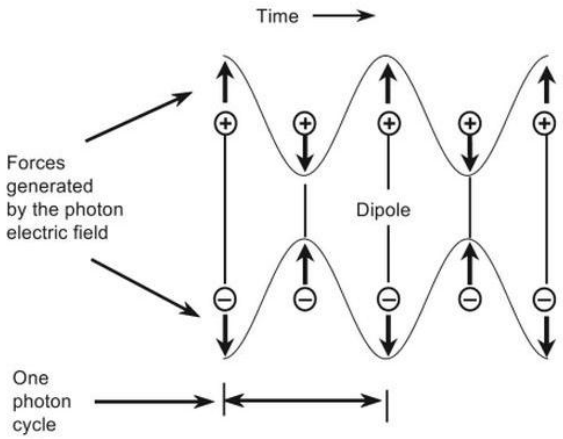

Figure 26: The interaction between the oscillating electric field of a photon and a molecular dipole. The dipole spacing changes at the same frequency of the incident photon.[109]

It is mentioned above that two frequencies of infrared radiation and molecular vibration need to match for the infrared absorption to occur. This reason is that the dipole moment of the molecule needs to be changed by the molecular vibration, in order to allow energy to transfer from a photon to a molecule. This is caused by the oscillating electric field introduced by infrared radiation. The oscillating electric field interacts with the dipole of a molecule, where it causes the oscillation of the dipole moment of the molecule and changes the dipole spacing periodically, as illustrated in Figure 26.

2.3 Raman spectroscopy

When a beam of electromagnetic wave (laser in the case of Raman spectrometer) irradiates on a material, the electromagnetic wave interacts with the molecules of the material. More specifically, the laser photon excites the molecule to a virtual energy level before a photon is instantly "scattered" away from the molecule. The "scattered" photo can possess the same, lower or higher energy, when compared with that of the incident one, due to the exchange of energy between the photon and the molecule. The resulting energy of the photon depends on the type of scattering, that is, Rayleigh, Stokes Raman and Anti-Stokes Raman scattering, respectively. The difference between the initial and resulting energy states causes a shift in the frequencies been the incident and the "scattered" photons, which can be used to identify molecules and characterise the structure of a material. This shift in frequencies is usually reported as wavenumber and plotted against scattering intensity to produce a Raman spectrum. The mechanisms of Rayleigh, Stokes Raman and Anti-Stoke Raman scatterings are illustrated in Figure 27.[109]

In the case of carbon materials, two characteristic bands (D and G) are usually observed in their spectra. D band usually appears around 1350 cm^{-1} while G band is around 1580 cm^{-1}. The former is associated with the hybridised vibrational mode related with carbon edges, which indicates the existence of disorder in the carbon structure. In contrast, the latter corresponds to the existence of graphite-like structures. Therefore, the intensity ratio of D and G bands can be regarded as an indication of the disorder of carbon materials.[110-112]

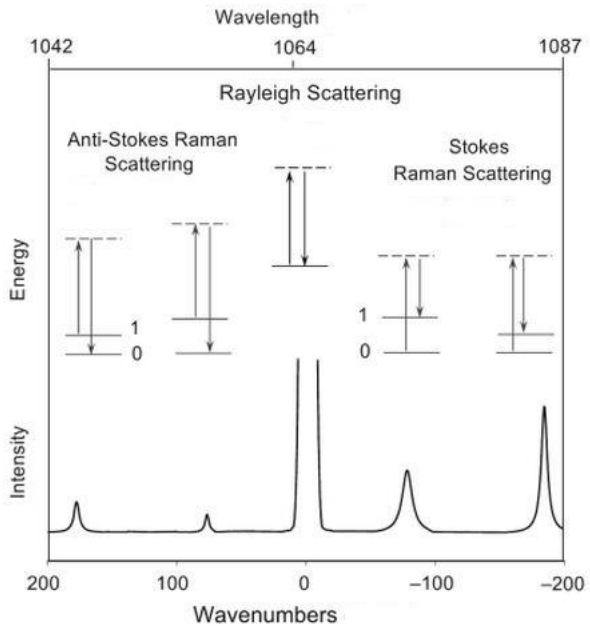

Figure 27: Schematic of Rayleigh, Stokes-Raman and Anti-Stokes-Raman scattering.[109]

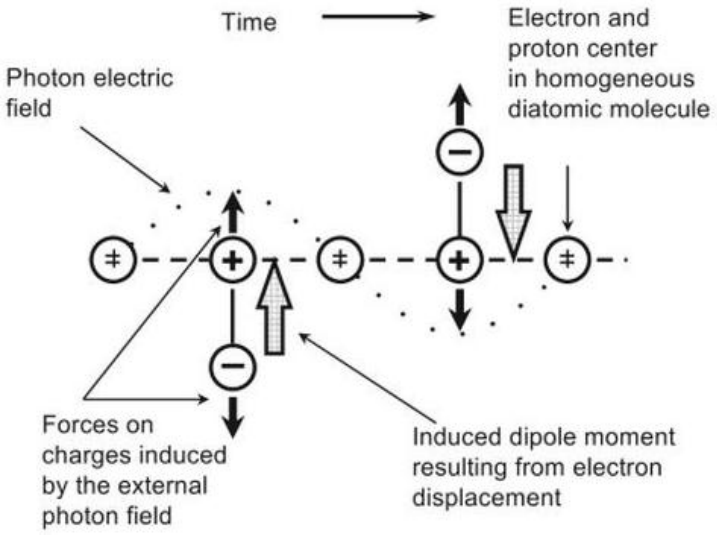

Figure 28: The interaction between the oscillating electric field of a photon and a homonuclear diatomic molecule. A dipole moment is induced by the photon electric field, which causes the displacement of the electron centre.[109]

It is previously mentioned that infrared absorption is caused by the change of molecular dipole moment induced by the oscillating electric field of infrared radiation. In the case of Raman scattering, the change of molecular dipole moment is induced by the deformation of electron cloud of a molecule by the external electric field of an

electromagnetic wave, that is, the polarisability of a molecule. Figure 28 shows how the electric field of a photon leads to an induced dipole moment in a homonuclear diatom.

Both infrared and Raman spectroscopy involve the interaction between the oscillating electric field introduced by an electromagnetic wave and the molecular vibration. However, the major difference is how the energy is transferred to/from a molecule and change the vibrational state of the molecule. Infrared spectroscopy involves the resonance interaction between the oscillating electric field and the existing dipole moment of a molecule. Therefore, those molecules with existing dipole moment are infrared active. In the case of homonuclear diatomic molecules, such as H_2, N_2 and O_2, they do not have existing dipole moment and thus are infrared inactive. However, the electron cloud of these diatomic molecules are still deformable in the case of Raman scattering. Therefore, they are Raman active molecules.[109]

2.4 X-ray photoelectron spectroscopy

X-ray photospectroscopy (XPS) is heavily used for the characterisation of surface elemental compositions and chemical functional groups of solid materials. In a typical XPS analysis, a beam of X-ray is irradiated on the sample surface under an ultra-high vacuum condition. If the energy of the photons is sufficient, as a result, core electrons in an atom can be struck out by the incident photons as photoelectrons into the vacuum. The kinetic energy of an emitted photoelectron can be quantitatively measured, and the binding energy of the electron can be calculated by the following equation:

$$E_{binding} = E_{photon} - (E_{kinetic} + \emptyset)$$

where $E_{binding}$ is the binding energy of the electron, E_{photon} is the energy of the incident photon, $E_{kinetic}$ is the kinetic energy of the emitted electron and Φ is the work function of the analyser. The binding energies of electrons in different electron orbitals are known for different chemical elements. Therefore, they can be used to identify atoms/ions of specific elements in a sample.[113, 114]

A photoelectron spectrum can be obtained by plotting "counts per second" vs. binding energy. "Counts per second" indicates the number of photoelectrons detected by the spectrometer.[113] The characteristic peaks (binding energies) in the spectrum can be used to identify chemical elements in a sample. When multiple elements are detected in an analysis, the area under these peaks (curves) can be used to calculate the compositions of detected elements. In addition, some peaks can be further deconvoluted into sub-peaks, because the same element can exist in different forms of chemical functional groups. The positions (binding energies) of sub-peaks can be used to identify these functional groups, and area under these sub-peaks (curves) can be used to calculate their compositions as well.

2.5 CHN analyser

It is mentioned earlier that XPS is a surface chemistry characterisation technique. Therefore, an additional elemental analysis is required to obtain the chemical composition of the whole sample. This is where CHN (carbon, hydrogen and nitrogen) analysis comes into play. In a typical CHN analysis, a small quantity (1-2 mg) of sample is weighed with a tin container, which can promote a violent exothermic reaction during the combustion in an oxygen-rich environment. This helps to raise the combustion temperature to approximately 1800 ℃, which ensures the whole sample is fully oxidised. After combustion, all products flow through specialised oxidation reagents, to produce carbon dioxide (CO_2), water (H_2O), nitrogen (N_2) and nitrogen oxides from carbon, hydrogen and nitrogen elements in the original sample. This process also removes undesirable gases contains sulphur, phosphorous and halogen elements. Then, the above-mentioned mixture of gases pass over copper, in order to remove excess oxygen and reduce the nitrogen oxides to elemental nitrogen. After the scrubbing process, the gas mixture is collected in a mixing chamber. This promotes the formation of a homogeneous mixture at constant temperature and pressure, which helps to speed up the analysis. The gas mixture is released when a pre-set pressure is reached, which means the volume of the gas mixture is also known. Then, the mixture passes through a series of traps. High-precision thermal conductivity detector filaments are equipped before and after traps. CO_2 and H_2O are completely absorbed by the traps.

The output signal between the detectors before and after a trap is proportional to the absorbed gases by traps and thus the compositions of carbon and hydrogen elements can be derived from the differential output signal. In addition to carbon and hydrogen, nitrogen gas is measured against pure helium carrier gas as a reference, where the composition of nitrogen can be derived from the difference in thermal conductivity.[115, 116]

2.6 General algorithms for porosity calculation

The calculation of porosities of porous carbon is an essential part of sample characterisation. The specific surface area, pore volume and pore size distribution were derived from either N_2 sorption isotherms at 77 K or CO_2 sorption isotherms at 273 K and calculated using corresponding algorithms. The general assumptions and derivation of algorithms for porosity calculation are presented in this section. Unless specified otherwise the calculation methods follow the instructions in the operation manual of Quantachrome gas sorption system.[117]

2.6.1 Classification of N_2 sorption isotherms

For materials with different porous structures, their corresponding N_2 sorption isotherms show different shapes and hysteresis. Therefore, the shape and hysteresis of a N_2 sorption isotherm can be used to analyse the porous structure of a carbon sorbent. According to the IUPAC (International Union of Pure and Applied Chemistry) recommendation, N_2 sorption isotherms can be classified into six major types, which are illustrated in Figure 29.[99, 117]

For the Type-I N_2 sorption isotherm, the N_2 uptake increases quickly with increasing relative pressure in the low pressure region. Then, it reaches a plateu in the relatively high pressure region, suggesting the sorption capcity has reached saturation. The Type-I N_2 sorption isotherm indicates the samples mainly consist of micropores (<2 nm). The relatively high N_2 uptake in the low pressure region is a consequence of N_2 filling in the micropores. The highest uptake in the high pressure region is determined by the accessible micropore volume of the material.

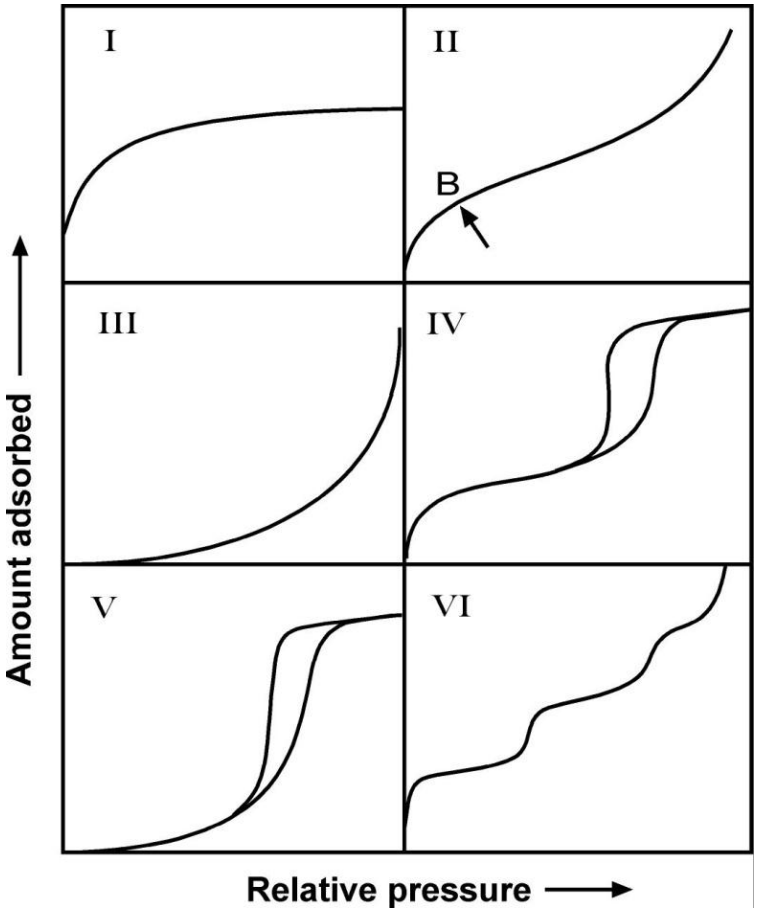

Figure 29: Classification of N_2 sorption isotherms.[99]

Type-II shows similar features with Type-I isotherm before it reaches a point B in Figure 29. Then, the N_2 uptake increases rapidly with increasing relative pressure. This type of isotherm indicates a non-porous or macroporous structure. The point B indicates the completion of monolayer adsorption and the start of multilayer adsorption.

Type-III shows a concave shape across the entire pressure range. This type of isotherm indicates a stronger adsorbate-adsorbate interaction over adsorbate-adsorbent interaction. Type-III isotherm is not common.

Type-IV shares similar features with those of Type-II at the initial stage of adsorption. However, the most characteristic feature of Type-IV is the hysteresis in the intermediate pressure region, that is, the gap area betweent the adsorption and desorption curves. The hysteresis is attributed to the gas condensation in the mesopores and thus this type of isotherm is an indication of mesoporous structures. The plateu at the final stage of adsorption suggests the completion of pore filling.

Type-V is similar to Type-IV, where both show hysteresis, which indicates the existence of mesopores. However, Type-V exhibits a concave shape at the initial stage of adsorption, which is a similar feature to Type-III and is an indication of weak adsorbate-adsorbent interaction.

Type-VI is a special isotherm, which shows multiple plateaus in the isotherm. It is an indication of stepwise multilayer adsorption. The shape of each plateau is related to the surface homogenity of an adsorbent and the chemistry of an adsorbate.

In summary, the shape and hysteresis of a N_2 sorption isotherm can help to qualitatively determine the type of porous stucture of a material. However, to quantitively characterise the porosities of a material, appropriate algorithms need to be applied.

2.6.2 Brunauer-Emmett-Teller equation

Brunauer-Emmett-Teller (BET) equation is widely used to calculate the specific surface area of a porous material.[117, 118] The BET equation is presented as follows:

$$\frac{1}{W\left(\left(\frac{P_0}{P}\right)-1\right)} = \frac{1}{W_m C} + \frac{C-1}{W_m C}\left(\frac{P}{P_0}\right) \qquad \text{Equation 6}$$

where, P_0 is the saturation pressure of an adsorbate (in this case, N_2) at an anlysis temperature, P is the equilibrium pressure, W is the amount of adsorbed gas at the relative pressure P/P_0, W_m is the amount of gas for the monolayer coverage on the sample surface, and C is a constant related to the energy of monolayer adsorption and thus an indication of the strength of adsorbate/adsorbent interactions.

In order to use the BET equation for surface area calculation, the following assumptions need to be made:

1. One adsorbate molecule only adsorbs on one adsorbent site and the adsorbent surface is homogenous;

2. The only interaction under consideration is the one-to-one adsorbate/adsorbent interaction. The interaction of the adsorbent surface with the first layer of gas molecules is much stronger than that with the second layer, also much stronger than the adsorbate-adsorbate interactions; and

3. The top-layer of adsorbed gas molecules is in equilibrium with the gas phase molecules, that is, the adsorption rate is the same as the desorption rate.

Based on the above assumptions, multiple data points on a N_2 sorption isotherm can be selected to calculate specific surface area. The selected data points are usually within P/P_0 of 0.05 ~ 0.35, where $1/[W(P_0/P)-1]$ and P/P_0 can be used to produce a linear BET plot. However, in the case of microporous adsorbents, data points are selected in an even lower relative pressure region. In the author's work, the selection of data points for BET calculation is suggested by the BET Assistant toolbox in the Quantachrome ASiQwin Software. The selection process is based on the criterion suggested by Rouquerol et al. that the value of C in the BET equation must be positive, because a negative C value means a BET plot has a negative intercept and thus the BET equation is invalid. Another criterion is that the value of $n(1-P/P_0)$ needs to continuously increase with P/P_0, where n is the amount of adsorbed gas, as suggested by ISO standard ISO/FDIS 9277:2010.

After the selection of data points, they can be used to produce a BET plot. The slope s and intercept i can be determined from the BET plot:

$$s = \frac{C-1}{W_m C} \qquad \text{Equation 7}$$

$$i = \frac{1}{W_m C} \qquad \text{Equation 8}$$

Therefore, W_m, which is the weight of adsorbed gas monolayer, can be calculated from the combination of Equation 7 and 8:

$$W_m = \frac{1}{s+i} \qquad \text{Equation 9}$$

Finally, the specific surface area can be calculated by using the following equation:

$$S = \frac{W_m N A_{cs}}{Mw} \qquad \text{Equation 10}$$

where N is the Avogadro's number (6.02×10^{23} molecules mol^{-1}), A_{cs} is the cross-sectional area of the adsorbate molecule, M is the molecular weight of the adsorbate molecule, w is the sample weight and S is the specific surface area of an adsorbent.

2.6.3 Total pore volume

Total pore volume is calculated with the amount of adsorbed gas at a relative pressure, where pores are completely filled with adsorbate molecules. This usually occurs when the relative pressure P/P_0 approaches unity. In the case of nitrogen sorption isotherm, the volume of adsorbed nitrogen gas at Standard Temperature and Pressure (STP) can be converted into the volume of liquid nitrogen that fills the pores at 77 K, which is the temperature of the liquid nitrogen bath used for the characterisation. Therefore, the following equation can be used to calculate the total pore volume:

$$V_{liq} = \frac{P_a V_{ads} V_m}{RT} \qquad \text{Equation 11}$$

where P_a is the ambient pressure, V_{ads} is the volume of adsorbed nitrogen gas, V_m is the molar volume of the liquid nitrogen (34.7 $cm^3\ mol^{-1}$), R is the ideal gas constant (8.314 J K-1 mol^{-1}), T is the ambient temperature and V_{liq} is the volume of liquid nitrogen, i.e. total pore volume.[117, 119]

2.6.4 Pore size distribution

It is mentioned previously in Chapter 1 Introduction that CO_2 uptake may be influenced by the pore size distribution, particularly, the volumes of micropores and ultramicropores of an adsorbent. In this case, pore size distribution and micropore volume can be derived from the 77 K N_2 sorption isotherm of an adsorbent by using the Density Functional Theory (DFT) model. Besides, the ultramicropore volume can be derived from the 273 K CO_2 sorption isotherm by using its corresponding DFT model as well. Furthermore, DFT models can be used to calculate accummulated specific surface area within a defined pore size range, in which the specific micropore surface area is included.

DFT models provide an accurate approach to describe the porous structure of an adsorbent, because both gas behaviours (inlcuding gas-gas and gas-solid interactions) and curvature of pore walls are considered in DFT models. Based on the above consideration, DFT models can generate simulated sorption isotherms, which are related to the experimental sorption isotherms by a Generalised Adsorption Isotherm (GAI) equation:

$$N\left(\frac{P}{P_0}\right) = \int_{W_{MIN}}^{W_{MAX}} N\left(\frac{P}{P_0}, W\right) f(W) dW \qquad \text{Equation 12}$$

where $N(P/P_0)$ is the experimental adsorption isotherm data, W_{MAX} and W_{MIN} are the maximum and minimum of pore widths, $N(P/P_0, W)$ is the isotherm data related with a single pore of width W and f(W) is the pore size distribution function.[117, 120]

The GAI equation considers the total isotherm to comprise of many "individual isotherms" related to many "individual single pores". The experimental adsorption isotherm data are obtained by the integration of those "individual isotherms" ($N(P/P_0, W)$) multiplied by their corresponding pore size distribution function (f(W)) from the maximum (W_{MAX}) to the minimum (W_{MIN}) pore width. Therefore, the pore size distribution can be obtained by solving the GAI equation.

For different types of materials (carbon, silica, zeolite) and probe molecules (N_2, Ar, CO_2), there are different DFT models available for the calculation of pore size distribution. Quantachrome ASiQWin Software provides a range of DFT models that can fit different test conditions. In the author's work, the 77 K N_2 on Carbon (slit/cylindrical pore) Non-Local Density Functional Theory (NLDFT) equilibrium model was applied to calculate pore size distribution, accummulated specific surface area, specific micropore surface area and micropore volume. The reason for this is that all the author's samples are carbon-based materials, are tested in the liquid nitrogen bath (77 K) and are tested with N_2 as the probe molecule. Furthermore, the author's carbon samples are expected to consist of both micropores and mesopores. The above-mentioned NLDFT model provides a slit-pore model for micropores (<2 nm) and a cylindrical-pore model for mesopores (>2 nm).

Additionally, the 273 K CO_2 on Carbon NLDFT model is applied to calculate ultramicropore volume. The use of N_2 as the probe molecule has a limitation on the micropore size analysis due to its slow diffusion rate at 77 K. This makes it difficult for N_2 to diffuse into the ultramicropores within a reasonable period. In comparison, CO_2 has a smaller molecular diameter, compared with that of N_2. However, what's more important, the diffusion rate of CO_2 at 273 K is higher than that of N_2 at 77 K due to the large temperature difference, which makes CO_2 a more suitable probe molecule for the micropore size analysis.

2.7 Polymer-derived carbon spheres

(Disclaimer: as part of the collaborative work on carbon spheres, the CO_2 uptake test with 85% N_2 and 15% CO_2 by TGA was carried out by Mr. Jingjing Liu from the University of Nottingham.)

2.7.1 Synthesis of polymer spheres

Poly(acrylonitrile-co-acrylamide) was prepared by the copolymerisation reaction of acrylonitrile (AN, 98.0%, Northern China Special Chemicals Development Centre, China) and acrylamide (AM, 98.0%, Northern China Special Chemicals Development Center, China) in a 100 ml round bottom flask with dimethyl sulfoxide (25 ml, DMSO, 99.5%, Tianjin Guangfujinxi Chemical Research Institute, China). α,α′-Azoisobutyronitrile (AIBN, Shanghai No.4 Reagent & H. V. Chemical Co., China) was used as the initiator for the radical polymerisation reaction and the initiator concentration was 1 wt% of the total monomers weight, i.e. 0.091 g AIBN. A range of experiments were carried out to determine the fluidity of the polymer solution for free-forming of polymer spheres under gravity. The experimental conditions were optimised for the formation of millimetre-sized polymer spheres. The solution was magnetically stirred in a water bath at a reaction temperature of 65 ℃ for 3 h. Several initial monomer molar ratios were used to prepare copolymers (acrylamide/acrylonitrile = 0:1, 1:10.9, 1:3.3, 1:1.5). The ratio of 1:3.3 produced a relatively spherical shape compared with the other ratios. Therefore, the corresponding polymer spheres were selected to produce carbon spheres. Theoretically, this ratio produces a copolymer with the molar ratio of monomer units acrylamide/acrylonitrile = 0.73:1.

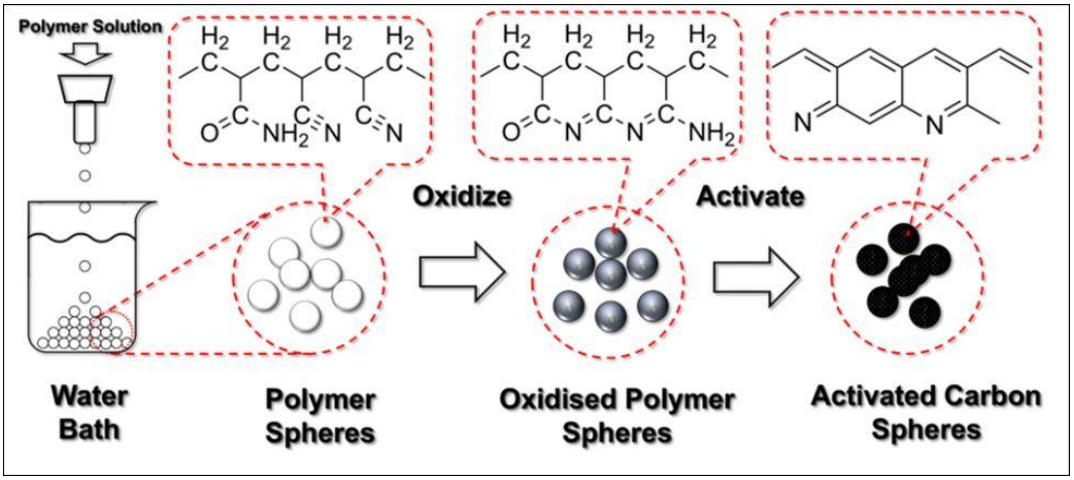

Figure 30: Schematic of the experimental procedures to produce activated carbon spheres.

An in-house facility was built to produce the polymer spheres, as illustrated in Figure 30. This set-up was adopted from an earlier work by Li et al.[121] The polymer solution was dripping through a 2 mm diameter nozzle. A glass beaker filled with distilled water (1000 ml) was placed below. The distance between the nozzle and the water surface was selected to be 15 cm. Different amounts of DMSO were added to the reaction solution to adjust the viscosity for easy dripping and formation of spherical drops, and the optimum addition was identified to be 25 ml. Then, the solution was poured in the syringe. The polymer solution drops were formed below the nozzles due to Plateau-Rayleigh instability under gravity and fell into the water bath. The surface of the polymer drop solidified immediately upon contact with water and sank to the bottom of the beaker. All polymer spheres were left in the water bath for 24 h. The distilled water was refreshed every 24 h until the smell of DMSO was removed. Then, the polymer spheres were dried in a vacuum desiccator at room temperature.

2.7.2 Oxidation

The dried spheres were loaded in a vertical furnace with an air compressor constantly pumping excess air through the furnace from the bottom to the top. The temperature was increased from ambient to 100 ℃ at a ramping rate of 2 ℃ min^{-1}, then at 0.1 ℃ min^{-1} from 100 to 200 ℃ and finally dwelled at 200 ℃ for an hour. This stage was to remove residual water and DMSO from the spheres. The slow ramping rate was to avoid violent vaporisation of residual gases, which would damage the sphere. Then the

temperature was again raised to 300 ℃ at 0.2 ℃ min^{-1} and held at 300 ℃ for the 8-hour oxidation reaction. At this stage, the slow ramping rate was to allow sufficient time for the oxidation reaction to take place and to prevent violent vaporisation of un-oxidised polymer from damaging the sphere.

2.7.3 Carbonisation and chemical activation

The oxidised polymer spheres (0.2 g) were soaked in the KOH solution (10 ml) in a 25 ml glass beaker. The concentrations of KOH gave effective KOH/sphere weight ratios of 1:1 and 2:1. The mixtures were left in a vacuum desiccator overnight and then dried in a vacuum oven at 80 ℃. The dried samples were carbonised and chemically activated in a horizontal tube furnace at 600, 700 and 800 ℃ under constant nitrogen gas flow. The ramping rate was 3 ℃ min^{-1} and the dwell time at the designated temperature was 1 h. After the carbonisation and chemical activation, the spheres were repeatedly washed with distilled water until a pH strip showed a neutral value. Then, the wet samples were dried in vacuum at 120 ℃ over night.

In addition to the general sample characterisation, the macropore volume (pore size up to 421μm) was measured by means of a mercury porosimeter (AutoPore IV, Micromeritics, USA) between 0.5 and 3600 psia. Besides the uptake tests in pure CO_2 environment, to simulate the practical CO_2 capture condition in post combustion power plants, CSA-700 was also tested for its CO_2 uptake in a gas environment with 15 vol% CO_2 and 85 vol% N_2 at 25 ℃. The test was carried out in a thermogravimetric analyser (TGA, Q500, TA instruments, USA). The sample was degassed at 150 ℃ for an hour in a constant pure N_2 flow. Then, it was cooled to 25 ℃ before the gas flow was switched from N_2 to the mixture of CO_2 and N_2 to measure its CO_2 uptake. The sample was also tested for its CO_2 uptakes over multiple cycles of adsorption and desorption by the temperature swing method. The temperatures were changed between 25 and 150 ℃ to adsorb and desorb CO_2.

2.8 London Plane leaf-derived carbon

(Disclaimer: as part of the collaborative work on leaf-derived carbon, the XRD analysis on leaf-derived carbon was carried out by Mr. Kaipei Qiu from UCL Chemistry.)

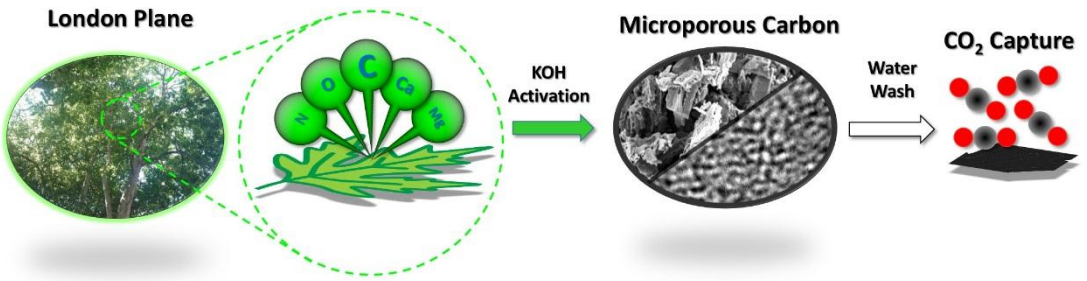

Figure 31: An illustration of London Plane leaf-derived carbon sorbents for CO_2 capture.

Fallen leaves from London Plane (*platanus* × *hispanica*) were collected from Gordon Square Garden near University College London's Bloomsbury Campus in July 2013. The leaves were washed to remove dust and dirt. The cleaned leaves were dried in a vacuum oven at 80 ℃ overnight. The dried leaves became crispy and were ground into small pieces by pestle and mortar. The ground leaves were carbonised at 600 ℃ for an hour in the horizontal tube furnace with constant nitrogen gas flow. The corresponding ramping rate was 3 ℃ min^{-1}. After carbonisation, the resulting carbon was mixed with potassium hydroxide (Fisher Scientific, UK) in the KOH/carbon weight ratios of 1:1, 2:1 and 3:1 in 10 ml distilled water. The mixture was ultrasonically agitated for 30 mins to achieve a uniform suspension in the KOH solution. The solution was then dried to a solid mixture of KOH and carbon in a vacuum oven at 80 ℃. The solid mixture was thermally activated at 600, 700 and 800 ℃ in the furnace, respectively, with the constant nitrogen flow for an hour. The corresponding ramping rate remained at 3 ℃ min^{-1}. The resulting carbon samples were washed repeatedly with distilled water until their pH values were neutral. In addition, another 700 ℃ treated sample was washed with 1M HCl acid to remove metal elements within. At the end, the samples were dried in the vacuum oven at 80 ℃ overnight. The samples are marked as LCx-y, where LC stands for leaf-derived carbon, x:1 is the weight ratio of KOH/carbon and y is the

thermal treatment temperature. The HCl acid washed sample was marked as LC2-700H.

In addition to the general sample characterisation, an X-ray diffractometer (XRD, Stadi P, STOE, Germany) was used to detect the existence of any crystals of metal or metal compounds in the samples.

2.9 Pine cone-derived carbon

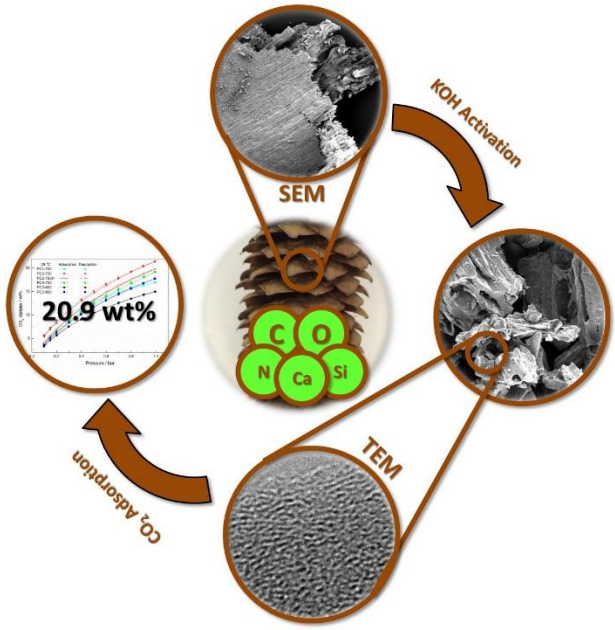

Figure 32: An illustration of pine cone-derived carbon sorbents.

Fallen pine cones from a pine tree (Spruce) were picked up in Linnainmaa, Tampere, Finland. The scales of the pine cones were peeled off and washed clean, which were then dried in a vacuum oven at 80 ℃ overnight. Subsequently, the dried scales were carbonised at 600 ℃ for an hour in a horizontal tube furnace with constant nitrogen gas flow, a ramping rate of 3 ℃ min^{-1} and dwell time of an hour. The carbonised scales were grounded into smaller particles and mixed with potassium hydroxide (Fisher Scientific, UK) in KOH/carbon mass ratios of 1:1, 2:1 and 3:1, respectively, in 10 ml distilled water. The mixture was agitated for 30 mins in an ultrasonic bath to obtain a uniform suspension of carbon in the KOH solution. The solution was then dried in a

vacuum oven at 80 ℃ to obtain a solid mixture of KOH and carbon. The chemical activation of carbon was carried out at 600, 700 and 800 ℃ in the furnace, respectively, with constant nitrogen flow for an hour. The corresponding ramping rate remained at 3 ℃ min^{-1}. The activated carbon samples were thoroughly washed in distilled water. For comparison, another KOH/carbon=2:1 and 700 ℃ sample was washed with 1M HCl acid to remove metal elements within the sample. Finally, all the samples were dried in the vacuum oven at 80 ℃ overnight. The samples are marked as PCx-y, where PC stands for pine cone-derived carbon, x:1 is the mass ratio of KOH/carbon and y is the chemical activation temperature. The acid washed sample was marked as PC2-700H.

2.10 Ball-milling of graphite

Graphite powder (<20 μm, synthetic, Sigma-Aldrich, UK), dry ice, potassium hydroxide pellets (BDH Prolabo chemicals, UK) were used as purchased. An 8000D spex ball-mill (SPEX SamplePrep, UK) was used for ball-milling the graphite powder. An ultrasonic bath (Fisherbrand, FB11002, UK) was used to mix the ball-milled graphite powder with KOH solution for chemical activation.

2 g graphite powder and 5 stainless steel milling balls (approx. 4 g/each) were mixed with 10 g dry ice in a stainless steel milling vial. The milling vial was sealed with a rubber ring and a stainless steel vial cap and then it was securely fixed in the mill. The mixture was ball-milled for six hours initially. Then, the mixture was refilled with another 10 g dry ice, and re-sealed again for the next six hours of milling. Next, the ball-milled graphite was washed with 1M HCl acid and a large amount of distilled water to remove impurities. The sample was mixed with 50 mL KOH solution in a 100 ml round bottom flask and the weight ratio of KOH to the sample was 2:1. The flask was placed in the ultrasonic bath for 3 hours to obtain a uniform suspension. After that, the suspension was dried in the oven at 100 ℃ overnight to form a solid mixture of carbon and potassium hydroxide. The dried sample was then transferred to the furnace for chemical activation. The temperature was increased from the ambient to 150 ℃ at the ramping rate of 5 ℃ min^{-1}, and dwelled at 150 ℃ for an hour. This stage was to remove physically adsorbed gas contaminants. After that, the temperature was

increased from 150 to 800 ℃ at a ramping rate of 2 ℃ min^{-1}, and dwelled at 800 ℃ for two hours. The sample was washed with distilled water and tested with pH strips until the pH value tested neutral. The samples were marked as BG-12hCO_2 and ABG-12hCO_2, where BG stands for ball-milled graphite, ABG stands for activated ball-milled graphite and CO_2 means graphite powder was ball-milled with dry ice, that is, in a pressurised CO_2 gas environment.. In order to identify the role of dry ice in this method, another group of samples were prepared by ball-milling without dry ice. They were marked as BG-12hAir and ABG-12hAir.

In addition to the general sample characterisation, an X-ray diffractometer (D4 Bruker, UK) was adopted to determine the crystallinity of the carbon structures. Instead of the automated gas analyser, a thermogravimetric analyser (TGA, Setsys 16/18, Setaram, France) was used to measure the CO_2 adsorption capacity. The samples were firstly degassed at 150 ℃ under pure argon flow for an hour. After that, the samples were cooled naturally in argon to 25 ^oC. Then, the gas was switched from argon to CO_2, and the CO_2 adsorption tests were carried out at 25 ^oC and under 1 bar CO_2. At the same temperature, CO_2 uptakes at high pressures (up to 15 bar) were measured by an intelligent gravimetric analyser (IGA, Hiden Isochema, UK).

2.11 Chemical activation of graphite oxide

(Disclaimer: the synthesis of KOH activated graphite oxide (GO) is a collaborative work with Mr. Jianwei Li. His work focuses on the synthesis of KOH activated GO while this author's work focuses on the characterisation of materials. The following analysis on graphite oxide-derived carbon is based on our joint discussion.)

2.11.1 Synthesis of graphite oxide

Graphite oxide (GO) powder was prepared by the modified Hummers method. Firstly, 2 g graphite powder was mixed with 46 ml sulphuric acid aqueous solution (98 vol%) and followed by the slow addition of 6 g $KMnO_4$ at 0 ℃ in an ice bath. The mixture was magnetically stirred thoroughly for 30 mins, which permits the oxidation of graphite. Then, the mixture was transferred to an oil bath at 30 ℃ to increase the

reaction rate. It was further stirred for another 2 hours. After that, 46 ml distilled water was slowly poured into the mixture, and the mixture was stirred for another 30 mins, during which the temperature of the mixture increased up to 40-45 ℃. A further 280 ml distilled water was added, followed by the addition of 20 ml H_2O_2 in order to remove residual KMnO4. After leaving the mixture in a round-bottom flask overnight, it was then divided into 12 tubes of samples and sulphuric acid was separated by means of 20 rounds of centrifuging. Then, the solid sample was washed by about 5 L distilled water. A neutral solution with pH=7 was indicated by pH strips. At the end, the prepared solution mixture was transferred to a 250 ml flask. The flask was soaked in liquid nitrogen for 5 mins, followed by freeze drying under vacuum (about 150 mbar) for a week.

2.11.2 Chemical activation of graphite oxide

Four groups of 400 mg GO powder were mixed with KOH in 20 ml distilled water in the KOH/carbon weight ratios of 0:1, 2:1, 4:1 and 6:1, respectively. The mixture was magnetically stirred for 2 hours to achieve a uniform suspension of GO powder. Then, the mixture was transferred to a vacuum oven and dried at 85 ℃ overnight. After that, the solid mixture of KOH and GO was transferred to the furnace for chemical activation reaction. The temperature was increased from the room temperature to 800 ℃ at the ramp rate of 5 ℃ min^{-1} and held at the designated temperature for an hour. Another two groups of KOH/GO=4:1 samples were activated at 700 and 900 ℃. After chemical activation, the sample was thoroughly washed with distilled water until the pH level was neutral as indicated by pH strips. At the end, the sample was dried in the vacuum oven at 85 ℃ overnight.

The samples are marked as AGOx-y, where AGO stands for activated graphite oxide, x is the KOH/GO weight ratio of x:1 and y is the activation temperature. In addition, AGO6-800 and AGO4-900 were washed by both 1M HCl acid and distilled water, in order to remove the aluminium contaminants caused by the etching of crucibles under the more aggressive chemical activation conditions. They are marked as AGO6-800H and AGO4-900H.

2.12 Treatment of errors

In order to get an indication of the errors associated with the experimental results from the author's work, also due to limited time on facilities and the priority for untested samples, only some samples were repeatedly tested for the purpose of error analysis.

For example, the sample was tested twice for the specific surface area analysis on the leaf-derived carbon LC2-700. One of the test results was 1592 $m^2 g^{-1}$ and the other was 1609 $m^2 g^{-1}$. This gave a difference of 17 $m^2 g^{-1}$. For pore volume, the two test results were 0.643 and 0.649 $cm^3 g^{-1}$. This gave a difference of 0.006 $cm^3 g^{-1}$. Likewise, the two test results for CO_2 uptake (25 ℃ and 1 bar) were 19.43 and 19.52 wt%, which gave a difference of 0.09 wt%. For nitrogen content, the sample was tested three times, which gave the results of 1.27, 1.21 and 1.24 at%. The difference between the maximum and minimum is 0.03 at%.

A further example was pine cone-derived carbon PC2-700. For specific surface area, the two test results were 1651 and 1701 $m^2 g^{-1}$, which gave a difference of 50 $m^2 g^{-1}$; for pore volume, they were 0.594 and 0.616 $cm^3 g^{-1}$, which gave a difference of 0.022 $cm^3 g^{-1}$; for CO_2 uptake, they were 20.85 and 20.86 wt%, which gave a difference of 0.01 wt%; for nitrogen content, they were 0.55, 0.56 and 0.52 at%, which gave a difference of 0.03 at%.

According to the above analysis, the difference between repeated experimental results is expected to be insignificant. There is no occasion in this thesis where a difference is to be treated as being of significance. In the following chapters, all the reported experimental results are rounded to the corresponding appropriate significance.

Chapter 3:

Polymer-derived Carbon Spheres

3.1 Introduction to carbon spheres

There are various precursors materials for the synthesis of carbon sorbents for CO_2 capture. Porous carbon sorbents derived from resorcinol-formaldehyde,[85] dialdehyde and diamine,[122] polyimine,[123] yeast,[124] fungi,[125] and urban wastes[126] show a wide range of capacities from 1 to 21 wt%. However, these studies only focused on relatively fine and irregular powder of tens of microns. Activated carbon fibres,[127-130] nanotubes[131, 132] and membranes[133, 134] for CO_2 capture are also reported in the literature. For practical applications in large scale CO_2 capture, such as CO_2 capture in a fluidised-bed, the ideal sorbent is in the form of porous spheres of several millimetres in diameter for optimum flow dynamics and CO_2 sorption.[135] Spherical carbon beads also reduce material abrasion due to smooth rotational impact. Furthermore, the low resistance can be readily maintained, because the dynamic stacking density of carbon spheres does not change under a given set of flow conditions. Ludwinowicz reported microporous carbon spheres derived from resorcinol-formaldehyde, which shows a CO_2 uptake of 20.7 wt% under 1 bar CO_2 and 25 ℃.[136] The sizes of the spheres are between 0.5-1 μm. Chen et al. reported nitrogen-doped carbon spheres derived from urea-phenol-formaldehyde, which exhibits a CO_2 capture capacity of 10.7 wt% at the same test conditions.[137] The sizes of the spheres range from 100 to 400 nm. A recent report shows phenolic resin-based activated carbon spheres with specific surface area of 2400 $m^2 g^{-1}$ and a total CO_2 uptake of 20.2 wt% (4.6 mmol g^{-1}) at 23 ℃ and 1 bar CO_2, but the size of the carbon spheres is only about 0.6 mm, limited by the manufacturing method.[138] The activated carbon spheres also rely on a rather large weight ratio of KOH/polymer (4:1) to produce a highly porous structure, leading to an extremely low carbon yield and low material strength. Such micro- and nano-sized carbon spheres are too buoyant to be effectively controlled under flue-gas conditions, and may readily clot filters during CO_2 removal. Therefore, millimetre-sized carbon spheres with effective CO_2 capture capabilities are desirable for practical CO_2 sorption applications, e.g., via a fluidised bed.

This section of the thesis reports a facile and effective method of producing millimetre-sized radially porous carbon spheres with an excellent CO_2 sorption capacity. Co-polymerised precursors are spheridised *via* the mechanism of Plateau–Rayleigh

instability[139] and solidified into a porous pre-form *via* a solvent-exchange process. The experimental results show that this method is effective in producing millimetre-sized carbon spheres with excellent structural integrity and exceptional CO_2 adsorption performance.

3.2 Characterisation of carbon spheres

3.2.1 Morphology of carbon spheres

The sphericity of carbon spheres depends on several factors. The roundness of the spherical head and the length of the tail depend on the concentration and viscosity of the polymer solution. With a higher concentration and viscosity, that is, the initial solution was diluted with less DMSO, it tended to produce a polymer sphere with an elliptical head with a thick long tail. In contrast, with a lower concentration and viscosity, it tended to produce a sphere with a flattened head but a short and slim tail. The shape of the spheres is also influenced by the distance between the nozzle and the water surface. A shorter distance may result in incomplete formation of the spherical shape due to insufficient time before the polymer solution drop enters the water bath. On the contrary, too long a distance may cause severe distortion of the spherical head, due to increased impact between the drop and the water bath surface. Distances of 10, 15, 20 and 25 cm were assessed and 15 cm was identified as appropriate to produce a relatively spherical geometry in the current case. In addition, the molar ratio of acrylamide/acrylonitrile also influences the shape of the sphere. With the same total weight (9.1 g) of monomers in the copolymerisation reaction, while the polymer spheres prepared with the ratio of 1:3.3 give the best spherical shape, those prepared with 0:1 and 1:10.9 exhibit certain degrees of flattened heads, similar to the situation where the polymer solution is over diluted. Acrylamide possesses a higher molecular weight (71 g mol^{-1}) than that of acrylonitrile (53 g mol^{-1}). The increasing acrylamide content raises the average molecular weight of the resulting copolymer and subsequently increases the viscosity of the polymer solution. However, acrylamide is a water-soluble monomer so that increasing acrylamide content also raises the hydrophilicity of the copolymer. Hence, the spheres prepared with the ratio of 1:1.5 partially dissolve in the water bath and also tend to agglomerate, so are difficult to

separate without damaging the spheres. Figure 33 shows uniformity and relative size of the polymer spheres, compared with that of a penny (~ 20 mm in diameter).

Figure 33: A pile of polymer spheres compare with the size of a penny, showing good uniformity and sphericity of the sphere.

In summary, the copolymer with the best spherical shape was made with an acrylamide–acrylonitrile molar ratio of 1 : 3.3. Therefore, it was selected to produce carbon spheres.

The polymer sphere in Figure 34a shows a smooth surface: the polar diameter R_1 (vertical) is 3.4 mm, slightly longer than the equatorial diameter R_2 (horizontal) of 3.3 mm, which gives a roundness ratio of R_1/R_2 = 1.03. Some scratches on the surface are indicative of the soft nature of this polymer. The cross-sectional image of the polymer sphere (Figure 34b) shows a hierarchical porous structure, typically with three regions: a relatively thin outer mantle of 0.5 mm in thickness with radial channels of about 0.08 mm in diameter, a thick inner mantle of 1 mm in thickness with radial channels of 0.3 mm in diameter and a relatively hollow core of 0.3 mm in diameter. This hierarchically and radially channelled porous structure is a direct consequence of

the solvent-exchange process that takes place between the polymer sphere and the water bath as explained below.

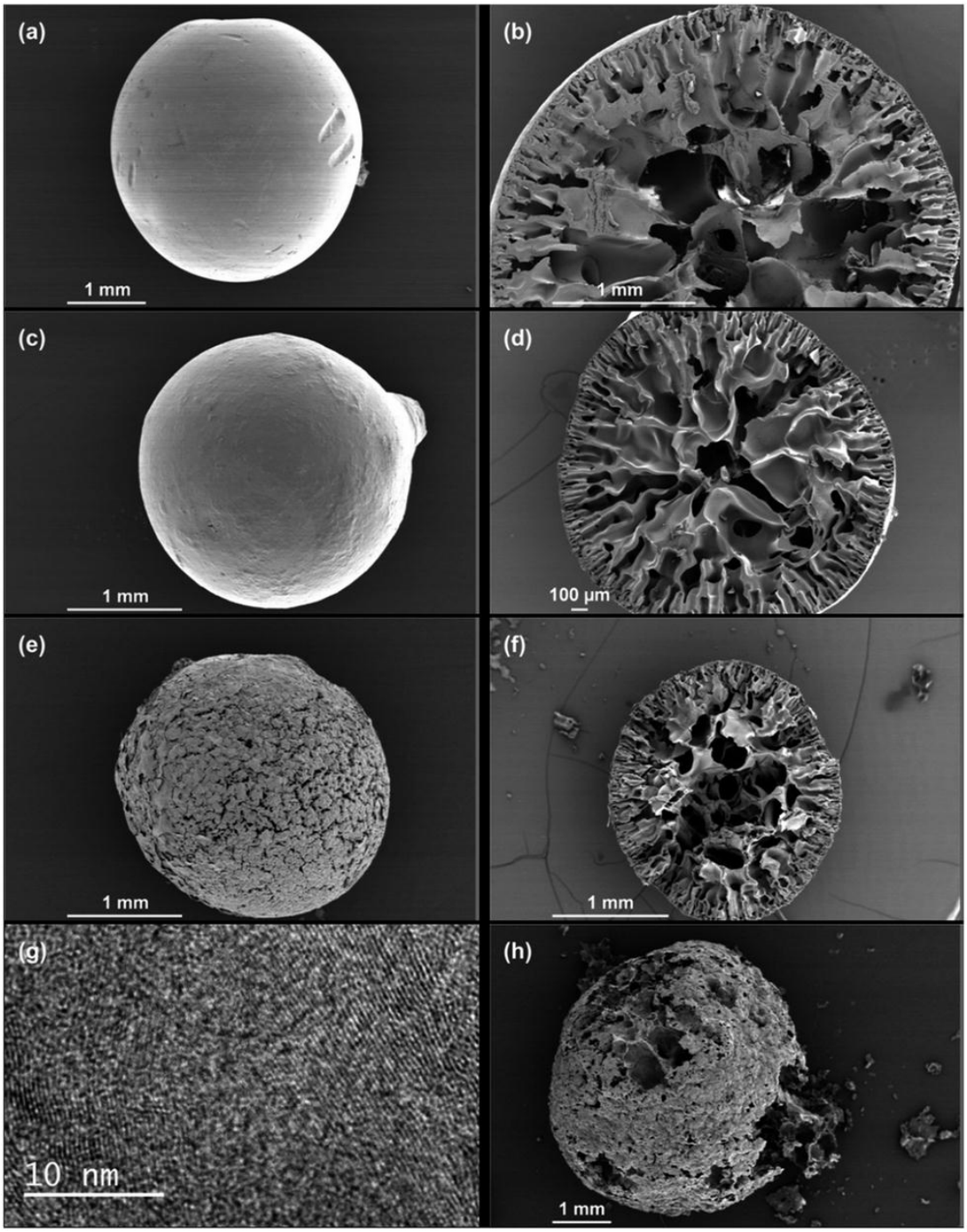

Figure 34: SEM images of (a) a typical polymer sphere, (c) an oxidised polymer sphere and (e) a carbon sphere activated with a KOH/sphere weight ratio of 1:1. (b, d and f) are their corresponding cross-sectional images. (g) A high resolution TEM image of the activated carbon sphere. (h) A fragment from a carbon sphere activated with a

higher KOH/sphere weight ratio of 2:1 – the original sample has already lost its structural integrity.

Since dimethyl sulfoxide (DMSO) is highly miscible with water, due to the concentration gradients of DMSO and water in the sphere and the water bath, DMSO tends to diffuse from the sphere into the water bath, and *vice versa*. As the polymer has low solubility in water, the polymer chains tend to partition or "precipitate out" with the exchanged water. This "solvent-exchange" based mechanism is schematically illustrated in Figure 35.

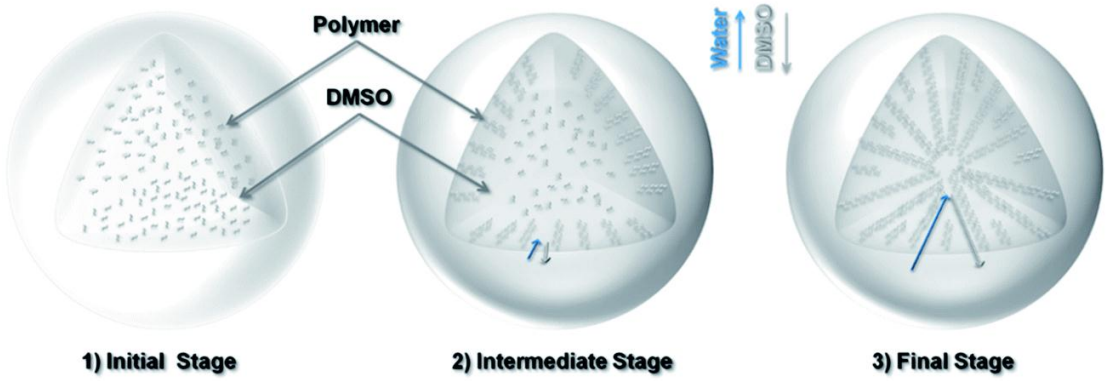

Figure 35: Schematic of the solvent-exchange process for the formation of a porous polymer sphere: (1) initial stage: the polymer is dissolved in a DMSO solvent drop; (2) intermediate stage: the exchange of solvents (DMSO↔water) and the formation of aligned channels near the surface; (3) final stage: progression of solvent exchange and the formation of larger channels and hollow core.

The exchange process starts with a spherical drop of polymer solution. At the beginning, the concentration gradients are steep across the interface of the solvents or the surface of the sphere, which leads to dense sites (or "nuclei") of polymer precipitates. The radial diffusion of the exchanging solvents results in radial flow channels, which become the porous channels at a later stage. As the exchange continues, the partitioned polymers at the surface region restrict the rate of further solvent exchange towards the centre. This process gradually allows more polymers to cluster together, driven by the reduction in surface energy, leading to increasingly large porous channels towards the inner region. Towards the end of the process, there are relatively fewer polymers in the core region, which becomes hollow upon solvent removal. Figure 34c shows the oxidised polymer sphere maintains its original spherical

shape but with a reduced diameter of 2.3 mm. The cross-sectional image (Figure 34d) indicates the radially channelled structure is retained. The interconnected porous structure allows KOH solution to diffuse across the entire structure during sample soaking. After KOH activation at 600 ℃, the sample surface is significantly etched, but the shape and integrity of the sphere are preserved, thanks to the mild activation condition (KOH/sphere=1:1). The cross-sectional image Figure 34f shows the radially channelled structure survives from the chemical activation, acting as the supporting framework of the sphere. The high resolution TEM image (Figure 34g) shows segmented graphitic platelets with well-aligned carbon layers. This observation differs from TEM images of carbon sorbents studied in previously mentioned literature, where carbon layers are randomly orientated. It is mentioned earlier that the solvent-exchange process helps to align the polymer chains radially. These aligned polymer chains form pyridine and pyridone rings after oxidation (Figure 36), which directly influences the formation and alignment of carbon layers after the carbonisation and activation. The cyclisation reaction is initiated by oxygen in the air, and that of poly(acrylonitrile-co-acrylamide), which can be initiated by its amide groups without oxygen. Both can occur simultaneously when the copolymer is oxidised in the air.

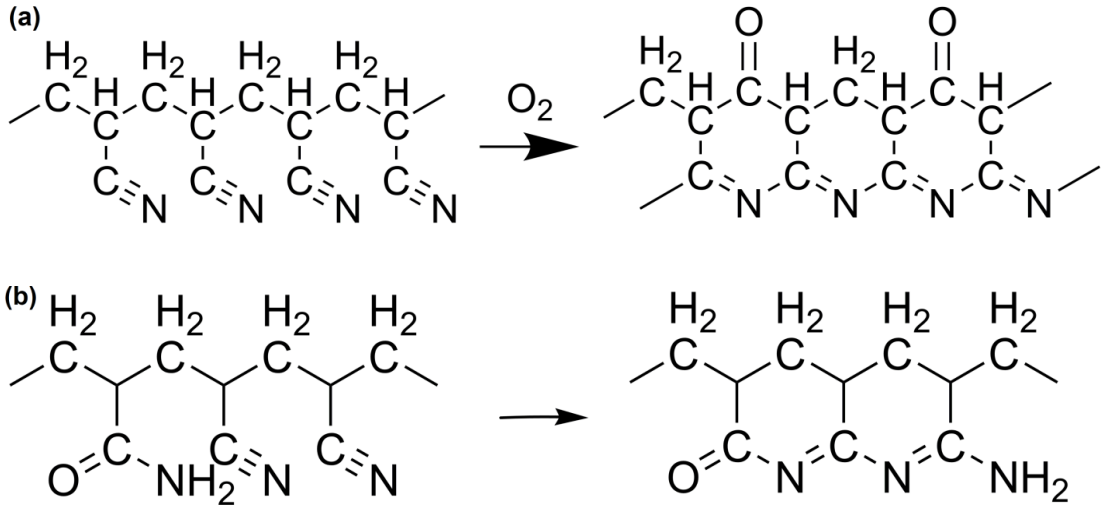

Figure 36: Mechanisms of (a) oxidation of polyacrylonitrile with the participation of O_2 and (b) cyclisation of poly(acrylonitrile-co-acrylamide) without the participation of O_2.[140]

It can be clearly observed in Figure 34h that there are nano-scale voids between edges of those graphitic platelets, which are the origins of micropores. However, too high a

ratio of KOH to spheres (KOH/sphere=2:1) leads to fragile samples and loss of sphericity (Figure 34h).

3.2.2 Porous structures of carbon spheres

The specific surface area and pore size distribution of carbon spheres were comparatively characterised by means of gas-sorption, using CO_2 and N_2 probes, and mercury porosimetry, respectively for ultramicro-, micro-/meso- and macropores. The results are summarised in Table 7.

Table 7: Porosity characteristics of carbon spheres prepared under different conditions.

Method	**N_2 Sorption**				**CO_2 Sorption**	**Hg Porosimetry**
Sample	**S_{N2}/m^2 g^{-1}**	**S_{Micro}/m^2 g^{-1}**	**V_{N2}/cm^3 g^{-1}**	**V_{Micro}/cm^3 g^{-1}**	**V_{CO2}/cm^3 g^{-1}**	**V_{Hg}/cm^3 g^{-1}**
CSC-600	5	0	0.01	0	0.07	1.67
CSA-600	520	400	0.32	0.15	0.15	1.64
CSA-700	1230	1120	0.55	0.43	0.25	2.08
CSA-800	2030	1710	0.99	0.71	0.26	3.08

"CSC-600" is the sphere carbonised at 600 °C without KOH activation. Its isotherm lies at the bottom of Figure 37a, and shows a small specific surface area of 5 m^2 g^{-1} and pore volume of 0.01 cm^3 g^{-1}. CSA-*x* (*x* = 600, 700, 800) stands for the carbon spheres activated at *x* ℃. With KOH activation, CSA-600 starts to develop a porous structure with a specific surface area of 520 m^2 g^{-1} and pore volume of 0.32 cm^3 g^{-1}.

In order to assess the ultramicropore (<0.7 nm) characteristics, CO_2 was used as a probe for sorption analysis. The corresponding micropore size distribution is plotted in Figure 37c. The results show that the ultramicropore volume (V_{CO2} in Table 7) is greater at a higher activation temperature, but the magnitude of increase is higher from CSA-600 to CSA-700 (by 71%) than from CSA-700 to CSA-800 (by 4.4%). The finding indicates that a higher activation temperature does not just result in an increased volume of

ultramicropores but also leads to more rapid growth of pore sizes. In addition, for the sample CSC-600, though its micropore volume is negligible from N_2 sorption, CO_2 sorption analysis shows that it possesses a small level of ultramicropores, which cannot be accurately analysed by the N_2 sorption technique.

(a)

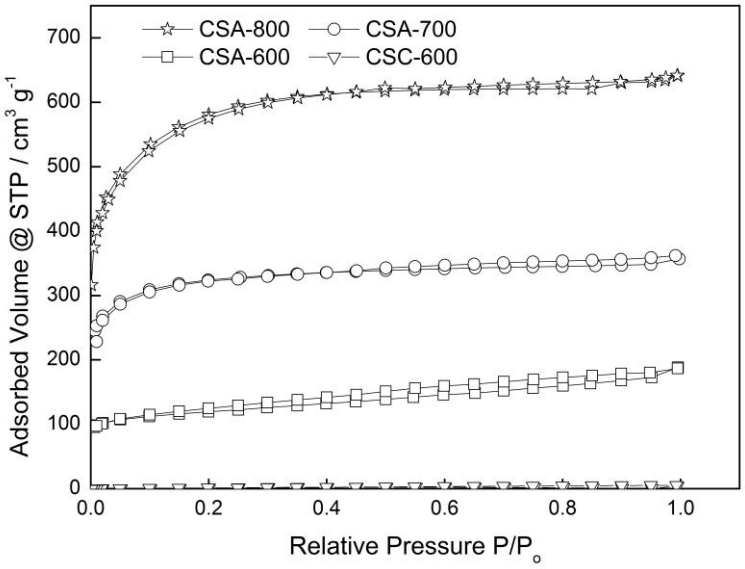

(b)

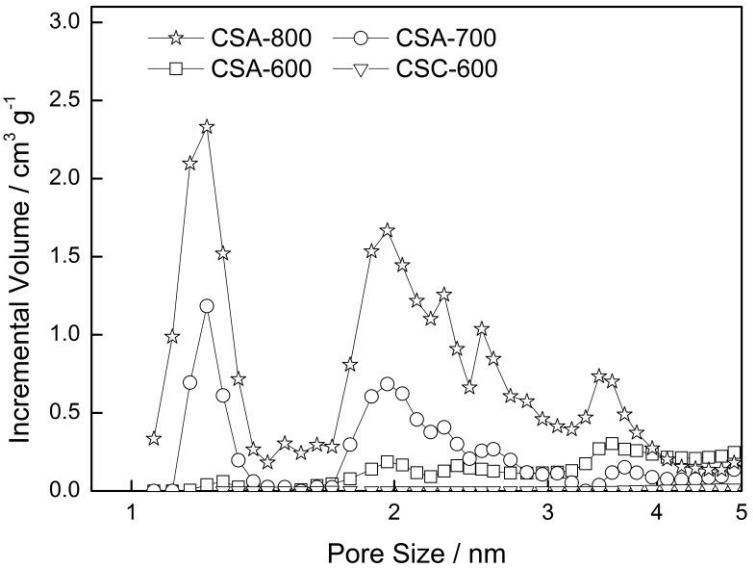

(c)

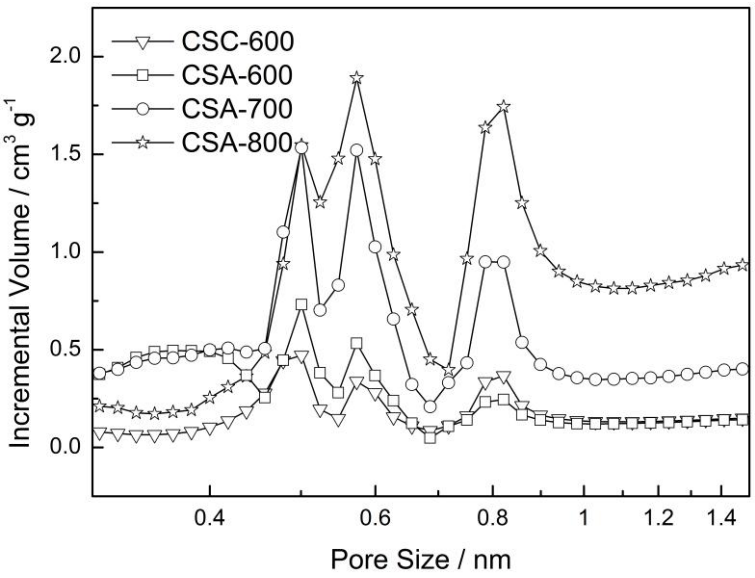

(d)

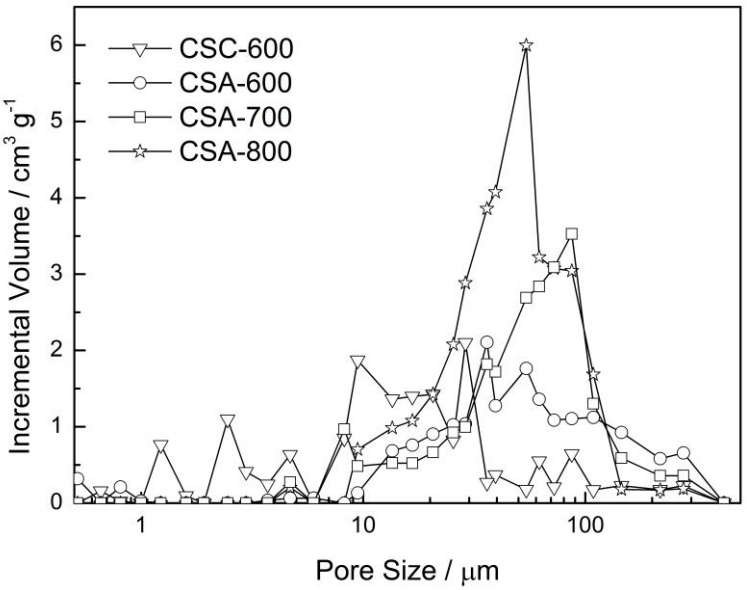

Figure 37: (a) Nitrogen sorption isotherms of samples prepared under different conditions and their corresponding (b) pore size distributions, (c) micropore size distribution and (d) macropore size distribution (dV/d(logd), d is pore size).

In addition to the micro- and mesopore analysis, Table 7 also summarises the macropore volumes (V_{Hg}) of the carbon spheres. The corresponding macropore size distribution is plotted in Figure 37d. This figure shows clearly that the macropores are mainly distributed between 10 to 100 μm, with some very large macropores between 200-400 μm, for all three types of samples; the former range corresponds to pores in the mantle region and the latter the inner region. The large macropores originate from the hierarchical macroporous channelled structure formed during the solvent-exchange

process. It is further enlarged due to more aggressive activation reactions at elevated temperatures. Such macropores should facilitate diffusion of CO_2 within the carbon spheres. However, an excess level of such macropores may reduce the volume capacity of CO_2 sorption in the sphere. Further study is under way to optimise the distribution of the pore sizes in those hierarchical porous carbon spheres.

3.2.3 Chemical composition of carbon spheres

The results of chemical composition analysis by XPS are summarised in Table 8. The relative FTIR and N-1s XPS spectra are presented in Figure 38. Figure 38a compares the FTIR spectra of the polymer, oxidised polymer (CSO) and activated carbon spheres. All FTIR spectra show one wider peak between 3700 and 3000 cm^{-1}, which corresponds with the N–H and O–H stretching vibration bands. The polymer sphere shows three sharper peaks from 2240 to 1450 cm^{-1}. The peak at 2244 cm^{-1} is attributed to the stretching vibrations of nitrile groups (–C≡N) from the acrylonitrile units in the polymer sphere, while the peak at 1670 cm^{-1} is attributed to the stretching vibrations of primary amide groups from the acrylamide (–CO–NH_2) units.[141] There is a small shoulder right beside the 1670 cm^{-1} peak at 1640 cm^{-1}, which originates from the stretching vibrations of carbonyls (C=O) from the primary amide groups. The peak around 1452 cm^{-1} is assigned to the in-plane bending vibrations of methylene bridges (–CH_2–) from both acrylonitriles and acrylamides. After the oxidation reaction, the peak around 2244 cm^{-1} completely disappears. In addition, the intensity of the amide peak at 1670 cm^{-1} is reduced and shifted to 1614 cm^{-1} and the shoulder at 1640 cm^{-1} disappears as well. It is consistent with the mechanism of the oxidation process whereby the nitrile and amide groups are removed through the formation of pyridinic rings in the cyclisation reaction. The peak at 1614 cm^{-1} is the evidence of the emerging pyridinic rings. The intensity of the methylene peak at 1452 cm^{-1} is increased and shifted to 1440 cm^{-1}, which can be attributed to the formation of carbon double bonds in the pyridinic rings.[141] After the activation reaction, the intensities of both peaks are greatly reduced due to further loss of nitrogen content and regular pyridinic structure due to chemical attack by KOH. Besides, there exist a range of weak peaks below 1300 cm^{-1} in the spectra. The spectrum of the polymer shows a relatively broad and weak band from 1200 to 1000 cm^{-1}, which can be assigned to C–N stretching vibrations. There are also two peaks at 858 cm^{-1} and 695 cm^{-1}, which can be assigned

to the out-of-plane bending of N–H and deformation of C–H. When it comes to the oxidised polymer CSO, multiple weak peaks appear in the range of 1300 to 1000 cm^{-1}, due to the ester and ether groups introduced by the oxidation process. For CSA-600, all the previously mentioned peaks below 1300 cm^{-1} disappear due to carbonisation and activation reactions at the elevated temperature.[141]

Table 8: Chemical compositions of carbon spheres determined from XPS analysis.

Sample	Chemical composition / at%						
	C	**O**	**N**	**K**	**Pyridinic**	**Pyrrolic**	**Pyridinic N-oxide**
CSO	67.3	14.0	18.7	0	43.0	**Pyridonic:** 47.0	10.0
CSC-600	82.7	4.2	13.1	0	42.5	42.8	14.7
CSA-600	78.6	12.3	6.8	2.3	30.3	57.6	12.1
CSA -700	80.8	11.5	5.9	1.8	24.3	62.3	13.4
CSA -800	84.2	9.9	4.8	1.1	17.6	67.6	14.8

(a)

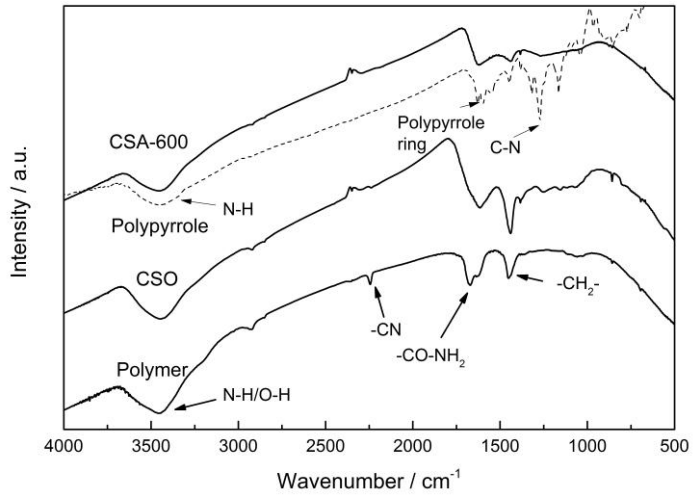

(b)

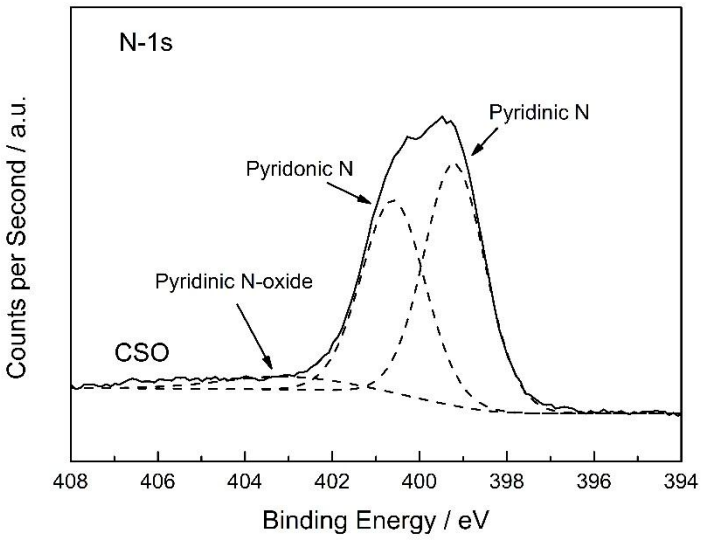
N-1s
Pyridinic N
Pyridonic N
Pyridinic N-oxide
CSO
Counts per Second / a.u.
408
406
404
402
400
398
396
394
Binding Energy / eV

(c)

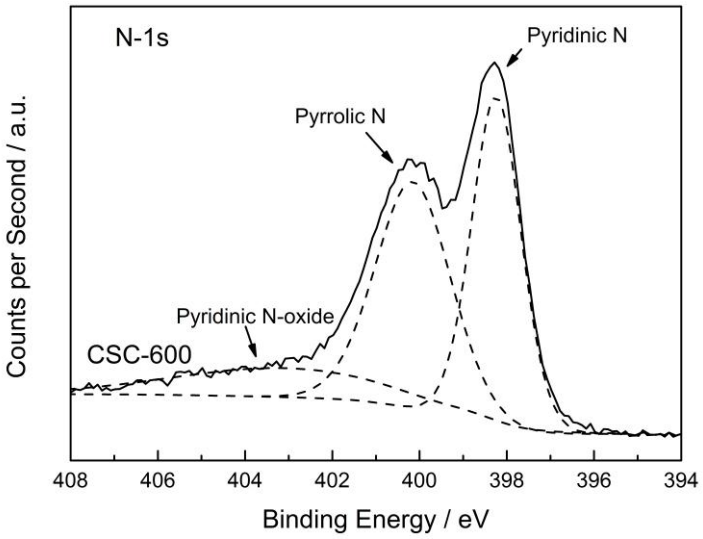
N-1s
Pyridinic N
Pyrrolic N
Pyridinic N-oxide
CSC-600
Counts per Second / a.u.
408
406
404
402
400
398
396
394
Binding Energy / eV

(d)

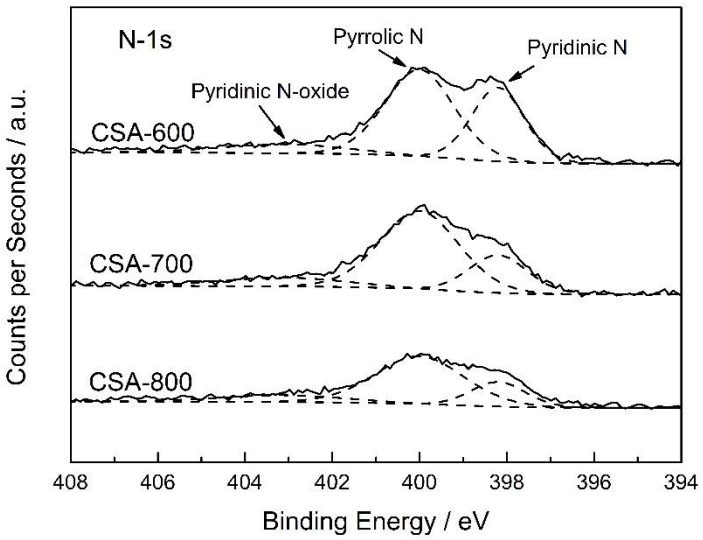
N-1s
Pyrrolic N
Pyridinic N
Pyridinic N-oxide
CSA-600
CSA-700
CSA-800
Counts per Seconds / a.u.
408
406
404
402
400
398
396
394
Binding Energy / eV

(e)

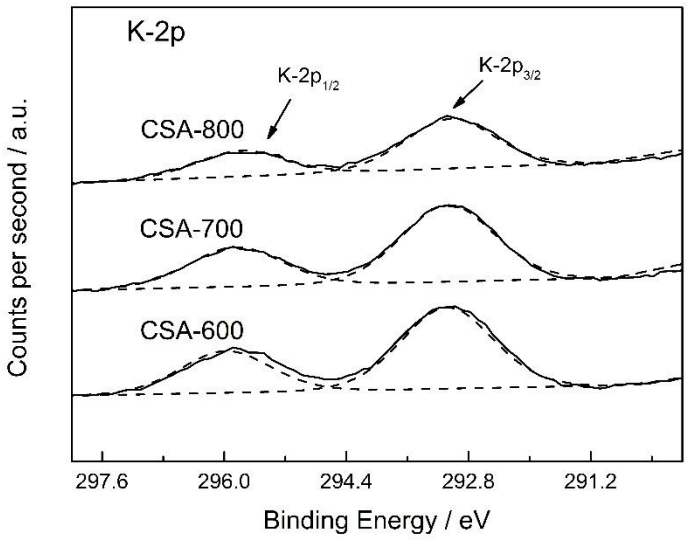

Figure 38: (a) Infrared spectra of the polymer, oxidised polymer (CSO), activated carbon sphere (CSA) and polypyrrole (dash line). XPS N-1s spectra of (b) the oxidised polymer spheres, (c) carbonised sphere (CSC-600) and (d) activated carbon spheres prepared under different conditions. (e) XPS K-2p spectra of activated carbon spheres.

Figure 38b–d reveal how nitrogen content varies with different sample preparation conditions. The spectrum of the oxidised polymer can be deconvoluted into three major peaks at 399.3, 400.7 and 403.1 eV (Figure 38b), which correspond to the existence of pyridinic, pyridonic and pyridinic N-oxide, respectively.[142] The emergence of these two peaks is consistent with the mechanism of the oxidation reaction.[140] Table 8 shows the variation of chemical composition with different preparation conditions. The carbonised sample CSC-600 shows a high nitrogen content of 13.1 at%. Chemical activation by KOH reduces the nitrogen content of CSA-600 to 6.8 at%, although only a mild activation condition of KOH/sphere = 1 is applied. Figure 38c and d reveal that all carbon spheres exhibit three major peaks at 398.2, 400.0 and 403.1 eV, respectively. These peaks suggest pyridinic nitrogen, pyrrolic nitrogen and pyridinic nitrogen oxides are the three major forms of nitrogen in the carbon spheres.[86, 142] The former two exist at the edge of the carbon structure, which increases the affinity of CO_2 towards the carbon structure due to the acidic nature of CO_2 and basic nature of the nitrogen dopants. Figure 38d shows all activated carbon spheres suffer severe reductions in peak intensities, compared with those of the carbonised sphere in Figure 38c. With the increasing activation temperature, the nitrogen content of CSA-600, 700 and 800 drops from 6.8 to 4.8 at%. In addition, Figure 38d shows that the intensities of the 398.2 eV

peaks are severely reduced compared with those of the 400.0 eV peaks. Table 8 also summarises the composition of different forms of nitrogen in carbon spheres. It is clear that the pyridinic nitrogen content is reduced with increasing temperatures from 600 to 800 ℃. This implies that pyridinic nitrogen is less stable than pyrrolic nitrogen at high temperatures with the same activation conditions. The loss of pyridinic nitrogen can be attributed to more aggressive chemical activation reactions at a higher temperature as discussed in the previous paragraph. Besides the nitrogen content, another interesting observation is the existence of residual potassium. An earlier study suggests that it can help to enhance CO_2 binding with the sorbent.[90]

Furthermore, in order to confirm the existence of pyrrolic nitrogen, the FTIR spectrum of CSA-600 can be compared with that of polypyrrole (dash line in Figure 38a). The infrared spectrum of polypyrrole shows three characteristic peaks. The wide peak located between 3500 and 3400 cm^{-1} can be attributed to the N-H stretching vibration. The peak at 1595 cm^{-1} can be associated with the polypyrrole ring stretching vibration, and the peak at 1273 cm^{-1} can be assigned to the C-N stretching vibration.[143] Comparing these characteristic peaks with those of polypyrrole, the infrared spectrum of CSA-600 shows relatively wide peaks around 1600 and 1300 cm^{-1}, which agrees with the infrared spectrum of polypyrrole. The peak around 1300 cm^{-1} is much less intense than that in the polypyrrole spectrum, due to much less pyrrolic nitrogen content in CSA-600. In addition, the binding energy of N-1s electron of CSA-600 can be compared with that of polypyrrole. The latter is around 399.9 eV, which further confirms the existence of pyrrolic nitrogen.[108] The FTIR and XPS spectra of polypyrrole can also be used to compare with those of the author's nitrogen-doped carbon samples in later chapters.

3.2.4 CO_2 adsorption on carbon spheres

Figure 39 depicts CO_2 adsorption isotherms at 0 and 25 ℃ from 0.1 to 1 bar of CO_2. The corresponding CO_2 uptakes at 1 bar CO_2 are summarised in Table 9. All samples have higher CO_2 uptakes at 0 ℃, which can be explained by the reduced kinetic energy of CO_2 gas molecules at a lower temperature. At 25 ℃, CSA-700 presents the highest CO_2 uptake of 16.7 wt% (3.8 mmol g^{-1}). It has a higher CO_2 uptake than CSA-600 of 9.4 wt% (2.1 mmol g^{-1}), due to much enhanced porous structure (from 520 to 1230 m^2

g^{-1}). Even its nitrogen content is reduced (from 6.8 to 5.9 at%). However, even with higher surface area and larger pore volume, CSA-800 shows a lower CO_2 uptake of 14.0 wt% (3.2 mmol g^{-1}) due to further reduction in the nitrogen content, especially the loss of pyridinic nitrogen (from 24.3 to 17.6 at% in Table 9). An earlier study has shown pyridinic nitrogen possesses higher basicity than pyrrolic nitrogen.[144] This is because pyridinic nitrogen has a lone pair of electrons with one electron donated to the conjugated π-system, while pyrrolic nitrogen donates two p-electrons that delocalise into the conjugated π-system. Therefore, pyridinic nitrogen has a higher affinity towards acidic CO_2 molecules than pyrrolic nitrogen.[145] Considering the experimental results from both structural and chemical analyses, it can be concluded that both porous structures and nitrogen content influence the CO_2 uptake of carbon spheres. The maximum CO_2 capacity is achieved by balancing both porous structure and pyridinic nitrogen content.

Table 9: CO_2 uptake under 1 and 0.15 bar CO_2 at 0 and 25 ℃.

Sample	CO_2 uptake / wt%			
	1 bar		0.15 bar	
	0 ℃	25 ℃	0 ℃	25 ℃
CSC-600	7.2	4.5	2.9	2.1
CSA-600	14.6	9.4	8.6	5.4
CSA-700	25.3	16.7	11.1	6.7
CSA-800	29.0	14.0	8.1	4.0

The isotherms of CSA-600 and CSA-800 intersect with each other at both 0 and 25 ℃ (Figure 39a and b), which shows CSA-600 has higher CO_2 adsorption capacities than those of CSA-800 at relatively low pressures. Furthermore, as shown in Table 9, the difference between their CO_2 uptakes of CSA-600 and CSA-700 under 1 bar is more significant than that under 0.15 bar. The results indicate that the level of nitrogen in the samples plays a more important role than that of porosities in the low pressure regime, because CSA-600 contains a higher amount of nitrogen than CSA-800, though the former possesses smaller specific surface area and pore volume than the latter.

Moreover, the intersection point changes from 0.18 to 0.35 bar when temperature is raised from 0 to 25 ℃. Similarly, the 0 ℃ isotherm of CSA-700 intersects that of CSA-800 slightly above 0.5 bar but its 25 ℃ isotherm is entirely above CSA-800. This further implies that the nitrogen content helps to enhance CO_2 adsorption at a low pressure and an elevated temperature.

In addition, even without chemical activation by KOH, the CSC-600 sample can adsorb 4.5 wt% (0.9 mmol g^{-1}) CO_2 at 25 ℃ under 1 bar CO_2. This is about half of the CO_2 uptake of the CSA-600, though the specific surface area of the former is two-orders of magnitude smaller. The author attributes this seemingly disproportional increase to other factors that influence CO_2 uptake, particularly here the nitrogen content. The preservation of a high nitrogen content (13.1 at%) in the CSC-600, or the loss of the same in CSA-600, means that there is a much higher density of effective binding sites (pyridinic N-sites per surface area) in the former than the latter case. This is particularly the case for CO_2 uptake at relatively low CO_2 partial pressures, whereas at a high CO_2 pressure, *e.g.* 20–30 bar, high surface area and large pore volume play a more important role.[146] It can be concluded from the above observation that nitrogen plays a key role in enhancing CO_2 uptake. Too high a nitrogen content may lead to excessive CO_2 binding and increases the energy for CO_2 desorption. Hence, it is important to optimise the nitrogen content.

(a)

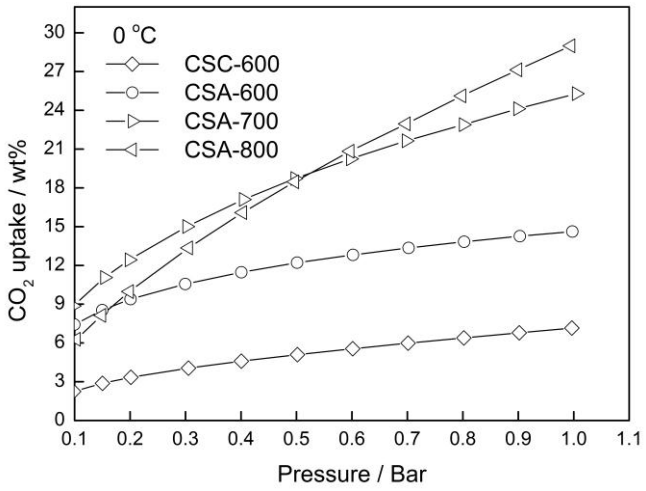

(b)

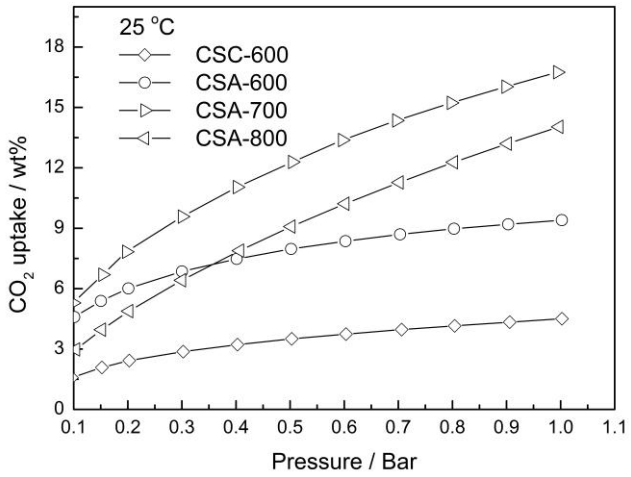

Figure 39: CO_2 adsorption isotherms of carbon spheres prepared under different conditions at (a) 0 and (b) 25 ℃ from 0.1 to 1 bar.

Figure 40a shows the CO_2 uptake of CSA-700 in a gas mixture of 15 vol% CO_2 and 85 vol% N_2. The test result shows that CSA-700 adsorb about 1.3 wt% N_2 when the temperature returns to 25 ℃ (see Figure 40a). However, it can still adsorb 9.3 wt% CO_2 even when the partial pressure of CO_2 is greatly reduced. Hence, the sample demonstrates a very high selectivity of CO_2 over N_2. Again, this can be attributed to the relatively high nitrogen content. This is an outstanding performance, compared with materials reported in the literature and tested under similar conditions.[147] Figure 40b shows the sample can maintain 91% adsorption capacity after five cycles of adsorption and desorption by temperature swing. The test condition is a simulation of the flue gas from a post-combustion power plant. Therefore, the above results further prove that such carbon spheres can exhibit exceptional performance in post-combustion CO_2 capture applications.

(a)

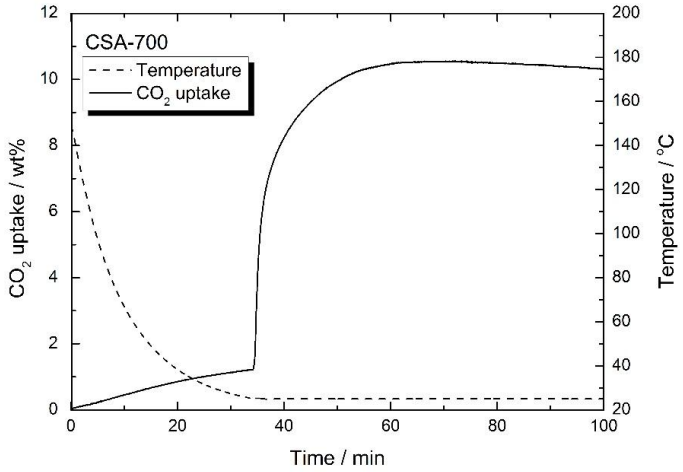

(b)

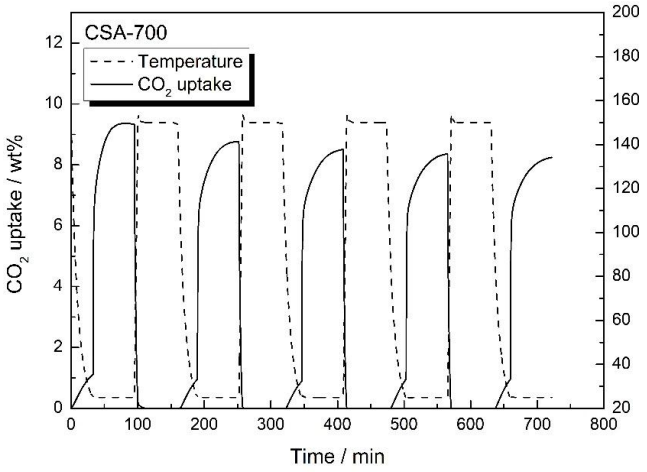

Figure 40: (a) The CO_2 uptake of CSA-700 in a 15 vol% CO_2 and 85 vol% N_2 gas flow at 25 ℃ in a single cycle of adsorption and (b) five cycles of adsorption and desorption.

3.2.5 Modification of porous carbon sphere structures

The author's research on carbon sphere has demonstrated its application to CO_2 capture. However, further studies need to be carried out in order to increase the mechanical strength of the carbon sphere. Current carbon spheres are relatively fragile, which may be related to the macroporous channelled structure of the sphere. If the diameters of those holes and channels can be further reduced, the mechanical strength of the sphere may be further improved. This can be approached by using mixed DMSO/water bath. Preliminary characterisations, such as SEM and BET, are reported in this section. More characterisation tests are proposed in Chapter 6 Future Work.

It was previously mentioned that the formation of a channelled porous structure is due to the exchange between water from the water bath and DMSO from the polymer/DMSO solution drop, that is, "the solvent-exchange process". A critical parameter of the solvent-exchange process is the diffusion rate between water and DMSO. In the previous case, where a pure water bath was applied, the concentration gradient between the polymer solution drop and water bath was steep. It resulted in a fast diffusion rate at the beginning of the exchange process and thus formed a relatively large porous channels. The fast exchange process also led to the quick depletion of polymer in solution and thus resulted in the formation of a hollow core at the centre of the sphere. Therefore, in contrast, the sizes of the pores and channels may be reduced if the exchange rate can be slowed. In this case, the addition of DMSO to the water

bath may be a simple way to slow the exchange rate, because the concentration gradient is reduced between the water bath and the polymer solution drop.

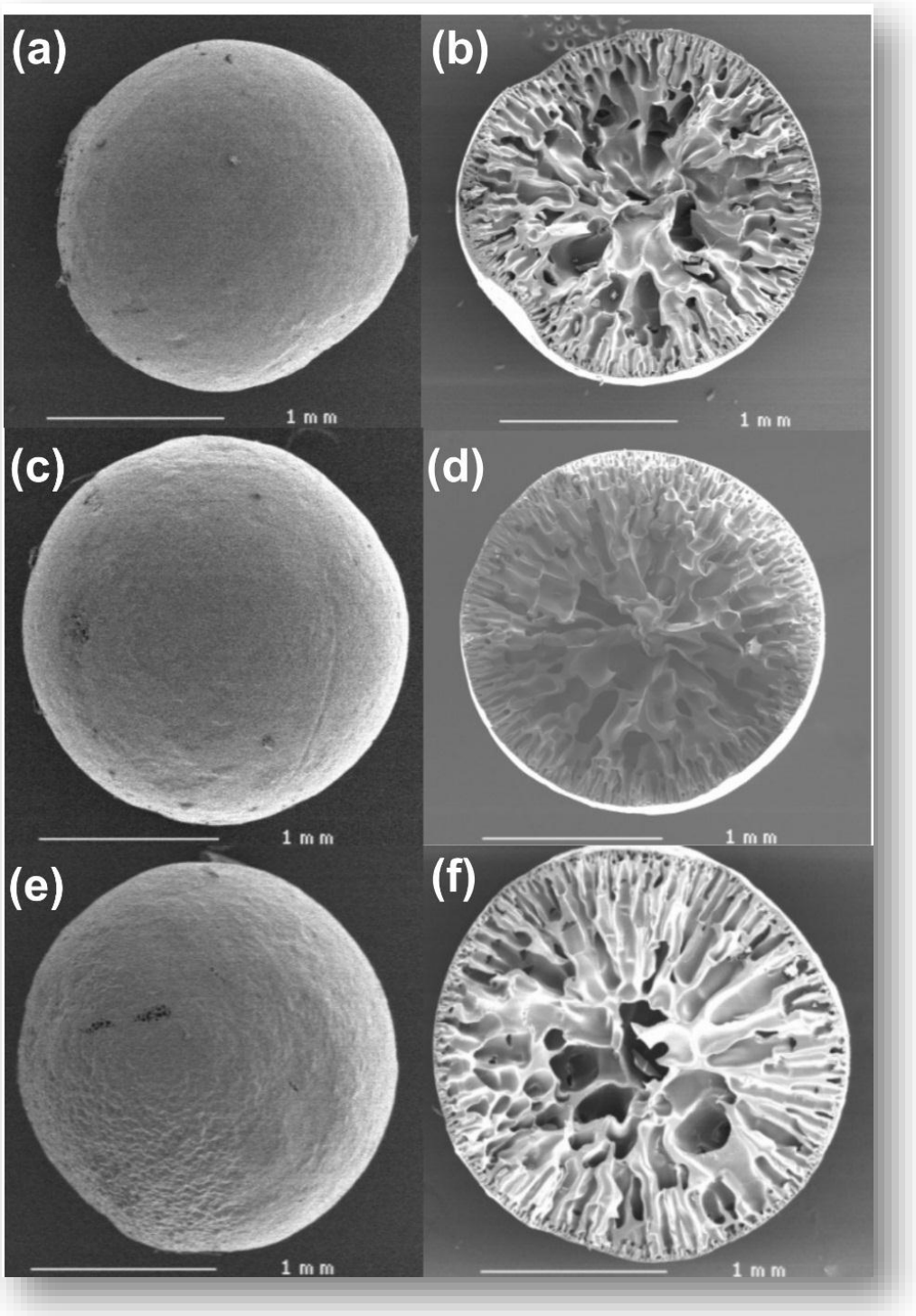

Figure 41: The surface morphology and cross-sectional SEM images of polymer spheres prepared with different water bath: (a) and (b) 10%DMSO/Water; (c) and (d) 20%DMSO/Water; (e) and (f) 35%DMSO/Water.

In the preliminary research, DMSO was mixed with water in the volume concentration of 10%, 20% and 35%. When the concentration was higher than 35%, the solidified polymer spheres tended to gradually dissolve in the DMSO/water bath, due to the high solubility of the copolymer in DMSO. Even when the concentration was lower than 35%, polymer spheres tended to stick to each other, which may be caused by the partial dissolution of copolymer at the surface of the spheres. The sample preparation follows the procedure for CSA-700, where the spheres are activated with KOH/sphere weight ratio of 1:1 and activation temperature of 700 ℃.

Figure 41 shows the surface morphology and cross-sectional SEM images of polymer spheres prepared with different concentrations of DMSO in the water bath (10%, 20% and 35%). The images show that the size of the sphere (about 2.2 mm) is clearly smaller than that produced by the pure water bath (about 3.3 mm). The same observation can be applied to the size of the porous channels as well. However, the most significant change is that all spheres do not show apparent hollow cores at the centre, compared with that of the sphere produced by the pure water bath.

Table 10: Porosities of carbon spheres prepared by different water bath.

DMSO Concentration	S_{N2} / m^2 g^{-1}	S_{Micro} / m^2 g^{-1}	V_{N2} / cm^3 g^{-1}	V_{Micro} / cm^3 g^{-1}
10%	1220	1140	0.53	0.42
20%	1870	1690	0.89	0.69
35%	2200	1830	1.11	0.76

(a)

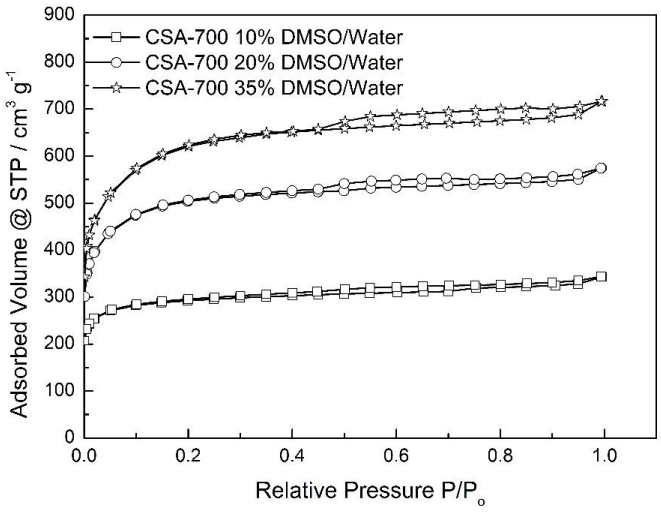

(b)

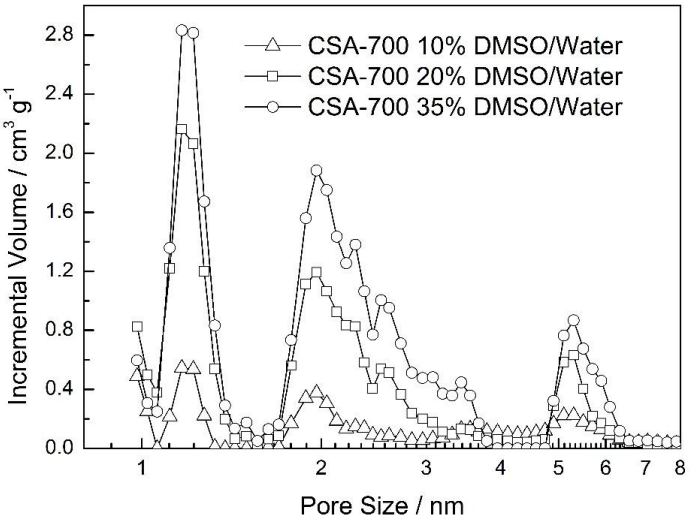

Figure 42: N_2 sorption isotherms and pore size distribution of carbon spheres prepared with different water bath.

Figure 42a and b are the N_2 sorption isotherms at -196 ℃ and pore size distribution of carbon spheres prepared with different water baths, respectively. The corresponding porosity parameters are summarised in Table 10. Both the figure and the table indicate carbon spheres have different levels of porosities. Considering all the samples went through the sample activation process, the change in porosity is very likely caused by the variation of the DMSO concentration in the water bath. The addition of DMSO to the water bath can reduce the size of the sphere, avoid the hollow core and thus produce a denser porous structure. Therefore, the denser porous structure may provide a relatively larger macropore surface area for KOH activation and thus produce a carbon sphere with a higher specific micropore surface area. It can be concluded from Table 10 that the specific surface area increases with the increasing concentration of DMSO in the water bath.

In conclusion, the macroporous carbon sphere structure can be modified by using mixed DMSO/water bath. The modified macroporous structure of the polymer sphere influences the microporous structure of the resulting carbon sphere.

3.2.6 Summary

An effective route is developed for the synthesis of hierarchically porous carbon spheres of millimetre scale. These are derived from a poly(acrylonitrile-*co*-acrylamide)

precursor, leading to enriched nitrogen content in the carbon structures. The carbon spheres show a porous structure with a hollow core and hierarchical porous mantle. The activation temperature influences both the porous structure and nitrogen content of the carbon spheres. The carbon sphere with the highest specific surface area (2030 $m^2 g^{-1}$) and pore volume (0.99 $cm^3 g^{-1}$) is produced with a weight ratio of KOH/sphere = 1 : 1 and activated at 800 ℃. This sample shows a high CO_2 capacity of 29 wt% (6.6 mmol g^{-1}) at 0 ℃ and under 1 bar CO_2. However, for sorption at 25 ℃, the highest CO_2 uptake of 16.7 wt% (3.8 mmol g^{-1}) is achieved with the carbon sphere activated at 700 ℃, due to an optimum balance of nitrogen content and microporosity. The latter also shows an outstanding CO_2 capture performance of 9.3 wt% (2.1 mmol g^{-1}) and high selectivity of CO_2 to N_2, even at a low CO_2 partial pressure in a mixed (CO_2 and N_2) environment. The results indicate that both microporosity and nitrogen content play an important role in enhancing the CO_2 uptake of the carbon spheres. The shape, size, capacity and selectivity of the hierarchically porous carbon spheres are all ideal properties for practical applications in large-scale post combustion CO_2 capture.

Chapter 4:

Biomass-derived Carbon

4.1 Leaf derived carbon sorbents

Biomass is a renewable and competitive carbon precursor, compared with many others (such as polymers), because of its abundant reserves, low-cost and simple mass production. In contrast, the synthesis of polymeric precursors usually involves complex procedures and strict control of synthesis conditions. Besides the materials introduced in Chapter 1 Introduction, Deng et al. reported a pine nut shell-derived porous carbon, which shows a CO_2 uptake of 22 wt% under 1 bar and 25 ℃.[148] Ello et al. reported an African palm shell-derived carbon and a coconut shell-derived carbon, which exhibit CO_2 adsorption capacities of 19.4 and 17.2 wt%, respectively, at the same test conditions.[149, 150] Plaza et al. reported an olive stone-derived carbon that adsorbs 10.7 wt% at 25 ℃ in pure CO_2 flow.[151] These examples suggest that there are a wide variety of biomass precursors available and biomass-derived carbon sorbents can achieve an excellent CO_2 capture performance.

This section of the thesis reports a facile synthesis of highly microporous carbon materials with a large surface area (>2000 m^2 g^{-1}) and pore volume over 1 cm^3 g^{-1} via direct carbonisation of London plane leaves followed by KOH activation. London Plane accounts for 50% of all planted trees in the urban area of London, and therefore generates a substantial amount of leaf wastes.[152] This natural biomass material can be a potential "zero-cost" carbon precursor, which offers a "green" approach to produce porous carbon materials and disposes of this major urban waste. Besides, we demonstrate that the nitrogen and/or metal-doped porous carbon obtained could be used as efficient CO_2 sorbents. In particular, the role of metal doping in both applications is studied. The results show that a small amount of Mg and Ca doping could effectively improve CO_2 sorption. The following experimental results show that the leaf-derived porous carbon is a promising "green" candidate for both CO_2 capture applications.

4.1.1 Morphologies of leaf and leaf-derived carbon

The freshly collected London plane leaves are bright green due to the existence of chlorophyll. However, the leaves became yellow and crisp after being dried in a vacuum oven. The dehydration converts chlorophyll into pheophytin.[153] With decreasing chlorophyll content, the orange, yellow, brown and grey colours of

carotenoid and pheophytin pigments emerge. After carbonisation, the leaves turn into black carbon.[154]

Figure 43 shows the morphological change from a leaf to a porous carbon structure. The macroporous sponge layer beneath the cuticle layer of the dried leaf is clearly exposed in the SEM image (Figure 43b). Several stomata on the cuticle suggest that it is the lower epidermis side of the leaf and thus the macroporous sponge layer can be observed beneath the epidermis. This macroporous structure of the sponge layer is retained even after carbonisation at 600 ℃. Such a well-preserved interconnected macroporous structure facilitates the impregnation of the carbonised sample by the KOH solution for rapid and uniform activation. The activated sample shows disintegrated porous carbon fragments of micrometre sizes. The corresponding high resolution TEM image (Figure 43d) reveals a large amount of randomly oriented graphitic platelets at the nanoscale. These disconnected graphitic platelets comprise of few-layered short graphenes, which create a large area of edges. As a result, the discontinuity in the carbon nanostructure leads to the formation of a large number of voids between the edges of platelets. These voids are the origin of micropores, which contribute to the large specific surface area and pore volume in the resulting samples.

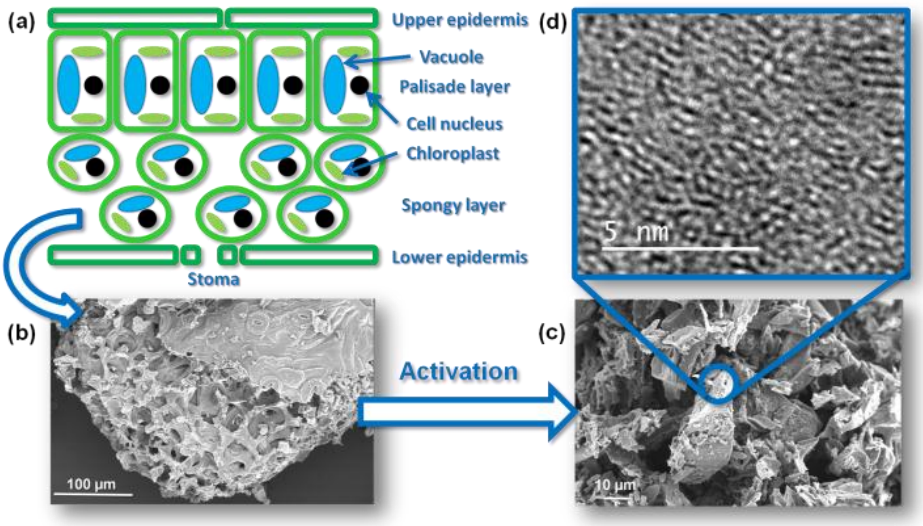

Figure 43: Illustration of leaf structure and its morphology and porous structure after chemical activation: (a) Schematic of a leaf cellular structure; (b) SEM image of a carbonised leaf; (c) Porous carbon fragments after KOH activation and (d) TEM image indicating an amorphous carbon structure after chemical activation.

4.1.2 Porous structure of leaf-derived carbon

The porosity characteristics of porous carbon sorbents, including total specific surface area (S_{N2}), specific micropore surface area (S_{Micro}), total pore volume (V_{N2}), micropore volume (V_{Micro}) and ultramicropore volume (V_{CO2}, <0.7 nm) are summarised in Table 11.

Table 11: Porosity characteristics of leaf-derived carbon sorbents.

Method	**N_2 Sorption**				**CO_2 Sorption**
Sample	**$S_{N2}/m^2\ g^{-1}$**	**$S_{Micro}/m^2\ g^{-1}$**	**$V_{N2}/cm^3\ g^{-1}$**	**$V_{Micro}/cm^3\ g^{-1}$**	**$V_{CO2}/cm^3\ g^{-1}$**
LC2-600	1210	1160	0.48	0.39	0.27
LC1-700	1360	1300	0.51	0.40	0.29
LC2-700	1600	1550	0.65	0.54	0.30
LC2-700H	1630	1580	0.66	0.56	0.31
LC3-700	2230	2130	1.03	0.89	0.28
LC2-800	1950	1810	0.88	0.72	0.32

(a)

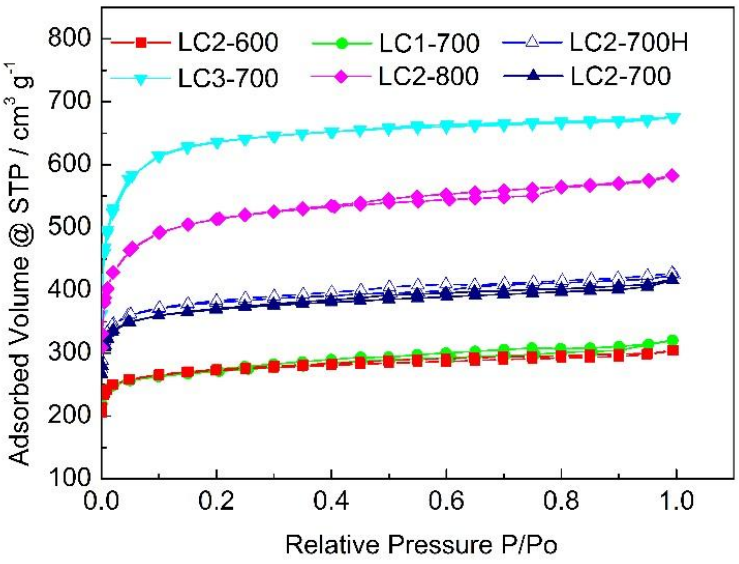

(b)

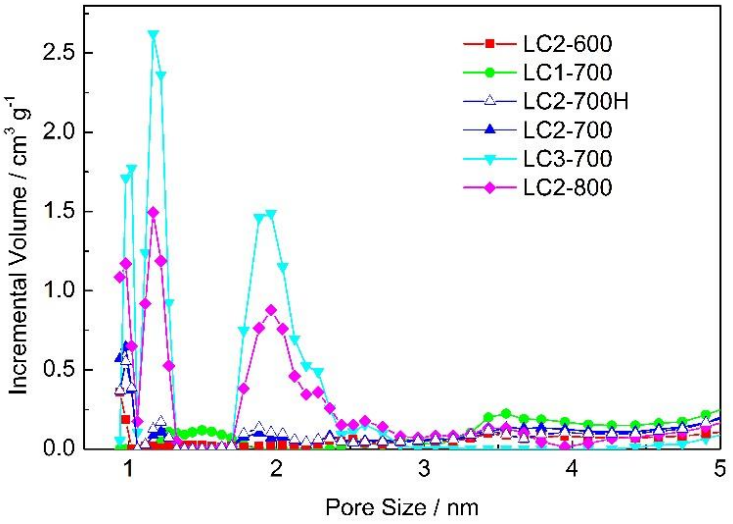

(c)

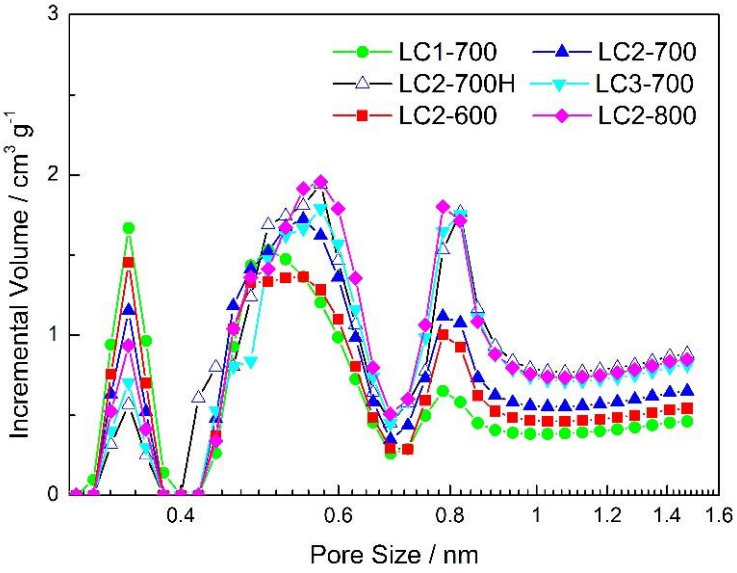

Figure 44: (a) N_2 sorption isotherms at -196 ℃, (b) corresponding pore size distributions of leaf-derived carbon sorbents and (c) micropore size distribution (dV/d(logd), d is the pore size).

Figure 44a shows that all N_2 isotherms exhibit typical features of the Type–I sorption isotherm, which suggests that the sorbents mainly consist of micropores. This is reflected in Figure 44b in that all sorbents show three major peaks in the micropore size regime (<2 nm) at 1, 1.2 and 2 nm, respectively. Table 11 shows the structural characteristics of carbon sorbents prepared with different weight ratios of KOH/carbon and activation temperatures. It can be concluded that the specific surface area and pore volumes increase with the KOH/carbon weight ratio and activation temperature. The sample LC3-700 prepared with KOH/carbon = 3:1 and at 700 ℃ presents the highest

specific surface area of 2230 m^2 g^{-1} and pore volume of 1.05 cm^3 g^{-1}. However, when it comes to ultramicropore volume (V_{CO2}, <0.7 nm), LC2-800 shows the highest value. Both less KOH/carbon weight ratios and activation temperatures result in poorer development of ultramicropores. The accumulation of KOH in localised area on the sample surface may result in reduced micropores due to excessive reactions between KOH and carbon. It has been well-discussed in the literature that the KOH activation reaction is significantly influenced by the KOH/carbon weight ratio and activation temperature.[97, 98, 155] The chemical activation reaction removes carbon atoms from the carbon structure to create porosity. Below 700 ℃, the activation reaction mainly produces potassium oxides and potassium carbonates with CO_2, H_2, CO and H_2O as the main gaseous products. The removal of carbon atoms is mainly carried out of by the gasification reaction between carbon and H_2O, where H_2O is generated from the dehydration reaction of KOH. Above 700 ℃, potassium carbonate further decomposes into potassium oxide and carbon dioxide; and carbon reduces carbon dioxide, potassium carbonate and potassium oxide into carbon monoxide and elemental potassium, respectively.[97, 98, 155] These additional carbon removal reactions raise the level of activation, either by creating more micropores or enlarging the sizes of existing pores. It is also important to note that the N_2 sorption isotherm of LC2-700H is at a similar position to LC2-700. In addition, LC2-700H shows a larger ultramicropore volume, which can be attributed to the acid-washing process.

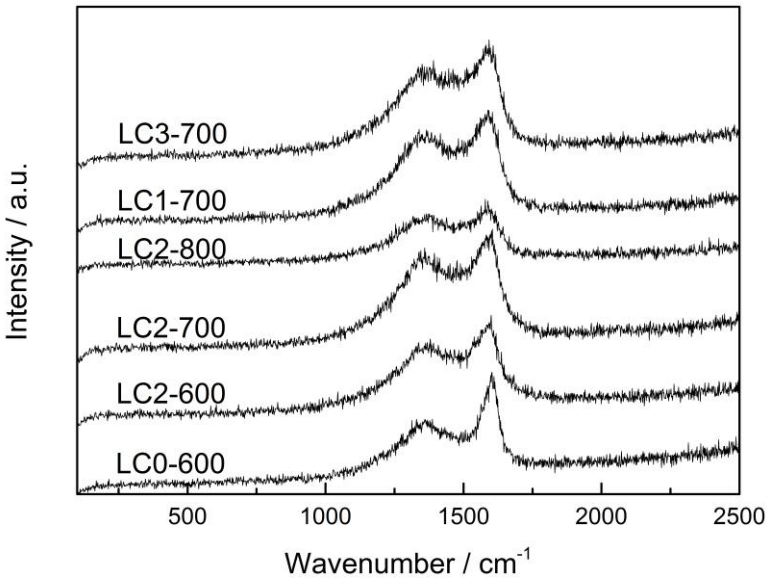

Figure 45: Raman spectra of leaf-derived carbon.

Table 12: The intensity ratio between D and G bands of leaf-derived carbon.

Sample	LC0-600	LC2-600	LC2-700	LC2-800	LC1-700	LC3-700
D/G ratio	2.04	2.20	2.68	2.79	2.63	4.02

In addition to the porosity analysis, leaf-derived carbon samples were also analysed by Raman spectroscopy. The Raman spectra of leaf-derived carbon are shown in Figure 45. Two characteristic bands can be observed in these spectra. The peak of D band is centred around 1360 cm^{-1}, while that of G band is centred around 1600 cm^{-1}. The intensities of these peaks vary with the samples prepared under different activation conditions. The intensity ratio between D and G bands are summarised in Table 12. It can be concluded from the table that the intensity ratio increases after the carbonised leaf LC0-600 is activated by KOH. Moreover, the intensity ratio increases when more aggressive KOH activation conditions are applied, that is, higher KOH/carbon ratios and activation temperatures.

4.1.3 Chemical analysis on leaf-derived carbon

The surface chemical composition of all samples were characterised by XPS and the results are summarised in Table 13. The analyser only detects carbon, oxygen and minor nitrogen in leaves without other anticipated elements, such as metallic elements. The reason is that a piece of leaf is protected by both upper and lower cuticles, which comprise of layers of waxes and dead cells with only cell walls but without the other living cell components, such as cytoplasm and nucleus.[156] The major components in cell walls are cellulose, hemicellulose and lignin, which mainly contain carbon and oxygen elements. The thickness of a cuticle layer can vary from 0.1 to 10 μm,[157] far beyond the detection limit of XPS analysis (1 to 10 nm).[113] Therefore, it cannot acquire the chemical information below both upper and lower cuticle layers. Even if some parts of the mesophyll layer are exposed (Figure 43), the thickness of the cell wall can vary from 0.1 to 10 μm as well,[158] which is still too thick for XPS analysis. In addition, within the original leaf, the levels of carbon and oxygen are much higher than the other elements. Therefore, their high peak intensities suppress peaks of other elements in this case.

Table 13: Chemical composition analysis of original, carbonised and activated leaves.

Sample	Chemical composition / at%								
	C	**O**	**N**	**K**	**Mg**	**Ca**	**Na**	**P**	**Cl**
Leaf	92.2	7.6	0.2	0	0	0	0	0	0
LC0-600	56.4	29.0	0.9	12.3	0	0	0.4	0	1.0
LC1-700	81.3	15.3	1.0	0	0.3	1.7	0	0.4	0
LC2-700	84.4	12.6	1.3	0	0.3	1.1	0	0.3	0
LC2-700H	85.5	12.0	2.5	0	0	0	0	0	0
LC3-700	86.5	11.9	0.4	0	0.3	0.9	0	0.	0
LC2-600	78.6	17.6	1.7	0	0.2	1.2	0	0.7	0
LC2-800	84.8	11.9	0.4	0	0.9	1.6	0	0.4	0

(a)

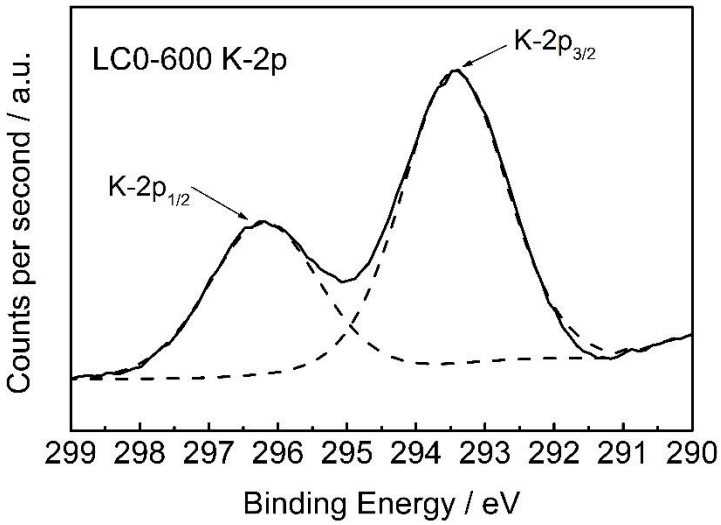

(b)

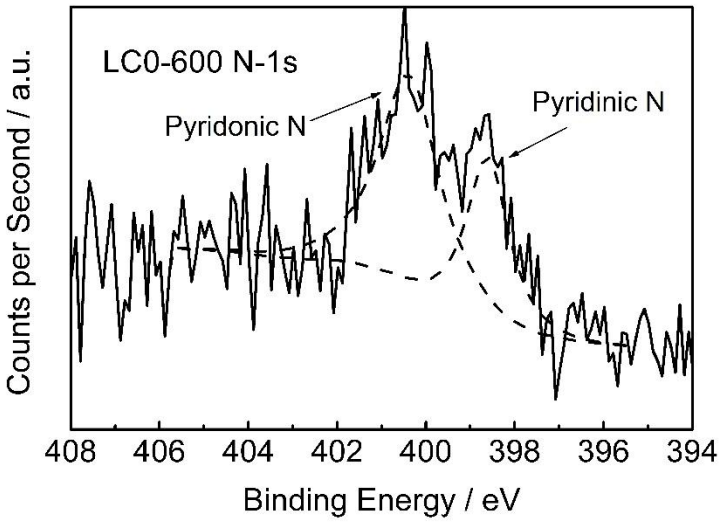
LC0-600 N-1s
Pyridonic N
Pyridinic N
Counts per Second / a.u.
408
406
404
402
400
398
396
394
Binding Energy / eV

(c)

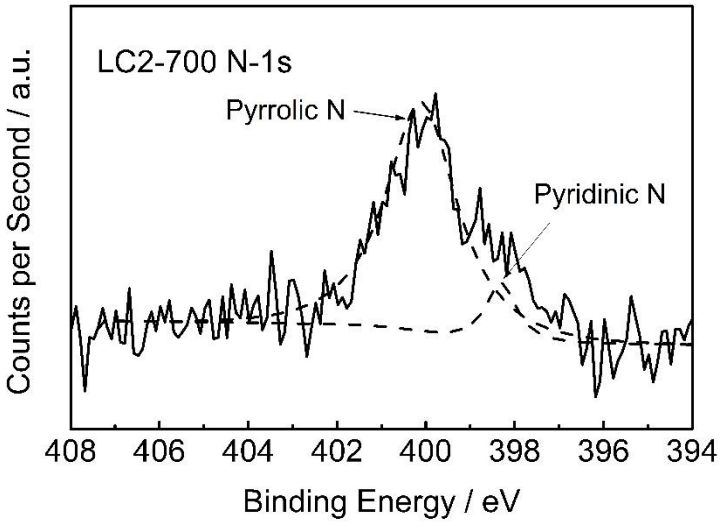
LC2-700 N-1s
Pyrrolic N
Pyridinic N
Counts per Second / a.u.
408
406
404
402
400
398
396
394
Binding Energy / eV

(d)

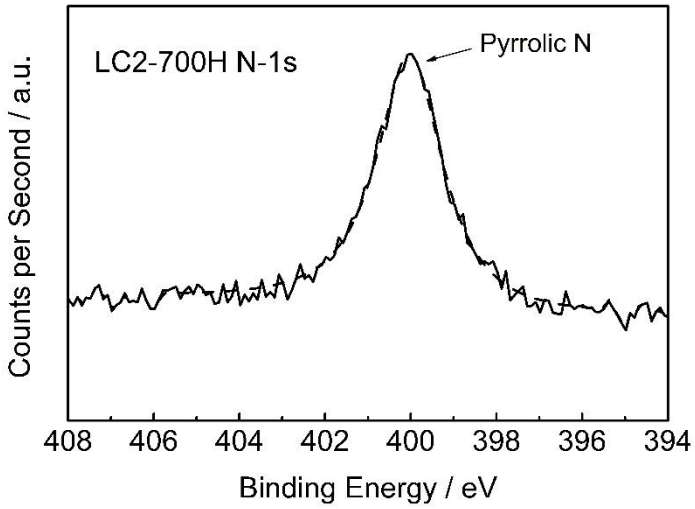
LC2-700H N-1s
Pyrrolic N
Counts per Second / a.u.
408
406
404
402
400
398
396
394
Binding Energy / eV

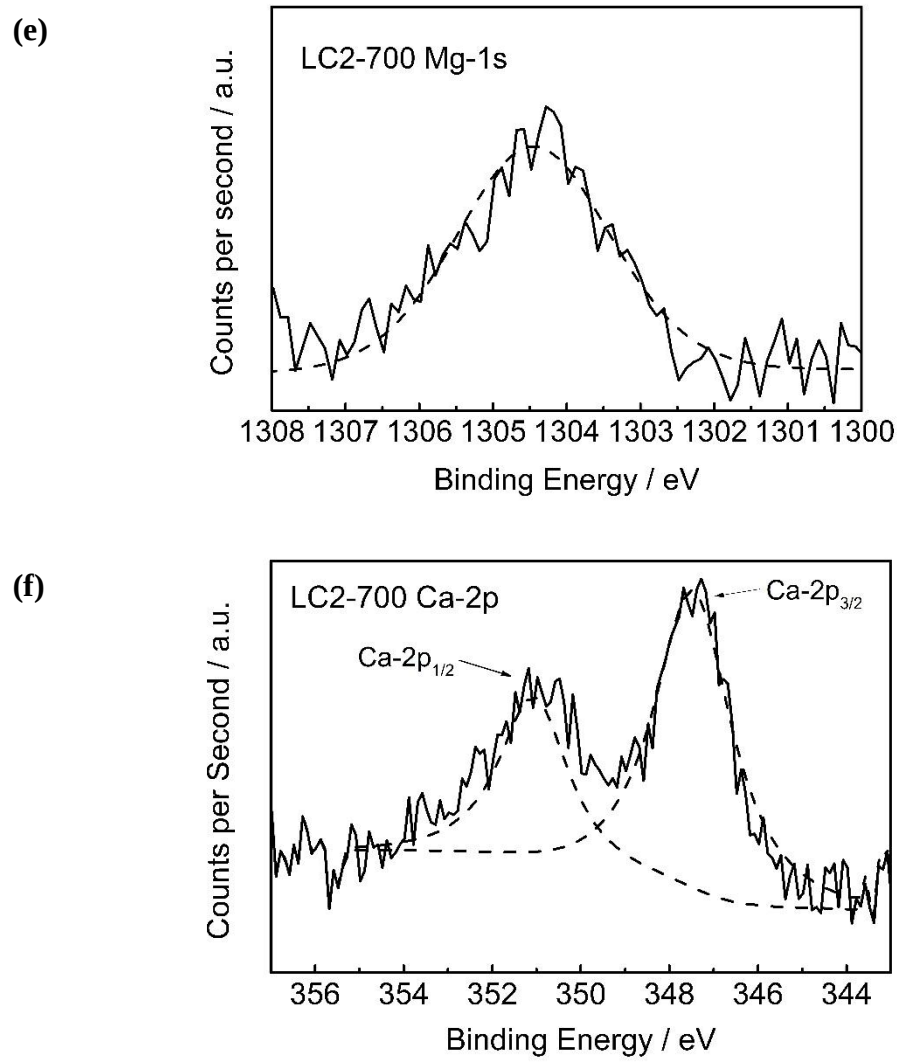

Figure 46: High resolution XPS spectra of major chemical elements in leaf-derived carbon.

After losing certain amount of carbon and oxygen, due to carbonisation and activation, it reveals more elements, such as potassium, magnesium, calcium, sodium, phosphate and chlorine. It also detects a higher level of nitrogen in the other samples after activation, thanks to the etching of cell walls, which exposes more intracellular nitrogen-containing compounds. The existence of these elements is anticipated because all of those are the essential elements in various nutrients for plants. Nitrogenous, phosphatic and potassic fertilisers are the three most used nutrients in agriculture. They are the key ingredients in various plant cell components, such as amino-acids and chlorophylls, catalysts for synthesis reactions and activators for enzymes.[154] Metal-

containing nutrients may be fertilised in the form of their corresponding chlorides due to their high solubility in water. This can explain the existence of chlorine in Table 13.

Potassium and sodium are important chemical components in plant cells. During carbonisation, organic cell membranes decompose at the high temperature and thus it releases the potassium and sodium contents in cytoplasm. As a result, these two elements can be detected after carbonisation. Figure 46a is the high resolution XPS K-2p spectra of the carbonised sample LC0-600. The K-2p spectrum shows two peaks at 296.3 and 293.4 eV, which correspond to the binding energies of K-2p1/2 and K-2p3/2 electrons, respectively.

The amount of nitrogen detected by XPS in the activated carbon samples is also influenced by the cell structure. Though it has been reported in the literature that nitrogen content in carbon is significantly reduced after chemical activation,[86] the 700 ℃ activated sample LC2-700 shows 1.3 at% nitrogen, which is even slightly higher than that in LC0-600 (0.9 at%). The same observation can be applied to LC2-600 and LC1-700. This phenomenon can be explained by the etching of cell walls and the expose of more nitrogen-containing compounds. There is severe loss of nitrogen in LC2-800 and LC3-700 due to more aggressive KOH activation.

Although the level of nitrogen is increased in LC2-700, the composition of different types of nitrogen dopants is still consistent with the earlier studies. Figure 46b, c and d are the high resolution N-1s spectra of LC0-600, LC2-700 and LC2-700H, respectively. The deconvolution of the LC0-600 spectrum shows two major peaks at 398.7 and 400.7 eV, respectively, which correspond to pyridinic and pyridonic types of nitrogen. The calculation of the area ratio of the two deconvoluted peaks suggests there are about 64 at% pyridonic and 36 at% pyridinic nitrogen. The level of pyridinic nitrogen is greatly reduced to 9 at% after chemical activation at 700 ℃ and the binding energies of two peaks shift to 398.2 and 400.1 eV, respectively. The 400.7 to 400.1 eV peak shift may correspond to the transformation of pyridonic to pyrrolic types of nitrogen, while the 398.7 to 398.2 eV peak shift may be due to the interaction between metal and pyridinic nitrogen,[142] where electrons are transferred from metal to pyridinic nitrogen.[159]

More inorganic elements, including magnesium, calcium and phosphorus, appear in the XPS spectra after activation, because the activation reaction between KOH and

carbon helps to etch through cell walls and expose what remain inside cells. In contrast, the K-2p, Na-1s and Cl-2p3 peaks completely disappear because the samples are thoroughly washed by distilled water. Figure 46e and f are the high resolution Mg-1s and Ca-2p spectra of LC2-700. The magnesium spectrum shows a single peak at 1304.1 eV, indicating the magnesium element exists in the form of +2 ions. A similar conclusion can be drawn from the calcium spectrum, which indicates calcium exists in the form of +2 ions. It has been discussed in an earlier studies that residual potassium content is detected after KOH chemical activation, even after the samples are washed.[90] In contrast, the author's XPS analysis does not detect residual potassium, which indicates both the intrinsic (from leaf cells) and extrinsic (from KOH) potassiums are not chemically grafted to the chemical structure of the resulting carbon samples. However, instead of potassium, magnesium and calcium are the residual metals in the resulting carbon structure. Furthermore, Table 13 shows all metal elements were washed away by 1M HCl acid (LC2-700H). In Figure 47, XRD analysis of all activated carbon samples have no diffraction peaks that are related to the crystal structures of magnesium and calcium or their corresponding metal oxides, which implies that those metal elements may not exist in those forms but are bonded with the resulting carbon structure in the form of cations.

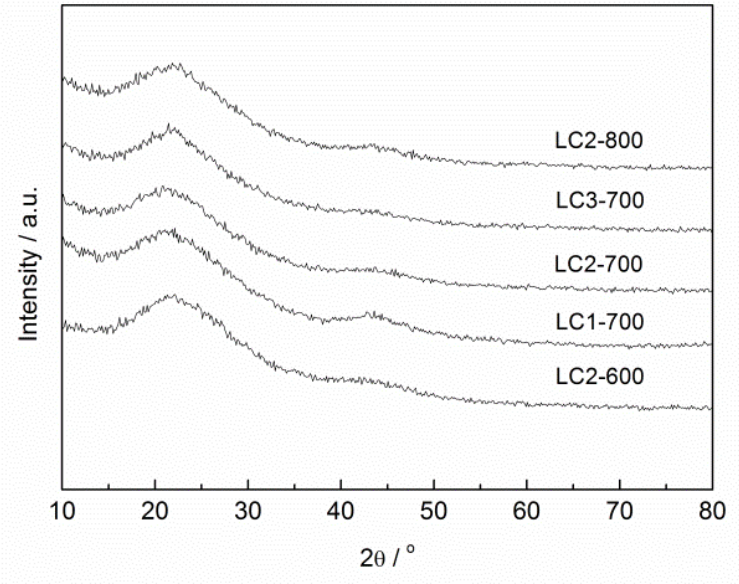

Figure 47: XRD diffraction pattern of leaf-derived carbon.

Table 14: Elemental composition of leaf-derived carbon by CHN analysis (unit: at%).

Sample	C	H	N	Other Elements
Leaf	52.12	6.67	2.21	39
LC0-600	72.58	2.23	2.18	23.01
LC2-600	57.21	2.55	1.17	39.07
LC2-700	58.44	2.64	1.02	37.9
LC2-800	60.3	1.89	0.1	37.71
LC1-700	60.25	1.71	0.66	37.38
LC3-700	51.22	2.59	0.14	46.05

Due to the detection limit of XPS, the elemental compositions of leaf and leaf-derived carbon were further analysed by a CHN elemental analyser (CE440, Exeter Analytical Ltd., UK). There are differences between the results given by CHN and XPS analyses, which indicates nitrogen and metal elements are non-uniformly distributed on the surface and in the bulk of leaf and leaf-derived carbon. Particularly, the nitrogen content detected by CHN in the leaf precursor is 2.21 at%, which is much higher than that detected by XPS (0.2 at%). The CHN analysis also shows that there are large proportions of "other elements", which may be attributed to oxygen and metal elements in the leaf. This further supports the author's discussion on the detection depth limit of XPS as a surface chemistry characterisation technique, when it is used for biomass precursor characterisation. This also suggests nitrogen is inherited from the biomass itself.

4.1.4 CO_2 uptake of leaf-derived carbon

CO_2 adsorption tests were carried out from 0.01 to 1 bar CO_2 at 0 and 25 ℃, respectively. The corresponding CO_2 adsorption isotherms and uptakes are plotted and summarised in Figure 48 and Table 15. LC2-700 shows the highest CO_2 uptake of 19.4 wt% at 25 ℃ under 1 bar CO_2, while LC2-800 exhibits the highest CO_2 uptake of 33.6 wt% at 0 ℃. At 0 ℃, all isotherms intersect with each other at different pressures below 0.7 bar. As the temperature increases to 25 ℃, the upper bound of the intersection points rise to about 0.8 bar in Figure 48b. These changes of intersection

points indicate an enhanced binding with CO_2 molecules at relatively lower pressures and higher temperatures. In addition, there is a 1.2 wt% difference between the CO_2 uptakes of LC2-700 and LC2-700H. This is a more significant difference in CO_2 uptake than that under 1 bar. It is mentioned in the porosity analysis that LC3-700 shows the highest specific surface area and LC2-800 possesses the highest ultramicropore volume, where these two porosity parameters are considered to have significant influences on CO_2 uptakes. However, both of them show relatively lower CO_2 uptake at 25 ℃. It implies porosity is not the only factor that influences CO_2 uptake.

Table 15: Summary of CO_2 uptakes of leaf-derived carbon under 1 and 0.15 bar CO_2.

Sample	CO_2 uptake / wt%			
	1 bar		0.15 bar	
	0 ℃	25 ℃	0 ℃	25 ℃
LC1-700	27.9	18.0	12.4	6.8
LC2-700	30.4	19.4	11.2	6.2
LC2-700H	32.3	18.5	10.1	5.0
LC3-700	30.5	17.3	8.8	4.3
LC2-600	27.4	14.9	11.0	5.3
LC2-800	33.6	18.6	9.8	5.0

(a)

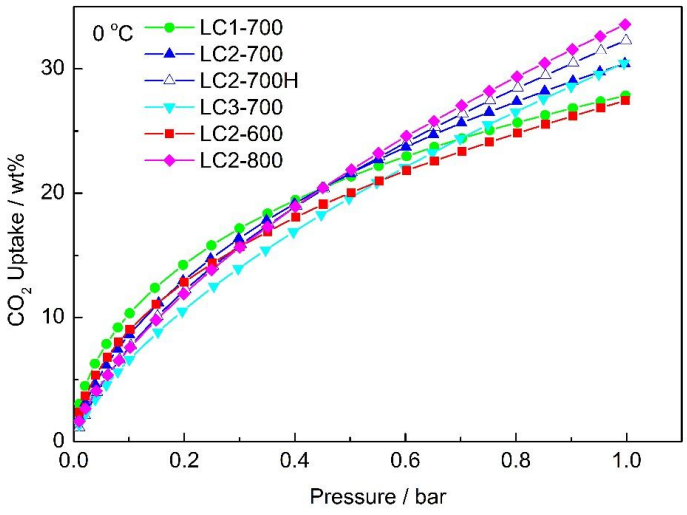

(b)

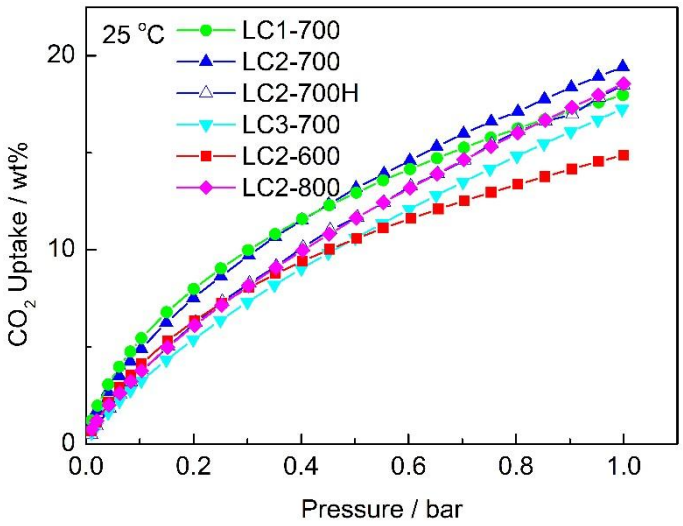

(c)

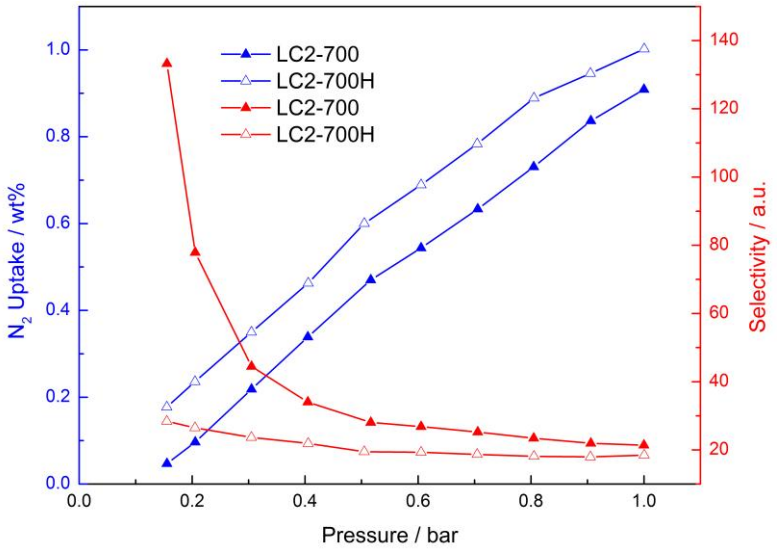

Figure 48: CO_2 adsorption isotherms of leaf-derived carbon sorbents at (a) 0 and (b) 25 ℃ from 0.1 to 1 bar. (c) N_2 adsorption isotherms and CO_2/N_2 selectivity of LC2-700 and LC2-700H at 25 ℃.

It has been discussed widely in the literature that the presence of nitrogen in the sample enhances CO_2 binding with carbon sorbents due to its basic nature.[86, 87, 160-162] Both pyridinic and pyrrolic nitrogens exist in nitrogen-containing carbon sorbents, but the former is more influential due to its lone pair of electrons and thus exhibits higher basicity than the latter.[163] Small quantities of nitrogen are found in all activated samples, but the level of pyridinic nitrogen is further reduced with increasing KOH/carbon weight ratio and activation temperature; correspondingly, its effect on CO_2 uptake also reduces. In addition to the nitrogen element, magnesium and calcium also exist in the samples in the form of ions. LC2-700 is the sample washed by distilled

water while LC2-700H is washed by 1M HCl acid to remove metal dopants. Figure 48a shows the acid-washed sample LC2-700H shows a higher CO_2 uptake than the water-washed counterpart at 0 ℃ at 1 bar. However, LC2-700 shows a higher CO_2 uptake at 25 ℃ in Figure 48b instead. In addition, in Figure 48a, the LC2-700 and LC2-700H isotherms intersect with each other at about 0.5 bar, which shows LC2-700 even has higher CO_2 uptakes than LC2-700H at a low pressure regime (<0.5 bar). At 25 ℃, the isotherm of LC2-700H is entirely below that of LC2-700. It is previously mentioned that no crystalline metal or metal oxides are found by XRD analysis and the corresponding XPS suggests both Mg and Ca exist in the form of cations. In consideration of the previously referenced study on extra-framework cations,[90] magnesium and calcium may also be grafted to the carbon structures in well dispersed form, as inherited from the leaf structure, and thus considerably enhance both the CO_2 binding through electrostatic interaction and the density of such active sites, leading to much increased CO_2 uptake.

In addition to CO_2 adsorption isotherms, Figure 48c shows the N_2 adsorption isotherms of LC2-700 and LC2-700H at 25 ℃. It clearly indicates that both samples have much lower uptakes of N_2 than that of CO_2. Figure 48c also shows that the sorption isotherm of LC2-700H is slightly higher than that of LC2-700. However, when the CO_2/N_2 selectivity (CO_2 uptake/N_2 uptake in wt%) is taken into consideration, LC2-700 exhibit much higher selectivity than that of LC2-700H in the low pressure region. However, the difference in selectivity reduces with the increasing pressure. This further demonstrates that metal dopants can help to enhance CO_2 binding on carbon under low pressures.

4.1.5 Heat of adsorption and influence of dopants

Figure 48b shows that there is an extra 0.9 wt% CO_2 uptake (at 1 bar CO_2 and 25 ℃) in LC2-700 compared with LC2-700H. Although the difference is insignificant, it should be noted that LC2-700 has lower specific surface area, pore volume and ultramicropore volume than LC2-700H. Therefore, the positive contribution of metallic dopants on CO_2 uptake can be offset by the reduced porosity.

(a)

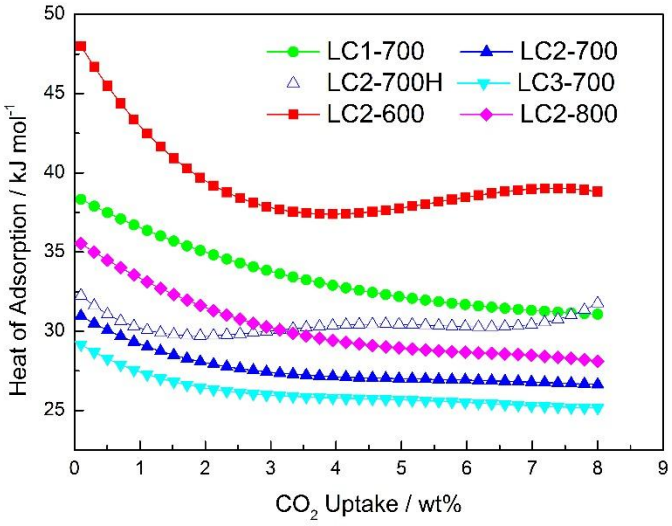

(b)

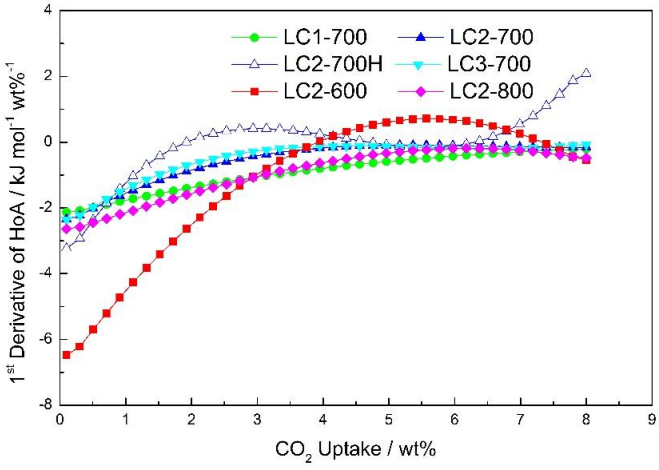

(c)

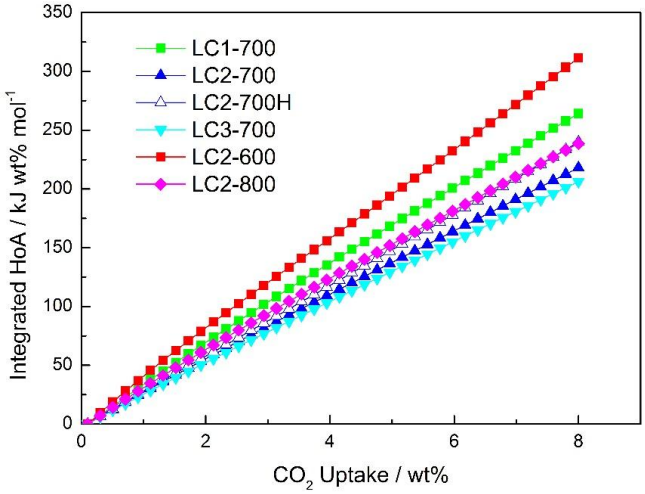

Figure 49: (a) 4th order Polynomial fitted heat of adsorption (HoA) plot and its corresponding (b) 1st order derivative and (c) integrated plots.

Figure 49a is the 4th order polynomial fitting of heat of adsorption between 0.1 and 8 wt% CO_2 uptakes. The fitting process basically reproduces the shapes of curves plotted with experimental data points and also helps to predict heat of adsorption at even lower CO_2 uptakes. The fitted curve in Figure 49a is used to produce 1st order derivative and integrated heat of adsorption plots, which are shown in Figure 49b and c, respectively. Differing from the CO_2 adsorption isotherm plots, LC2-600 shows higher heat of adsorption than those of all the other samples, while LC3-700 is at the bottom of the diagram. The heat of adsorption of a sample can be influenced by both its dopants and porosity. Considering LC2-600 has the least developed porous structure, its high heat of adsorption can be solely attributed to dopants. However, LC2-600 possesses a considerable amount of both nitrogen and metal dopants. Therefore, it is difficult to distinguish their respective effects on the CO_2 uptake. It can be noted in Figure 49a that LC1-700 shows the second highest heat of adsorption and shows a less developed porous structure than LC2-700. It also has a lower nitrogen content but higher calcium content than LC2-700. Therefore, the higher heat of adsorption should be attributed to the existence of calcium dopants.

The 1st order derivative plot is an indication of how steeply the heat of adsorption reduces with increasing CO_2 uptake, in another word, the CO_2 molecule coverage on carbon surface. At low CO_2 uptakes, that is, when CO_2 molecules just start to form monolayer coverage, they preferably adsorb on the active sites in the first place, such as nitrogen and metal dopants. This is reflected in Figure 49a in that all samples except the acid-washed LC2-700H show observable higher heat of adsorption at the lower CO_2 uptake regime. In addition, Figure 49b shows LC2-600 has a much steeper curve before it reaches a plateau, which suggests its heat of adsorption drops much more steeply than those of the other samples. This is attributed to the mixed contribution of both active and normal carbon sites to the heat of adsorption. The latter contributes less to the heat of adsorption, which lowers the overall heat of adsorption. After the formation of monolayer coverage, active sites may have much less influence on the second layer (or above) CO_2 molecules and thus the sample exhibits even lower heats of adsorption. Therefore, it explains the plateau regime in Figure 49a and similar 1st order derivative of HoA in Figure 49b for all the samples at higher CO_2 uptake regime. Considering LC2-600 has both relatively higher levels of nitrogen and metal contents,

compared with those of the other samples, it leads to high heats of adsorption at low CO_2 uptakes and the heat of adsorption drops steeply when the active sites is covered by CO_2 molecules.

Furthermore, Figure 49c integrates heat of adsorption from 0.1 to 8 wt% CO_2 uptake, which is an indication of overall effect of active sites throughout different levels of CO_2 uptakes. Figure 49c shows that the integrated heat of adsorption of all samples exhibits almost a linear relationship with CO_2 uptake. The positions of the linear plots in Figure 49c is consistent with Figure 49a, where LC2-600 occupies the highest place. It indicates the positive influence of active sites on enhanced CO_2 binding across all levels of CO_2 uptakes.

4.1.6 Porous carbon from various leaf precursors

Although London Plane is the most planted tree in the London urban area, in practice, various kinds of trees are planted and distributed across the whole of London for the purpose of biodiversity and aestheticism. Various leaves from different trees may have different biological structures and chemical compositions, which leads to different porosities and chemical compositions of carbon sorbents derived from them. Preliminary characterisations, such as BET and CO_2 uptake, have been carried out. More characterisations are proposed in Chapter 6 Future Work.

Various kinds of leaf litter were collected from the Gordon Square Garden near UCL campus, where London Plane leaves had also been collected. The collected leaves include Cydonia Oblonga (Common Quince), Carpinus Betulus (Common Hornbeam), Laburnum Anagyroides (Common Laburnum) and Japan Rosaceae (Prunus). Porous carbon sorbents were produced under the same preparation conditions as those for the London Plane leaves. The leaves were firstly carbonised at 600 ℃ and then the carbonised leaves were activated with a KOH/carbon weight ratio of 2:1 and an activation temperature of 700 ℃. The so-derived activated carbon sorbents were then washed with distilled water and dried overnight in an 80 ℃ vacuum oven before any characterisations were undertaken. The carbon samples were marked as LA-A, CO-A, CB-A and JR-A, where LA stands for Laburnum Anagyroides, CO for Cydonia Oblonga, CB for Carpinus Betulus and JR for Japan Rosaceae. The letter "A" means the sample is activated by KOH.

Table 16: Porosities of carbon sorbents derived from different leaves.

Sample	S_{Total} / m^2 g^{-1}	S_{Micro} / m^2 g^{-1}	V_{Total} / cm^3 g^{-1}	V_{Micro} / cm^3 g^{-1}
LA-A	1060	880	0.55	0.35
CO-A	1380	1230	0.62	0.46
CB-A	1800	1770	0.75	0.67
JR-A	1580	1550	0.67	0.60

The nitrogen sorption isotherms are plotted in Figure 50a and Figure 50b depict their corresponding pore size distribution. The total specific surface area, micropore surface area, total pore volume and micropore volume are derived from the isotherms and summarised in Table 16.

(a)

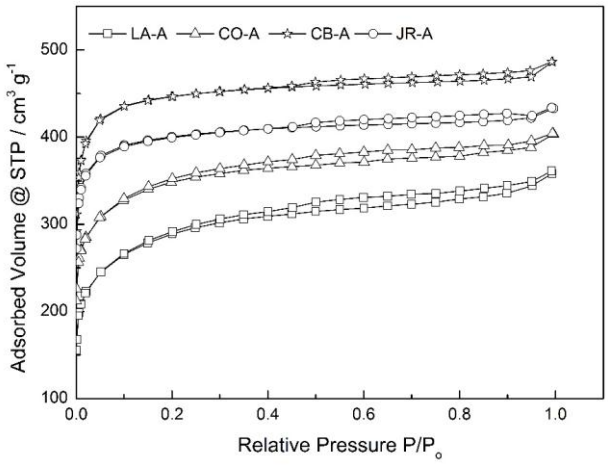

(b)

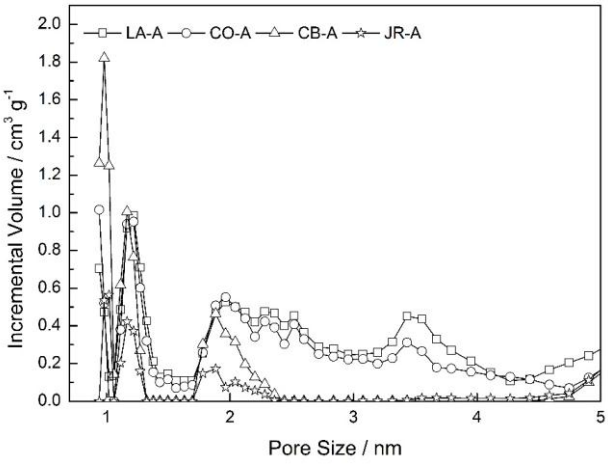

Figure 50: N_2 sorption isotherms and pore size distribution of carbon sorbents derived from different leaves.

The N_2 sorption isotherms in Figure 50a show steep N_2 uptakes at the low partial pressure region ($P/P_0<0.1$). The rate of gas sorption slows with increasing partial pressure where the isotherm reaches a plateau. These are the characteristic features of the Type-I sorption isotherm, which indicates that all activated leaf samples mainly contain micropores (<2nm). However, all isotherms show hysteresis between 0.1 and 0.99, indicating that they all have certain degrees of mesopore development. All of these observations are quantified in Table 16. It is noticed that activated leaf samples exhibit large variation in their porosities. The total specific surface area varies from 1060 to 1800 $m^2\ g^{-1}$, while the total pore volume varies from 0.55 to 0.75 $cm^3\ g^{-1}$. Another important property is the ratio of micropore volume to total pore volume. For LA-A, 63.5% total pore volume is made up of micropores, but this proportion is increased to 74.4% for CO-A, 88.7% for CB-A and 89.7% for JR-A. Considering all samples are prepared under the same conditions, these relatively significant differences in porosity imply different leaves have undergone different levels of chemical activation. Because different leaves have different biological structures, this may influence the resulting porous carbon.

Table 17: CO_2 uptakes of carbon sorbents derived from different leaves.

Sample	CO_2 uptake / wt%	
	0 ºC	**25 ºC**
LA-A	17.4	9.6
CO-A	24.5	13.8
CB-A	29.9	17.4
JR-A	30.7	16.4

The CO_2 sorption isotherms of carbon sorbents are plotted in Figure 51 and the corresponding CO_2 uptakes at 1 bar are summarised in Table 17. It is clear that carbon sorbents derived from different leaves show different CO_2 uptakes, although all the samples are produced under the same preparation conditions. Their CO_2 uptakes are also more or less different from that of London Plane leaf-derived carbon. Table 16 and Table 17 also show the sample with larger surface area exhibits higher CO_2 uptake.

However, the sample JR-A shows a slightly higher CO_2 uptake than that of CB-A, which is most likely due to a higher ultramicropore volume.

(a)

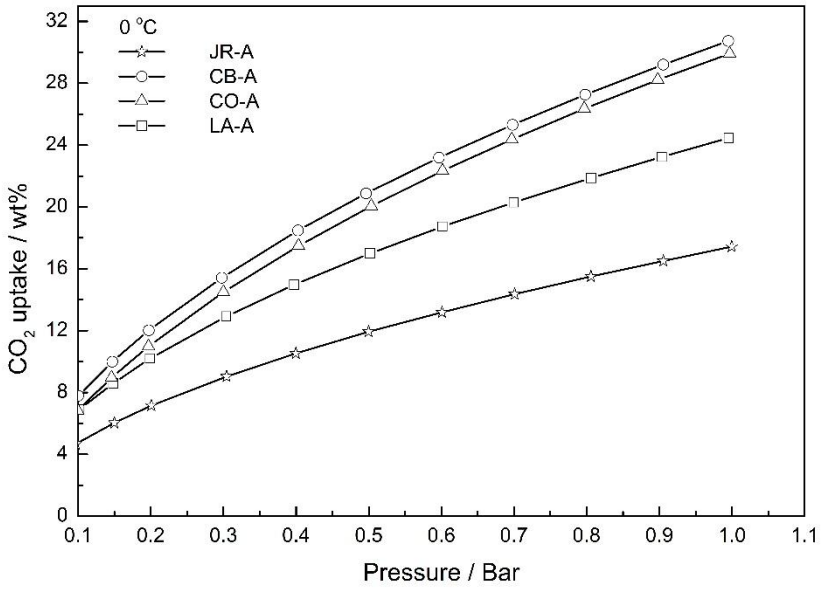

(b)

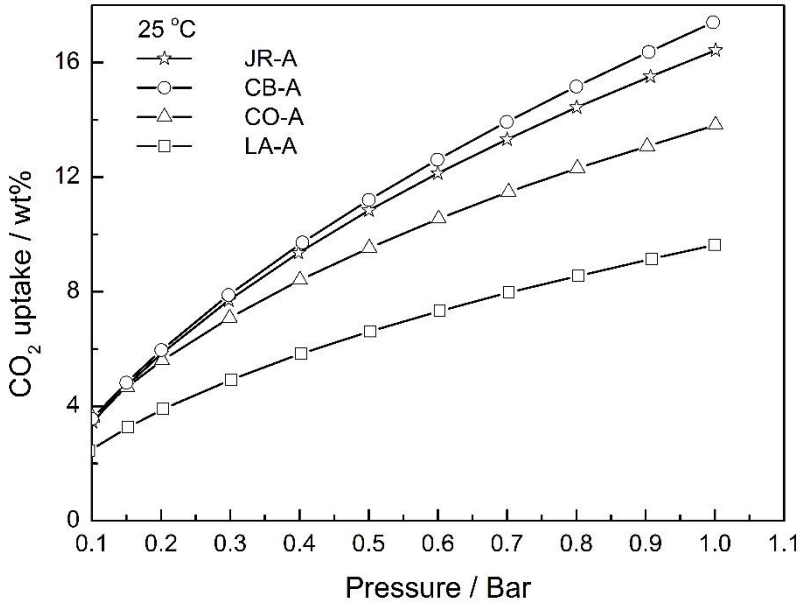

Figure 51: CO_2 adsorption capacities of carbon sorbents derived from different leaves.

In summary, under the same activation condition, different leaf precursors produce carbon sorbents with different porosities and thus varied CO_2 uptakes. Further elemental analysis need to be carried out to clarify the influence of the residual chemical dopants in those leaf-derived carbon on CO_2 capture.

4.1.7 Summary

London Plane leaf waste, rich in lignocelluloses with cellular structures, is an ideal precursor for microporous carbon for the production of low-cost but high performance carbon materials. The KOH/carbon weight ratio and activation temperature are the two major factors that largely influences the resulting porous structure and chemical composition of the resulting materials. Equally important are the biological structure and chemistry of the leaves, particularly well dispersed nitrogen, magnesium and calcium dopants in the derived carbon. Activated at 700 ℃ and with a KOH/carbon weight ratio 2:1, washed by distilled water, the sample shows the highest CO_2 uptake of 19.4 wt% under 1 bar CO_2 and 25 ℃, as a result of the highly developed microporous structure and the preservation of nitrogen and elemental metal contents doped in the carbon materials. The dopants exist in the form of aromatic nitrogen and metal cations, respectively, which can enhance CO_2 binding on carbon by means of Lewis basicity and electrostatic interactions. To summarise, here the author presents a facile synthesis of highly microporous carbon, derived from "zero-cost" London Plane leaf wastes, which has shown excellent potential in CO_2 capture. The optimal performance in both applications is determined by the combined effect of the highly developed microporous structure plus the intrinsic nitrogen and metal doping.

4.2 Pine cone-derived carbon sorbents

Pine cone is the woody fruit of a pine tree. A major component of a pine cone is the dense and tough scale, which is a carbon-rich biomass waste. Pine cones have been used for the production of activated carbon for the removal of heavy metals and organic compounds in contaminated water.[164] However, to the author's best knowledge, the CO_2 capture performance of pine cone-derived carbon has never been studied and its chemistry has not been discussed in detail, especially, the metal and nitrogen dopants inherited from pine cones.

Here, porous carbon is derived from pine cones by means of chemical activation with KOH. The corresponding characterisation shows excellent uptake of 20.9 wt% at 25

℃ and 1 bar CO_2, matching the highest reported CO_2 uptake (21.2 wt%) on biomass derived carbon sorbents tested in the same conditions in the recent literature.[91] Elemental analysis also reveals that calcium is the only residual metallic element left in carbon sorbents and it has a positive influence on the CO_2 capture of the sorbent.

4.2.1 Morphologies of pine cone-derived carbon

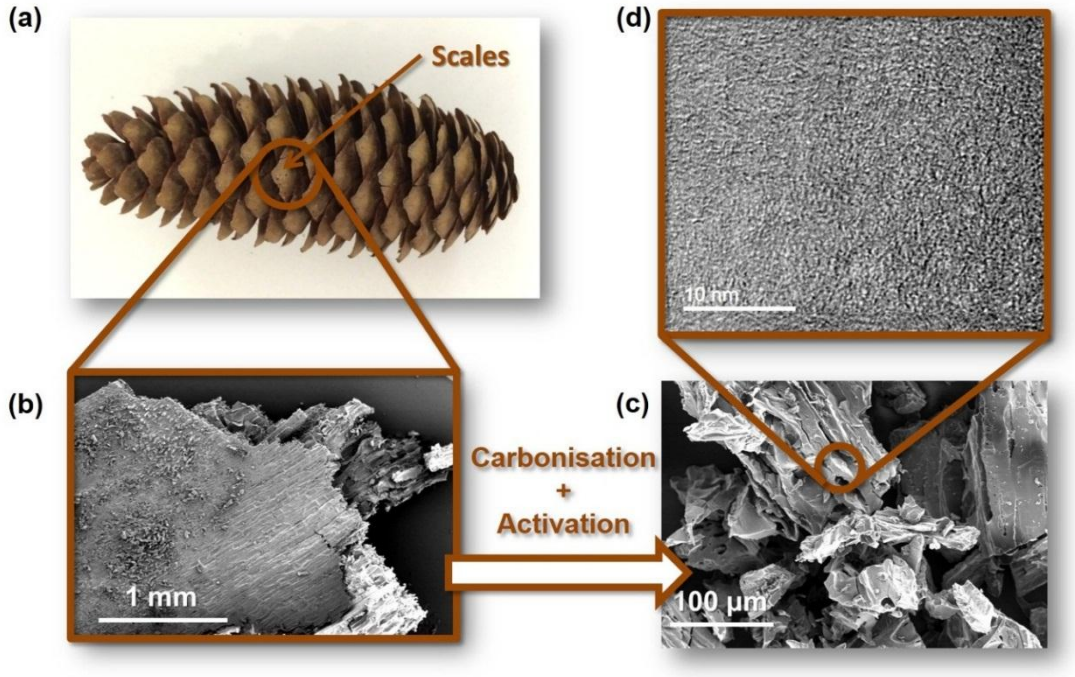

Figure 52: (a) A photograph of a pine cone and its scales; SEM images of (b) a piece of dried scale and (c) porous carbon particles after KOH activation; (d) A high resolution TEM image of nano-scale porous carbon fragments.

Figure 52 shows the preparation procedure and morphological changes from the original pine cone scales to porous carbon particles. Figure 52a shows that the dried pine cone scales have a yellowish brown colour. After carbonisation, the shape of the scales is well preserved but their colour turns black.

Figure 52b shows that a piece of pine cone scale exhibits a relatively rough surface and well-aligned cellulose fibres. Although the shape of the scale remains after carbonisation at 600 ℃, the sample becomes crisp and can be ground into particles for the subsequent mixing process in the KOH solution. Figure 52c shows that, after

chemical activation, the sample turns into porous carbon particles of random shapes and varied sizes. Pores of micrometre size can be also spotted at the surface of these particles. The high resolution TEM image (Figure 52d) reveals an amorphous carbon nanostructure, where the nano-scale micropores originate from the spaces between a large number of irregularly arranged carbon fragments.

4.2.2 Porous structure of pine cone-derived carbon

The porous structures of pine cone-derived carbon were analysed by means of nitrogen and CO_2 sorption at -196 and 0 ℃, respectively. The specific cumulative surface area (up to 40 nm, S_{N2}), specific micropore surface area (S_{Micro}), total pore volume (V_{N2}), micropore volume (V_{Micro}, <2 nm) and ultramicropore volume ($V_{CO2,}$ <0.7nm) are summarised in Table 18.

(a)

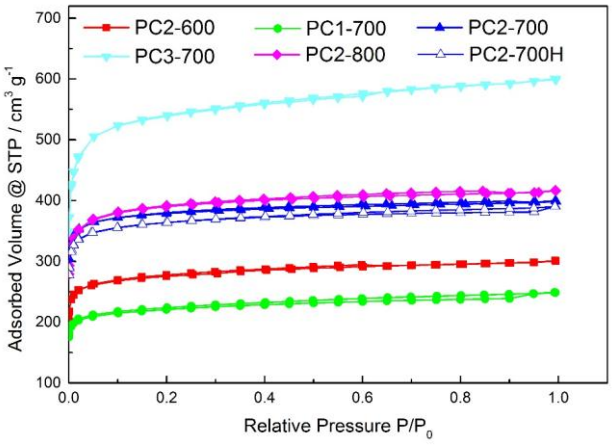

(b)

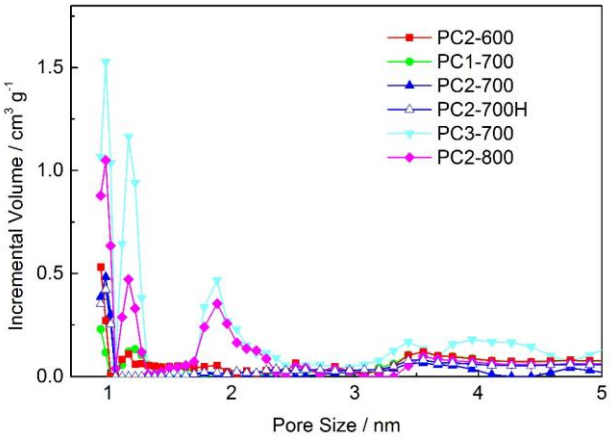

(c)

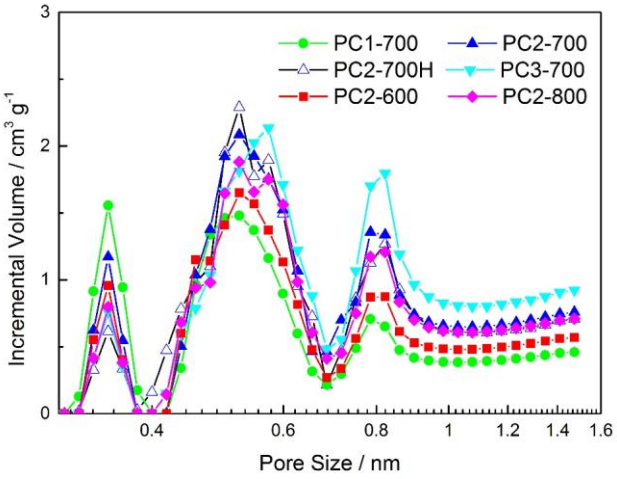

Figure 53: (a) N_2 sorption isotherms at -196 ℃, (b) corresponding pore size distribution and (c) micropore size distribution of pine cone-derived carbon sorbents.

Table 18: Porosity characteristics of pine cone-derived carbon.

Method	**N_2 sorption**				**CO_2 sorption**
Sample	**S_{N2} /m^2 g^{-1}**	**S_{Micro} /m^2 g^{-1}**	**V_{N2}/cm^3 g^{-1}**	**V_{Micro} /cm^3 g^{-1}**	**V_{CO2}/cm^3 g^{-1}**
PC2-600	1260	1220	0.47	0.41	0.28
PC1-700	1170	1140	0.39	0.34	0.28
PC2-700	1680	1670	0.61	0.56	0.34
PC2-700H	1640	1610	0.60	0.53	0.32
PC3-700	2110	2060	0.89	0.78	0.32
PC2-800	1650	1620	0.64	0.58	0.30

All the N_2 sorption isotherms in Figure 53a are typical Type-I sorption isotherm, which indicates that all carbon sorbents possess microporous structures. Figure 53b shows the pore size distributions of porous carbon sorbents derived from their corresponding N_2 sorption isotherms. All of those show three major peaks in the micropore size range (<2 nm) at 1, 1.2 and 1.9 nm, respectively. There is also a weak and broad peak at 3.5 nm, which suggests the existence of a small proportion of mesopores. Table 18 shows that the porosities of carbon sorbents are mainly influenced by the KOH/carbon mass ratio and the activation temperature. On the one hand, both specific surface area and

pore volume have an approximately linear relationship with the KOH/carbon mass ratio, and the sample PC3-700 prepared at 700 ℃ and KOH/carbon=3:1 shows the highest specific surface area of 2110 $m^2 g^{-1}$ and pore volume of 0.89 $cm^3 g^{-1}$. However, PC2-700 exhibits the highest ultramicropore volumes of 0.34 $cm^3 g^{-1}$. This indicates that a higher KOH/carbon ratio helps to develop a porous structure with a higher specific surface area and pore volume, but also enlarges the sizes of the micropores, which results in a reduced ultramicropore volume.

On the other hand, activated with the same KOH/carbon mass ratio (KOH/carbon=2:1), the sample shows a significant increase in both specific surface area and pore volume, when the activation temperature rises from 600 to 700 ℃. However, the 700 and 800 ℃ treated samples have similar specific surface areas and pore volumes, but the ultramicropore volume is reduced from 0.34 to 0.30 $cm^3 g^{-1}$. The reduction in the ultramicropore volume is almost equal to the increased total pore volume (from 0.61 to 0.64 $cm^3 g^{-1}$). It has been mentioned in the literature that KOH and carbon are subject to different reaction mechanisms at different activation temperatures. Below 700 ℃, the chemical activation reaction is mainly based on the dehydration of KOH and the gasification of carbon, which removes carbon atoms to generate porous structures. Above 700 ℃, it is the reduction of CO_2, K_2O and K_2CO_3 by carbon that further develops the porous structure.[97] The slightly reduced surface area and increased pore volume suggests that the higher activation temperature does not encourage the development of more ultramicropores but enlarges the size of existing pores instead.

In addition, in Figure 53a, the PC2-700H isotherm is at a similar position to PC2-700 with a slightly lower N_2 uptake, which indicates the HCl acid wash has a limited influence on the resulting porous structure. It is also reflected in Table 18 that PC2-700H and PC2-700 show very similar porosity characteristics.

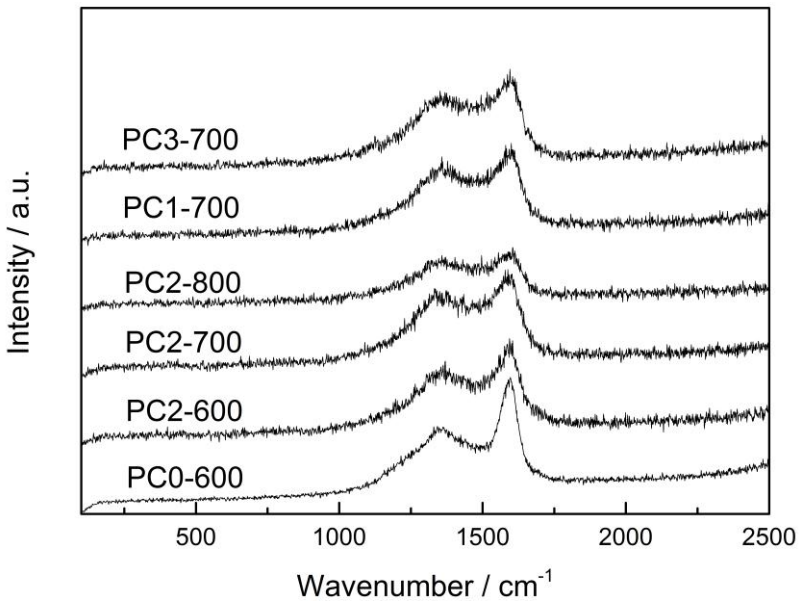

Figure 54: Raman spectra of pine cone-derived carbon.

Table 19: The intensity ratio of D and G bands of pine cone-derived carbon.

Sample	PC0-600	PC2-600	PC2-700	PC2-800	PC1-700	PC3-700
D/G ratio	2.34	2.55	2.80	3.05	2.62	3.87

Similar to the case of leaf-derived carbon, the Raman spectroscopy analysis shows that the intensity ratio of D and G bands increases after KOH activation. Figure 54 is the Raman spectra of pine cone-derived carbon and Table 19 summarises their corresponding intensity ratios, The D/G ratio increases from 2.55 to 3.05 when the activation temperature increases from 600 to 800 ℃, while the D/G ratio increases from 2.62 to 3.87 when the KOH/carbon ratio increases from 1:1 to 3:1. In both cases of leaf and pine cone-derived carbon, the intensity ratio increases when more aggressive KOH activation conditions are applied. This indicates that the carbon structure becomes more defective under more aggressive KOH activation reactions, such as more carbon edges generated due to KOH etching.

4.2.3 Chemical analysis on pine cone-derived carbon

The surface chemistry of pine cone-derived carbon is characterised by XPS and the characterisation results are summarised in Table 20. As in the case of leaf-derived carbon, the device only detects carbon and oxygen elements, which are inherited from the lignocellulosic compounds (cellulose, lignin, hemicelluloses and pectin) in pine

cones.[165, 166] Other anticipated elements, such as nitrogen and metals, are not detected, because the thicknesses of cellulosic fibres and cell walls are beyond the detection limit of XPS.

After carbonisation, potassium and silicon elements become detectable. The emergence of potassium may be caused by the decomposition of cell membranes and the subsequent release of potassium cations in the cell cytoplasm. Figure 55a shows the high resolution XPS K-2p spectrum of the carbonised pine cone PC0-600 and it shows two peaks at 295.6 and 292.9 eV, which correspond to the binding energies of K-2p1/2 and 2p3/2 electrons, respectively. Silicon is another element detected after carbonisation, which may be due to the damaged cell structure caused by carbonisation, considering silicon is an essential element in plant cell walls. After KOH activation, the proportion of silicon is increased from 0.29 to 0.79 wt%, because the chemical activation reaction further etches fibres and cells, exposing more silicon compounds. Figure 55d shows the high resolution XPS Si-2p spectrum of the activated sample PC2-700. The hill in the spectrum starts from 105 to 100 eV, which covers the binding energies of a range of oxidised silicon. The curve can be deconvoluted into three sub-peaks at 103.6, 102.6 and 101.5 eV, which correspond to Si^{4+}, Si^{3+} and Si^{2+} oxidised states of silicon.[167]

Nitrogen and calcium are the two elements detected after KOH activation. The potassium peak disappears in the spectrum after the sample is washed by distilled water, which indicates both intrinsic (from cells) and extrinsic (from KOH) potassium can be removed from the carbon structure by distilled water washing. The emergence of nitrogen may originate from the etching of cell walls by means of chemical activation and the fixation of nitrogen by means of reaction between pectin and intracellular proteins.[168] Figure 55b shows the high resolution XPS N-1s spectrum, which has a single peak centred at 400.0 eV. This peak corresponds to the binding energy of the pyrrolic type of nitrogen.[142] It has been reported in the literature that the amount of nitrogen in carbon decreases with the increasing KOH/carbon weight ratio and activation temperature.[86, 160] However, it can be concluded from Table 20 that the nitrogen content does not vary much with the KOH/carbon mass ratio. As mentioned previously, the cell structure is etched by means of chemical activation and thus it exposes more chemical compounds inside. A higher KOH/carbon mass ratio can

lead to a higher degree of etching, which results in the exposure of more nitrogen–containing compounds within cells. This compensates for the reduced nitrogen content caused by chemical activation. Hence, the overall N content is more or less unchanged by the activation at a given temperature.

Table 20: Chemical composition of pine cone-derived carbon.

Sample	Chemical composition / at%					
	C	**O**	**N**	**K**	**Ca**	**Si**
Pine Cone	89.2	10.8	0	0	0	0
PC0-600	83.9	12.7	0	3.1	0	0.3
PC2-600	81.3	16	1.3	0	0.6	0.8
PC1-700	86.5	12.1	0.5	0	0.4	0.5
PC2-700	83.4	15	0.5	0	0.5	0.6
PC2-700H	83.7	14.8	1	0	0	0.5
PC3-700	86.5	12	0.5	0	0.4	0.6
PC2-800	86.2	12.2	0.5	0	0.7	0.4

Besides nitrogen, calcium is another element that was detected after chemical activation. Figure 55c shows the high resolution XPS Ca-2p spectrum with two peaks at 350.8 and 347.3 eV, which corresponds to the binding energies of Ca-2p1/2 and 2p3/2 electrons. It indicates calcium exists in the form of +2 cations. It has been reported in some biological studies that calcium plays the cross-linking role in cell walls, which is bound with pectin.[169] In an earlier study on residual potassium in carbon, the author proposed the residual potassium may exist in the form of extra-framework cations.[90] In the case of pine cone-derived carbon, the potassium is washed away by distilled water and calcium becomes the residual metal in the resulting carbon structure. Then, the calcium cations may still be bound with the resulting carbon structure, which originates from lignocellulosic compounds, including pectins. After

the sample is washed by 1M HCl acid, all the metal element is removed, but the silicon remains in the carbon structure.

(a)

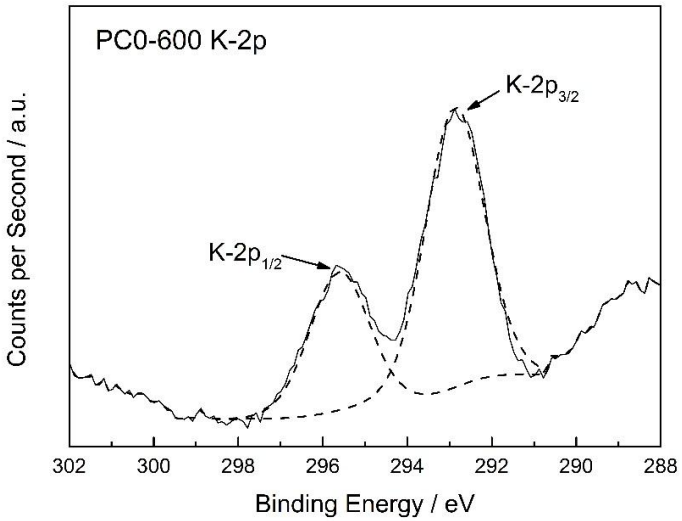

(b)

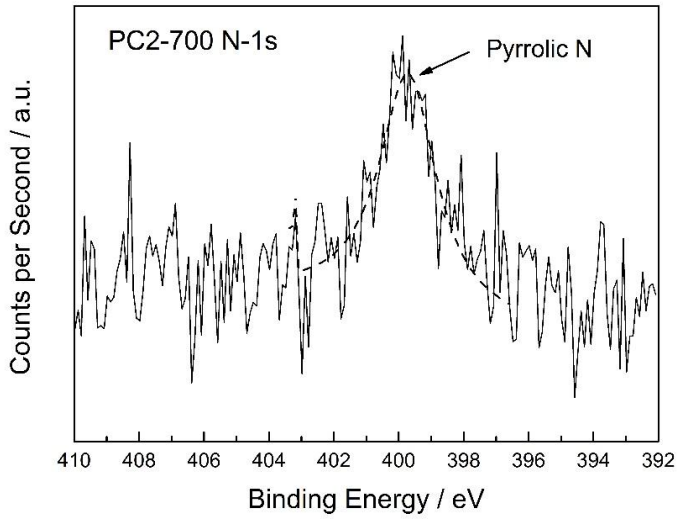

(c)

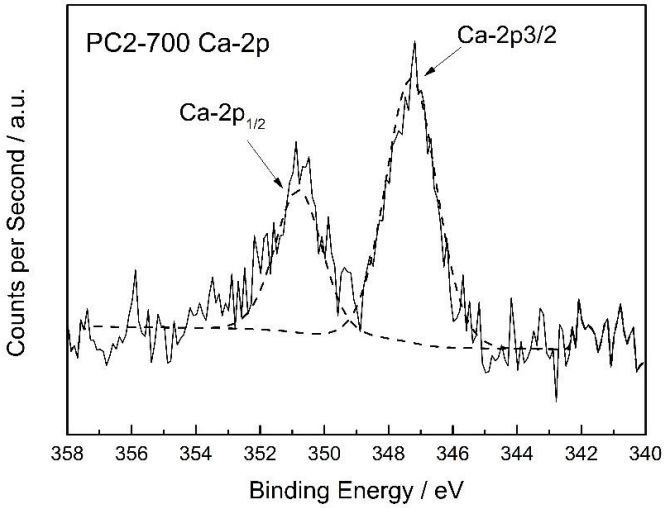

(d)

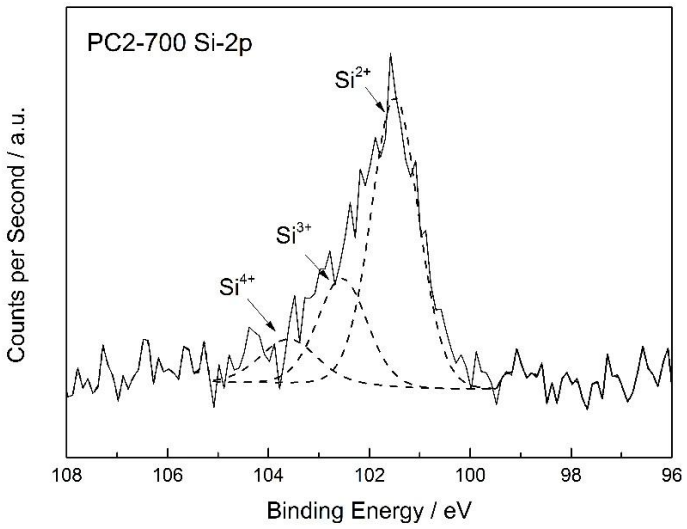

Figure 55: High resolution XPS spectra of chemical elements in pine cone-derived carbon.

Table 21: Elemental composition of pine cone-derived carbon by CHN analysis (unit: at%).

Sample	C	H	N	Other Elements
Pine Cone	46.78	5.5	0.3	47.42
PC0-600	84.56	2.17	0.55	12.72
PC2-600	71.4	1.79	0.72	26.09
PC2-700	61.67	2.11	0.12	36.1
PC2-800	64.42	1.08	0.06	34.44
PC1-700	70.04	0.61	0.16	29.19
PC3-700	65.25	0.97	0.03	33.75

Similar to the case of leaf-derived carbon, a CHN analysis was also applied to pine cone-derived carbon to obtain the elemental composition of the whole sample. The corresponding results are summarised in Table 21. A small proportion of nitrogen (0.3 at%) was detected by the CHN analyser, while none was detected by XPS, due to the detection limit of XPS. It can also be noted that nitrogen content in pine cone is much less than that in London Plane leaf, because the main function of pine cone shell is protection rather than photosynthesis. Moreover, the activated sample LC2-600 shows

an even higher nitrogen content than those of the original pine cone and carbonised pine cone LC0-600. This may be attributed to the loss of "other elements" caused carbonisation/activation and the non-uniform distribution of chemical elements within biomass. In conclusion, the result of CHN analysis further confirms that nitrogen dopants in pine cone-derived carbon is inherited from the biomass precursor. Furthermore, both XPS and CHN analyses show the level of nitrogen content is low in all pine cone-derived carbon. Therefore, the influence of nitrogen dopant on CO_2 capture can be expected limited.

4.2.4 CO_2 uptakes of pine cone-derived carbon

The CO_2 adsorption capacities of pine cone-derived carbon were carried out from 0.01 to 1 bar CO_2 at the temperatures of 0 and 25 ℃, respectively. Their CO_2 adsorption isotherms are plotted in Figure 56 and the corresponding CO_2 uptakes at 1 and 0.15 bar CO_2 are summarised in Table 22.

It can be concluded from the figure that PC2-700 shows the highest CO_2 uptake of 20.9 wt% under 1 bar CO_2 and 25 ℃. To the best of the author's knowledge, it almost matches the best reported CO_2 uptake of biomass-derived carbon in the literature so far (21.2 wt%) [15]. In contrast, at 0 ℃, PC3-700 and PC2-700 possess very similar CO_2 uptakes of 34.4 and 34.2 wt%, respectively. Compared with PC2-700, PC3-700 has a more developed porous structure and similar level of nitrogen content. However, it has a lower calcium content than that of PC2-700, which implies that the CO_2 uptake is not only influenced by porous structures and nitrogen content, but also by the intrinsic calcium dopant from the pine cone precursor. However, PC3-700 also has a slightly smaller ultramicropore volume than that of PC2-700 (about 4% smaller). Some earlier studies in the literature have proposed that ultramicropore (<0.7 nm) has the dominant influence on the CO_2 uptake of non-doped carbon sorbents, due to the enhanced adsorption potential in ultramicropores.[86, 91] Therefore, it is important to distinguish between the influences of microporosity and metal dopants.

Table 22: CO_2 uptakes of pine cone-derived carbon under 1 and 0.15 bar CO_2.

Sample	CO_2 uptake / wt%			
	1 bar		0.15 bar	
	0 ℃	25 ℃	0 ℃	25 ℃
PC1-700	27.4	18.4	12.5	7.2
PC2-700	34.2	20.9	12.0	6.6
PC2-700H	32.5	20.0	11.0	5.6
PC3-700	34.4	19.4	10.4	4.7
PC2-600	27.2	16.6	10.4	5.1
PC2-800	30.5	18.9	10.3	5.2

PC2-700 and PC2-700H were washed by distilled water and 1M HCl acid, respectively. Table 18 indicates PC2-700 and PC2-700H possess similar porous structures with slightly smaller ultramicropore volume (similar to that of PC3-700, also about 4% smaller). Table 20 shows that calcium is washed away by 1M HCl in PC2-700H, which leaves nitrogen as the only dopant within. It has been discussed in the literature that pyridinic and pyrrolic nitrogens are two common types of nitrogen dopants in carbon materials.[86] Pyridinic nitrogen has much higher basicity than pyrrolic nitrogen, due to the possession of a lone pair of electrons. In contrast, pyrrolic nitrogen shows alkalescence. In the author's case, a small amount of nitrogen is detected in both samples (≤1 at%) and it only exists in the pyrrolic form. PC2-700H even almost doubles the nitrogen content of PC2-700. However, Table 22 shows that PC2-700H exhibits a reduced CO_2 uptake of 20.0 wt% at 25 ℃, compared with that of PC2-700. Even under 0.15 bar, PC2-700 still shows 1 wt% higher CO_2 uptake than that of PC2-700H.

(a)

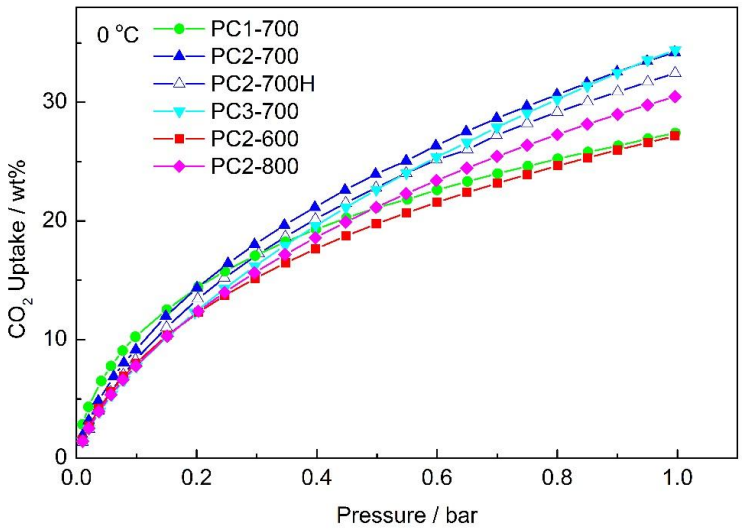

(b)

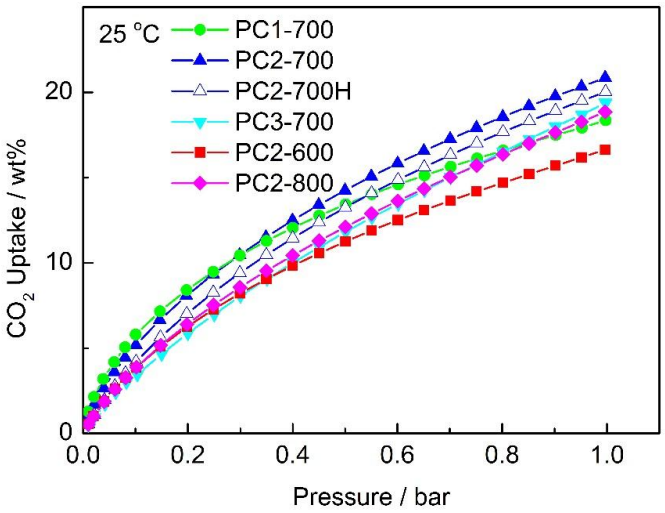

(c)

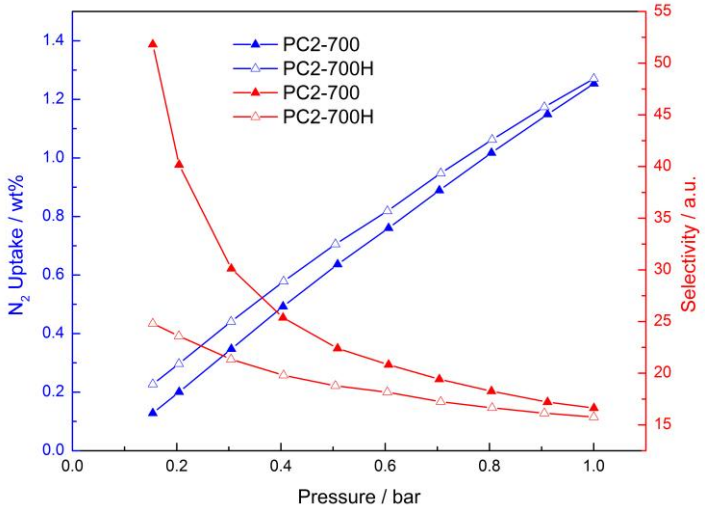

Figure 56: CO_2 adsorption isotherms of pine cone-derived carbon at (a) 25 and (b) 0 ℃ from 0.01 to 1 bar. (c) N_2 adsorption isotherms and CO_2/N_2 selectivity of PC-700 and PC2-700H at 25 ℃.

In addition to CO_2 adsorption isotherms, Figure 56c shows the N_2 adsorption isotherms of PC2-700 and PC2-700H at 25 ℃. Figure 56c is similar to Figure 48c (London Plane leaf-derived carbon), where both carbon samples have much lower uptakes of N_2 than their CO_2 uptakes. Likewise the sorption isotherm of PC2-700H is slightly higher than that of PC2-700, but the CO_2/N_2 selectivity of PC2-700 is higher than that of PC2-700H in the low pressure region. The selectivity is calculated in terms of CO_2/N_2 uptake in wt% (note selectivity can also be determined in mmol g^{-1} as well). The difference in selectivity reduces with the increasing pressure as well. Considering that LC2-700H contains a higher nitrogen content, it further demonstrates the positive influence of calcium dopant on CO_2 binding, especially in the case of low pressure CO_2 adsorption.

4.2.5 Heat of adsorption

Figure 57a shows the 3rd order polynomial fitted to the heat of adsorption (HoA) curve. The fitting process extends the lower and upper limits of CO_2 uptake to 0.1 and 8 wt%, respectively. Therefore, the extended data can be used to further analyse the heat of adsorption at both low and high CO_2 molecule coverage. PC1-700 shows the highest heats of adsorption than those of the other samples throughout the calculated CO_2 uptake range, while PC2-700 and PC2-700H stay at the bottom. This is very different from the CO_2 uptake isotherms in Figure 56 a and b, where PC2-700 is at the top. Considering PC1-700 has the least developed porous structure, its high heat of adsorption can only be attributed to the existence of nitrogen and calcium dopants. In addition, PC2-600 possesses the second highest position below that of PC1-700 in Figure 57c but the highest nitrogen content, which indicates that the nitrogen dopant is not the major contributor to the heat of adsorption.

(a)

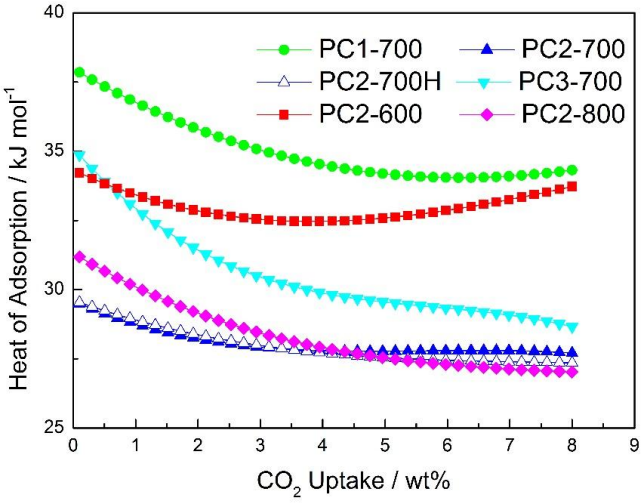

(b)

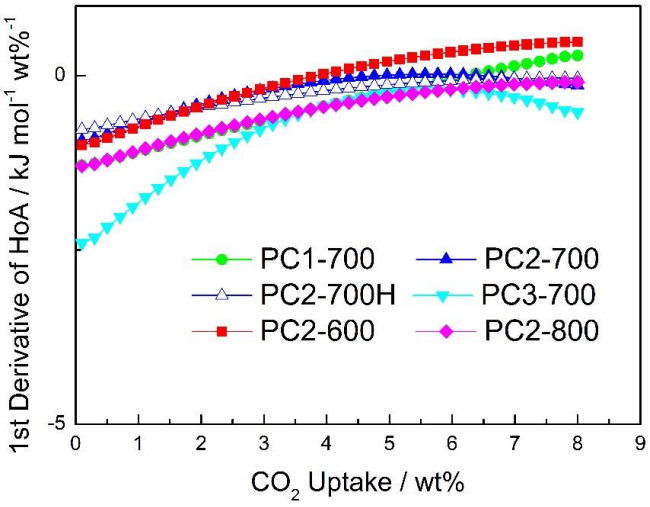

(c)

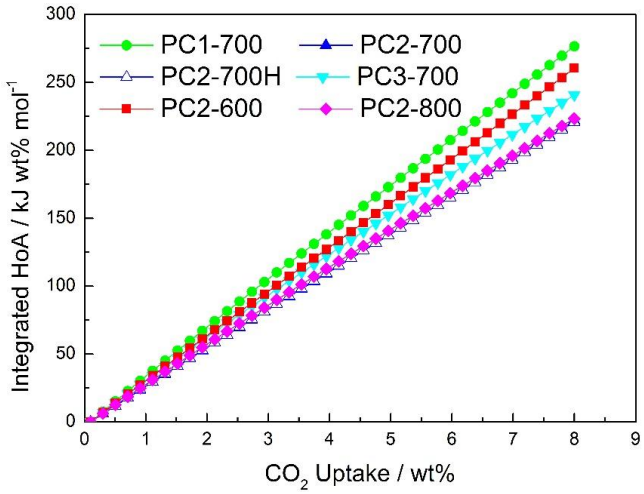

Figure 57: (a) 3rd order Polynomial fitted heat of adsorption (HoA) curves of pine cone derived carbon and its corresponding (b) 1st order derivative and (c) integrated HoA plots.

Figure 56a shows that PC2-700 exhibits an extra 0.9 wt% CO_2 uptake at 25 ℃ and 1 bar CO_2 when compared with that of PC2-700H. This reduction can be attributed to both reduced ultramicropore volume (by 4%) and the removal of metal dopants. However, PC2-700H doubles the level of nitrogen content of PC2-700, and this can partially offset the detrimental effect caused by reduced porosity and metal content. Furthermore, Table 20 shows that PC2-700 possesses a calcium content of 0.5 at%. By simple calculation, even if the "offset effect" by doubled nitrogen dopants is ignored, for every atomic percentage of calcium dopant, the CO_2 uptake can be raised by 1.8 wt%. In both studies on the naturally metal-doped carbon sorbents, XPS characterisations show that metal dopants exist in the form of +2 cations, which may enhance CO_2 capture by means of electrostatic interaction. It would appear that metal cations can be exposed to the gas environment and play the role of an active site for enhanced CO_2 binding,

4.2.6 Summary

Pine cone is an effective biomass precursor for the production of low-cost but high-capacity microporous carbon sorbents for CO_2 capture. It is rich in lignocellulosic compounds and naturally contains calcium and nitrogen elements within its cellular structures, which introduces naturally-doped calcium cations and nitrogen dopant in the resulting carbon structure. The porous structure of the carbon sorbent is mainly controlled by the KOH/carbon mass ratio and the activation temperature. The CO_2 uptake characterisation shows that the CO_2 uptake of carbon sorbent is influenced by its porous structure (especially its ultramicropore volume). However, further analysis demonstrates both nitrogen and calcium dopants also have considerable and beneficial effects on CO_2 uptakes. Activated at 700 ℃ and with a KOH/carbon mass ratio 2:1, washed by distilled water, the sample shows the highest CO_2 uptake of 20.9 wt% under 1 bar CO_2 and 25 ℃. To our knowledge, it has almost matched the highest CO_2 uptake of biomass-derived carbon sorbent presented in the literature, owing to the highly developed microporous structure and the naturally-doped nitrogen and calcium in carbon. In conclusion, the nitrogen and metal-doped pine cone-derived carbon is an excellent sorbent for CO_2 capture.

Chapter 5:

Graphite-based Carbon Precursor

5.1 Chemically activated ball-milled graphite

Graphite is less frequently reported as a precursor material to produce porous carbon sorbents for CO_2 capture when compared with polymers and biomass. This is due to its low porosity and weak affinity towards CO_2.[170] In addition, graphite has relatively higher resistance to chemical activation than those of polymeric and biomass precursors, due to its crystalline carbon structure. Therefore, instead of graphite, graphite oxide (GO) has the potential to be activated to generate porous carbon structure for CO_2 capture. Xia et al. reported a porous graphite-based carbon sorbent prepared by the activation reaction of graphite oxide with CO_2.[171] The resulting porous sorbent showed a CO_2 uptake of 7.7 wt% under 1 bar and 0 ℃. Zhao et al. reported an aminated graphite oxide for CO_2 capture. The sorbent exhibited a CO_2 adsorption capacity of 5.4 wt% at 30 ℃ in 85%N_2/15%CO_2 gas flow.[172] Other than GO-derived carbon, Meng et al. reported an ammonised graphite nanofibres, which showed a CO_2 uptake of 2.7 wt% under 1 bar and 0 ℃.[173] They also reported the synthesis of thermally exfoliated graphene nanoplates and activated graphite fibres that exhibit CO_2 adsorption capacity of 6.4 and 5.9 wt%, respectively, under 1 bar and 25 ℃.[174, 175]

In 2012, Jeon et al. reported a low cost and high yield mechanochemical method to produce graphene nanosheets by ball milling graphite powders with dry ice, following the suspension of the ball-milled graphite in N-methyl-2-pyrrolidone (NMP).[176] During the ball-milling process, the graphite powder undergoes a mechanochemical reaction with dry ice (CO_2), and CO_2 is grafted onto the edge of the ball-milled graphite, forming carboxylate groups. It is arguably that this author tries to relate the ball-milling of graphite in dry ice (CO_2) to the concept of CO_2 capture. In practice, it is difficult to carry out CO_2 capture by ball milling, considering that CO_2 capture usually takes place in a gaseous environment rather than dry ice. However, ball milling may be a simple and effective way to produce porous carbon sorbents from graphite powder. The ball-milling method can be tailored and simplified to meet the need for the production of porous carbon sorbents for CO_2 capture. Therefore, this section reports an experimental approach to produce porous carbon sorbents by ball milling for CO_2 capture.

5.1.1 Surface oxygen-containing functional groups

Figure 58: Sparking of ball-milled sample when opening the milling vial, indicating that the milled carbon is enriched with fresh dangling bonds of carbon, which are rapidly oxidised upon exposure to oxygen (air).

When the stainless steel vial is opened after 12 hours of ball milling, violent sparkling occurs (Figure 58), which is consistent with the phenomenon observed in Jeon et al.'s work.[176] According to their study, this is due to a hydration reaction that takes place at the edge of the ball-milled graphite. The ball milling is a mechanochemical process that triggers the reaction between CO_2 and ball-milled graphite, grafting carboxylate groups onto the edge of broken graphite structure. When these carboxylate groups are exposed to atmospheric moisture, violent exothermic hydration reactions transform the carboxylate group into the carboxylic acid groups. Simultaneously, both atmospheric oxygen and moisture also react with the carbon surface, generating hydroxyl (-OH) groups. This contributes to additional thermal release. With considerable thermal energy released in a short period, this burns off some carbon, which displays as sparks. This sparking phenomenon can be recognised as an indicator of surface hydration reaction, as the exposure of ball-milled graphite in an inert gas atmosphere does not exhibit any spark. To clarify the role of dry ice in the mechanochemical reaction, another group of graphite powders was ball milled without dry ice. The resulting ball-milled sample did not spark when opened in air.

Table 23: Elemental compositions of ball-milled graphite samples.

Sample	Chemical composition / at%	
	C	**O**
Graphite	97.3	2.7
BG-12hCO_2	84.4	15.6
ABG-12hAir	90.4	9.6
ABG-12hCO_2	93.1	6.9

XPS was used to analyse the chemical compositions and surface functional groups of both ball-milled and chemically activated ball-milled graphite samples. The corresponding characterisation results are summarised in Table 23. Pristine graphite shows 97.3 at% carbon and 2.7 at% oxygen contents. Oxygen may come from the residual water left on the graphite powder and a small amount of pre-existing oxygen-containing surface functional groups. All the other samples exhibit reduced carbon but increased oxygen content. After ball milling with dry ice for 12 hours, the oxygen content is raised 6 times in BG-12hCO_2 (15.6 at%). The sample ball-milled without dry ice (BG-12hAir) clearly shows a lower oxygen content of 9.6 at%. In this case, oxygen is mainly originated from atmospheric oxygen, moisture and carbon dioxide in the milling vial. The majority of oxygen is removed during the high temperature chemical activation process. Overall, it results in a reduced oxygen content of 6.9 at% in ABG-12hCO_2.

High resolution XPS scans were performed to analyse the oxygen-containing functional groups. Figure 59 shows high resolution spectra of C-1s and O-1s peaks of graphite, BG-12hCO_2 and BG-12hAir. All C-1s peaks can be divided into three sub-peaks that correspond to C-C, C-OH and O=C-OH groups, while all O-1s peaks can be divided into two sub-peaks that correspond to C-OH and O=C-OH groups. The pristine graphite shows a strong sub-peak at 284.5 eV. This sub-peak is associated with the C-C in the graphitic structure, while the other two peaks are associated with C-OH (285.4 eV) and O=C-OH (288.6 eV). The C-OH and O=C-OH peaks show much lower

intensity than that of C-C (Figure 59a). This is to be compared with the C-1s spectrum of BG-12hCO_2, where the C-OH and O=C-OH show much higher intensities (Figure 59c), especially the apparent increase in O=C-OH peak intensity. As with the C-1s spectra, the high resolution O-1s spectra show the pristine graphite has two very weak sub-peaks associated with C-OH (533.4 eV) and O=C-OH (532.0 eV) (Figure 59b). These two peaks become much stronger in the O-1s spectrum of BG-12hCO_2 (Figure 59d). The same analysis can be applied to compare the O-1s spectra of BG-12hCO_2 and BG-12hAir. In the absence of dry ice during the ball-milling process, BG-12hAir shows weaker sub-peaks of C-OH and O=C-OH in both C-1s (Figure 59e) and O-1s (Figure 59f) spectra, compared with those of BG-12hCO_2. In conclusion, XPS analysis reveals that C-OH and O=C-OH are the two major oxygen-containing functional groups at the sample surface after the ball-milling process. The presence of dry ice in the ball-milling process helps to enrich these surface oxygen-containing functional groups.[176, 177]

(a)

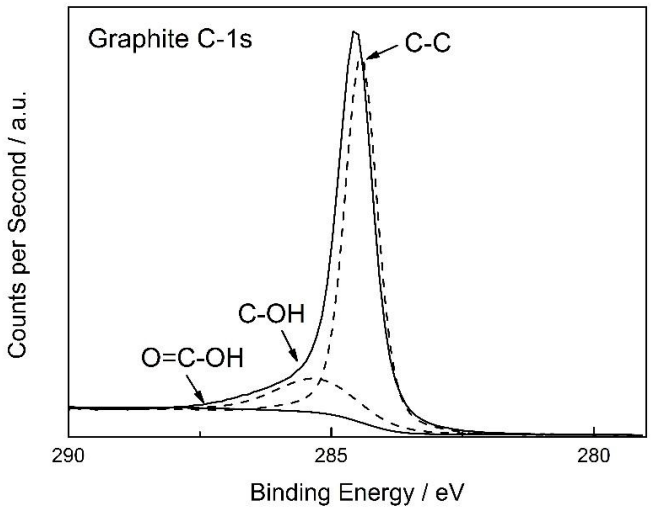

(b)

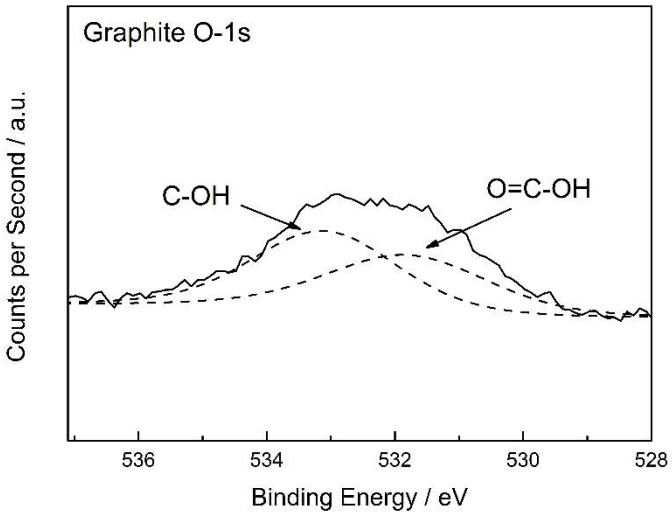

(c)

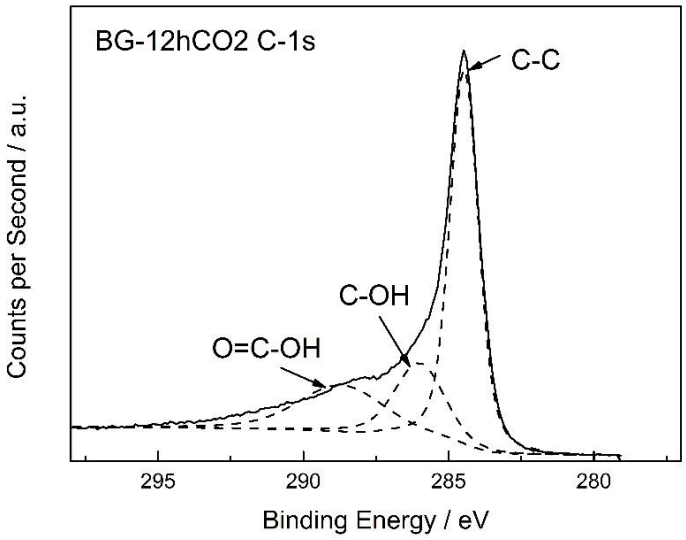
BG-12hCO2 C-1s
C-C
C-OH
O=C-OH
Counts per Second / a.u.
295
290
285
280
Binding Energy / eV

(d)

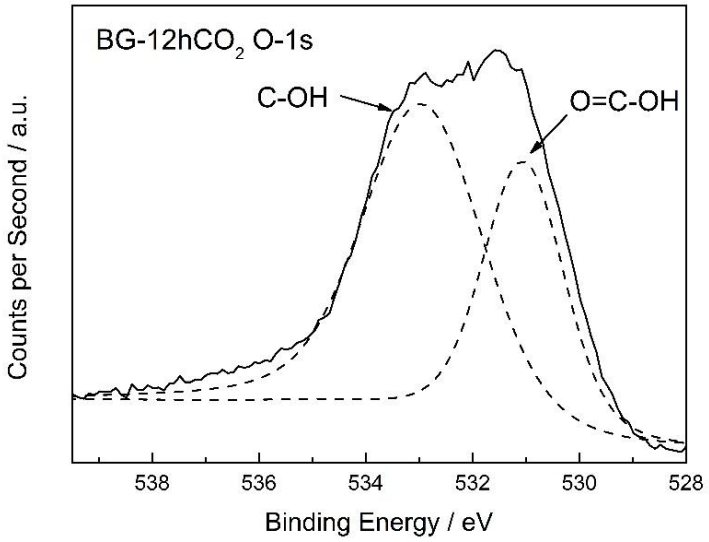
BG-12hCO2 O-1s
C-OH
O=C-OH
Counts per Second / a.u.
538
536
534
532
530
528
Binding Energy / eV

(e)

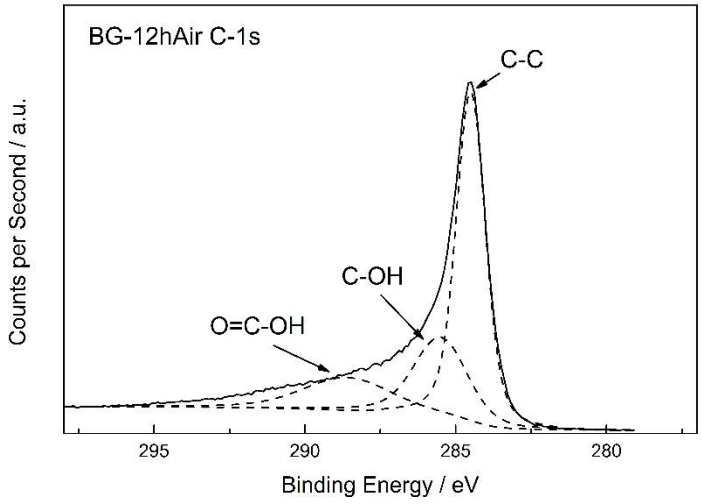
BG-12hAir C-1s
C-C
C-OH
O=C-OH
Counts per Second / a.u.
295
290
285
280
Binding Energy / eV

(f)

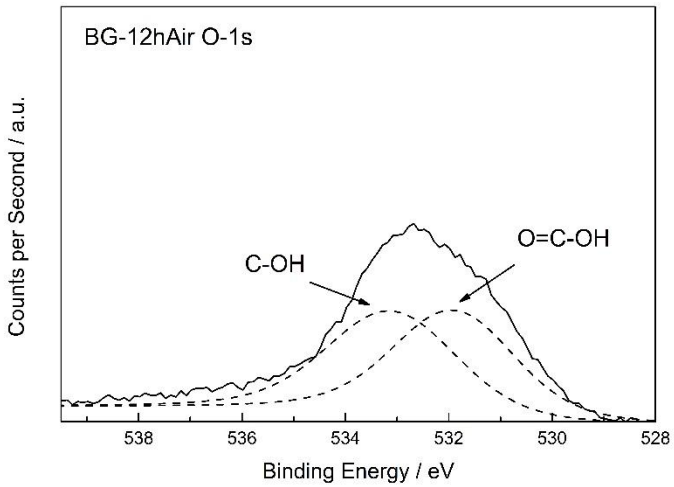

Figure 59: High resolution XPS spectra with detailed C-1s scan of (a) Graphite, (c) BG-12hCO_2, (e) BG-12hAir and O-1s scan of (b) Graphite, (d) BG-12hCO_2, (f) BG-12hAir.

5.1.2 Development of porous structure

SEM images in Figure 60 reveal the morphology transformation from pristine graphite to porous carbon. Figure 60a shows pristine graphite has a smooth surface with no apparent porous structure. Its particle size ranges from 20 to 30 μm. After ball milling for 12 hours, Figure 60b indicates that the majority of the particles are greatly reduced to less than 10 μm in diameter. Although there are still large particles, the majority have been broken down. After the chemical activation at 800 ℃, the sample ABG-12hCO_2 exhibits a notable macroporous structure (Figure 60c). Figure 60d is the high resolution TEM image of ball-milled graphite after chemical activation. It shows pristine graphite has completely lost its crystalline structure after ball-milling and chemical activation. This is further confirmed by the following XRD and Raman analysis.

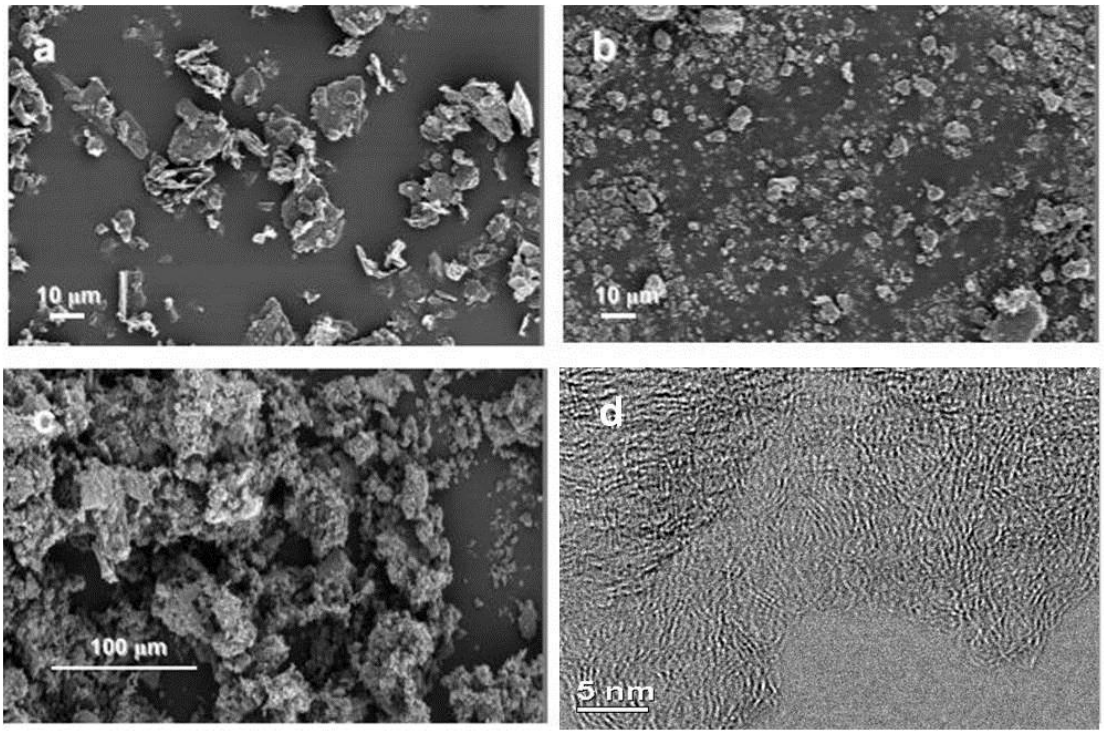

Figure 60: The SEM images of (a) the pristine graphite powders; (b) the graphite powder after ball milled for 12 hours (BG-12hCO_2); (c) the ball-milled sample after chemical activation (ABG-12hCO_2); (d) High resolution TEM image of ball-milled graphite after chemical activation.

(a)

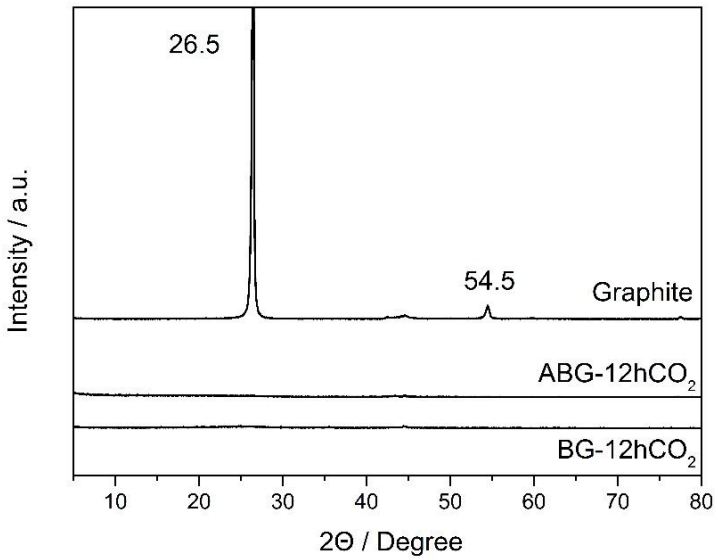

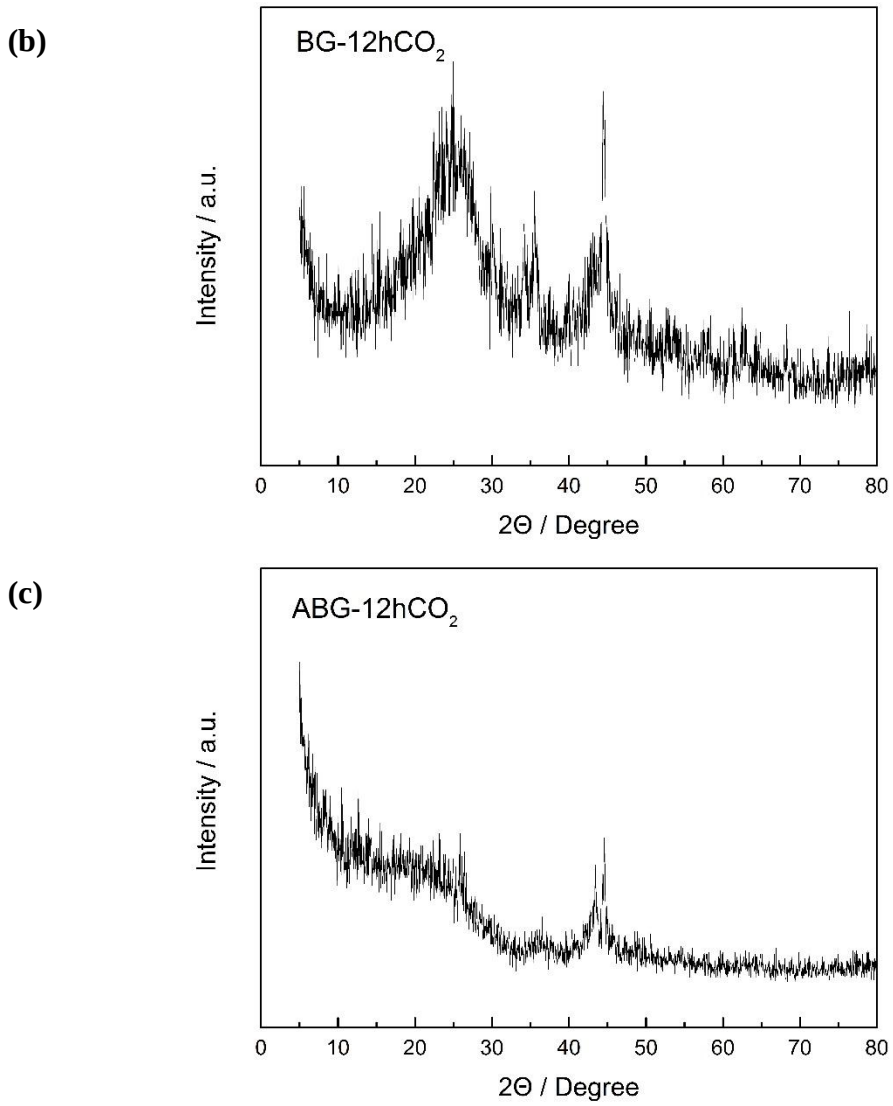

Figure 61: XRD patterns of ball-milled graphite samples (a) pristine graphite, (b) BG-12hCO_2 and (c) ABG-12hCO_2.

The characterisation results from X-ray diffraction (Figure 61) and Raman spectroscopy (Figure 62) are consistent with both SEM and TEM observation. The XRD pattern of pristine graphite exhibits a strong peak at 26.5 °, which corresponds to the graphite (002) plane diffraction.[178] This diffraction peak is completely smoothed out in the BG-12hCO_2 and ABG-12hCO_2 XRD patterns. Zooming into the range between 10 ° and 30 °, weaker and broader diffraction peaks can be found in the XRD pattern of BG-12hCO_2 (Figure 61b), because of the structural distortion caused by the ball-milling process. This may also hint at the existence of small graphitic carbon fragments with an ordered structure. However, this weak peak completely disappears in the XRD pattern of ABG-12hCO_2 (Figure 61b) due to chemical activation.

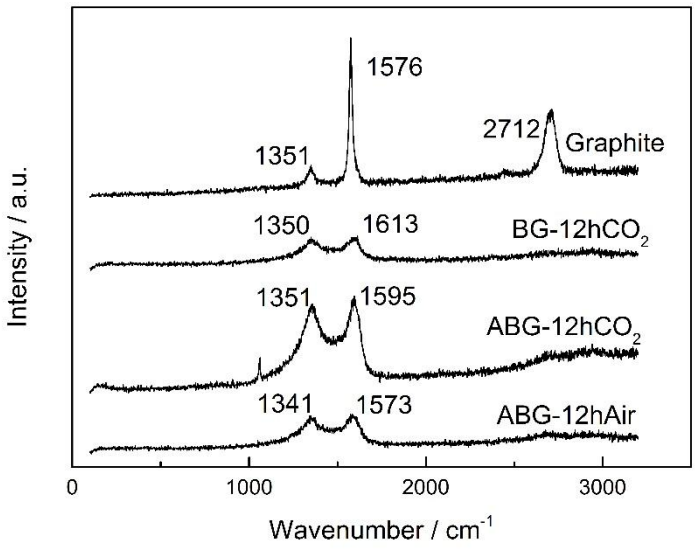

Figure 62: Raman spectra of ball-milled samples.

Raman spectroscopy analysis shows the pristine graphite powder has three primary peaks with a weak primary D band at 1351 cm^{-1}, a strong G band at 1576 cm^{-1} and a secondary D band at 2712 cm^{-1}. The low intensity ratio of D to G band (I_D/I_G = 0.19 in this case) indicates pristine graphite powder has large particle size. This value is increased from 0.19 to 1.55 after the 12 hours ball-milling. Meanwhile, the secondary D band disappears from the spectrum. This indicates the reduction of particle size and the increase of structural disorder, which is consistent with the SEM images and the XRD result. After chemical activation, the I_G/I_D ratio is increased to 2.06, indicating a further reduction in particle size. For comparison, the sample ABG-12hAir, which was prepared in the absence of dry ice, had a lower I_D/I_G ratio of 1.69, suggesting a larger particle size, compared with that of ABG-12hCO_2.

5.1.3 Porosity characterisation

The porosity characteristics of carbon samples were determined by the N_2 adsorption and desorption isotherms at -196 ℃, which are shown in Figure 63. The adsorption isotherms of these samples quickly reach plateaus at about P/P_o=0.2, which indicates the existence of micropores. At the relative pressure range between 0.2 and 0.8, the quantity of adsorbed N_2 increases at a relatively slow rate, but the isotherms rise very quickly at the region beyond 0.8. These are correlated with the end of micropore filling and the start of mesopores and macropores filling.

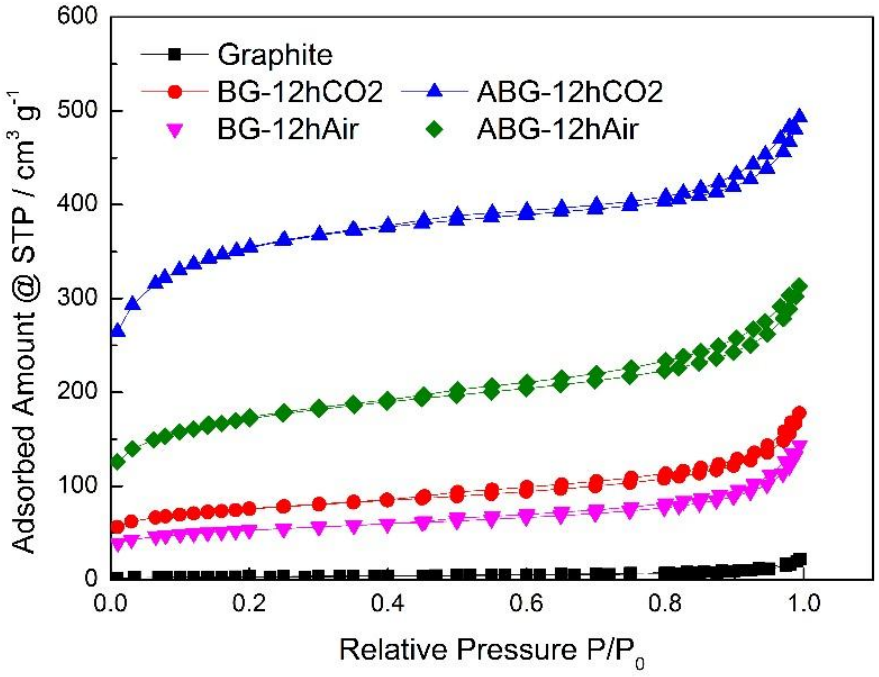

Figure 63: N_2 adsorption isotherm of ball-milled samples.

Four major characteristic parameters were calculated from the isotherms and they are summarised in Table 24. Pristine graphite powder shows a very low specific surface area, total pore volume and micropore volume, compared with those of the other samples. After 12 hours ball-milling with dry ice, the sample started to show a notable development of porous structure. The specific surface area has increased 20 times and total pore volume 8 times. Besides the significant increase in specific surface area and total pore volume, it is important to note that the pristine graphite shows little micropore volume, while the micropores appear in the ball-milled sample. As discussed previously, the large and crystalline graphite powder is broken down into small and disorder fragments, which increases the opportunity for these fragments to create interspacing between them. The major advance in the development porous structure is the chemical activation step, where the specific surface area is about 4 times greater than that of the ball-milled sample BG-12hCO_2.

Table 24: Porosities of ball-milled graphite samples.

Sample	$S_{BET}/m^2\ g^{-1}$	$V_{Total}/cm^3\ g^{-1}$	$V_{Micro}/cm^3\ g^{-1}$
Graphite	10	0.03	0
BG-12hCO2	250	0.28	0.06
ABG-12hCO2	1170	0.76	0.32
BG-12hAir	180	0.22	0.04
ABG-12hAir	580	0.49	0.13

a. The specific surface area is calculated by the BET equation;

b. The total pore volume is calculated with the quantity of N_2 adsorbed at P/Po = 0.99; and

c. The micropore volume is calculated by the t-plot method.

In addition, the pristine graphite sample ball-milled without dry ice (BG-12hAir) exhibits a smaller specific surface area of 180 $m^2\ g^{-1}$, compared with that of BG-12hCO2. A larger initial surface area benefits the following chemical activation step in terms of providing a larger contact area for mixing KOH and carbon. This is clearly shown in the BET result of ABG-12hAir. The absence of dry ice in the ball milling process results in reduced surface area and other porosity parameters. In consideration of elemental analysis in the previous section, the sample with richer surface oxygen functional groups (ABG-12hCO2) has larger specific surface area and pore volume than the sample with less (ABG-12hAir). This suggests oxygen functional groups may help to prevent particle agglomeration during ball milling process. It is interesting to note that the total pore volume of BG-12hAir is 21% lower than that of BG-12hCO_2. However, the total pore volume of ABG-12hAir is 37% less than that of ABG-12hCO2. This shows that the initial porous structure influences the resulting porous structure development by chemical activation.

5.1.4 CO_2 adsorption

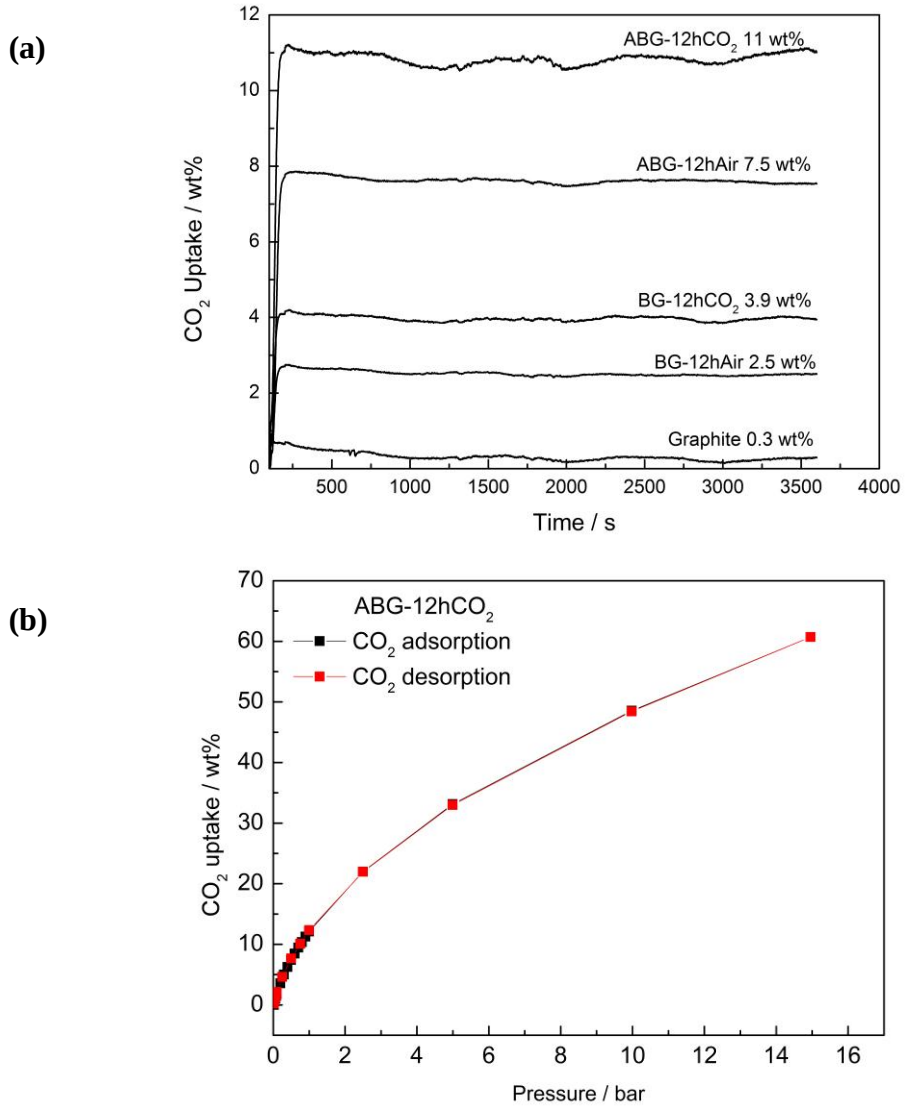

Figure 64: CO_2 adsorption capacities and kinetics of (a) samples ball-milled with and without dry ice; (b) the high pressure CO_2 adsorption up to 15 bar.

The CO_2 adsorption capacities and kinetics are measured at 25 ℃ and in a pure CO_2 flow by TGA. The corresponding results are presented in Figure 64a, and they are consistent with porosity parameters in Table 24. The pristine graphite has almost no CO_2 adsorption capacity (0.3 wt%), considering its extremely low specific surface area (10 m^2 g^{-1}) with its non-porous structure. After ball milling for 12 hours, the sample BG-12hCO2 starts to exhibit the capability to adsorb CO_2 (3.9 wt%) due to the increase in specific surface area (250 m^2 g^{-1}) and pore volume (0.20 cm^3 g^{-1}) by means of physical cracking and amorphous carbon transformation. The activated sample ABG-12hCO_2 shows a much higher CO_2 adsorption capacity of 11.0 wt%, owing to the

significant increase in specific surface area and pore volume, especially the micropore volume. All samples ball-milled without dry ice have less CO_2 uptake than that of samples prepared with dry ice. This is consistent with the results of porosity analysis. Furthermore, the total pore volume of ABG-12hAir is 36% lower than that of ABG-12hCO_2. However, its micropore volume is 60% lower. Considering its CO_2 uptake is 4.5 wt% less than that of ABG-12hCO_2, this shows the significance of the micropore development for CO_2 adsorption. Besides the CO_2 uptake, all materials show quick CO_2 adsorption kinetics, where the maximum uptake is reached in about 100 seconds. The high pressure CO_2 adsorption test was performed by IGA and the corresponding isotherm was plotted in Figure 64c. The result of CO_2 uptake under 1 bar CO_2 and 25 ℃ is consistent with the result of the TGA test. It also shows the sample's CO_2 uptake can reach 60.7 wt% at 15 bar. Therefore, there is about 50 wt% uptake difference between 1 and 15 bar CO_2 adsorption. This indicates a relatively good work capacity of the sorbent in the case of pressure swing operation for CO_2 capture.

5.1.5 Summary

In summary, this section demonstrates a ball-milling method to produce porous carbon from pristine graphite. This method involves ball milling of graphite powder with dry ice to break large crystalline graphite powders into smaller carbon fragments. Ball-milling also introduces rich oxygen-containing functional groups, which help to avoid the agglomeration of carbon particles during the milling process. It also provides the ball-milled sample with an initial porous structure for the following chemical activation with KOH. KOH is used as the activating agent to further reduce the size of the carbon fragments and to disorder the carbon structure, creating pores in the form of interparticulate spacing. At 25 ℃, the sample ABG-12hCO_2 shows a CO_2 uptake of 11.0 wt% and 60.7 wt% under 1 and 15 bar CO_2, respectively. Sample characterisation reveals that the increase in CO_2 uptake is mainly due to improved porous structure by both ball-milling and chemical activation. This section has demonstrated the ball-milling method as a new approach to the production of porous carbon sorbents for CO_2 capture from graphitic carbon precursors.

5.2 Chemical activation of graphite oxide

Graphite oxide (GO) is obtained by subjecting graphite to strong oxidising agents. The oxidised graphite loses its regular structure but still keeps its carbon layer structure. The oxidising process also introduces oxygen-containing functional groups to both the edge and basal plane of graphite, including hydroxyl, carboxylate and epoxy groups.[179, 180] Chemical activation has been applied to graphite oxides to produce activated GO with a high surface area porous structure. Activated GO has frequently been studied for its electrical properties, such as its conductivity and capacitance.[181-183] However, little research has been reported on its application to CO_2 capture. An activated and exfoliated graphite oxide has been reported to have a specific surface area of 3100 m^2 g^{-1}.[181] Therefore, it may possess potential capacity for CO_2 adsorption. In addition, GO consists of only carbon, oxygen and hydrogen, which eliminates the influence of chemical dopants on CO_2 capture in the resulting activated GO. Therefore, the characterisation results of activated GO can be compared with those of polymer- and biomass-derived carbon sorbents. This can help to distinguish the infuence of porous structure and chemical dopants on CO_2 capture.

5.2.1 Morphology of activated GO

The SEM and TEM images in Figure 65 show the morphology and structural transformation from the untreated to activated GO. Figure 65a shows the untreated GO has a smooth surface with random shapes and sizes. Figure 65b shows the morphology of the sample (AGO0-800) carbonised at 800 ℃ without KOH activation. The carbonised sample exhibits a rough surface and the sample consists of large agglomerations rather than individual particles. However, no apparent porous structure is observed. Figure 65c shows the morphology of the sample activated at 800 ℃ and with a KOH/GO weight ratio of 4:1. Macropores of micrometre sizes are clearly observed in the image.

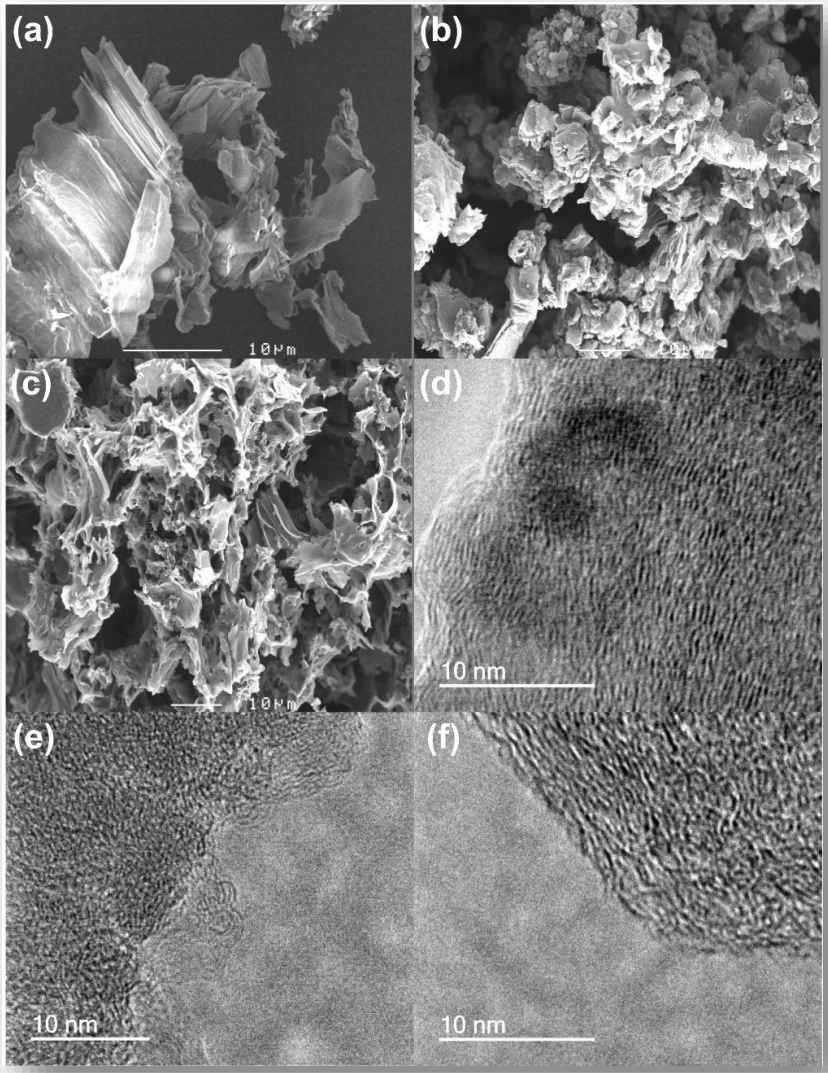

Figure 65: SEM images of (a) graphite oxide, (b) AGO0-800 and (c) AGO4-800 and the corresponding high resolution TEM images of (d) AGO0-800, (e) AGO4-800 and (f) AGO6-800, respectively.

In addition to the SEM images, TEM images reveal an interesting change of GO structure before and after chemical activation. Figure 65d is the TEM image of AGO0-800. Although the image shows a non-crystalline structure, relatively well-aligned dark and bright strips can be observed locally, indicating localised graphitic structure exists at the nanoscale. These localised graphitic platelets disappear in Figure 65e when the sample is activated by KOH with the KOH/GO weight ratio of 4:1. Chemical activation further reduces the size of these graphitic platelets by the reaction between KOH and carbon. This increases the number of possible ways to arrange these platelets, i.e.

increases the structural irregularity. Figure 65f is the TEM image of the sample activated with a higher KOH/GO weight ratio of 6:1. The localised graphitic structure is re-observed in the TEM image. This may be caused by more aggressive chemical activation due to the use of a greater quantity of KOH. The reaction removes parts of the sample that are susceptible to KOH activation, most likely to be the amorphous phase. As a result, it leaves more graphitic parts, which are more resistant to KOH activation.

5.2.2 Porosities of activated GO

The specific surface area and pore size distribution of graphite oxides are summarised in Table 25. Their corresponding N_2 sorption isotherms, pore size distribution and micropore size distribution are plotted in Figure 66.

Table 25: Porosities of activated graphite oxides.

Method	**N_2 sorption**				**CO_2 sorption**
Sample	**S_{N2} /m^2 g^{-1}**	**S_{Micro} /m^2 g^{-1}**	**V_{N2}/cm^3 g^{-1}**	**V_{Micro} /cm^3 g^{-1}**	**V_{CO2}/cm^3 g^{-1}**
AGO0-800	100	0	0.26	0	0.03
AGO2-800	490	260	0.60	0.11	0.12
AGO4-800	1380	620	1.14	0.31	0.13
AGO6-800H	200	40	0.32	0.03	0.06
AGO4-700	1060	500	0.91	0.26	0.11
AGO4-900H	660	160	0.79	0.11	0.09

Figure 66a shows activated GOs have different N_2 uptakes and thus different levels of porosity. All sample isotherms show hysteresis between adsorption and desorption curves, which indicates mesopores exist in the activated GOs. This is reflected in Figure 66b where higher peaks are observed in the region of pore size larger than 2 nm. From the bottom to the top, Figure 66a also shows the shapes of the isotherms gradually change from Type III-like to Type I-like isotherms, indicating different levels of micropore development under different activation conditions.

(a)

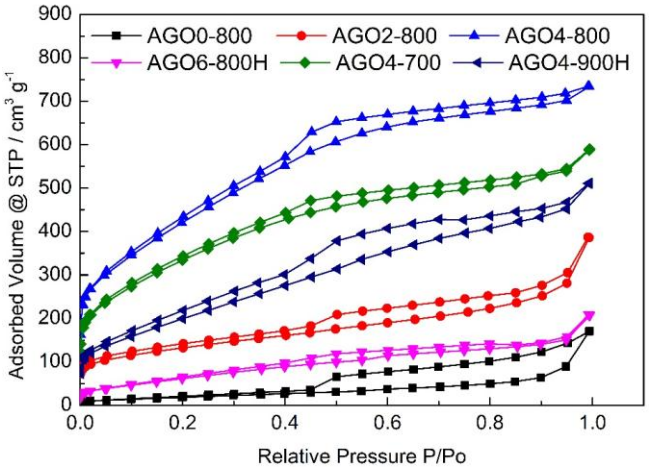

(b)

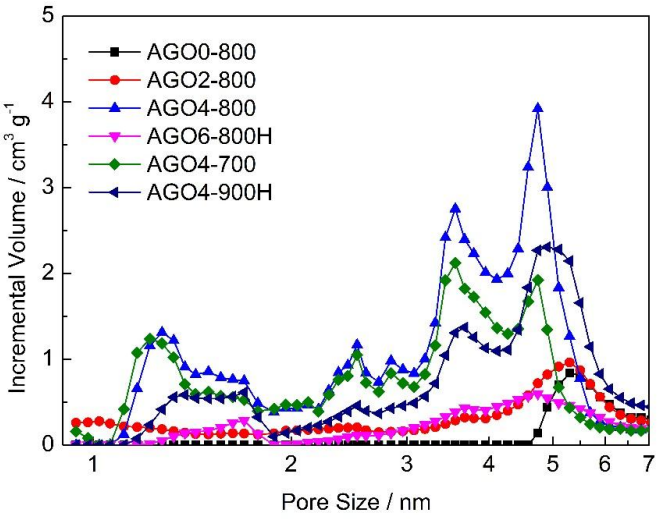

(c)

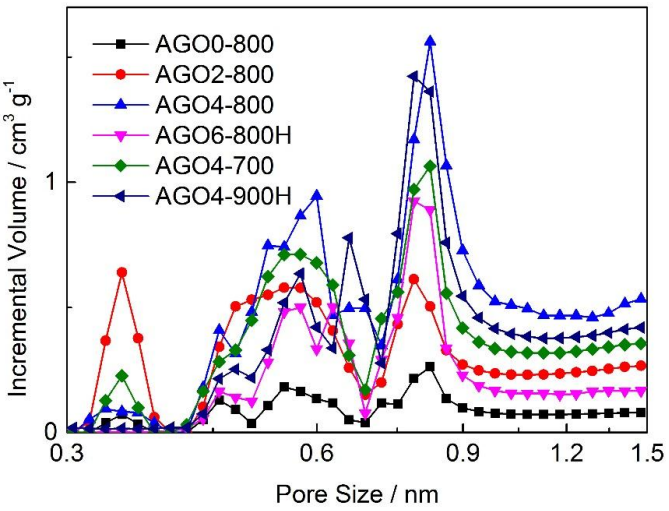

Figure 66: (a) N_2 sorption isotherms at -196 ℃, (b) pore size distribution and (c) micropore size distribution of activated graphite oxides (dV/dlogd, d is pore size).

The quantified porosities in Table 25 are derived from the N_2 sorption isotherms in Figure 66a. In the table, AGO0-800 exhibits little development in porous structure,

which indicates the carbonisation process does not have a major influence on the pore development. The specific surface area, total pore volume and micropore volume increase when the KOH/GO weight ratio increases from 0:1 to 4:1 or the activation temperature from 700 to 800 ℃. However, when the ratio and the temperature are increased to 6:1 and 900 ℃, there is a sudden drop in porosities. This is consistent with the observation in the TEM images in Figure 65. A higher KOH/GO ratio or activation temperature results in a more aggressive chemical activation reaction. The reaction leaves larger graphitic platelets that are more resistant to KOH activation. As a result, there are fewer ways for those platelets to arrange themselves and to create pores between them. In addition, Table 25 also shows activated GO samples have different levels of ultramicropore development (<0.7 nm). Different from the other porosity parameters, AGO4-800 shows the highest ultramicropore volume of 0.13 cm^3 g^{-1}. AGO2-800 and AGO4-700 also exhibit similar ultramicropore volumes of 0.12 and 0.11 cm^3 g^{-1}. However, the ultramicropore volume is greatly reduced when a higher KOH/GO ratio or activation temperature is applied, that is, 0.06 cm^3 g^{-1} for AGO6-800H and 0.09 cm^3 g^{-1} for AGO4-900H.

5.2.3 Chemical composition of activated GO

The surface chemistry of activated GO samples is characterised by XPS and the corresponding chemical compositions are summarised in Table 26. The high resolution C-1s XPS spectra of GO, carbonised and activated GO are shown in Figure 67.

Table 26 shows that carbon and oxygen are the two major elements detected by XPS in both untreated and activated GO samples. There is also a small amount of sulphur detected at the surface of all the samples. The residual sulphur is possibly due to the use of concentrated sulphuric acid as the oxidising agent during GO synthesis. AGO6-800H and AGO4-900H are the two samples washed by 1M HCl in addition to the distilled-water washing, due to the existence of aluminium caused by the etching of crucibles. The characterisation result shows residual aluminium is removed by the acid washing.

Table 26: Chemical composition of activated graphite oxides.

Sample	Chemical composition / at%		
	C	**O**	**S**
GO	66.3	32.4	1.3
AGO0-800	93.9	5.7	0.4
AGO2-800	87.9	12.1	0
AGO4-800	93.9	5.9	0.2
AGO6-800H	91.9	8.0	0.1
AGO4-700	92.1	7.0	0.9
AGO4-900H	91.4	6.4	2.2

(a)

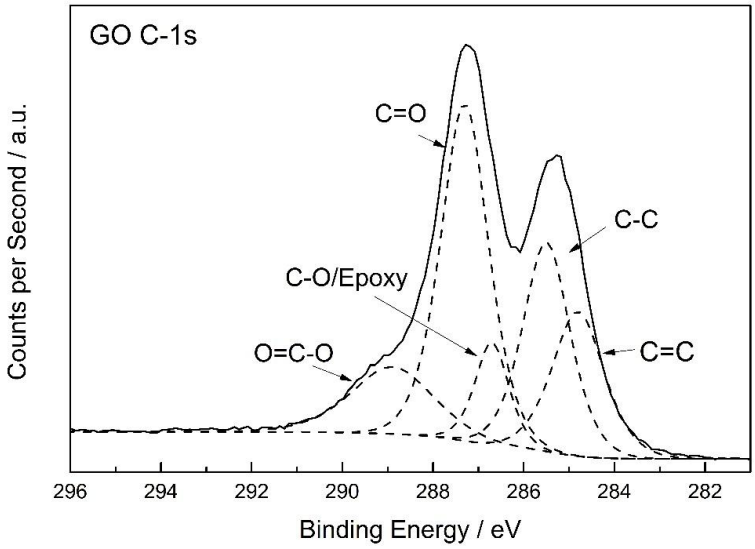

(b)

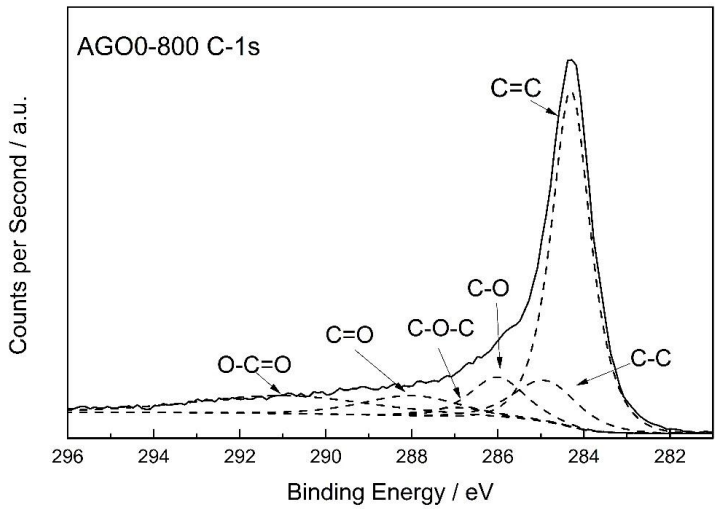

(c)

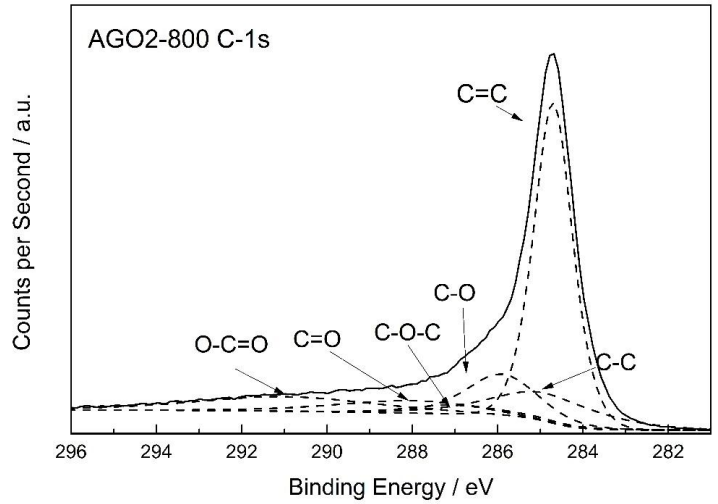

Figure 67: XPS high resolution C-1s spectra of (a) original GO, (b) AGO0-800 and AGO2-800.

In addition, Table 26 shows the oxygen content of the untreated GO is greatly reduced after chemical activation. Figure 67a, b and c are the XPS high resolution C-1s spectra of GO, AGO0-800 and AGO2-800, respectively. Figure 67a shows the C-1s spectrum of GO can be deconvoluted into five peaks, which can be attributed to the binding energies of C=C (284.7 eV), C-C (285.5 eV), C-O (286.7 eV, both hydroxyl and epoxy), C=O (287.3 eV) and O=C-O (289.0 eV).[184] After carbonisation, Figure 67b shows that AGO0-800 possesses the same surface oxygen functional groups. However, the number of sp^2 carbon (C=C) is greatly increased, while the other are significantly reduced. This indicates that most oxygen functional groups are not stable at this high temperature. It is noticed in Figure 67b that a small amount of epoxy groups (287.0 eV)[185] still exist in AGO0-800 even after carbonisation. However, these epoxy

groups are almost wiped out after chemical activation by KOH (Figure 67c). Furthermore, the intensities of C=O and C-C peaks are also reduced. It is very likely due to the removal of carbon atoms by chemical activation and those sites are more susceptible to KOH attack.

5.2.4 CO_2 adsorption on activated GO

Table 27: CO_2 uptakes of activated graphite oxides under 1 and 0.15 bar.

Sample	CO_2 uptake / wt%			
	1 bar		0.15 bar	
	0 ℃	25 ℃	0 ℃	25 ℃
AGO0-800	3.0	1.3	0.8	0.02
AGO2-800	12.9	7.8	4.9	2.9
AGO4-800	15.9	7.1	3.3	1.5
AGO6-800H	8.1	3.0	1.3	0.4
AGO4-700	13.5	7.1	3.4	1.6
AGO4-900H	12.7	5.9	2.0	0.8

The CO_2 sorption isotherms of activated GO at 0 and 25 ℃ are plotted in Figure 68. The corresponding CO_2 uptakes at 1 bar CO_2 are summarised in Table 27. All activated GO samples show relatively lower CO_2 sorption capacities, compared with those of polymer- and biomass-derived carbon sorbents. The lower CO_2 uptake can be attributed to smaller ultramicropore volumes and the absence of chemical dopants.

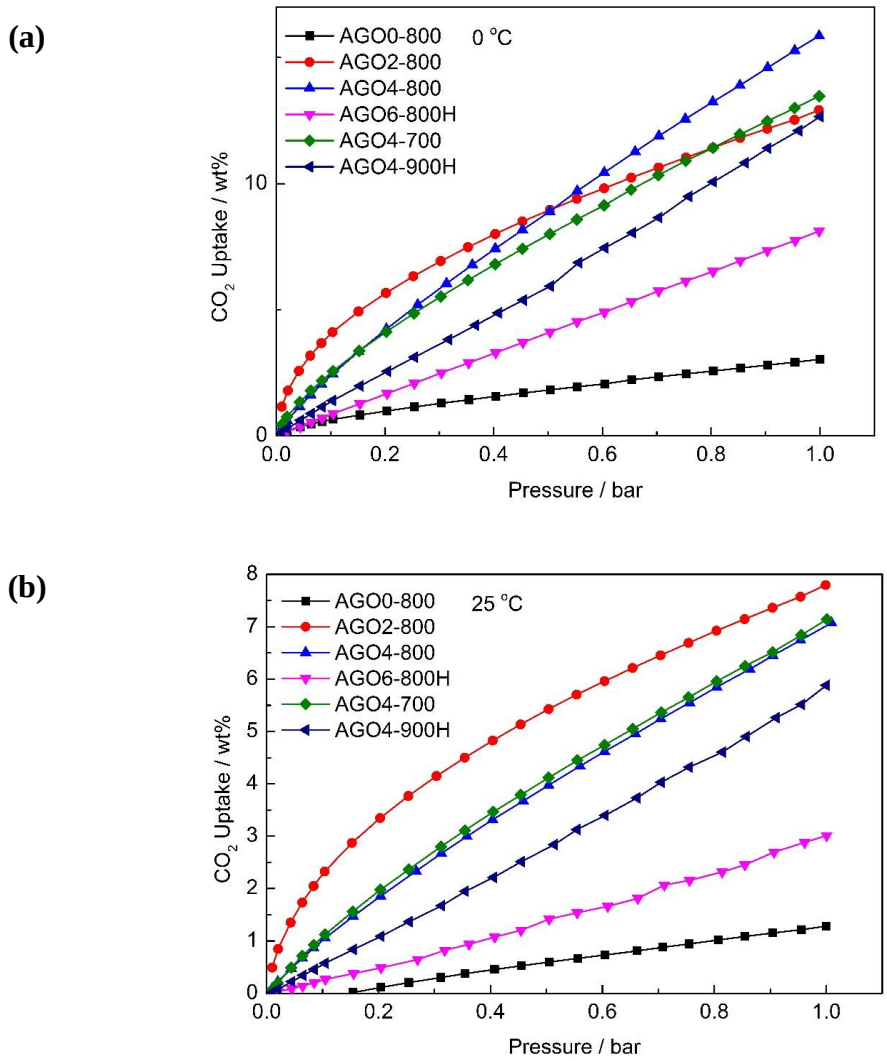

Figure 68: CO_2 sorption isotherms of activated graphite oxides at (a) 0 ℃ and (b) 25 ℃.

Table 27 shows that AGO2-800, AGO4-800 and AGO4-700 exhibit similar CO_2 uptakes of 7.8, 7.1 and 7.1 wt% under 1 bar CO_2 and at 25 ℃. This is due to the similar levels of ultramicropore development in these samples. Figure 68b shows the 25 ℃ isotherm of AGO2-800 is higher than all the other sample isotherms. However, Figure 68a shows the 0 ℃ isotherm of AGO2-800 is only higher than those of the other below 0.5 bar. Above 0.5 bar, the isotherm of AGO2-800 is below that of AGO4-800 (also below both AGO4-800 and AGO4-700 above 0.8 bar). In Figure 66c, AGO2-800 shows more ultramicropores distributed in the pore size region less than 0.5 nm. Therefore, the higher CO_2 uptake of AGO2-800 below 0.5 bar at 0 ℃ may be attributed to the larger ultramicropore volume of pore size less than 0.5 nm, rather than those with less than 0.7 and 2 nm. The higher CO_2 uptake of AGO2-800 at 25 ℃ suggests that

those ultramicopores can also help to enhance CO_2 binding on the sorbents at relatively higher adsorption temperatures

5.2.5 Summary

In this work, graphite oxide is used as the precursor material and KOH is applied as the activating agent to produce activated graphite oxides. The activated GO samples require higher KOH/GO weight ratios and activation temepratures to achieve comparable porosities of carbon sorbents derived from polymer and biomass. However, even with similar specific surface area and pore volume, activated GO samples possess only smaller ultramicropore volumes, compared with those of polymer- and biomass-derived carbon sorbents. As a result, all activated GO samples show much lower CO_2 uptakes. Without chemical dopants, the CO_2 uptake of the activated GO is only influenced by its porous structure. The characterisation result shows the sample with a higher ultramicropore volume exihibits a higher CO_2 uptake. However, further analysis shows that ultramicropores less than 0.5 nm may help to enhance CO_2 adsorption on carbon sorbents at low pressures and high adsorption temperatures.

Chapter 6:

General Discussion and Conclusions

6.1 General Discussion

6.1.1 Comparison of the precursor materials

Three types of precursor material were used in this doctoral research: polymeric, biomass and graphitic materials. These show significant influence on both the choice of sample preparation process and the properties of resulting carbon sorbents.

Generally speaking, on the one hand, polymeric and graphitic precursors have known chemical structures and usually comprise simple chemical components. Their chemical structures and compositions can be tailored to meet specific applications. For example, in the author's work on carbon spheres, acrylonitrile is selected as one of the monomers because it is a nitrogenous chemical and the insolubility of polyacrylonitrile in water. Therefore, the above characteristics of acrylonitrile can be used for producing nitrogen-containing polymer spheres in the water bath through the "solvent exchange" process. Acrylamide is selected as the other monomer because it possesses a higher molecular weight than that of acrylonitrile and it is also a nitrogen-containing chemical. Therefore, the average molecular weight of the copolymer can be increased without compromising the nitrogen content in the resulting polymer sphere. On the other hand, biomass precursors can be directly carbonised and activated to produce porous carbon and thus this avoids the complicated preparation of precursor materials. However, biomass precursors are usually rich in all kinds of chemical compounds and different biomass precursors may have different biological structures and chemical compositions. Therefore, the porosities and chemistry of the so-derived carbon sorbents may vary as well.

More specifically, on the aspect of the sample preparation, polymeric, biomass and graphitic precursors show different levels of resistance to KOH chemical activation. Compared to graphitic precursors, polymeric and biomass precursors are more susceptible to KOH attack. This is because polymeric and biomass precursors tend to form amorphous carbon structures after carbonisation. In the case of graphitic precursors, as indicated in the author's work, a large amount of localised graphitic platelets still remain within the sample after carbonisation, even after chemical

activation. Those graphitic platelets have a higher resistance to KOH attack than that of amorphous carbon, due to the more stable aromatic ring structure.

On the aspect of the resulting carbon sorbents, the influence of precursor materials is reflected in the porous structures and chemical compositions of the samples. Polymer- and biomass-derived carbon sorbents possess relatively higher specific surface area than those of graphitic precursor-derived carbon sorbents, when they are subject to the same chemical activation conditions. For example, under the chemical activation conditions of KOH/precursor=1:1 and activation temperature 700 ℃, the carbon sphere CSA-700 has a specific surface area of 1230 $m^2 g^{-1}$. For the leaf-derived carbon LC1-700, it is 1360 $m^2 g^{-1}$, and for the pine-cone-derived carbon PC2-800, it is 1170 $m^2 g^{-1}$. However, even when the use of KOH/precursor ratio is doubled (2:1) and a higher activation temperature is applied (800 ℃), the ball-milled graphite- (ABG-12hCO2) and the graphite oxide-derived carbon sorbents (AGO2-800) only show specific surface area of 1170 and 490 $m^2 g^{-1}$, respectively. This is a direct consequence of the above-mentioned influence of the precursor material on the sample preparation process. This difference in porous structures results in varied CO_2 uptakes of carbon sorbents derived from different precursor materials.

Furthermore, due to the choice of nitrogen-enriched polymer as the precursor, the resulting carbon sphere also possess a high nitrogen content (5.9 at% in CSA-700). As indicated in the corresponding discussion, this can benefit the CO_2 capture performance of the sorbent. However, in the case of biomass-derived carbon, nitrogen and metal dopants are inherited from the precursor. Therefore, the concentration of the chemical dopants in the resulting sorbents cannot be intentionally controlled. In addition, the biological nitrogen compounds in biomass are usually not stable at the applied activation temperatures (600 – 800 ℃). As a result, the nitrogen content in the resulting carbon sorbents are comparatively lower (1.3 at% in LC2-700 and 0.5 at% in PC2-700).

6.1.2 Specific surface area vs. pore volume

As discussed previously, KOH activation of different carbon precursors produce carbon sorbents with varied specific surface area and pore volume. However, the relationship between the specific surface area and pore volume has seldom been

discussed in detail. In this section, the relationship between the specific surface area and pore volume is theoretically studied with the consideration of pore geometries.

Before any mathematical derivation, a few prerequisites and assumptions are made as follows:

1. Pores are classified into four types in accord with their sizes (H), that is, ultramicropore (H<0.7 nm), supermicropore (0.7 nm<H<2 nm), mesopore (2 nm<H<50 nm) and macropore (H>50 nm);

2. Two pore geometries are adopted for the mathematical derivation – slit pore geometry (for all types of pores) and slit/cylindrical pore geometry (slit pore for pore size < 2 nm and cylindrical pore for pore size > 2nm);

4. Despite pore geometry, pores can consist of either single or multiple carbon layers. Each layer has the same number of carbon atoms; and

3. In the case of single carbon layer pore wall, all carbon structures possess a maximum specific surface area of 2630 m^2 g^{-1} (including both outer and inner surface),[186] which is the theoretical surface area of graphene.

When the slit pore model is applied, pore volume is only influenced by the number of carbon layers and pore size. The equation for the calculation of pore volume is as follows:

$$V = \frac{1}{4} \times \frac{S}{n} \times H \qquad \text{Equation 13}$$

$$S = \frac{4nV}{H} \qquad \text{Equation 14}$$

where V is pore volume, H is pore size, that is, the distance between two walls, S is the specific surface area (2630 m^2 g^{-1}), and n is the number of carbon layers in one side of the wall. In addition, "$\frac{1}{4}$" is "$\frac{1}{2} \times \frac{1}{2}$", which indicates only the inner surface and one side of the pore wall are considered for the calculation of pore volume.

The above equation indicates that, for a given number of carbon layers, the pore volume has a linear relationship with the specific surface area (Figure 69a).


Slit Pore
n
H

(a)

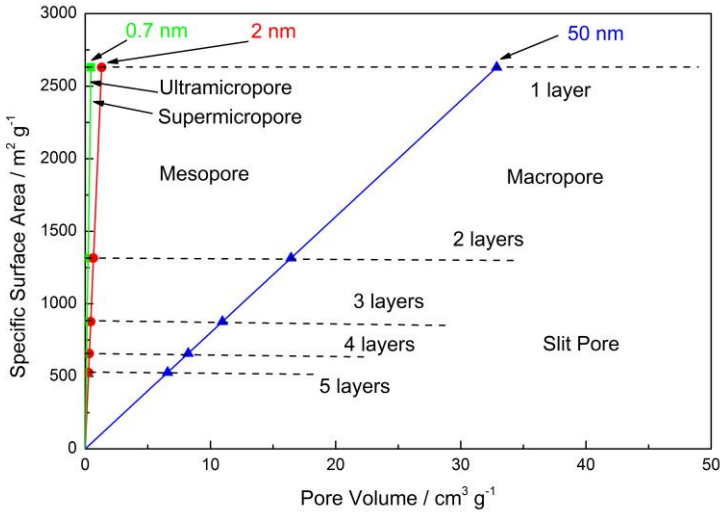
0.7 nm
2 nm
50 nm
Ultramicropore
Supermicropore
1 layer
Mesopore
Macropore
2 layers
3 layers
4 layers
Slit Pore
5 layers
Specific Surface Area / m2 g-1
Pore Volume / cm3 g-1

(b)

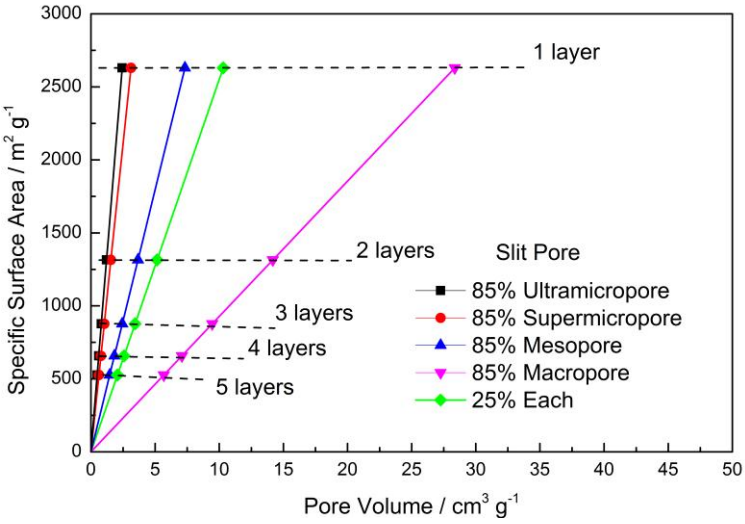
1 layer
2 layers
Slit Pore
3 layers
4 layers
5 layers
85% Ultramicropore
85% Supermicropore
85% Mesopore
85% Macropore
25% Each
Specific Surface Area / m2 g-1
Pore Volume / cm3 g-1

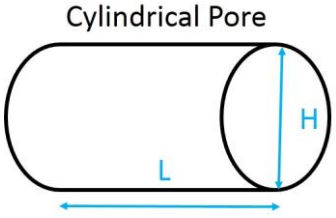
Cylindrical Pore
H
L

(c)

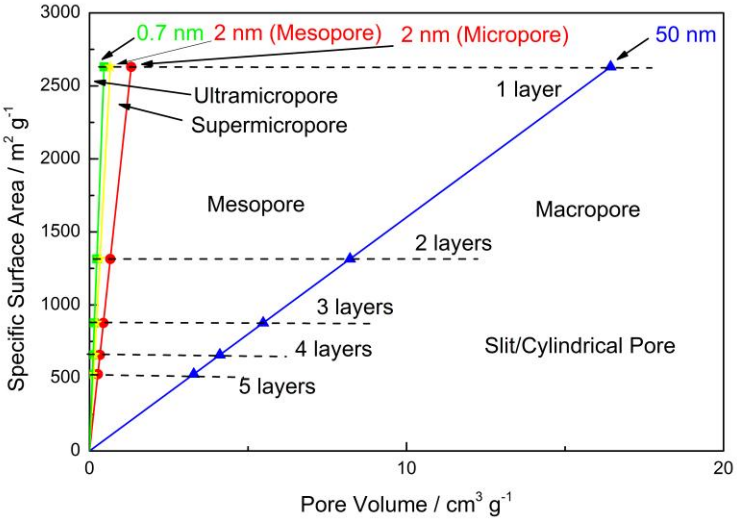

(d)

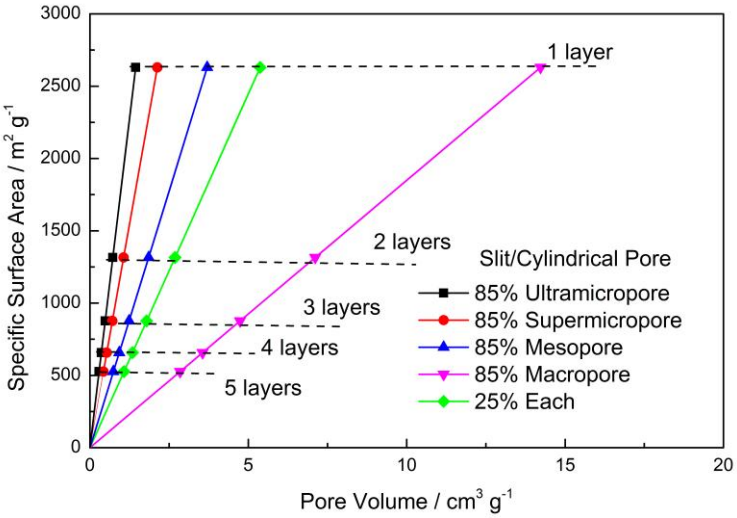

(e)

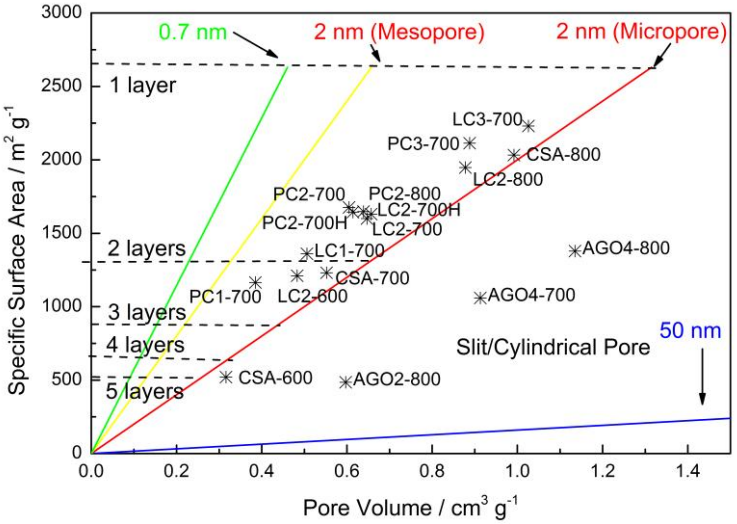

Figure 69: Specific surface area vs. pore volume plots based on (a) a slit-pore geometry for all pore sizes and (c) a slit geometry for ultra- and supermircopores and cylindrical

geometry for meso- and macropores, respectively. (b) and (d) the theoretical relationship between specific surface area and pore volume of porous structures that comprise different proportions of ultra-, super-, meso- and macropores. (e) Comparison of experimental to theoretical relationship between specific surface area and pore volume.

The linear curves in Figure 69b are related to the porous carbon structures that consist of different compositions of ultramicropore (0.7 nm), supermicropore (2 nm), mesopore (10 nm) and macropore (50 nm). For example, in Figure 69b, the black curve is related to the porous structure with 85% ultramicropore, 5% supermicropore, 5% mesopore and 5% macropore. Similarly, for the red curve, it comprises 85% supermicropore; the blue curve, 85% mesopore; the green curve, 85% macropore; purple curve, 25% of each type of pore. Figure 69b shows that, compared with the green and the red curves in Figure 69a, the slope of the curve is slightly reduced when a small amount of supermicropore, mesopore and macropre are added in the ultramicroporous structure. In contrast, the slope is slightly increased when a small of ultramicropore, supermicropore and mesopore are added in the macroporous structure. This observation is consistent with the practical experience that the specific surface area of a carbon sample increases significantly with micropore development.

Besides the slit pore geometry, slit/cylindrical pore geometry can also be applied, where slit pore geometry is used for pore size < 2 nm and cylindrical pore geometry is used for pore size > 2nm. For the pore size < 2 nm, the relationship between the specific surface area and the pore volume is the same as previously-derived:

$$S = \frac{4nV}{H} \qquad \text{Equation 15}$$

However, when the cylindrical pore geometry is considered for the mesopore and macropore, the pore volume is calculated as follows:

$$V = Al = (\frac{H}{2})^2\pi \times \frac{S}{2a}\frac{1}{H\pi} = \frac{1}{8} \times \frac{S}{a} \times H \qquad \text{Equation 16}$$

$$S = \frac{8nV}{H} \qquad \text{Equation 17}$$

where V is the volume of the cylinder, A is the area of the cross-section of the cylinder, l is the length of the cylinder, H is pore size (i.e., the diameter of the cylinder), S is the

specific surface area and a is the number of carbon layers. The corresponding linear curves are plotted in Figure 69c and d.

The supermicropore and mesopore with H=2 share the same linear curve in Figure 69a, due to the same pore geometry (slit pore) used for calculation. However, Figure 69c clearly shows distinct curves for supermicropore and mesopore, where the slope of mesopore curve is twice larger than that of supermicropore curve, as indicated in Equation 15 and 17 ($\frac{8n}{H}$ for cylindrical pore and $\frac{4n}{H}$ for slit pore). This is the same with the macropore linear curve in both figures. The linear curves in Figure 69d are also similar to those in Figure 69b. However, due to the use of cylindrical pore geometry for both mesopore and macropore, all curves show comparatively larger slopes.

In Figure 69e, porous carbon samples in this doctoral research are fitted into the slit/cylindrical pore geometry plot in Figure 69c. Figure 69e clearly shows most porous carbon samples are located between the yellow and red curves. This implies the porous structures of those samples may consist of both micropores and mesopores with mixed slit and cylindrical pores. Activated graphite oxide samples are located on the right of the red curve, which is consistent with the higher proportion of mesopores in their porous structures, compared with those of the other samples. Moreover, a majority of samples are located between the "1 layer" and "2 layers" dash lines, while some are located between the "2 layers" and "3 layers" dash lines. This suggests those samples comprise mixed "1 layer" and "2 layers" carbon pore walls. Under comparatively more aggressive chemical activation conditions, LC3-700, LC2-800, PC3-700 and CSA-800 are closer to the "1 layer" dash line, indicating those sample may contain higher proportions of single layer carbon fragments.

6.1.3 Different methods for surface area calculation

Table 28: Comparison between specific surface area ($S/m^2\ g^{-1}$) calculated by the BET equation and the NLDFT model.

Sample	LC1-700	LC2-700	LC2-700H	LC3-700	LC2-600	LC2-800
S_{BET}	1080	1460	1510	2360	1050	1940
S_{DFT}	1360	1600	1630	2230	1210	1950

Sample	PC1-700	PC2-700	PC2-700H	PC3-700	PC2-600	PC2-800
S_{BET}	890	1510	1440	2090	1090	1530
S_{DFT}	1170	1680	1640	2110	1260	1650

Sample	CSA-600	CSA-700	CSA-800	AGO2-800	AGO4-800	AGO4-700
S_{BET}	490	1230	2140	470	1530	1200
S_{DFT}	520	1230	2030	490	1380	1060

Table 28 is the comparison of specific surface area calculated by both BET equation and NLDFT model. The specific surface area is frequently calculated by BET equation in the literature. However, Table 28 clearly shows there are differences between those results. It is mentioned earlier in the "Experimental Section" that the use of BET equation is based on several prerequisites, which assume an ideal surface -flat and homogeneous for gas adsorption. In contrast, DFT methods take materials and pore geometries into consideration, which are more accurate approaches to calculating both specific surface area and pore volume. The BET equation can either underestimate or overestimate the specific surface area of a sample. The underestimation is due to extreme curvature of ultramicropores (<0.7nm) and the relatively large size of the probe molecule (N_2). This is reflected in the case of most samples listed in Table 28, where the surface area calculated by the BET equation is smaller than that by the NLDFT model. The overestimation is caused by the probe molecule filling in the centre of the supermicrpore (>0.7nm). This is the case with LC3-700, CSA-800, AGO4-800 and AGO4-700, where these two samples possess relatively larger proportions of supermicropores, due to the use of a greater quantity of KOH or a higher temperature for chemical activation.

Although DFT methods are more accurate than the BET equation, the BET equation is still the most applied method in the literature for the calculation of specific surface area. This is very likely a matter of "tradition" or for the purpose of comparison with experimental data in the literature. In the following discussion on the specific CO_2

uptake vs. porosity, in order to be consistent with the experimental data in the literature, specific surface area calculated by the BET equation is used for the analysis.

6.1.4 Specific CO_2 uptake vs. porosity

In addition to the CO_2 sorption isotherms, CO_2 uptakes and specific CO_2 uptakes of carbon sorbents are also plotted in Figure 70 against their corresponding porosity parameters. Specific CO_2 uptake is calculated by dividing CO_2 uptake by porosity.

(a)

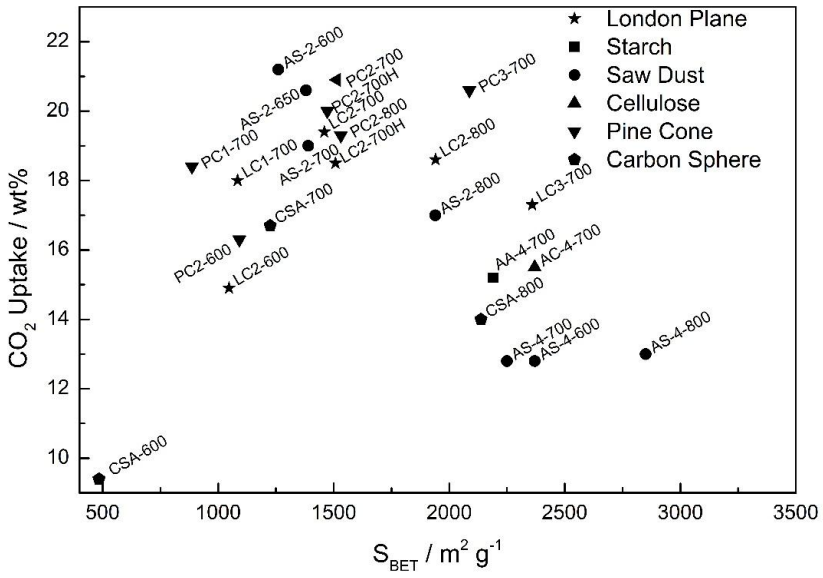

(b)

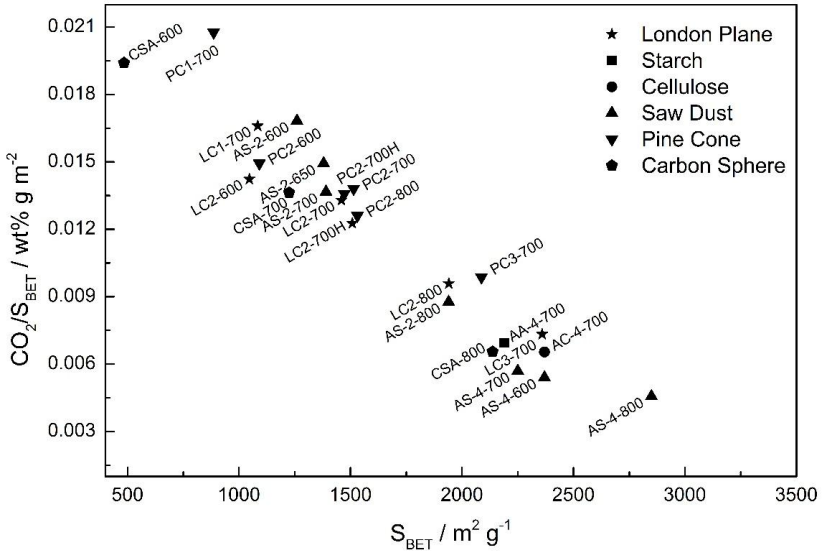

(c)

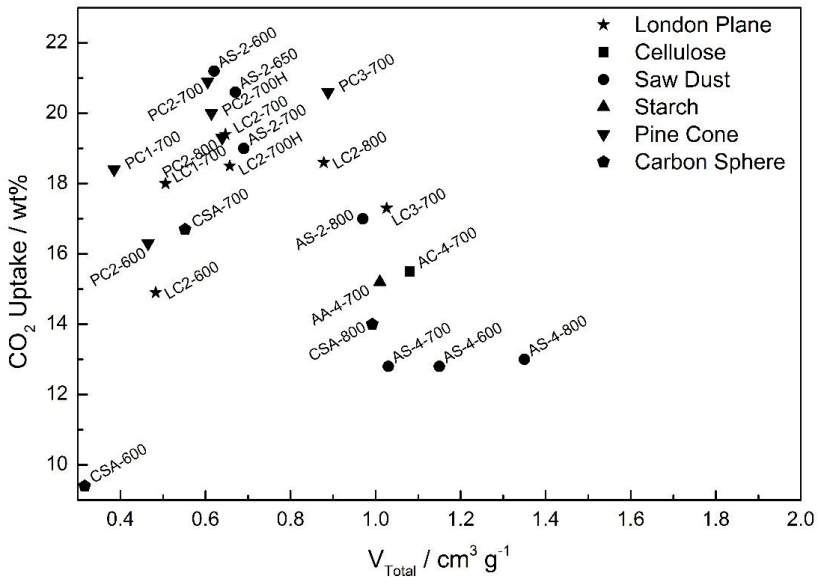
London Plane
Cellulose
Saw Dust
Starch
Pine Cone
Carbon Sphere
CO2 Uptake / wt%
VTotal / cm3 g-1
PC2-700
AS-2-600
AS-2-650
PC2-700H
PC3-700
PC1-700
PC2-800
LC2-700
AS-2-700
LC1-700
LC2-700H
LC2-800
CSA-700
AS-2-800
LC3-700
PC2-600
AC-4-700
LC2-600
AA-4-700
CSA-800
AS-4-700
AS-4-600
AS-4-800
CSA-600

(d)

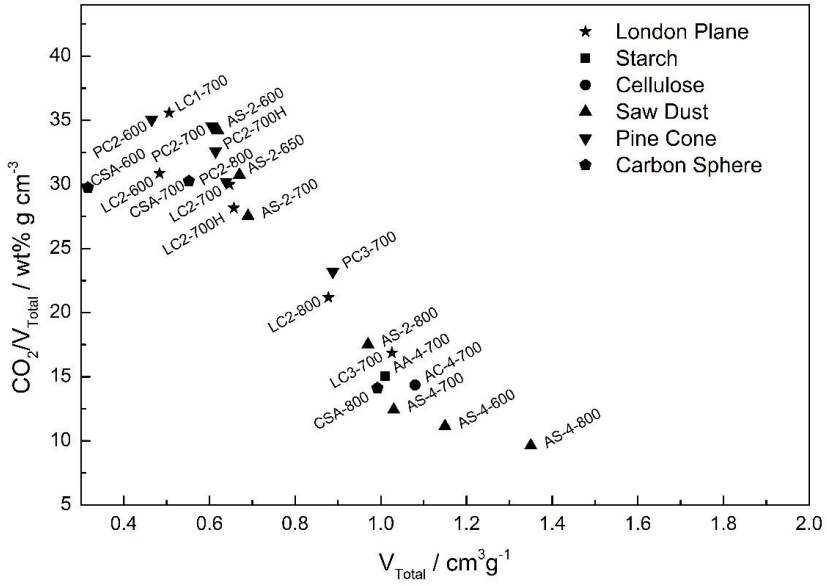
London Plane
Starch
Cellulose
Saw Dust
Pine Cone
Carbon Sphere
CO2/VTotal / wt% g cm-3
VTotal / cm3g-1
PC2-600
LC1-700
AS-2-600
CSA-600
PC2-700
PC2-700H
LC2-800
CSA-700
PC2-800
AS-2-650
LC2-700
LC2-700H
AS-2-700
PC3-700
LC2-800
AS-2-800
LC3-700
AA-4-700
AC-4-700
CSA-800
AS-4-700
AS-4-600
AS-4-800

(e)

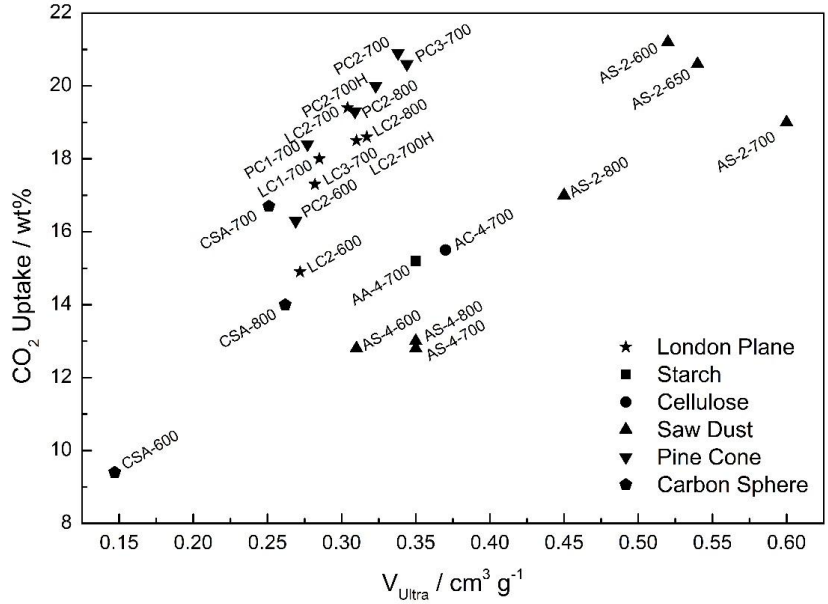
London Plane
Starch
Cellulose
Saw Dust
Pine Cone
Carbon Sphere
CO2 Uptake / wt%
VUltra / cm3 g-1
PC2-700
PC3-700
AS-2-600
PC2-700H
AS-2-650
PC2-800
LC2-700
LC2-800
AS-2-700
PC1-700
LC2-700H
LC1-700
LC3-700
AS-2-800
CSA-700
PC2-600
AC-4-700
LC2-600
AA-4-700
CSA-800
AS-4-600
AS-4-800
AS-4-700
CSA-600

(f)

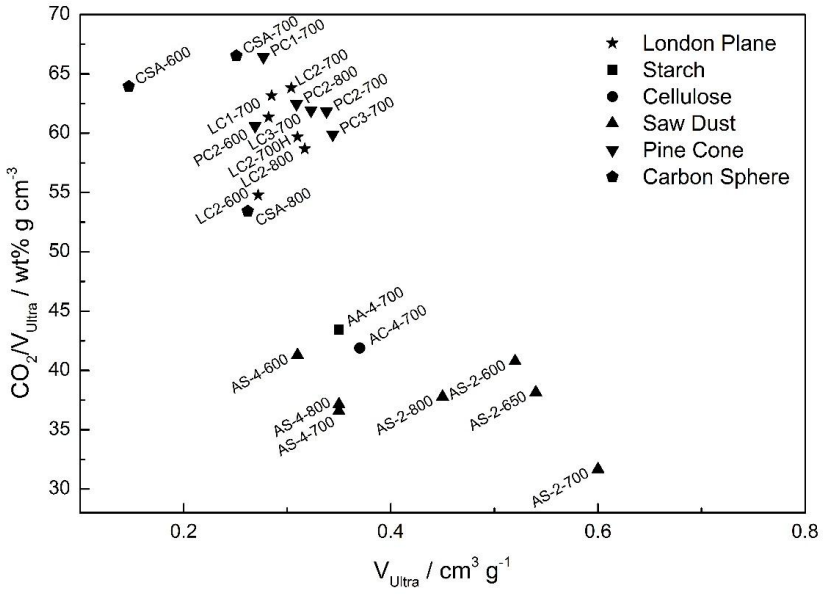

Figure 70: CO_2 uptake vs. porosity parameters (a) BET surface area, (c) total pore volume and (e) ultramicropore volume; (b), (d) and (f) are their corresponding specific CO_2 uptake versus porosity parameter.

CO_2 uptake is plotted against porosity parameters in Figure 70a, c and e, including specific surface area, total pore volume and ultramicropore volume. The experimental data come from biomass precursors recorded in the literature as well as the author's work on pine cones, London Plane leaves and carbon spheres.[91] It is noted from Figure 70a and c that specific surface area and pore volume does not necessarily play a dominant role in CO_2 adsorption. Those with higher specific surface area and pore volume do not necessarily have higher CO_2 uptakes. Figure 70e suggests those samples with higher ultramicropore volumes may also have higher CO_2 uptakes. However, there are samples with similar ultramicropore volumes exhibiting large differences in CO_2 uptakes (on the top-middle of the figure). This indicates ultramicropore volume is not the only factor that influences CO_2 uptake. CO_2 uptake per unit surface area, total pore volume and ultramicropore volume (specific CO_2 uptake) are also plotted in Figure 70(b, d and f) against porosity parameters. In this case, all three figures show a clearly decreasing trend of specific CO_2 uptake with increasing porosities, which indicates those samples with lower porosities show higher CO_2 uptake per unit porosity (mostly the pine cone- and leaf-derived carbon). It should be noted that PC1-700, LC2-600 and CSA-600 occupy the highest positions at the top left of Figure 70b, d and f, which indicates that they have high CO_2 uptake per unit porosity. The common characteristics

of these samples are the possession of either relatively high nitrogen or metal content or a combination of the two. However, all of them show comparatively smaller porosities. This observation indicates that nitrogen and metal dopants play a more important role than porosity for the low pressure CO_2 capture (i.e. ≤ 1 bar).

6.1.5 Artificial neural network

An artificial neural network was built with Matlab R2013a to analyse the relationship between the influencing factors and CO_2 uptakes at 25 ℃ and under 1 bar CO_2. In this work, nitrogen, calcium, magnesium contents and ultramicropore volume were selected as input parameters, and the CO_2 uptakes at 25 ℃ and 1 bar CO_2 as the target parameter. In total, 31 experimental data pairs from this work and the literature were selected as the input data for building the network.[91, 162, 187-189] Within these experimental data pairs, 21 data pairs were used for training, while 5 for validation and 5 for testing. The training process was carried out by the "nftool" (neural network fitting toolbox) of Matlab by using the training function of "trainlm" (Levenberg-Marquardt backpropagation). After several trials, the network with 20 neurons and 1 hidden layer gave the best outcome with the R_{Train}=0.9404, $R_{Validation}$=0.9972 and R_{Test}=0.9154, respectively. Therefore, this network was chosen for the subsequent simulation.

After the network was trained, it was used to simulate the influences of input parameters on CO_2 uptake. The simulation was carried out with the "nntool" (open network/data manager) of Matlab. Before the simulation, the following data processing was applied to the input parameters:

1. For each simulation, one of the four input parameters was set to be the variable, where its simulated data range was within the value range of its corresponding input parameter. The other three were kept as constants, where the value of each constant was the average of the maximum and minimum of the input parameter. The corresponding values are summarised in Table 29.

2. For the chemical composition of each sample from the literature, its unit was converted into "at%" where necessary, while its value was recalculated into the composition of C, O, N, Ca and Mg, in order to be consistent with the author's work. If an element was not detected in a sample in the literature, it was input as "0".

Table 29: Summary of constants and variables for simulation.

Simulated Parameter	Max	Min	Average (Constant)	Input Data Range (Variable)
N content	6.7	0.00	3.4	0.3 – 6.0
Ca content	1.7	0.00	0.8	0.2 – 1.6
Mg content	0.9	0.00	0.4	0. – 0.6
V_{Ultra}	0.60	0.13	0.36	0.14 – 0.60

*For chemical content, the unit is "at%"; for ultramicropore volume, the unit is "$cm^3 g^{-1}$".

3. For both chemical composition and ultramicropore volume, if either of those (or both) was not reported for a sample in the literature, it was input as "NaN" (Not a Number).

The simulated output data are plotted in Figure 71. It is clearly observed from Figure 71 that the CO_2 uptake increases rapidly with the increasing calcium, magnesium contents and ultramicropore volume. However, the CO_2 uptake does not vary regularly with increasing nitrogen content. These predicted influences of input parameters on CO_2 uptake are consistent with the analysis in the previous chapter, which emphasises that metal dopant and ultramicropore are the two key determinants for CO_2 capture performance of porous carbon materials. The irregular change of CO_2 uptake with nitrogen content can be explained by the existence of various nitrogen functional groups. It is mentioned in the previous chapter that nitrogen dopant can exist in different forms, such as pyridinic and pyrrolic nitrogen. The former has a higher affinity towards acidic CO_2 molecules due to its higher basicity. The composition of different forms of nitrogen is not frequently reported in the literature. Therefore, it is difficult to distinguish their individual influences on CO_2 capture. Furthermore, it is also observed from Figure 71 that the Mg content curve is slightly steeper than that of Ca content. This suggests that Mg dopant may have a greater influence than that of Ca dopant on CO_2 uptake according to the prediction. It shows that this network can help to distinguish the contribution of different metal dopants on CO_2 uptake.

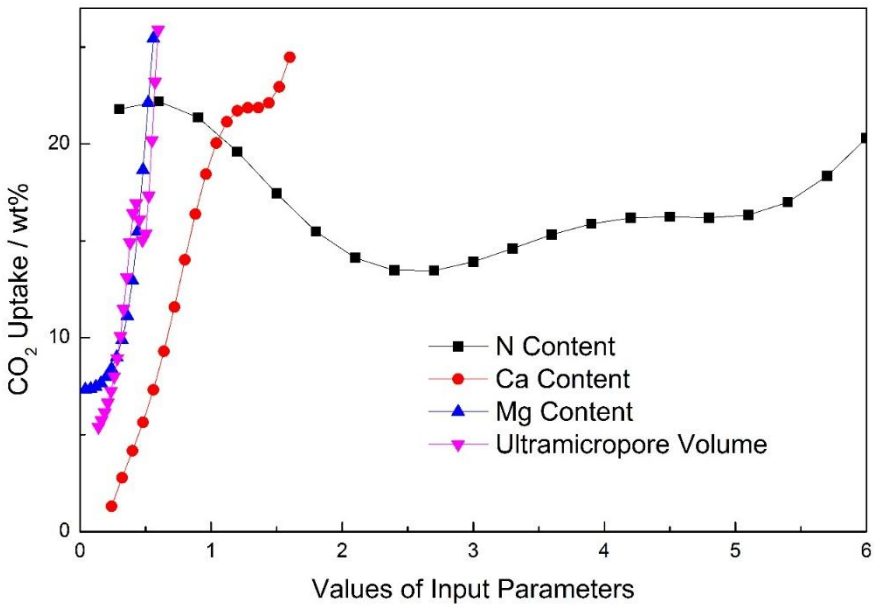

Figure 71: The predicted influence of input parameters on CO_2 uptake.

This chapter summarises all the experimental data in the current work on polymer-, biomass- and graphitic precursor-derived carbon sorbents

1. The precursor materials have significant influence on the porous structures and chemistry of the resulting carbon sorbents, because they have different resistance to the KOH activation and different chemical compositions;

2. The value of specific surface area can differ when different calculation methods are applied, due to different assumptions of carbon surface;

3. The analysis on the specific CO_2 uptake further demonstrates the positive influence of ultramicropores, nitrogen and metal dopants on CO_2 capture, that is, more CO_2 molecules are adsorbed on the unit surface area of those samples with relatively larger ultramicropore volume, nitrogen or metal contents; and

4. The ANN simulation shows CO_2 uptake increases with increasing ultramicropore volume, magnesium and calcium contents but varies irregularly with the increasing nitrogen content. This is very likely due to various chemical forms of nitrogen dopant and their different affinities towards CO_2 molecules.

6.2 Conclusions

This project seeks to develop highly cost-effective carbon-based porous sorbents for CO_2 capture. Several precursor materials have been comparatively examined to determine both their potential for this purpose and the effects of porosity and chemical doping on the CO_2 capacity and performance in general. Specific conclusions can be drawn as follows:

1. In the study of the polymeric precursor, copolymerised acrylonitrile and acrylamide was used successfully as a nitrogen-containing precursor material and a novel dripping device was built to produce millimetre-sized polymer spheres. The polymer spheres produced in this way possess a macroporous channelled structure due to the "solvent-exchange" process between the polymer solution drop (DMSO) and the water bath. The macroporous structure allows a uniform diffusion and distribution of the activating agent during soaking in the KOH solution. The polymer spheres are oxidised in air and activated with KOH at high temperatures to produce nitrogen-doped microporous carbon spheres. The carbon sphere, prepared at KOH/sphere weight ratio of 1:1 and 700 ℃, shows the highest uptake of 16.7 wt% in the pure CO_2 of 1 bar at 25 ℃ and 9.3 wt% in the mixed 15% CO_2/85% N_2 gas environment.

2. In the study on the biomass precursor, both London Plane leaves and Spruce pine cones were successfully used as low-cost waste materials to produce microporous carbon sorbents. In both studies, prepared at the activation temperature of 700 ℃ and the KOH/cabon weight ratio of 2:1, the resulting carbon sorbents show excellent CO_2 uptakes of 19.5 wt% for leaf-derived carbon and 20.9 wt% for pine cone-derived carbon, respectively. The CO_2 uptake of pine cone-derived carbon has matched the highest CO_2 uptake reported in the literature for biomass precursors (21.2 wt%). The characterisation results show the excellent CO_2 capture performance is attributed to the highly microporous structure derived from KOH chemical activation and nitrogen, magnesium and calcium dopants naturally inherited from the biomass precursors. An artificial neural network model was built to analyse the influence of ultramicropore volume and chemical dopants on CO_2 adsorption. The simulated result further supports the conclusion that ultramicropores and metal dopants effectively enhance CO_2 adsorption on carbon sorbents. The network also indicates nitrogen dopant has limited

influence, which may be due to the existence of various nitrogen functional groups and their different affinities towards CO_2 molecules.

3. The study on graphtic precursors included chemical activation of graphite oxide and ball-milled graphite. Compared with the results of polymer- and biomass-derived carbon, graphitic precursor-derived carbon sorbents with similar porosities show lower CO_2 uptakes (up to 11 wt%). The characterisation results show graphitic precursors have a higher resistence to KOH chemical activation, compared with those of polymeric and biomass precursors. Therefore, the chemical activation of graphitic precursors requires a higher KOH/carbon weigtht ratio (4:1) and a higher activation temperature (800 ℃) to generate a similar specific surface area to those of polymer- and biomass-derived carbon. Even so, the ultramicropore volume of the graphite oxide-derived carbon is still much lower than those of polymer- and biomass-derived carbon. Further analysis indicates KOH tends to attack the vulnerable sites in graphitic precursors, such as the edge of the ball-milled graphite and epoxy bridges of graphite oxide. The low CO_2 uptakes of graphitic precursor-derived carbon further support the finding that ultramicropore and chemical dopant are two key determining factors for CO_2 uptake.

Preliminary work has been undertaken to modify the size and macroporous structure of polymer spheres, characterise CO_2 capture performance of carbon sorbents derived from various leaf precursors and improve the prediction of CO_2 uptakes on nitrogen- and metal-doped carbon sorbents by artificial neural network. The furture work on the above–mentioned research is also proposed at the end of this thesis.

6.3 Future Work

6.3.1 Modification of porous carbon spheres

A novel method was introduced to produce nitrogen-containing polymer spheres, which were then used as a spherical carbon precursor in the production nitrogen-doped carbon spheres. The mechanical strength of the carbon sphere was related to that of the polymer sphere. In order to improve the mechanical strength of the polymer sphere, preliminary work had been carried out to modify the macroporous structure of the polymer sphere by using mixed DMSO/water bath.

To clarify the influence of mixed DMSO/water bath on the resulting porous carbon sphere structure, high resolution microscopic imaging and macroporous structure analysis (such as mercury porosimetry) will be necessary to quantify the porosity of modified spheres . Furthermore, it is unknown if the change of water bath may cause any change in the chemical composition of the polymer sphere. In addition, it may be expected that the corresponding CO_2 capture performance will be influenced by both varied porous structures and chemical properties of carbon sorbents as well. Therefore, their CO_2 uptakes also need to be measured accordingly.

Besides the water bath, the mechanical strength of the polymer sphere may be further enhanced by using an alternative monomer with a higher molecular weight than that of acrylamide (such as itaconic acid, 130 g mol^{-1}), to copolymerise with acrylonitrile. In this way, the resulting copolymer may have a higher average molecular weight and thus the so-derived polymer sphere may have a higher mechanical strength. However, this needs to be balanced against the nitrogen content in the polymer precursor. Therefore, the corresponding chemical, structural and CO_2 uptake analyses need to be carried out to determine if the change of monomers may significantly influence CO_2 capture performance of the resulting carbon spheres.

In order to measure the mechanical strength of carbon spheres, a test device can be built by using piezoelectric materials. The mechanical strength can be measured through the deformation of a piezoelectric material caused by the applied stress on the sample.

Owing to the relative fragility and small size of the carbon sphere in current research, the device needs to be carefully designed to address the above problems.

6.3.2 Further work on various leaf precursors

London Plane leaf-derived carbon has shown a promising performance in CO_2 capture. Furthermore, preliminary characterisation results show that the porous structures of carbon sorbents can vary with different leaf precursors even when they are activated under the same conditions. Therefore, as a consequence, their CO_2 uptakes are different due to their different porosities. It is most likely the varied porous structures are due to the different biological structures of the leaves. Different leaves may possess different macroporous structures. This may result in different levels of chemical activation, due to different distribution of KOH in the macroporous structures during the soaking process. Therefore, further work on the plant anatomy needs to be performed in order to study the macroporous structures of the leaves.

In addition, further elemental analysis needs to be carried out to clarify the chemical forms and compositions in the resulting carbon sorbents derived from those leaf precursors. Different leaves may possess different concentrations of chemical compounds. This may lead to different compositions of nitrogen and metal dopants in the resulting carbon sorbents. These nitrogen and metal dopants may influence the CO_2 uptakes of so-derived carbon sorbents. Therefore, XPS analysis needs to be performed to determine the types and compositions of surface functional groups on those carbon sorbents.

6.3.3 ANN analysis on metal-doped carbon sorbents

At the end of the study on the biomass-derived carbon sorbents, artificial neural network (ANN) was applied as a modelling tool to analyse the relationship between porosity, nitrogen dopant, metal dopants and CO_2 uptake. The analysis adopts the experimental results from biomass-derived carbon and those from the literature as the input data. The simulated results show the CO_2 uptake increases significantly with increasing amount of ultramicropore and metal dopants but varies irregularly with different concentrations of nitrogen dopant. It is possible that nitrogen dopant exists in the type of different nitrogen-containing functional groups. Those nitrogen functional

groups have varied levels of basicity and thus different affinities towards acidic CO_2 molecules, due to different electron distribution on these functional groups (such as lone electron pairs).

However, besides the controversy related to the ANN method, it also has some limitations and the current model needs to be further improved:

1. The quantity of the input data needs to be further expanded. The current network is trained with 31 data pairs from the author's experimental work and from the literature. There are a limited number of available experimental data because there has been little research on metal-doped carbon sorbents for CO_2 capture. The network model can be further improved and thus would become more reliable. This can only be achieved with further development in this area of research. New experimental data can be imported into the network and the network can be re-adjusted accordingly.

2. A significant problem with ANN is that the modelling process considers all input data are "absolutely correct". For example, it was previously mentioned nitrogen dopant can exist in the type of different functional groups (such as pyridinic, pyrrolic and pyridonic nitrogen) and they have varied affinities towards CO_2 molecules. Many literature reports only mention the chemical composition of nitrogen dopant without further analysis on the composition of the nitrogen functional groups. Therefore, the chemical composition of nitrogen dopant can only be used as a single parameter in the input data for the network training. This may introduce uncertainties into the network and thus reduce the reliability of the network.

3. ANN modelling requires relating all possible input parameters to one/multiple output parameter. Besides the composition of nitrogen, the composition of metal is also uncertain in much of the literature that reports biomass-derived carbon sorbents. It is well-known that biomass is rich in metal elements. However, metal elements are seldom reported in the literature. It is possible that metal contents are ignored due to relatively small quantities of these elements, unless those samples are washed by acids. If metal dopants indeed exist in the resulting carbon sorbents, then the CO_2 uptake of biomass-derived carbon may be enhanced by the existence of metal dopants. Without considering their contribution, the network training may assign more weight to the

other parameters. Then, the training process tends to generate networks that show that the other parameters rather than metal content have larger influence on CO_2 uptake.

In summary, in order to improve the reliability of the network, more experiments on metal-doped carbon sorbents for CO_2 capture need to be carried out to expand the input data. The chemical properties of dopant elements in carbon sorbents need to be clarified, in order to distinguish their individual effects on the CO_2 capture performance of carbon sorbents. The reliability of the network will also be improved by discovering and studying more influencing factors of a material on CO_2 capture.

Appendices

List of publications

Published manuscript:

B. Zhu et al., *Nitrogen-enriched and hierarchically porous carbon macro-spheres – ideal for large-scale CO_2 capture*, ***J. Mater. Chem. A***, 2014, **2**, 5481-5489,

Prepared manuscripts:

B. Zhu et al. *Naturally Derived Porous Carbon with Selective Metal- and/or Nitrogen- Doping for Efficient CO_2 Capture and Oxygen Reduction*

B. Zhu et al., *Naturally Calcium-doped Microporous Carbon Derived from Pine Cone with Superior CO_2 Capture Capacities*

B. Zhu et al., *Development of Porous Carbon by Ball Milling for Carbon Dioxide Capture*

J. Fan, B. Zhu et al., *Does the drying method affect the nanoparticle morphology of mesoporous bioactive glass*

References

[1] H. J. Herzog, E. M. Drake, E. E. Adams, *CO_2 Capture, Reuse, and Storage Technologies for Mitigating Global Climate Change: A White Paper*, Energy Laboratory, Massachusetts Institute of Technology, Massachusetts, USA **1997**, p.5.

[2] G. Marland, T. A. Boden, R. J. Andres, A. L. Brenkert, C. A. Johnston, *Trends: A compendium of data on global change* **2003**, 34.

[3] IEA, *CO_2 Emission from Fuel Combustion 2012*, OECD Publishing, Paris, France **2012**, pp.9.

[4] F. Birol, *World Energy Outlook 2013 Special Report: Redrawing Energy Climate Map*, International Energy Agency, Paris, France **2013**, p.13.

[5] P. Kitcher, *Science* **2010**, *328*, 1230.

[6] N. Oreskes, *Science* **2005**, *307*, 355.

[7] IPCC climate report: humans 'dominant cause' of warming, http://www.bbc.co.uk/news/science-environment-24292615.

[8] IPCC, *Climate Change 2013: The Physical Science Basis, Cambridge University Press*, Cambridge, UK **2014,** p.17.

[9] The Core Writing Team, *Climate Change 2007: Synthesis Report*, Intergovernmental on Climate Change, Valencia, Spain **2008**, p.5.

[10] An illustration of greenhouse effect, http://www.co2crc.com.au/images/imagelibrary/gen_diag/greenhouseeffect_media.jpg.

[11] D. Jacob, *Introduction to Atmospheric Chemistry*, Princeton University Press, Princeton, USA **1999**, p.126.

[12] J. T. Kiehl, K. E. Trenberth, *Bulletin of the American Meteorological Society* **1997**, *78*, 197.

[13] G. U. American, *Chapman Conference on Water Vapor in the Climate System*, American Geophysical Union, Washington, D.C., USA **1995**.

[14] J. F. B. Mitchell, *Rev. Geophys.* **1989**, *27*, 115.

[15] J. Hansen, R. Ruedy, M. Sato, K. Lo, *Rev. Geophys.* **2010**, *48*, RG4004.

[16] Global Annual Mean Temperature, http://data.giss.nasa.gov/gistemp/tabledata_v3/GLB.Ts+dSST.txt.

[17] M. Den Elzen, M. Meinshausen, *Clim. Policy* **2006**, *6*, 545.

[18] IEA, *Energy Technology Perspectives 2010: Scenarios and Strategies to 2050*, OECD Publishing, Paris, France **2010**, p.61.

[19] A. Pittock, *Climate Change: The Science, Impacts and Solutions*, CSIRO Publishing, London, UK **2009**, p.82.

[20] M. Wolf, *Proceedings of the IRE* **1960**, *48*, 1246.

[21] O. Edenhofer, R. Pichs-Madruga, Y, Sokona, K. Seyboth, S. Kadner, T. Zwickel, P. Eickemeier, G. Hansen, S. Schlomer, C. Stechow, P. Matschoss, *Renewable Energy Sources and Climate Change Mitigation: Special Report of the Intergovernmental Panel on Climate Change*, Cambridge University Press, Cambridge, UK **2011**, p.369.

[22] D. Pimentel, A. Marklein, M. A. Toth, M. N. Karpoff, G. S. Paul, R. McCormack, J. Kyriazis, T. Krueger, *Hum. Ecol.* **2009**, *37*, 1.

[23] B. B. F. Wittneben, *Environ. Sci. & Policy* **2012**, *15*, 1.

[24] B. Metz, *Carbon Dioxide Capture and Storage: Special Report of the Intergovernmental Panel on Climate Change*, Cambridge University Press, Cambridge, UK **2005**, p.3.

[25] C. S. Conseils, *Dossier de concertation: Projet pilote de captage et de stockage geologique de CO_2 dans le bassin de Lacq*, Total Company, **2007**, p.40.

[26] W. H. Wiser, *Energy Resources: Occurrence, Production, Conversion, Use*, Springer, New York, USA **2000**, p.211.

[27] Office of Compliance, *Office of Compliance Sector Notebook Project: Profile of the fossil fuel electric power generation industry*, Office of Compliance, Office of Enforcement and Compliance Assurance, U.S. Environmental Protection Agency, Washington, D.C., **1997**, p.3.

[28] D. M. D'Alessandro, B. Smit, J. R. Long, *Angew. Chem. Int. Edit.* **2010**, *49*, 6058.

[29] P. H. M. Feron, C. A. Hendriks, *Oil & Gas Sci. Technol.* **2005**, *60*, 451.

[30] C. Higman, M. van der Burgt, *Gasification*, Elsevier Science, Burlington, USA **2003**, p.10.

[31] C. E. G. Padro, F. Lau, *Advances in Hydrogen Energy*, Springer, New York, USA **2000**, p.95.

[32] L. I. Eide, D. W. Bailey, *Oil & Gas Sci. Technol.* **2005**, *60*, 475.

[33] C. Descamps, C. Bouallou, M. Kanniche, *Energy* **2008**, *33*, 874.

[34] UPDATE 3-Duke's Edwardsport coal-fired power plant enters service,

http://uk.reuters.com/article/2013/06/10/utilities-operations-duke-edwardsport-idUSL3N0EM2G720130610

[35] P. Brimblecombe, *Air Composition and Chemistry*, Cambridge University Press, Cambridge, UK **1996**, p.314.

[36] J. Park, J. S. Park, H. P. Kim, J. S. Kim, S. C. Kim, J. G. Choi, H. C. Cho, K. W. Cho, H. S. Park, *Energy Fuels* **2006**, *21*, 121.

[37] T. Uchida, T. Goto, T. Yamada, T. Kiga, C. Spero, *Energy Procedia* **2013**, *37*, 1471.

[38] C. Prinet, S. Thibeau, M. Lescanne, J. Monne, *Energy Procedia* **2013**, *37*, 3610.

[39] Y. Tan, L. Jia, Y. Wu, *Energy Fuels* **2013**, *27*, 7000.

[40] M. R. Abu-Zahra, Z. Abbas, P. Singh, P. Feron, Carbon Dioxide Post-Combustion Capture: Solvent Technologies Overview, Status and Future Directions, in *Materials and Processes for Energy: Communicating Current Research and Technological Developments* **2013**.

[41] Carbon capture: Turning coal into coke, http://english.cntv.cn/program/china24/20101125/103945.shtml

[42] G. T. Rochelle, *Science* **2009**, *325*, 1652.

[43] Y. J. Lin, T. H. Pan, D. S.-H. Wong, S. S. Jang, Y. W. Chi, C. H. Yeh, *Ind. Eng. Chem. Res.* **2010**, *50*, 1338.

[44] Solvent Absorption, http://www.co2crc.com.au/images/imagelibrary/cap_diag/solvent_absorption_media.jpg

[45] S. I. Plasynski, Z. Y. Chen, Review of CO_2 capture technologies and some improvement opportunities, in *Abstracts of Papers of the American Chemical Society*, Washington, D.C., USA **2000**, *220*, 1155.

[46] R. L. Burwell, *Pure & Appl. Chem.* **1976**, *46*, 71.

[47] S. Nahahiro, *Modern dictionary: physical chemistry*, Discovery Publishing House, New Delhi, India **1990**, p.73.

[48] H. Hiller, R. Reimert, F. Marschner, H. J. Renner, W. Boll, E. Supp, M. Brejc, W. Liebner, G. Schaub, G. Hochgesand, C. Higman, P. Kalteier, W. D. MÃ¼ller, M. Kriebel, H. Schlichting, H. Tanz, H. M. Stonner, H. Klein, W. Hilsebein, V. Gronemann, U. Zwiefelhofer, J. Albrecht, C. J. Cowper, H. E. Driesen, Gas Production

in *Ullmann's Encyclopedia of Industrial Chemistry*, Wiley-VCH Verlag GmbH & Co. KGaA, **2000**, p.94.

[49] S. Ren, Y. Hou, W. Wu, S. Tian, W. Liu, *RSC Adv.* **2012**, *2*, 2504.

[50] S. Choi, J. H. Drese, C. W. Jones, *ChemSusChem* **2009**, *2*, 796.

[51] Physical Adsorption, http://www.co2crc.com.au/images/imagelibrary/cap_diag/principles_of_adsorption_media.jpg

[52] P. D. Bergman, E. M. Winter, Z. Y. Chen, *Energy Conversion and Management* **1997**, *38*, S211-S216.

[53] P. J. E. Harlick, F. H. Tezel, *Microporous and Mesoporous Materials* **2004**, *76*, 71.

[54] R. V. Siriwardane, M. S. Shen, E. P. Fisher, J. Losch, *Energy Fuels* **2005**, *19*, 1153.

[55] K. T. Chue, J. N. Kim, Y. J. Yoo, S. H. Cho, R. T. Yang, *Ind. Eng. Chem. Res.* **1995**, *34*, 591.

[56] Flat sheet membrane, http://www.co2crc.com.au/images/imagelibrary/cap_diag/flatsheet_membrane_media.jpg

[57] Hollow fibre membrane, http://www.co2crc.com.au/images/imagelibrary/cap_diag/hollow_fibre_membrane_media.jpg

[58] Spiral wound menbrane, http://www.co2crc.com.au/images/imagelibrary/cap_diag/spiral_wound_membrane_media.jpg

[59] D. Shekhawat, D. R. Luebke, H. W. Pennline, *A Review of Carbon Dioxide Selective Membranes*: A Topical Report, US Department of Energy **2003**, p.11.

[60] J. R. Li, R. J. Kuppler, H. C. Zhou, *Chem. Soc. Rev.* **2009**, *38*, 1477.

[61] R. W. Baker, K. Lokhandwala, *Ind. Eng. Chem. Res.* **2008**, *47*, 2109.

[62] E. Favre, *J. of Membrane Sci.* **2007**, *294*, 50.

[63] J. F. Brennecke, B. E. Gurkan, *J. Phys. Chem. Lett.* **2010**, *1*, 3459.

[64] J. L. Anthony, S. N. V. K. Aki, E. J. Maginn, J. F. Brennecke, *Int. J. Environ. Technol. Management* **2004**, *4*, 105.

[65] C. Cadena, J. L. Anthony, J. K. Shah, T. I. Morrow, J. F. Brennecke, E. J. Maginn, *J. Am. Chem. Soc.* **2004**, *126*, 5300.

[66] S. N. V. K. Aki, B. R. Mellein, E. M. Saurer, J. F. Brennecke, *J. Phys. Chem. B* **2004**, *108*, 20355.

[67] J. Tang, H. Tang, W. Sun, M. Radosz, Y. Shen, *J. Polym. Sci. A Polym. Chem.* **2005**, *43*, 5477.

[68] J. L. Anderson, J. K. Dixon, J. F. Brennecke, *Acc. Chem. Res.* **2007**, *40*, 1208.

[69] J. L. Anderson, J. K. Dixon, E. J. Maginn, J. F. Brennecke, *J. Phys. Chem. B* **2006**, *110*, 15059.

[70] M. Rahmati-Rostami, C. Ghotbi, M. Hosseini-Jenab, A. N. Ahmadi, A. H. Jalili, *The Journal of Chemical Thermodynamics* **2009**, *41*, 1052.

[71] V. Manovic, E. J. Anthony, *International journal of environmental research and public health* **2010**, *7*, 3129.

[72] R. Barker, *J. Appl. Chem.* **1973**, *23*, 733.

[73] A. I. Lysikov, A. N. Salanov, A. G. Okunev, *Ind. Eng. Chem. Res.* **2007**, *46*, 4633.

[74] S. K. Bhatia, D. D. Perlmutter, *AIChE J.* **1983**, *29*, 79.

[75] J. C. Abanades, D. Alvarez, *Energy Fuels* **2003**, *17*, 308.

[76] K. S. Walton, M. B. Abney, M. Douglas LeVan, *Microporous and Mesoporous Materials* **2006**, *91*, 78.

[77] R. Hernandez-Huesca, L. Diaz, G. Aguilar-Armenta, *Separation and Purification Technology* **1999**, *15*, 163.

[78] A. R. Millward, O. M. Yaghi, *J. Am. Chem. Soc.* **2005**, *127*, 17998.

[79] M. Eddaoudi, J. Kim, N. Rosi, D. Vodak, J. Wachter, M. O'Keeffe, O. M. Yaghi, *Science* **2002**, *295*, 469.

[80] C. Pevida, M. G. Plaza, B. Arias, J. Fermoso, F. Rubiera, J. J. Pis, *Appl. Surf. Sci.* **2008**, *254*, 7165.

[81] Y. Q. Li, K. x. Li, *Carbon* **2010**, *48*, 3974.

[82] H. Marsh, F. R. Reinoso, *Activated Carbon*, Elsevier Science, London UK **2006**, p.29.

[83] T. C. Drage, A. Arenillas, K. M. Smith, C. Pevida, S. Piippo, C. E. Snape, *Fuel* **2007**, *86*, 22.

[84] M. G. Plaza, C. Pevida, A. Arenillas, F. Rubiera, J. J. Pis, *Fuel* **2007**, *86*, 2204.

[85] G. P. Hao, W. C. Li, D. Qian, A. H. Lu, *Adv. Mater.* **2010**, *22*, 853.

[86] M. Sevilla, P. Valle-Vigon, A. B. Fuertes, *Adv. Funct. Mater.* **2011**, *21*, 2781.

[87] C. Chen, J. Kim, W. S. Ahn, *Fuel* **2012**, *95*, 360.

[88] Y. Li, K. Li, *Journal of Applied Polymer Science* **2011**, *121*, 3466.

[89] J. Lan, D. Cao, W. Wang, B. Smit, *ACS Nano* **2010**, *4*, 4225.

[90] Y. Zhao, X. Liu, K. X. Yao, L. Zhao, Y. Han, *Chem. Mater.* **2012**, *24*, 4725.

[91] M. Sevilla, A. B. Fuertes, *Energ, & Environ. Sci.* **2011**, *4*, 1765.

[92] M. C. Gutierrez, D. Carriazo, C. O. Ania, J. B. Parra, M. L. Ferrer, F. del Monte, *Energ. & Environ. Sci.* **2011**, *4*, 3535.

[93] M. Sevilla, A. B. Fuertes, *Chemistry-A European Journal* **2009**, *15*, 4195.

[94] I. Norberg, Carbon *Fibres from Kraft Lignin*, Doctoral Dissertation, KTH Royal, **2012**, p.2.

[95] M. M. Tang, R. Bacon, *Carbon* **1964**, *2*, 211.

[96] M. Molina-Sabio, M. T. Gonzalez, F. Rodriguez-Reinoso, A. Sepulveda-Escribano, *Carbon* **1996**, *34*, 505.

[97] J. Romanos, M. Beckner, T. Rash, L. Firlej, B. Kuchta, P. Yu, G. Suppes, C. Wexler, P. Pfeifer, *Nanotechnology* **2012**, *23*, 015401.

[98] J. Wang, S. Kaskel, *J. Mater. Chem.* **2012**, *22*, 23710.

[99] K. S. W. Sing, K. S. W. Sing, D. H. Everett, R. Haul, L. Moscou, R. A. Pierotti, J. Rouquerol, T. Siemieniewska, *Pure and Appl. Chem.* **1982**, *54*, 2201.

[100] W. A. Steele, *Surf. Sci.* **1973**, *36*, 317.

[101] K. Mosher, J. He, Y. Liu, E. Rupp, J. Wilcox, *Int. J. Coal Geol.* **2013**, *109-110*, 36.

[102] M. Inagaki, F. Kang, *Carbon Materials Science and Engineering*, Tsinghua University Press, Beijing, China **2006**, p.65.

[103] P. Billemont, B. Coasne, G. De Weireld, *Langmuir* **2010**, *27*, 1015.

[104] D. W. Siderius, L. D. Gelb, *J. chem. Phys.* **2011**, *135*, 084703.

[105] Y. I. Lim, S. K. Bhatia, *J. Membrane Sci.* **2011**, *369*, 319.

[106] J. Delhommelle, P. Millie, *Mol. Phys.* **2001**, *99*, 619.

[107] N. F. A. Van der Vegt, *Macromolecules* **2000**, *33*, 3153.

[108] NIST XPS Database, http://srdata.nist.gov/xps/

[109] P. Larkin, *Infrared and Raman Spectroscopy: Principles and Spectral Interpretation*, Elsevier Science, Oxford, UK **2011** p.14-16.

[110] W. H. Weber, R. Merlin, *Raman Scattering in Materials Science*, Spring Science & Business Media, New York, USA **2000** p.319.

[111] J. Hodkiewicz, *Application Note: 51891 Characterizing Carbon Materials with Raman Spectroscopy*, Thermo Fisher Scientific, Madison USA.

[112] C. S. S. R. Kumar, *Raman Spectroscopy for Nanomaterials Characterization*, Springer Science & Business Media, New York, USA **2012** p.301.

[113] P. van der Heide, *X-ray Photoelectron Spectroscopy: An introduction to Principles and Practices*, John Wileys & Sons, Hoboken, USA **2011** p.1-12.

[114] S. Hofmann, *Auger and X-Ray Photoelectron Spectroscopy in Materials Science: A User-Oriented Guide*, Springer, Springer Science & Business Media, New York, USA **2012** p.43-44.

[115] P. E. Hemming, *C, H, N Micro-analysis: A Comparative Review of The Effects of Instrument Design on Analytical Performance*, Exeter Analytical Ltd.

[116] R. A. Nadkarni, *Modern Instrumental Methods of Elemental Analysis of Petroleum Products and Lubricants*, ASTM International, Baltimore, USA **1991**, p.35.

[117] Quantachrome Instruments, *AUTOSORB-1 AS1Win Version 1.50 Operating Manual*, *Boynton Beach, USA* **2004**.

[118] S. Brunauer, P. H. Emmett, E. Teller, *J. Am. Chem. Soc.* **1938**, 60, 309.

[119] S. Lowell, J. E. Shields, M. A. Thomas, M. Thommes, *Characterization of Porous Solids and Powders: Surface Area, Pore Size and Density*, Kluwer Academic Publishers, Dordrecht, Netherlands **2004**, p.111-112.

[120] H. Kral, J. Rouquerol, K. S. W. Sing, K. K. Unger, *Characterization of Porous Solids*, Elsevier Science, Amsterdam Netherlands **1988**, p.151-154.

[121] Y. Li, K. Li, G. Sun, *Mater. Lett.* **2011**, *65*, 1022.

[122] J. Wang, Q. Liu, *Nanoscale* **2014**, 6, 4148.

[123] J. Wang, I. Senkovska, M. Oschatz, M. R. Lohe, L. Borchardt, A. Heerwig, Q. Liu, S. Kaskel, *J. Mater. Chem. A* **2013**, 1, 10951.

[124] W. Shen, Y. He, S. Zhang, J. Li, W. Fan, *ChemSusChem* **2012**, *5*, 1274.

[125] J. Wang, A. Heerwig, M. R. Lohe, M. Oschatz, L. Borchardt, S. Kaskel, *J. Mater. Chem.* **2012**, *22*, 13911.

[126] M. Olivares-Marin, M. M. Maroto-Valer, *Greenhouse Gas. Sci. Technol.* **2012**, *2*, 20.

[127] H. An, B. Feng, S. Su, *International Journal of Greenhouse Gas Control* **2011**, 5, 16.

[128] R. Thiruvenkatachari, S. Su, H. An, X. X. Yu, *Progress in Energy and Combustion Science* **2009**, 35, 438.

[129] H. An, B. Feng, S. Su, *Carbon* **2009**, 47, 2396.

[130] W. Shen, S. Zhang, Y. He, J. Li, W. Fan, *J. Mater. Chem.* **2011**, 21, 14036.

[131] C. Lu, H. Bai, B. Wu, F. Su, J. F. Hwang, *Energy Fuels* **2008**, 22, 3050.

[132] F. Su, C. Lu, W. Cnen, H. Bai, J. F. Hwang, *Science of The Total Environment* **2009**, 407, 3017.

[133] X. He, J. A. Lie, E. Sheridan, M. B. Hagg, *Energy Procedia* 2009, 1, 261.

[134] X. He, M. B. Hagg, *Journal of Membrane Science* **2011**, 378, 1.

[135] G. Olofsson, Z. Ye, I. Bjerle, A. Andersson, *Ind. Eng. Chem. Res.* **2002**, *41*, 2888.

[136] J. Ludwinowicz, M. Jaroniec, *Carbon* **2015**, 82, 297.

[137] A. Chen, Y. Yu, Y. Zhang, W. Zang, Y. Yu, Y. Zhang, S. Shen, J. Zhang, *Carbon* **2014**, 80, 19.

[138] N. P. Wickramaratne, M. Jaroniec, *J. Mater. Chem. A* **2013**, 1, 112.

[139] R. Mead-Hunter, A. J. C. King, B. J. Mullins, *Langmuir* **2012**, *28*, 6731.

[140] H. Fu, *Carbon Fibre and Graphite Fibre*, Chemical Industry Press, Beijing, China **2010**. p.145.

[141] G. Socrates, *Infrared Characteristic Group Frequencies*, John Wiley & Sons, New York, USA **1980**.

[142] J. R. Pels, F. Kapteijn, J. A. Moulijn, Q. Zhu, K. M. Thomas, *Carbon* **1995**, *33*, 1641.

[143] I. Y. Jeon, H. J. Choi, L. S. Tan, J. B. Baek, *J. Polym. Sci. A Polym. Chem.* **2011**, 49, 2529.

[144] F. P. Richter, P. D. Caesar, S. L. Meisel, R. D. Offenhauer, *Ind. Eng. Chem.* **1952**, *44*, 2601.

[145] G. Liu, X. Li, J. W. Lee, B. N. Popov, *Catal. Sci. Technol.* **2011**, *1*, 207.

[146] G. Srinivas, V. Krungleviciute, Z. X. Guo, T. Yildirim, *Energ. & Environ. Sci.* **2014**, *7*, 335.

[147] N. Sun, C. Sun, H. Liu, J. Liu, L. Stevens, T. Drage, C. E. Snape, K. Li, W. Wei, Y. Sun, *Fuel* **2013**, *113*, 854.

[148] S. Deng, H. Wei, T. Chen, B. Wang, J. Huang, G. Yu, *Chemical Engineering Journal* **2014**, 253, 46.

[149] A. S. Ello, L. K. C. de Souza, A. Trokourey, M. Jaroniec, *Journal of CO_2 Utilization* **2013**, 2, 35.

[150] A. S. Ello, L. K. C. de Souza, A. Trokourey, M. Jaroniec, *Microporous and Mesoporous Materials* **2013**, 180, 280.

[151] M. G. Plaza, C. Pevida, B. Arias, J. Fermoso, M. D. Casal, C. F. Martin, F. Rubiera, J. J. Pis, *Fuel* **2009**, 88, 2442.

[152] London Plane Platanus x hispanica, http://www.kew.org/visit-kew-gardens/explore/attractions/trees?page_id=119

[153] H. Daun, *Produce Degradation: Pathways and Prevention*, Taylor & Francis, Boca Raton, USA **2005**, p.200.

[154] M.Roberts, M. J. Reiss, G. Monger, *Advanced Biology*, Nelson, Cheltenham, UK **2000**, p.15 & p.203.

[155] A. N. El-Hendawy, *Appl. Surf. Sci.* **2009**, *255*, 3723.

[156] C. Starr, R. Taggart, C. Evers, L. Starr , *Volume 4 - Plant Structure & Function (Biology the Unity & Diversity of Life)*, Cengage Learning, Belmont, UK **2012**, p.461.

[157] M. Riederer, L. Schreiber, *J. Exp. Bot.* **2001**, *52*, 2023.

[158] P. S. Nobel, *Physicochemical and Environmental Plant Physiology*, Elsevier Science, Oxford, UK **2009**, p.32.

[159] T. Fuller, Proton Exchange Membrane Fuel Cells 8: ECS Transactions: Volume 16, Electrochemical Society 2008.

[160] B. Zhu, K. Li, J. Liu, H. Liu, C. Sun, C. E. Snape, Z. Guo, *J. Mater. Chem. A* **2014**, *2*, 5481.

[161] Y. Zhao, L. Zhao, K. X. Yao, Y. Yang, Q. Zhang, Y. Han, *J. Mater. Chem.* **2012**, *22*, 19726.

[162] L. Liu, Q. F. Deng, X. X. Hou, Z. Y. Yuan, *J. Mater. Chem.* **2012**, *22*, 15540.

[163] L. Ohannesian, A. Streeter, *Handbook of Pharmaceutical Analysis*, Taylor & Francis, New York, USA **2001**, pp.200-201.

[164] G. Duman, Y. Onal, C. Okutucu, S. Onenc, J. Yanik, *Energy Fuels* **2009**, *23*, 2197.

[165] M. E. Argun, S. Dursun, M. Karatas, M. Guru, *Bioresource technol.* **2008**, *99*, 8691.

[166] C. Dawson, J. F. V. Vincent, A. M. Rocca, *Nature* **1997**, *390*, 668.

[167] A. Thogersen, J. H. Selj, E. S. Marstein, *J. Electrochem. Soc.* **2012**, *159*, D276-D281.

[168] H. Im, F. Rasouli, M. Hajaligol, *J. Agric. Food Chem.* **2003**, *51*, 7366.

[169] S. Inanaga, A. Okasaka, *Soil Sci. Plant Nutr.* **1995**, *41*, 103.

[170] S. M. Hong, S. H. Kim, K. B. Lee, *Energy Fuels* **2013**, 27, 3358.

[171] K. Xia, X. Tian, S. Fei, K. You, *International Journal of Hydrogen Energy* **2014**, 39, 11047.

[172] Y. Zhao, H. Ding, Q. Zhong, *Appl. Surf. Sci.* **2012**, 258, 4301.

[173] L. Y. Meng, K. S. Cho, S. J. Park, *Carbon Lett.* **2010**, 11, 34.

[174] L. Y. Meng, S. J. Park, *J. Colloid and Interface Sci.* **2012**, 386, 285.

[175] L. Y. Meng, S. J. Park, *J. Colloid and Interface Sci.* **2010**, 352, 498.

[176] I. Y. Jeon, Y. R. Shin, G. J. Sohn, H. J. Choi, S. Y. Bae, J. Mahmood, S. M. Jung, J. M. Seo, M. J. Kim, D. W. Chang, *P. Natl. A. Sci.* **2012**, *109*, 5588.

[177] S. Stankovich, D. A. Dikin, R. D. Piner, K. A. Kohlhaas, A. Kleinhammes, Y. Jia, Y. Wu, S. T. Nguyen, R. S. Ruoff, *Carbon* **2007**, 45, 1558.

[178] Z. Q. Li, C. J. Lu, Z. P. Xia, Y. Zhou, Z. Luo, *Carbon* **2007**, 45, 1686.

[179] A. Lerf, H. He, M. Forster, J. Klinowski, *J. Phys. Chem. B* **1998**, *102*, 4477.

[180] D. R. Dreyer, S. Park, C. W. Bielawski, R. S. Ruoff, *Chem. Soc. Rev.* **2010**, *39*, 228.

[181] Y. Zhu, S. Murali, M. D. Stoller, K. J. Ganesh, W. Cai, P. J. Ferreira, A. Pirkle, R. M. Wallace, K. A. Cychosz, M. Thommes, *Science* **2011**, *332*, 1537.

[182] L. L. Zhang, X. Zhao, M. D. Stoller, Y. Zhu, H. Ji, S. Murali, Y. Wu, S. Perales, B. Clevenger, R. S. Ruoff, *Nano Lett.* **2012**, *12*, 1806.

[183] M. D. Stoller, S. Park, Y. Zhu, J. An, R. S. Ruoff, *Nano Lett.* **2008**, *8*, 3498.

[184] W. Chen, L. Yan, P. R. Bangal, *J. Phys. Chem. C* **2010**, *114*, 19885.

[185] Y. L. Huang, H. W. Tien, C. C. Ma, S. Y. Yang, S. Y. Wu, H. Y. Liu, Y. W. Mai, *J. Mater. Chem.* **2011**, *21*, 18236.

[186] Y. Zhu, S. Murali, W. Cai, X. Li, J. W. Suk, J. R. Potts, R. S. Ruoff, *Adv. Mater.* **2010**, *22*, 3906.

[187] R. Wang, P. Wang, X. Yan, J. Lang, C. Peng, Q. Xue, *ACS Appl. Mater. Interfaces* **2012**, *4*, 5800.

[188] W. Hao, E. Bjorkman, M. Lilliestrale, N. Hedin, *Appl. Energ.* **2013**, *112*, 526.

[189] K. C. Kemp, V. Chandra, M. Saleh, K. S. Kim, *Nanotechnology* **2013**, *24*, 235703.